

ABSTRACT

Title of dissertation: DESIGN OF THREE DEGREES-OF-FREEDOM
MOTION STAGE FOR MICRO MANIPULATION

Yong-Sik Kim, Doctor of Philosophy, 2014

Dissertation directed by: Professor Satyandra K. Gupta
Department of Mechanical Engineering

A miniaturized translational motion stage has potentials to provide not only performances equivalent to conventional motion stages, but also additional features from its small form factor and low cost. These properties can be utilized in applications requiring a small space such as a vacuum chamber in a scanning electron microscopy (SEM), where hidden surface can decrease by manipulating objects to measure. However, existing miniaturized motion stages still have several cm³ level volumes and provide simple operations.

In this dissertation, Micro-electro-mechanical systems (MEMS)-based motion stages are presented for micro-scale manipulations and related applications. Since most MEMS based multiple degrees-of-freedom (DOFs) motion stages still remain for in-plane motions, a nested structure approach is utilized to implement both in-plane motions and out-of-plane motions. One independent stage is embedded into another stage with structural and electrical isolations among engaged stages and MEMS actuators and displacement amplifiers are also investigated for reasonable performance.

3-axis motions are divided into two in-plane motions and one out-of-plane motion; an in-plane 1 DOF motion stage (called an X-stage) and one out-of-plane 1 DOF motion stage (called a Z-stage) are designed and characterized experimentally. Based on the two stages, the XY-stage is designed by merging one X-stage into the motion platform of the other X-stage with a different orientation (called an XY-stage). With this nested approach, the fabricated XY-stage demonstrated in-plane motions larger than 50 μm with ignorable coupled motion errors. Based on this nested approach, the 3-axis motion stage is also implemented by utilizing the nested structure twice; integrating the Z-stage with the motion platform of the XY-stage (called an XYZ-stage). The XYZ-stage demonstrated out-of-plane motions about 23 μm as well as the in-plane motions.

Two presented motion stages have been utilized in the manipulation of micro-scale object by the cooperation of the two XY-stages inside a SEM chamber. The large motion platform of the X-stage is also utilized in a parallel plate type rheometer to measure the material properties of viscoelastic materials.

DESIGN OF THREE DEGREES-OF-FREEDOM MOTION STAGE
FOR MICRO-MANIPULATION

By

Yong-Sik Kim

Dissertation submitted to the Faculty of the Graduate School of the
University of Maryland, College Park in partial fulfillment
of the requirements for the degree of

Doctor of Philosophy

2014

Advisory Committee:

Professor Satyandra K. Gupta, Chair/Advisor

Dr. Nicholas G. Dagalakis, Co-advisor

Professor Hugh A Bruck

Professor Don L. DeVoe

Associate Professor Sarah Bergbreiter

Associate Professor Christopher Cadou (Dean's representative)

© Copyright by
Yong-Sik Kim
2014

Dedication

to my wonderful family

Acknowledgments

First and foremost I would like to thank Dr. Satyandra K. Gupta, my advisor and mentor for giving me the opportunity to conduct research under his guidance. His boundless energy and attitude helped me refining my skills for better research every single day. His wonderful analytic skills and motivational power helped in solving challenging research issues and overcome obstacles during the course of my dissertation.

This dissertation is the result of the collaboration with MEMS groups at Intelligent System Division in National Institute of Standards and Technology (NIST). I would like to express my thanks to Dr. Nicholas G. Dagalakis for providing me constant support in conducting challenging experiments with MEMS sensors and actuation mechanisms. His close monitoring in conducting experiments and thoughtful insights helped me conceptualizing various methods presented in this dissertation.

I would like to thank Dr. Hugh A. Bruck, Dr. Don L. DeVoe, Dr. Sarah Bergbreiter, and Dr. Christopher Cadou for serving in my dissertation committee despite of having busy academic and research responsibilities of their own. I would also take this opportunity to thank Dr. Chiara Ferraris for supplying a cementitious reference material to conduct experiments with MEMS-based rheometer.

I also want to thank Dr. Lei Chen in NIST Center for Nanoscale Science and Technology (CNST) for supporting my MEMS fabrication works. I am also grateful to Dr. Seung Ho for being prompt in answering all my questions despite of his busy schedule. Many thanks to University of Maryland, Department of Mechanical

Engineering, and the Institute of Systems Research for providing research facilities and administrative supports.

I would also like to thank Dr. Richard Gates for his valuable advice and support on the experiments, when the X-, XY-, Z-, and XYZ-stages are experimentally tested for their own frequency response. I would also like to thank Dr. Sagar Chowdhury, Dr. Petr Svec, Dr. Arvind Ananthanarayanan, and Dr. Atul Thakur for their constructive comments and careful supports.

I would like to thank Korean American Internet Fishing Club for me to look at my researches with various points of views. I am also thankful to my family for all the wishes that helped me focus on my PhD plan. Finally, I would like to extend my deepest gratitude to my parents, Jae-Hyun Kim and Hong-Sun Jeon for their emotional support and affection throughout my life.

Table of Contents

List of Tables	viii
List of Figures	ix
Chapter 1 Introduction	1
1.1 Background	1
1.2 Motivation	5
1.3 Research issues	9
1.4 Dissertation scope and outline	11
Chapter 2 Literature Review: MEMS based motion stages	14
2.1 MEMS in-plane electrothermal actuators	17
2.2 MEMS based out-of-plane electrothermal actuators	28
2.3 MEMS-based electrostatic actuators	33
2.4 MEMS-based electromagnetic actuators	40
2.5 Piezoelectric actuators	43
2.6 Characterization of the MEMS motion stage	45
2.6.1 Range of motion	46
2.6.2 Force	48
2.6.3 Mechanical amplifier	49
2.6.4 Degrees of freedom (DOFs) and coupling errors	53
2.6.5 Kinematic mechanisms	60
2.6.6 Resolution	61
2.6.7 Natural frequency at low frequency range	62
2.6.8 Bulk micromachining: Silicon-on-insulator Multi-User Multi-Processes (SOI-MUMPs)	63
2.7 Summary	65
Chapter 3 MEMS based thermally actuated single DOF stage	70
3.1 Introduction	70
3.2 Design of the X-stage	73
3.2.1 The analysis for the dual-bent beam electrothermal actuator	74
3.2.2 The motion platform with eight folded springs	78
3.2.3 Design constraints; thermal limit	79
3.3 Finite element analysis (FEA)	80

3.4 Fabrication	83
3.5 Experimental results.....	85
3.6 Viscoelastic material testing for a SRM 2492	86
3.7 Summary	91
Chapter 4 Optimization of MEMS electrothermal actuator for a single DOF stage.....	93
4.1 The flexure hinge design.....	94
4.2 The lever ratio	99
4.3 The number of beam in the actuator	101
4.4 The analytic analysis for the electrothermal actuator	102
4.5 Design constraint: buckling	105
4.6 Design constraint: thermal melting down	107
4.7 The optimization process for the displacement of the X-stage	108
4.8 Finite element analysis (FEA)	111
4.9 Experimental results.....	114
4.9.1 The range of motion of the MEMS X-stage.....	115
4.9.2 The frequency response	116
4.10 Summary	117
Chapter 5 MEMS-based in-plane 2-DOF motion stage.....	119
5.1 Introduction.....	119
5.2 Design of the XY-stage.....	122
5.2.1 The MEMS design of the SKM	124
5.2.2 The mathematical analysis for the chosen single DOF stage.....	127
5.2.3 Design constraints; thermal melting and buckling.....	133
5.3 Finite elements analysis (FEA).....	136
5.4 Fabrication	141
5.5 Experimental characterization of the MEMS XY-stage	142
5.5.1 The range of motion of the MEMS XY-stage and its coupled motion error	142
5.5.2 The frequency response	145
5.6 The multi-probe finger manipulation system.....	147
5.7 Summary	149
Chapter 6 MEMS-based out-of-plane motion stage	151
6.1 Introduction.....	151
6.2 Design of the motion stage	155

6.3 Design analysis	157
6.4 Finite element analysis (FEA)	161
6.4.1 The optimization of the step feature	161
6.4.2 Stress distribution.....	163
6.4.3 The frequency response, stiffness, and maximum force of the motion stage	164
6.5 Fabrication	166
6.6 Experimental results.....	168
6.7 Discussion.....	173
6.8 Summary	175
Chapter 7 MEMS-based 3-DOFs motion stage	176
7.1 Introduction.....	176
7.2 Design of the 3-DOF motion stage	178
7.2.1 The X-stage and the Y-stage.....	182
7.2.2 The Z-stage	187
7.3 Fabrication	192
7.4 Experimental characterization of the MEMS 3 axis-stage.....	197
7.4.1 The range of motion.....	197
7.4.2 Compensation for reducing coupled motion errors.....	201
7.4.3 The frequency response of the proposed XYZ-stage	204
7.4.4 The characteristics of the proposed XYZ-stage	205
7.5 Summary	207
Chapter 8: Conclusions	209
8.1 Intellectual contributions	209
8.2 Anticipated Benefits.....	211
8.3 Future Directions	213
Glossary	217
Bibliography	218

List of Tables

Table 1.1: PKM and SKM [38].....	7
Table 2.1: Electrothermally actuated micro- and nano-positioning stages for in-plane motions.....	24
Table 2.2: Electrothermally actuated micro- and nano-positioning stages for out-of-plane motions.....	31
Table 2.3: Electrostatic actuators and electrostatically actuated micro- and nano-positioning stages.....	34
Table 2.4: Electromagnetic actuators and related micro- and nano-positioning stages.....	42
Table 2.5: Piezoelectric actuators and related micro- and nano-positioning stages.....	44
Table 2.6: Multi-DOFs MEMS-based positioning stages.....	59
Table 3.1: The dimensional range of the design parameters.....	79
Table 4.1: Three different flexure hinge models.....	98
Table 4.2: The dimensional range of the design parameters.....	110
Table 4.3: The dimensional range of the design parameters.....	111
Table 5.1: The dimensional range of the design parameters.....	134
Table 5.2: Material properties of silicon.....	136
Table 5.3: The coupled motion between the X- and Y-stages.....	145
Table 6.1: The design parameters in the Z-actuator.....	160
Table 7.1: 3 DOF MEMS-based positioning stages.....	178
Table 7.2: Design parameters in the X-stage, the Y-stage and the Z-stage.....	183
Table 7.3: The maximum displacements and the coupled motions of the XYZ-stage without compensation.....	199
Table 7.4: MEMS-based positioning stages in specific cases.....	206

List of Figures

Figure 1.1: ANSxyz50 Attocube.....	3
Figure 1.2: PI H-840 6-Axis Hexapod.....	4
Figure 2.1: PI P-611.3 NanoCube® XYZ Piezo Stage Compact Multi-Axis Piezo System for Nanopositioning.....	15
Figure 2.2: An electrothermal actuator based on a combination of a hot arm and a cold arm	17
Figure 2.3: The chevron type electrothermal actuator	20
Figure 2.4: The cascade type based on bent-beam actuators	21
Figure 2.5: Electrostatic actuator parallel plate type.....	33
Figure 2.6: Electrostatic comb drive type	39
Figure 2.7: An electromagnetic actuator.....	40
Figure 2.8: Piezoelectric poisoning stage	43
Figure 2.9: The inchworm type electrothermal actuator.....	50
Figure 2.10: The lever between an actuator and a motion platform	51
Figure 2.11: A compliant displacement amplifier	52
Figure 2.12: A parallel kinematic XY stage	54
Figure 2.13: An implementation of a parallel kinematic XY stage	55
Figure 2.14: A schematic diagram of a serial kinematic XY stage.....	57
Figure 2.15: Cross sectional view of a structure with a SOI-MUMPs.....	64
Figure 3.1: A MEMS based X-stage for rheological measurement set-up	73
Figure 3.2: 3D CAD models of the 1-DOF motion stage	74
Figure 3.3: The conceptual design of the X-stage	75
Figure 3.4: the design of the dual bent-beam electrothermal actuator	77
Figure 3.5: The folded spring design	78
Figure 3.6: FEA result of the displacement by driving voltages.....	81
Figure 3.7: FEA simulation results by the temperature rise of 542.6 °C	82
Figure 3.8: The SEM images of a fabricated X- stage.....	83
Figure 3.9: The SEM images of a fabricated 1-DOF motion stage	84
Figure 3.10: Experimental results of the displacement of the 1-DOF motion	86
Figure 3.11: A Bingham model plot	88
Figure 3.12: Measured experimental data of SRM 2492 from the presented method in this study	91
Figure 3.13: The combination of experimental data with the results previously reported.....	91
Figure 4.1: The schematic diagram of the X-stage	94
Figure 4.2: The flexure hinge compliant mechanism.....	95
Figure 4.3: The schematic diagram of the lever mechanism adapted in the XY-stage.....	99
Figure 4.4: The expected maximum displacement with various lever ratios and beam numbers(n)	102
Figure 4.5: the design parameters engaged in the adapted electrothermal actuator.....	103

Figure 4.6: The calculated displacement of the motion platform with the excitation of the temperature rise of 530 °C (in μm unit)	112
Figure 4.7: The calculated stress distribution over the X-stage	113
Figure 4.8: The optical microscopic images of the MEMS based X-stage.....	115
Figure 4.9: The experimentally measured displacement of fabricated X-stages	116
Figure 4.10: Frequency response of the X-stage.....	117
Figure 5.1: The schematic diagrams of the XY stage	123
Figure 5.2: SEM images of the SKM XY-stage	125
Figure 5.3: SEM images of the electric path over the flexure hinge.....	126
Figure 5.4: The schematic diagrams of the actuator and the rotational flexure	128
Figure 5.5: the lever mechanism adapted in the XY-stage	131
Figure 5.6: FEA of the proposed XY stage.....	139
Figure 5.7: FEA of the proposed XY stage.....	140
Figure 5.8: Fabrication sequence of SOI wafer for the XY stage.....	141
Figure 5.9: Experiments with fabricated XY-stages	144
Figure 5.10: Frequency response bode diagram	146
Figure 5.11: A multi-finger manipulation system with a 2x1 layout.....	148
Figure 5.12: A multi-finger manipulation system.....	149
Figure 6.1: 3D models of the Z-stage	156
Figure 6.2: Diagrams for the analysis	158
Figure 6.3: A comparison of out-of-plane deformation from equation (6.1) and FEA as a function of the position along the beam from one end.....	159
Figure 6.4: The out-of-plane displacement based on the step length and step	162
Figure 6.5: Stress distribution calculated by finite element analysis	164
Figure 6.6: The mode shape of the Z-stage at its first resonant mode	165
Figure 6.7: The fabrication flow	166
Figure 6.8: The scanning electron microscope (SEM) images of the Z-stage	167
Figure 6.9: Experimentally measured displacement results with analytic ones.....	169
Figure 6.10: Measured deformation profiles in the actuation	170
Figure 6.11: Measured deformation profiles in the actuation	171
Figure 6.12: Reliability test.....	173
Figure 7.1: Integration strategy of three individual stages for the XYZ-stage	179
Figure 7.2: The schematic diagram of the X-stage	181
Figure 7.3: Mechanical response by the temperature rise of 530 °C in finite element analysis	186
Figure 7.4: The design of the Z-actuator from the Z-stage	188
Figure 7.5: Experimentally measured out-of-plane displacement of the Z-actuator.....	189
Figure 7.6: The mechanical response of the Z-actuator.....	191
Figure 7.7: SEM images of the fabricated full XYZ-stage	192
Figure 7.8: SEM images of the fabricated XYZ-stage.....	194

Figure 7.9: SEM images of the backside of the fabricated XYZ-stage	196
Figure 7.10: Experimental results of the X-stage and the Y-stage motion	198
Figure 7.11: Experimental results of the Z-axis displacement in the XYZ-stage	201
Figure 7.12: The compensation of the coupled motion error in the X-stage by the motion of the Y-stage; the red dots for original behavior and blue dots for compensated behavior	204
Figure 8.1: A hexapod for 6 DOF motion based on three XY-stages [117]	213
Figure 8.2: Three finger manipulation system	215

Chapter 1 Introduction

1.1 Background

A motion stage is a high-precision positioning device to restrict an object to designated motions. Moving or positioning an object within an acceptable range is so important and popular that motion stages have been utilized in a variety of applications from piezo-actuated motion stages of a few cm^3 [1,2] to an electrically actuated robot crane that is more than a hundred meters tall [3]. Among various applications, motion stages can also be utilized in micro- and nano-meter scale applications, including biological testing and manipulation [4–7], optical accessing and implementation [8–12], micro-structure assembling [13–16], and metrological utilization [17–19] for their nanometer-level accuracy and resolutions. For these applications, conventional precision manufacturing technologies have been used, but they are limited by their minimum volume size and capabilities. In these cases, the motion stages have come from micro-electro-mechanical systems (MEMS) [20], which can be interesting alternatives for their implementation. MEMS fabrication technologies initially came from semi-conductor industries and are based on an additive manufacturing concept, so they are equipped with various etching technologies, including a deep silicon etcher [21], depositing methods like chemical vapor deposition (CVD), and designing with contact lithography [20].

The MEMS-based motion stage has its own advantages. First, they have the capability to provide the performance or characteristics equivalent to a conventional motion stage in micro-level world. MEMS-based motion stages are particularly known for their nano-meter level accuracy and resolution, so they have been utilized in

applications requiring precision positioning such as controlling an optical fiber [10,22–24], manipulating a biological cell [6,7], assembling nano-structures [14,25], and scanning with optical lenses [8,11]. Second, the small form-factor of the motion stage inherited from MEMS technologies can extend its application field. This property makes MEMS-based motion stages useful, when existing conventional motion stages are too big to install. For example, a motion stage is beneficial for the manipulation of an object under a scanning electron microscope (SEM) whose vacuum chambers are too small for the installation of conventional motion stages. However, there are a few conventional motion stages with a small footprint. Attocube [1], shown in Fig. 1.1, is the smallest motion stage yet reported and is capable of generating XYZ motions up to 5 mm with a volume of $24 \times 24 \times 25 \text{ mm}^3$. However, they are very rare and also cost more than fifty thousand dollars per stage. Considering these properties, MEMS-based motion stages can offer a reasonable and affordable alternative in micro-level or nano-level applications [26]. Third, the batch process in MEMS foundries is favorable in mass-production, which can reduce the total cost and make MEMS-based devices disposable and portable. With expensive and bulky motion stages, the cooperation among multiple motion stages is hard to implement due to the gap between them and their cost.

In summary, contrary to conventional motion stages, MEMS-based motion stages have the following advantages; an affordable price, nano-meter level accuracy, and a small form factor. With these features, MEMS-based motion stages can be utilized in applications that require strong portability or disposability or in areas with limited space for motion stages. Due to these features, MEMS-based motion stages have been used widely in applications such as manipulation [7,13,27,28], laser control [10], precision

positioning for scanning electron microscopy (SEM) [29–32], atomic force microscopy [19,33], scanning tunneling microscopy [13], and micro-grippers [6,7,28,34–36].



Figure 1.1: ANSxyz50 Attocube [1]

Parallel kinematic mechanisms (PKM) and serial kinematic mechanisms (SKM) are two principal kinematic mechanisms widely used in conventional motion stages. An example of a 6 Degrees-of-freedom (DOF) motion stage (called a Stewart platform or a hexapod), shown in Fig. 1.2, is implemented based on a PKM [37], which controls all six actuators at a same time to move an end-effector or a motion platform to a desired position with six DOF. In a PKM, the end effector is connected to all the actuators engaged in the system. With this approach, any motion error caused by one actuator can be compensated for by the others. Due to this feature, this PKM has been frequently used for applications that require higher DOF, including rotational motions. Contrary to PKM, SKM is widely used in 3 DOF or less for its simplicity. A typical implementation of 3 DOF motion based on SKM is shown in Fig. 1.1 [1], where three single DOF motion stages are stacked for three DOF motions. This stacked structure is straightforward to design and its control scheme is simple and easy to use. However, the wiring or electric

connection of the stacked stages can cause motion errors due to wire stiffness. Both PKM and SKM have their own advantages and disadvantages, so an appropriate selection is needed for a successful design process.



Figure 1.2: PI H-840 6-Axis Hexapod [37]

In summary, a MEMS-based motion stage has various advantages over conventional motion stages, such as nano-meter level resolution or accuracy, smaller form-factor, and lower cost. That said MEMS-based motion stages also have their own disadvantages or weakness, like short travel distances or coupled motion errors from their limited fabrication technologies. However, with improved design and appropriate manufacturing approaches, MEMS-based motion stages can overcome their limitations and their application has been extended in both industry and research.

1.2 Motivation

Many design constraints about MEMS motion stages come from the fact that their fabrication methods evolved from semi-conductor industries, which are well known for their planar circuitries. Existing MEMS-based motion stages based on planar structures or monolithic designs provide less flexibility and performance than conventional motion stages based on 3D spatial structures.

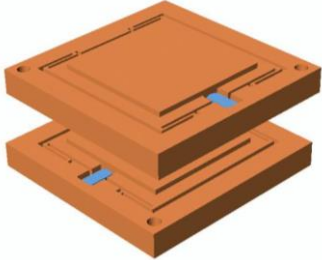
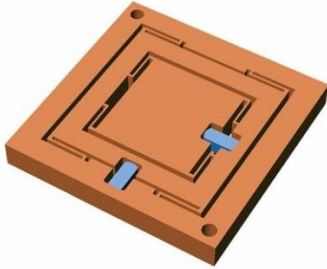
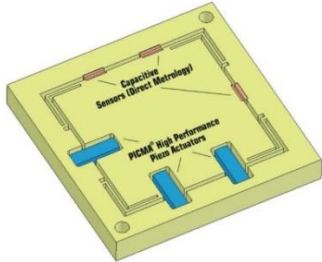
It is important to investigate the implementation approaches available for MEMS-based motion stages. Since many MEMS devices remain in a monolithic or planar structure, indirect approaches are frequently used to improve the capabilities of MEMS motion stages. Three commonly used implementations for MEMS and their characteristics are described in Table 1.1. Type A is a stacked structure based on SKM, with which 2 DOF motion is implemented by stacking one 1 DOF motion stage onto another. It is also possible to build a conventional 3 DOF motion stage in the stacked structure. The advantage of this approach, using the existing 1 DOF motion stage without significant modification, is that it provides straightforward direct control for 2 DOF motion. However, this structure can have a higher center of gravity and the manual assembly of the upper level of the stacked structure can be challenging in micro-scale MEMS devices because conventional bulky manipulators can damage MEMS devices accidentally. It is also hard to align two MEMS devices accurately. Moreover, the electrical connections or cabling of the upper structure present another issue. In stacked structures, an upper structure should be free to move or float. However, wire stiffness is considerable compared with the stiffness of MEMS motion stages. Thus, this can result in translational or rotational motion error. In addition, the wiring bonding process itself

requires a few mg of forces, which can damage MEMS devices easily because they have only a few N/m levels of stiffness.

Type B is a nested structure, which is a modified version of the stacked structure in type A. Instead of stacking one onto the other, one is fully embedded to the other. With this, nested structure, the MEMS device has improved dynamics and a lower center of gravity than the stacked structure. The most beneficial advantage of a nested structure, however, is that it is most compatible with MEMS fabrication technologies, allowing a manual assembly process to be avoided. In addition, electric wiring issues can be corrected with embedded electric paths. When an appropriate stage for out-of-plane motion is engaged, this approach has the capability of providing XYZ motions in MEMS. Except for these features, type B still has almost the same characteristics as type A. However, instead of the homogeneous stages used for type A, heterodyne stages are required to embed one stage into the others. This difference among the engaged stages can result in different behavior along the X and Y axes.

Type C is a typical implementation of PKM for a 2 DOF motion stage. In type C, all actuators are connected directly to a motion platform, as shown in Table 1.1. Any motion error during its operation can be compensated for by multiple actuators engaged for accurate motions. However, for successful operation, type C requires accurate mathematical models between its inputs and the corresponding outputs. Type C is very compatible with MEMS fabrication technologies and especially is perfect for generating in-plane 2 DOF motion or XY-motions [13] or $XY\theta$ motion stages [11]. However, the motion stage including out-of-plane motion or XYZ-motions is quite difficult to implement in MEMS-based motion stages on this PKM.

Table 1.1: PKM and SKM [38]

	Design	Mechanism	Advantage	Disadvantage
A		SKM	Modular, simple, ease to design and build,	More inertia than C, Higher center of gravity, Moving cable or wires Difficult to implement in MEMS
B		SKM	Lower of center of gravity Better dynamics than B	Asymmetric dynamic along X and Y axes Same disadvantage to A
C		PKM	Better repeatability than A and B, Flatness, Accurate motion Easy to implement in MEMS for in-plane motion only	Complex controller than A and B, Embedded sensors or pre-processing are needed Difficult to implement in MEMS for out-of-plane motion

It is true that 3 DOF or 3-axis motions are more efficient than pure in-plane motions in many applications, such as manipulation of 3D objects or bio cells, etc, because raising an object and jumping over another target are such common

manipulations and require spatial motions. Thus, it is worth developing a MEMS-based motion stage capable of generating 3-axis motion or XYZ motions.

A considerable number of MEMS motion stages have been designed based on type C, which will be discussed in detail in Chapter 2. Contrary to this, it is important to note that only a few MEMS-based motion stages are available based on SKM. Since SKM has its own advantages, like simple control and an easy design, and many commercial products for 3 DOF motions or less have been developed based on SKM, it is worthwhile to design and build a motion stage based on SKM in MEMS. With these considerations in mind, it is also beneficial at least one reliable method of reusing existing MEMS devices. In designing 3 DOF motion stages, it saves effort and reduces design steps to find and use appropriate 1 DOF motion stages. It is well known that most existing MEMS devices are so dedicated to a specific application that it might be better to develop a whole new one rather than modify an existing MEMS design. However, reusing an existing motion stage design will not only save significant time spent designing the multi-DOF motion stages, but also guarantees a minimum level of performance inherited from the chosen motion stage. Thus, as will be shown, an XYZ-motion stage is implemented by selecting and optimizing existing motion stages and then merging them together based on a nested structure. Even when there is no appropriate motion stage available, this integration concept is still useful by dividing the design process of an XYZ motion stage into three components; the X, Y, and Z stages, respectively. This “divide-and-conquer” design approach is also beneficial in developing a complex design because two or more sub-problems become simple enough to be solved directly.

In addition to this, it is also beneficial to develop motion stages based on electrothermal actuators. Currently more than 95 % motion stages in MEMS are based on electrostatic actuators because of their fine motion at high frequencies and their simple design, as discussed in the following chapter. Since each actuation mechanism has its own advantages and disadvantages, thermally actuated motion stages can be beneficial due to their higher force level, higher reliability in harsh conditions, and increase stiffness as compared to electrostatically actuated motion stages. These features are desirable especially in micro-manipulation and dirty environments.

Based on these considerations, it would be beneficial to develop MEMS-based XYZ motion stages with new features: a nested structure based on SKM, electrothermal actuators, a mechanical displacement amplifier, or a lever and a motion platform. For a successful design, it is necessary to develop a dedicated analysis for an electrothermal actuator and a mechanical displacement amplifier and algorithms for coupled motion errors and reasonable implementation by introducing new features such as floating anchors, supporting frames, and levers to overcome any existing problems.

1.3 Research issues

This dissertation addresses the problems and challenges of existing MEMS based motion stages. The main research issues this study will address are as follows:

1. Characterize the integration of thermal actuation with a transmission mechanism to realize a high force, large displacement 1 DOF motion stage: The XYZ motion stage presented in this dissertation is composed of two X-stages and one Z-stage. For desirable performance, like high force or large displacement, a similar 1 DOF

motion stage (called an X-stage) has been selected from previous research and optimized to meet its expected performance. Given that certain characteristics of the XYZ-stage are inherited from the engaged stages, its basic characteristics depend on the X-stage. The electrothermal actuator in the X-stage is also well known for its few milli-Newton level force and high reliability in a dusty environment. However, its range of motion is less than 20 μm , which is relatively short in micro-manipulation or other applications. In order to overcome this, a certain amount of force must be converted into additional displacement via a mechanical displacement amplifier (which in this dissertation is a lever). The analysis and the optimization of the electrothermal actuator in this dissertation are based on the fact that the actuator is under external mechanical load from the motion platform and the lever.

2. Model the thermal actuation under an external load to implement a 1 DOF motion stage with a low level of stiffness: The motion platform of the X-stage is designed to support a nested structure, but this can also be used as an interface for other applications. One expected application of the X-stage is a parallel plate-type rheometer, which measures the material properties of viscoelastic materials by applying shear force and measuring its response. In order to apply shear force properly, it is necessary to know the area contacting a target material. This can be implemented by placing a target material between the motion platform and one stationary plate. In order to use the X-stage as a sensor, it should respond sensitively to changes in external resistance. To achieve this, the X-stage is modified to have more flexibility in this application.

3. Model and control of coupled motion error in 2 DOF and 3 DOF actuations: An XY-stage is implemented by embedding one X-stage into the motion platform of another X-stage with a different orientation. For successful implementation, any side-effects created by this integration should be minimized. Expected drawbacks include a reduction in its range of motion and the increment of coupled motion error. Successful mechanical isolation among the engaged stages can minimize any reduction of its original performance and avoid coupled motion error as much as possible. This study introduces additional features for this isolation to support the main components of the XY-stage.
4. Modeling the thermal actuation for 1 DOF out-of-plane motion based on standard bulk micromachining technologies: An out-of-plane single DOF motion stage is rare in its ability to provide performance similar to an adapted X-stage, as will be shown in the literature review. Based on design considerations, including successful integration capability, similar displacement and stiffness to the X-stage, a Z-stage is designed and introduced in this dissertation. The presented Z-stage will be built based on the same fabrication methods used for the X-stage and demonstrate similar range of motion and stiffness.

1.4 Dissertation scope and outline

There are various MEMS-based motion stages designed for material testing, micro-manipulation, and metrology, etc. However, this dissertation focuses on some interesting features that have not been well supported by existing MEMS-based devices. For a reasonable design process, this dissertation focuses on the following aspects of MEMS-based motion stages.

1. For the characterization of the motion stage, maximum available displacement or force, frequency response, and coupled motion errors are taken into consideration.
2. The total chip size or footprint is less than 10 mm x 10 mm and the electrothermal actuator is also less than 2 mm in length, because the SEM for micro-manipulation has a vacuum chamber providing a volume of less than 50 mm x 50 mm x 70 mm. In order to be installed inside a scanning electron microscope (SEM) and operated efficiently, the total footprint of a MEMS-based motion stage needs to be less than 10 mm x 10 mm.
3. Most MEMS fabrication technologies used in this dissertation are bulk micromachining and the main processes in this dissertation follow Silicon-On-Insulator Multi-User-Multi-Processes (SOI-MUMPs [39]), which are standard and without any additional processes like wafer bonding or Focused Ion Beam milling (FIB). In these processes, the starting material is an SOI wafer, which consists of three layers: a top silicon layer (called a device layer), middle silicon dioxide layer (called a buried oxide layer), and bottom silicon layer (called a handle layer). The top silicon layer is 30 μm fixed for commercially available products.
4. The combination of electrothermal actuators and electrostatic actuators can reduce any side-effects created by the nested structure due to their different operation principles. However, for simplicity, only electrothermal actuation is discussed in this dissertation.
5. The applications for which this dissertation aims are demonstrating a manipulation of a micro-scale object inside SEM and utilizing the presented motion stages for commercial applications.

The rest of the dissertation is organized as follows. The next chapter surveys literature on MEMS-based motion stages, different actuation mechanisms, and various displacement amplifiers. Chapter 3 presents the design and optimization of the X-stage for a specific application; rheological measurement of cementitious materials. Chapter 4 extends the X-stage discussed in Chapter 3 for a large stroke and a stiff structure, which will be utilized for the nested structure. Chapter 5 describes the XY-stage based on the X-stage in Chapter 4 for designing grippers for cooperated manipulation. Chapter 6 describes a novel out-of-plane motion stage, or Z-stage, for a nested structure. Compared to previously developed Z-stages, this Z-stage is designed to provide similar performance to the X-stage discussed in Chapter 4 and be compatible with the fabrication processes used for the X-stage. Chapter 7 describes the XYZ-stage based on the integration of the XY-stage in Chapter 5 and the Z-stage in Chapter 6 with a dual nested structure. With this dual nested structure, its mechanical behavior is monitored to discover any side-effects. Finally, Chapter 8 summarizes the contributions of the current work, highlights anticipated benefits of this research in micro-manipulation or further applications as well as metrology, and outlines future work.

Chapter 2 Literature Review: MEMS based motion stages

In this chapter, the literature related to the dissertation goal and scope described in Chapter 1 has been surveyed. A MEMS-based XYZ motion stage is presented to generate linear translational motions along the X, Y, and Z axes with reasonable characteristics for manipulation of micro-objects. This motion stage is called an XYZ-stage in this dissertation. Relevant researches are described based on their importance and similarity to this dissertation.

A typical motion stage is composed of actuators, a motion platform (or an end-effector) and mechanical guides between them. Actuators are supposed to convert electric signal, hydraulic pressure or compressed air into a physical motion. With these conversions, they can control the position of a motion platform. In a motion stage, the position change of a motion platform relative to a base (or a fixed reference) is a main concern. Various interfaces can be adapted in a motion platform depending on their applications. For example, robotic arms prefer to use a gripper or a jig as their end effectors to manipulate objects efficiently. In motion stages, a flat simple rectangular plate, shown in Fig. 2.1, is preferred to place an object.

This motion platform is also linked to mechanical guides, which are designed to restrict the unnecessary motion of a motion platform and allow only the relevant motions, which determines the mechanical relationship between the motion platform and the actuators. Ball bearing, roller bearing, flexure, and cylindrical sleeve are frequently used as mechanical guides in conventional motion stages.



Figure 2.1: PI P-611.3 NanoCube® XYZ Piezo Stage Compact Multi-Axis Piezo System for Nanopositioning [2]

When the motion platform needs to be controlled more than one direction, multi-degrees-of-freedom (DOFs) motion stages can be used. The multi-DOF motion stage can be built by either using multiple single DOF motion stage simultaneously or a dedicated multi-DOF motion stage. “Two-axis” motion stage is able to generate in-plane 2 DOFs motion and called as an XY-stage. “Three-axis” motion stage can produce 3 DOFs motions along X, Y, and Z axes and be called as an XYZ-stage. Sometimes, rotational motion can be included called a rotary stage. The motion stage can produce four or more DOFs motion when it is combined with rotary stages. When multiple single DOF motion stages are integrated for multi-DOF motion stages, the integration method and the properties of single DOF motion stages determine whole characteristics of a motion stage.

In section 2.1 and 2.3, MEMS electrostatic actuators and electrothermal actuators for in-plane motions are surveyed. These actuators are widely used in MEMS applications and have demonstrated reasonable performances. Advantages and drawbacks of each actuator are summarized and listed in Table 2.1 and Table 2.3 from their applications.

In section 2.2, out-of-plane motion stages based on electrothermal actuators are surveyed. The presented XYZ-stage in this dissertation is composed of two in-plane motions along X and Y axes and one out-of-plane motion along Z axis. For successful integration among them, it is necessary to find candidates appropriate for this integration. To achieve this, current out-of-plane actuators are reviewed and compared. Current MEMS fabrication technologies are also taken into consideration, because of their limited capabilities in MEMS.

In section 2.4 and 2.5, electromagnetic actuators and piezoelectric actuators are studied intensively. These actuators have their own applications, which are hard to find alternatives except them. Electromagnetic actuators are good at out-of-plane motion from its combination of permanent magnet and micro-coils and stiff piezoelectric actuators are frequently used in fine and accurate motion. Their advantages and limits are also discussed and compared with the others.

In section 2.6, kinematic mechanisms for MEMS-based motion stages are discussed, which includes a mechanical displacement amplifier, and kinematic mechanisms among multiple DOF motions. Serial kinematic mechanisms (SKM) and parallel kinematic mechanisms (PKM) are surveyed to find an appropriate one for the presented XYZ-stage. PKM is more popular at MEMS XY-stages for its affordable implementation. However, PKM is challenging in XYZ-motion due to the fact that PKM is limited to implement Z motion or out-of-plane structure. In addition to this, PKM shows displacements shorter than SKM, because the final output will be the intersection of all the engaged actuators. Contrary to PKM, SKM is not easy to implement in MEMS for its electric connection to suspended structures, which can be overcome by a nested

structure. A nested structure is to embed one independent system fully into the other. Other properties such as a force level, a resolution, a frequency response, and coupled motion error are also important to evaluate motion stages. The characteristics obtained from these surveys are utilized to compare and evaluate the performance of motion stages presented in this dissertation.

2.1 MEMS in-plane electrothermal actuators

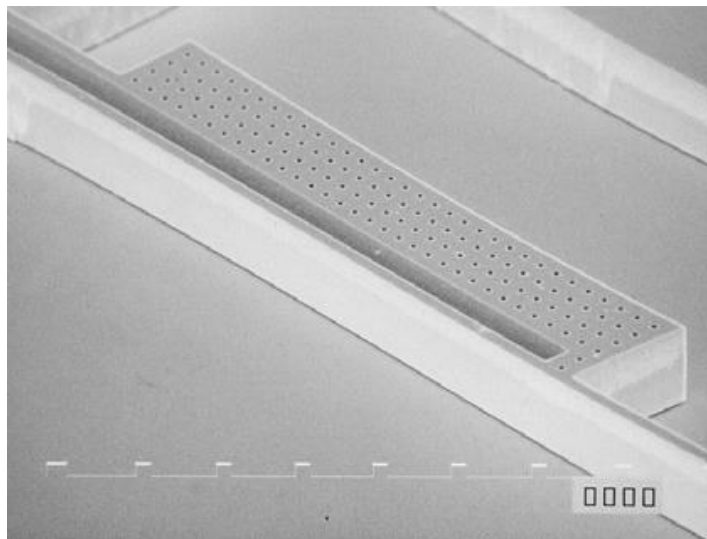


Figure 2.2: An electrothermal actuator based on a combination of a hot arm and a cold arm [40]

The characteristics of a positioning stage depend on various features including its actuating mechanisms, actuators, and micro-transmissions. The literature review starts with details about actuators including basic principles, and their advantages and disadvantages. Once an actuation mechanism is determined, appropriate kinematic mechanism or mechanical linkages will follow for their motion platform.

Electrothermal actuators utilize Joule heating for their operations. The current passing through actuators raises the temperature of the actuators, which results in thermal expansion. This can be converted into a meaningful displacement output by the actuator.

A laser or a high intensity beam can be used to raise the temperature of the electrothermal actuator and can eliminate complex electric connection issues for a remote control [41]. However, this remote access is not efficient resulting in poorer performance than conventional actuators.

The force from a thermal expansion of the beam is reported as tens of milli-Newton level force, which is similar level to piezoelectric actuators and is almost tens to hundreds times larger than electrostatic actuators. This is one advantage of electrothermal actuators in applications requiring enough forces.

However, the displacement by a thermal expansion is relatively smaller than the other actuators; the coefficient of thermal expansion of Silicon [42] is 2×10^{-6} , which indicates about 0.2 % elongation of the beam with a maximum temperature of Silicon. When an electrothermal actuator has less than 1 mm length, this value can produce 20 microns. Considering its length, this level of displacement is not enough in many cases. In order to overcome this shortage, mechanical amplifiers, such as lever or amplifying linkages, have been used with electrothermal actuators [43,44]. The appropriate lever design can increase its range of motion by converting some degree of its force, but inappropriate design, including lever ratio, can result in poor performance as well.

Two designs of electrothermal actuators are widely used designs: a chevron type (or a bent-beam type) and a combination of a hot arm and a cold arm. The simple combination of a hot arm and a cold arm is illustrated in Fig. 2.2 [40] and a chevron type (or called bent-beam type) is in Fig. 2.3 [45]. In a combination of a cold arm and a hot arm, the temperature rise of a hot arm is much higher than that of a cold arm due to the

geometric difference between the two arms. This different temperature rise causes a hot arm expanded longer than a cold arm. Since these two arms are tightly coupled to each other at their ends, this thermal difference results in a bending motion toward a cold arm. Another advantage of this combination is that it is easy to generate out-of-plane motion when one arm is deposited on top of another and normal to the wafer plane [46]. This approach is simple to fabricate and is able generate a relatively long range of motion efficiently.

However, this combination generates a curved motion, not a straight one, so this actuator can be utilized in specific applications, including optical switches or grippers. In addition to this, the bending motion causes shear force in connecting area between a hot arm and a cold arm and can present the reduction of its lifetime, because the connecting area is composed of multiple layers and adhesive force among layers is relatively weak.

A bent-beam or a chevron type electrothermal actuator is alternatives of the combination of a hot arm and a cold arm [18, 26, 29, 33]. As shown in Fig. 2.3, typical chevron type electrothermal actuator consists of multiple beams in a row, where two beams are connected to each other with a bent angle. When electrical current flows from one end to the other end of the beam, thermal expansion of the beams generates a linear motion toward a designated direction by the bent angle indicated by the arrow in Fig. 2.3. This symmetric layout in bent beam actuators produces a linear motion along its shaft and has been used for motion stages and micro-manipulation.

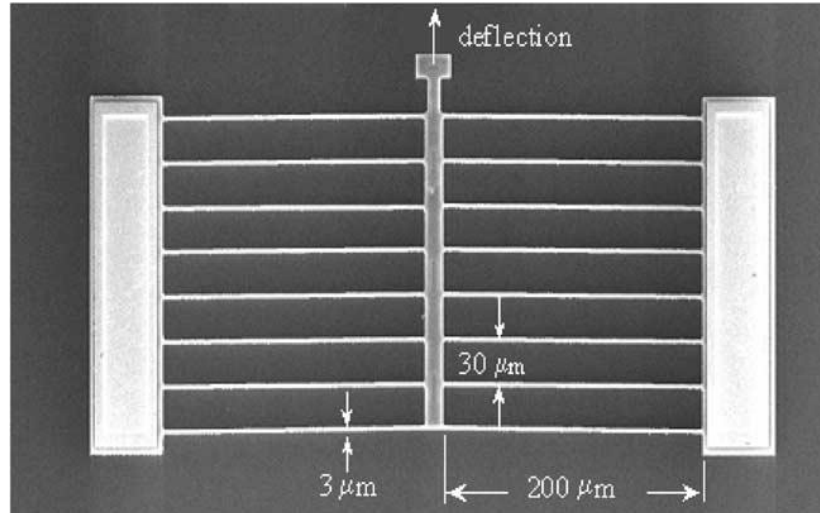


Figure 2.3: The chevron type electrothermal actuator [48]

A few relevant electrothermal actuators are listed in Table 2.1 for in-plane motion and Table 2.2 for out-of-plane motion. Syms et al. 2002 [40] demonstrates a typical combination of a cold arm and a hot arm electrothermal actuator and use it to move and align an optical fiber. For optical fibers with diameters from a few microns to tens of microns, a displacement amplifier is used with this actuator with which displacements more than $600\ \mu\text{m}$ is generated and observed. However, the footprint of the proposed system is relatively huge compared to other MEMS devices. In addition to this, the extended cantilever beam as a mechanical amplifier works successfully with a curved motion, not a linear motion.

A photo-thermal actuator utilizes a focused high-intensity light to raise the temperature of the actuator, instead of physically connected electric power [41]. The actuator has a big receiver to absorb thermal energy from an illuminating light source efficiently. This approach makes a remote control possible and electric connection simple,

although the expected displacement of this actuator is relatively lower than direct electric connection.

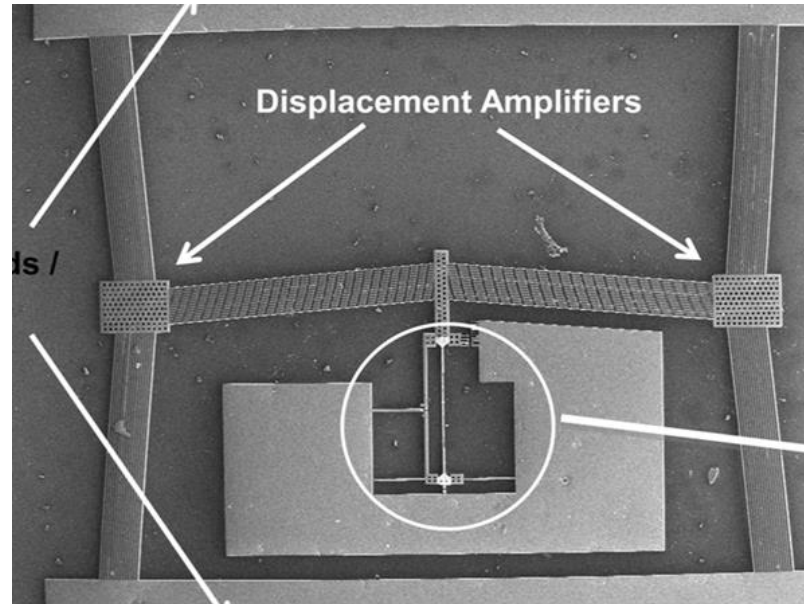


Figure 2.4: The cascade type based on bent-beam actuators [49]

The maximum range of motion from the electrothermal actuator is relatively shorter than the other actuators, because the thermal expansion of beams is very small or 10^{-6} level. In order to overcome this performance issue, Que et al. 2001 [50] suggested a cascade structure shown in Fig. 2.4, where multiple actuators are connected like a cascaded structure. Contrary to a single beam actuator, output displacement at its final end is an accumulation of the engaged actuators allowing a larger displacement.

Cao *et al.* 2007 [51] developed a bidirectional electrothermal actuator utilizing Lorentz force; a current flowing through the electrothermal actuator is affected by external magnetic field resulting in additional force. Electrothermal actuators utilize Joule heating and their electrical current density is important, not their directions. However, current direction can determine the direction of motion by their Lorentz force. To achieve

this, instead of a bent-beam, a flat beam is used and will be bent by this Lorentz force. In this case, this electrothermal actuator with a flat-beam is able to move forward or backward, since Lorentz force will determine the direction of a motion. However, its maximum displacement is not large, because the force by Lorentz force is a few micro-Newton level of force and the beam is designed to be more flexible to utilize this Lorentz force efficiently.

Luo *et al.* 2005 [52] reported three different electrothermal actuator utilizing vertical bars and constraint beams, which enable one actuator to be folded multiple times to fit in allowable spaces. The suggested actuator with 800 μm long beams produces displacement of more than 30 μm , which is similar to a maximum displacement of a cascaded actuators with similar sizes [47]. However, it is important to insulate the constraints beams thermally from the actuator, because those constraints beams should remain on a same length to produce large displacement. This indicates thermal insulation structure is needed, which is not easy to implement in SOI-MUMPs [39].

Zhu *et al.* 2006 [53] utilizes electrothermal actuators for tensile testing of micro-scale materials. To achieve this, material testing system is composed of an actuator to generate a precision motion, an embedded sensor, and the reasonable thermal isolation between the material to test and the actuator. The tensile material test needs enough force, so that the electrothermal actuator is utilized. In a material test, one piece of a sample is placed between the actuator and the embedded sensor. The bent beam angle of the actuator is 30 degrees, which is several times larger than typical bent-beam type actuators indicating that the actuator is optimized for its desired force and displacement level.

Chu *et al.* 2003 [43] reported a 2 degrees-of-freedom (DOFs) positioner with two embedded capacitive sensors. The 2 DOFs motion is designed by connecting the shaft of one actuator to another with an orthogonal orientation. This connection is straightforward and an efficient method. However, the shaft used in this stage is designed to be flexible to reduce coupled motion error between the two actuators, which causes lower stiffness and poor frequency response. In order to measure its displacement with sub-nanometer resolution, a compliant displacement amplifier called high amplification compliant micro-transmission has been adapted as shown in Fig. 2.4 [54]. With this amplifier, the embedded sensor can get 3.37 times larger signals resulting in higher sensitivity. This micro-transmission is also based on a monolithic layer and well compatible with MEMS fabrication technologies.

Duc *at al.* 2008 [34] reported a novel polymer-based electrothermal actuator, which consists of a silicon frame and multiple polymer stacks. The silicon frame operates as a micro-heater and consists of serpentine beams for an efficient heat exchanger. The gaps among serpentine beams are filled with a SU-8, which is expanded thermally to produce a displacement. When an electrical current flows through serpentine beams, a Joule heating will heat up the polymer resulting in in-plane motion. A micro-gripper is also demonstrated by connecting two polymer actuators orthogonally, which is able to cover a workspace of $17\ \mu\text{m} \times 11\ \mu\text{m}$. This polymer stack is simple to build, but a combination of polymer structure results in the stiffness of $11.4\ \text{N/m}$ and a force level of $814\ \mu\text{N}$, which are relatively smaller than typical electrothermal actuators ranging hundreds N/m and mN level force.

Murthy et al. 2009 [55] introduced 4 DOFs micro-robot based on electrothermal actuators. The main components are built on conventional MEMS fabrication methods and then assembled for 4 DOFs motion; two 2 DOFs electrothermal actuators are connected to each other by a vertical link, which is also linked to another 2 DOFs actuator through a copper wire for 4 DOFs motion. The robot demonstrated a displacement of 46.5 μm and a rotational angle up to 11.1 degrees.

Some interesting and relevant electrothermal actuators are selected from previous research and tabulated in Table 2.1 with their important characteristics, including the footprint, DOFs, force, power, and other interesting features.

Table 2.1: Electrothermally actuated micro- and nano-positioning stages for in-plane motions

Reference	DOF	Motion range	Force (mN)	Power (mW)	Foot print (in μm unit)	Features
Oliver et al, 2003 [41]	1	12 μm 5.7 deg.	0.0054 mN	220	2 x 350 (L) x 4 (W)	Photo-thermal, Cascaded type
Syms, 2002 [40]	1	600 μm	-	250	1400 (L) x 30 (W) x 100 (T)	Bimorph type, 100 Hz (1 st resonant frequency), mechanical amplifier by a suspended cantilever
		65 μm	-	250	4000 (L)	-
Park et al, 2001 [47]	2	33.4 μm	0.15	250 - 300 (6V – 8V)	500 – 1000 (L) x 6.5 (T)	Rotary actuator Cascaded type
	1	104 μm	0.204	< 12 V	500 – 1500 (L) x 8 -14 (T)	Inchworm type, Electroplating of Ni

Comtois et al, 1997 [56]	1	22.5 μm	0.030 – 0.045	38 - 43	150 (L)	1.57 kHz (1 st resonant frequency)
					300 (L)	485 Hz (1 st resonant frequency)
Chu and Gianchandani, 2003 [43]	2	19 μm	72.5	1300	3000 (L) x 36 (W) x 60 (T)	SOI wafer, Capacitive sensor with 0.3 nm resolution, Mechanical amplifier with 3.37 ratio
Cragun and Howell, 1999 [57]	1	20 μm	142.9	200	300 (L) x 3 (W) x 3.5 (T)	Bent-beam type
		12 μm	76.2	170	250 (L)	-
Lott et al, 2002 [48]	1	13 μm	-	-	200 (L) x 3 (W)	Bent-beam type, Surface micromachining
Que et al, 2001 [50]	1	10 μm	8.3	130 mA	410 (L)	Cascaded type
		70 μm (expected)	2.5 – 0.5	-	2000 (L)	
Kim et al, 2012 [27]	2	60 μm (X)	125.3 mN (expected)	5 V	1000 (L) x 16 (W) x 30 (T)	0.71 kHz (1 st resonant frequency in the X-stage),
		55 μm (Y)				2.63 kHz (1 st resonant frequency in the Y-stage), 1:11 lever ratio
Sebastien et al, 2005 [44]	1	13 μm	-	5 V	600 (L) x 12 (W) x 10 (T)	A 1:10 lever, 7 nm resolution
Zhu et al., 2006 [53]	1	0.7 μm	43.2 mN	15 mA	300 (L) x 8 (W) x 3.5 (T)	material testing applications, SOI wafer

Zhang et al., 2008 [4]	1	9 μm	-	380	-	Bent-beam type - polymer
Luo et al, 2005 [52]	1	33 μm	-	T=700K Insulating beam or supporting beam	800 (L)	Spring cascaded type
		25 μm	-		800 (L)	deflector
		20 μm	-		400 (L)	Bent-beam type with constraint beams and vertical bars
Cao et al., 2007 [51]	1	4.5 μm	100 μN	20 – 40	200 (L) x 2 (W) x 3.5 (T)	Bidirectional motion from the electromagnetic force and electrothermal actuator
		40 μm	20 mN	1000 – 3000	2000 (L) X 5 – 15 (W) x 50 (T)	SOI wafer
		80 μm	Several mN	2000 – 4000	2000 (L) X 5 – 15 (W) x 50 (T)	Made of nickel only
Maloney et al., 2004 [58]	1	> 2 mm	6.7 mN	12 V	1000 (L) x 10 (W) x 50 (T)	Inchworm type
Guan and Zhu, 2010 [45]	1	1.1 μm	-	11 mA	200 (L) x 2 or 8 (W)	Z-shaped straight beam, Its force is between comb drive and bent-beam thermal actuator.
Lin and Chiou 2012 [59]	2	25 μm	15 mg	5 V	630 (L) x 30 (W) x 100 (T)	PKM with decoupling folded-flexure beams, Displacement of 31 μm makes coupling motion of 0.4 μm , SU8 isolator
		-	-	-	-	
Kapels et al., 2000 [60]	1	250 nm	20 mN	35 mA	400 (L) x 20 (W)	Design for fracture tests

Baker et al., 2004 [61]	1	18 μm	180 μN	300	300 (L) x 4 (W) x 2.25 (T)	Bent-beam type
Duc et al., 2008 [34]	2	17 μm (X)	196 μN	2.5 V	365 (L) x 120 (W)	Polymer thermal actuator, a micro-gripper, Coordinated manipulation by 2x1 layout
		11 μm (Y)	814 μN		-	
Chen et al., 2002 [62]	1	23 μm	-	7 mA	Hot arm: 250 (L) x 2 (W) x 3.5 (T), Cold arm: 215 (L) x 15 (W)	Standard a hot arm and a cold arm type actuator
Hubbard and Howell 2005 [63]	1	52 μm (bi-stable mode) +/- 8 μm (normal mode)	-	-	1 st : 200 (L) 2 nd : 700 (L) 3430 x 1630	Modified cascade type A combination of a bi-stable mode actuator and a normal actuator
Shay et al., 2008 [64][28]	3 (X, Y, θ)	33 μm (X) 10 μm (Y) 9 deg. (θ)	850 μg	-	720 x 720 200 (L) (estimated)	Designed for a micro-conveyor
Anderson et al., 2009 [28]	1	2 μm	-	10 V	2 x 200 (L) x 2 (W) x 5 (T)	2-fingers gripper system Pick-and-place operation for manipulation
Murthy and Popa 2009 [55]	4	50 μm x 50 μm x 75 μm	-	20 V	3000 x 2000 x 1000	0.5 μm / 0.015 deg. repeatability Compliant region for assembly
Moulton and Ananthasuresh 2001 [65]	1	-	-	-	-	Cascaded type
	3	33 μm	-	19 V	-	3 x 2 array
Kim et al., 2008 [7]	-	-	-	-	5000	20 nN force resolution

There are some observations on Table 2.1; (i) the actuators based on surface micromachining technologies demonstrate micro-Newton level of force [26, 28, 33, 36, 42, 43], meanwhile the actuators based on bulk micromachining technologies produces milli-Newton level of force [18, 37, 39]. This difference comes from their thickness; surface micromachining allows a few μm thickness, but bulk micromachining can handle up to hundreds μm thickness. (ii) It is fairly hard to compare energy efficiency of presented electrothermal actuators due to a lack of information. (iii) The electrical source commonly used in the electrothermal actuators varies from driving voltages of 5 V to 15 V or input watts of 100 to 300 mW. (iv) Electrothermal actuators show relatively higher energy consumption than electrostatic and electromagnetic actuators. (v) Most electrothermal actuator requires firmly fixed grounds (called an anchor) for maximizing its output. Without these anchors, thermal expansion of beams cannot be converted into a displacement completely. Based on these features, successful operation of electrothermal actuators need anchors to hold their both ends and enough electrical power.

2.2 MEMS based out-of-plane electrothermal actuators

The electrothermal actuators for out-of-plane motions are surveyed in this section and summarized in Table 2.2. Out-of-plane motion is a motion normal or vertical to wafer plane. Most MEMS fabrication processes are based on monolithic structures and focus on in-plane structures. Considering this kind of situation, in-direct fabrication processes are required for out-of-plane motion, which prevents out-of-plane actuator from being used widely in various applications.

Given that 3 DOFs stages presented in this dissertation require the integration of an out-of-plane stage with two in-plane stages, out-of-plane actuator or motion stage

needs to have good integration capability with MEMS in-plane actuators and similar characteristics with chosen in-plane actuators or motion stages. From this point of view, several relevant out-of-plane electrothermal actuators are surveyed and summarized in Table 2.2.

One direct method to build structures for an out-of-plane motion is to manually rotate in-plane electrothermal actuators and arrange them normal to a wafer plane [66]. This process does not require additional effort to design and build out-of-plane actuators and out-of-plane actuators are the same with in-plane actuators, so that out-of-plane actuator can have similar properties with in-plane actuator, including a range of motion, a maximum force and stiffness. However, this manual assembly is hard to control accurately enough to guarantee equivalent performances over multiple chips. In addition to this, a latch structure used for the assembly process has a possibility to cause a motion error or a wrong aligned motion. Based on this observation, manual assembly process or utilizing in-plane actuators does not fit well with advantages from MEMS technologies.

One widely used design is a bimorph actuator or a combination of a hot arm and a cold arm [32, 53–56]. This bimorph actuator can generate in-plane motion by placing two arms on the same plane or out-of-plane motion by placing one arm onto the other. The bimorph type actuator demonstrates better energy efficiency and a larger displacement than other electrothermal actuators. However, this bimorph type is desirable to produce a curved motion but not appropriate at a linear motion. For large stroke, this bimorph type tends to have a long and slender shape. In this case, it is not easy to integrate this type with other MEMS devices for their applications. In addition to this, thermal insulation is

required at the end of the bimorph type actuator to prevent any thermal effect on a target physically contacted.

In order to improve an out-of-plane motion, various designs and principles are applied to an electrothermal actuator [71–74]. Buckling effect of a beam is a simple method to generate out-of-plane motions without complex fabrication processes. Buckling occurs when an internal load of a beam is over its buckling limit [58, 60]. However, buckling operates at bi-stable mode, which is difficult to control its motion accurately between pre-buckling mode and post-buckling mode.

Varona et al. 2009 [73] reported a novel out-of-plane electrothermal actuator generating an out-of-plane motion, which is inclined to a wafer plane, not normal. This actuator is designed by a combination of notches for an out-of-plane motion and bent-beams for an in-plane motion allowing a skewed out-of-plane motion. This actuator will be advantageous in applications requiring inclined motions such as Stewart platform, which needs six inclined actuators for 6 DOF motion. There are, however, no details about its working principle or following papers for this design.

Chen *et al.* 2003 [75] and Chen et al. 2008 [71] applied a step-bridge structure to a single beam electrothermal actuator for out-of-plane motion. Similar to a combination of a hot arm and a cold arm, this step-bridge structure on a single flat beam is also able to generate out-of-plane motions, when thermally expanded beams generate rotational motions near a step-bridge. In addition to this deformation, buckling effect is also utilized to increase its maximum out-of-plane displacement. This step-bridge shape needs to be fabricated through surface micromachining technologies and sacrificial layers. Thus, it is

hard to utilize bulk micromachining technologies for implementing the same design for a few milli-Newton level of force and hundreds N/m level of stiffness.

Table 2.2: Electrothermally actuated micro- and nano-positioning stages for out-of-plane motions

Reference	DO F	Motion range (μm)	Power or a driving voltage	Foot print (unit in μm)	Features
Tsang et al., 2006 [66]	1	42.9	82 <i>mW</i>	166 (L) x 8 (W) x 10 (T)	Out of plane by an erected actuator manually
Sehr et al., 2002 [46]	1	1.7	-	1400 (L) x 3 (W) x 6 (T)	Bimorph type, 20.9 kHz at 1 st resonant frequency
Yan et al., 2004 [67]	1	6.2	9 <i>V</i>	217 (L) x 10 (W) x 2 (T)	Bidirectional motions, Three layers
Atre 2006 [68]	1	8	6 <i>V</i>	126 (L) x 8 (W) x 30 (T)	Bimorph type
Kim et al., 2013 [76]	1	85	-	2000 (L) x 50 (W) x 30 (T)	4.41 kHz at 1 st resonant frequency 13 mN force calculated
Chen et al., 2003 [75]	1	9	6 <i>V</i>	240 (L) x 10 (W) x 2 (T)	Bimorph type with bridge shape, 35.8 kHz at 1 st resonant frequency
Chen et al., 2008 [71]	1	13	120 <i>mW</i>	600 (L) x 27 (W) x 2.2 (T)	Single layer step shape, 88.1 kHz at 1 st resonant frequency
Micahel et al., 2008 [72]	1	31	9 <i>V</i> pulse	1200 (L) x 40 (W)	Based on buckling, Bi-stable mode, No notch
Varona et al., 2009 [73]	1	4.3	12 <i>V</i>	200 (L) x 1.5 – 2 (T)	Multi-poly silicon layers, inclined motion not vertical nor horizontal motion
Girbau et al., 2007 [69]	1	1.75	3 <i>V</i>	-	V-shaped bimorph type
McCarthy et al., 2006 [74]	1	53	50 deg. C	3000 (L) x 30 (T)	Based on buckling

Li and Uttamchandan ni 2009 [70]	1	32	11 V	3950 (L) and 1800 (L)	0-90% rise time: 17.3 ms
-------------------------------------	---	----	------	--------------------------	--------------------------

A simple step shape is also used to generate an out-of-plane motion [76], which is based on SOI wafers and bulk micromachining technologies. The actuator with this step feature and its optimized design demonstrated out-of-plane motions near 80 μm . In addition to this performance, one motion platform is also attached to the actuator with a thermal isolation layer in order to reduce thermal effect on the motion platform.

Various out-of-plane motion stages or actuators are surveyed based on the considerations, including an integration capability to existing in-plane actuators, a range of motion, a stiffness level, and a force level equivalent to those in the X-stage. Several relevant out-of-plane motion stages or actuators are summarized in Table 2.2 with some features: (1) given similar dimensions or sizes, out-of-plane actuators generate relatively lower performance than in-plane actuators, because most MEMS fabrication methods focus on in-plane structures. (2) Direct design or dedicated design for out-of-plane motions is rare. Indirect methods such as combination of in-plane actuator or limited 2.5D structures require sophisticated conversion mechanism, which is not efficient. (3) It is rare to find an out-of-plane motion stage with a motion platform or different end effectors. It is necessary to have a motion platform in electrothermally actuated motion stages, because a motion platform can be used to reduce a thermal drawback from the actuators. Therefore, it is reasonable to design a dedicated out-of-plane stage or actuator and also desirable to have similar characteristics with the in-plane actuators or stages to merge together.

2.3 MEMS-based electrostatic actuators

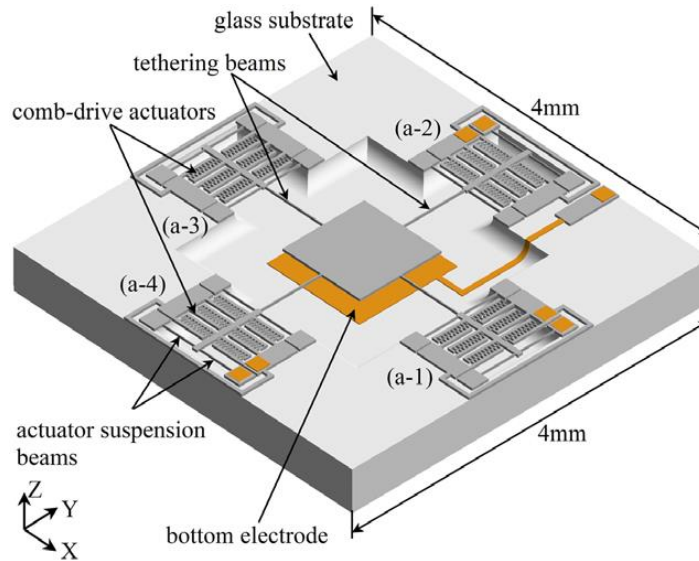


Figure 2.5: Electrostatic actuator parallel plate type [31]

Electrostatic actuators utilize electrostatically attractive or repulsive forces among charged electrodes [77]. The gap between the electrodes and the size of the electrodes are important design parameters to characterize their maximum forces or displacement. The widely used electrostatic actuators are parallel plate types and comb drive types. The parallel plate type consists of two electrodes facing each other, as shown in Fig. 2.5, where the grey plate in the middle of the device faces a yellow plate for their operations.

One advantage of parallel plate type actuators is that they can be utilized for an out-of-plane motion easily, when their parallel plates are parallel to the wafer plane. However, the implementation of the parallel plate type requires wafer bonding or assembly processes to place one electrode on top of the other.

Table 2.3: Electrostatic actuators and electrostatically actuated micro- and nano-positioning stages

Reference	DOF	Motion range (μm)	Force (μN)	Power (V)	Resolution	Frequency	Foot print (unit in mm)	Features
Hoehn et al., 2003 [77]	2	50	150	30 - 60	2 nm	127 Hz	7.5 mm ²	SKM
Horsley et al., 1999 [78]	1	2.8	58 - 78	12	2 nm	1.1 kHz - 450 Hz	2 x 2.2 x 0.05	Parallel-plate type (comb)
Kim and Chun, 2001 [33]	1	1.4	50.4	15	100	18.5 kHz	1x0.3x20 μm (T)	SOI wafers Comb type
Jaecklin et al., 1992 [79]	1	7.3	0.1	14.5	-	-	4.8 mm ²	Folded spring
	2	10 x 10	-	20	50 nm	-	0.5(L)x 0.8 μm W) x 2 μm (T)	PKM 4 beam supporters a Motion platform
Cheung et al., 1996 [80]	1	8	0.32	-	Less than 0.01 μm	3208 Hz	0.310 x 0.340 x 0.0017	Comb Embedded sensor
Kim and Kim, 2002 [22]	2	50 x 50	11.7	$\sqrt{500}$	-	360 Hz	7x7	SCS, PKM, 2 X and 2 Y actuators, beam supporters
Jaecklin et al., 1993 [81]	2	7	0.15	15	80 nm	4.3 kHz	2.5x2.5 (estimated)	Poly-silicon comb actuator
Sun et al., 2002 [82]	2	3.7	53.2	-	10 nm	748.46 Hz (X) 3427.6 Hz (Y)	3.2x3	SOI wafers

Mukhopadhyay et al, 2008 [29]	3 X, Y, theta	27 (alone)	188 (from equation)	85	-	465 Hz	-	PKM
		18 (combined)						
Koo et al., [30]	2	0.57 deg. (alone)	-	-	-	-	-	PKM
		1.72 deg. (combined)						
Liu et al., 2007 [31]	3	18	-	100	1.01 nm	500 Hz	-	PKM
		21	-	100	5 nm (closed loop)	-	-	
Liu et al., 2007 [31]	3	25 (X)	-	30	17.3 nm	-	4x4	PKM, Comb drive with a parallel plate type, Wafer bonding
		25 (Y)	-	30 -		-	-	
		3.5 (Z)	-	14.8	-	-	-	
Dong and Ferreira, 2009 [32]	3	24 (X)	-	180	-	2090 Hz	-	PKM, SOI, End-effector: cantilever
		24 (Y)	-	180	-		-	
		7 (Z)	-	4.5	-	-	-	
V. Milanovic et al., 2004 [83]	2	-22 to 22 deg. (X)	-	80 - 150	-	11.378 kHz	0.8x0.8	Up & down comb, SOI
		(IHFF500 model)						
de Jong et al., 2010 [84]	3 (X, Y, θ)	+/- 10 (X, Y) +/- 2 deg. (θ)	-	50	-	-	4x4 (approximation)	PKM, In-plane, crosstalk less than 20 pm, SOI wafers

Brouwer et al., 2010 [85]	6	+/- 10	-	-	-	3.8 kHz	540x540 x58	Scale up version, Not fabricated
Dong et al., 2007 [86]	2	15 (X, Y)	-	45	1 μ m	960 Hz	4x4 (approximation)	SOI wafers
Ando 2004 [87]	3	1.1 (X)	-	97	10 nm	-	-	SOI wafers, Focused Ion Beam (FIB) for slope
		0.13 (Z)	-	105		-		
Pang et al., 2009 [88]	2	20	-	55	-	440 Hz	10 x 10 Platform : 6x6	Four actuators at four corners
Sun et al., 2008 [13]	2	+/- 10	-	28.5	+/- 0.1 μ m	983 Hz	9.4 x 9.4	DRIE process Anodic bonding
Laszczyk et al., 2010 [9]	2	+/- 28 (X)	-	100	26 nm	290 Hz	10 x 10 x 430 μ m	SOI wafers, DRIE, SKM, Insulation gap
		+/- 37 (Y)	-			550 Hz	-	
Swinkels 2012 [89]	3	+/- 75 (X, Y) +/- 15 deg.	-	-	22 nm 10 m deg.	266 Hz	5 x 5 (approx.)	PKM, SOI wafers, DRIE
Kim et al., 2006 [89]	1	5.22 deg. at initial cond. 19.2 deg.	-	53	-	2953 Hz	1 x 1 16 μ m x 750 μ m	Rotational motion, plastic deformation

		3.75 deg. at first 24.8 deg.	-	65	-	2499 Hz	0.8 x 1.5 16 μm (W) x 800 μm (L) :torsional spring	
Han et al., 2011[90]	1	3.4 (FEA)	-	53	-	-	800 μm x 800 μm	a lever, out-of-plane motion, parallel-plate, capacitor not actuator
Takahashi et al., 2009 [91]	3	+/- 12 (X)	-	80	-	0.8 kHz	3 x 3 (approx.)	SOI wafers, DRIE, SKM
		+5 ~ -8 (Y)	-	145	-	3.3 kHz	-	
		0.5 (Z)	-	32	-	1.8 kHz	-	
Kwon et al., 2006 [92]	2	55	-	79	-	280 Hz	2 x 2	Spider legs, PKM
Lie et al, 2007 [93]	1	+/- 2.55	98 μN	-	0.15 nm	-	2 x 4	A lever
Chiou et al., 2008 [94]	1	-	-	-	-	-	-	Cascaded type
Su et al., 2005 [95]	1	-	-	-	-	129.9 kHz 130.078 kHz	-	SOI, A lever
Ren et al., 2011 [96]	1	1.45	-	47	-	-	503 μm x 503 μm	A lever, Out-of-plane, PolyMUMPs process

The other commonly used design is the comb drive type, which is composed of inter-digitated fingers as shown in Fig. 2.6. This inter-digitated finger shape is an economical method to increase its electrode area efficiently with a given space. This type is also good at reducing the change of force during its operation. The performances of some interesting electrostatic actuators or stages are listed in Table 2.3. The electrostatic actuators have some noticeable features; the driving voltages vary from 12 V to 150 V, which is relative highly than other actuator. This high voltage has a possibility to attract dusts around the actuator during operation, which can cause serious problems when the dusts can build any electric connection between electrodes. Other than this, the electrostatic actuators show good frequency response at high frequency and low energy consumption, and a long range of motion.

Several interesting features about the electrostatic actuator can be drawn from Table 2.3; (1) the electrostatic actuators have been used in 2 DOFs or 3 DOFs motion stages more often than any other actuators. (2) Their frequency responses provide 10 to 100 times wider bandwidth than electrothermal actuators. (3) Compared to electrothermal actuator, driving voltages of the electrostatic actuator are relatively high. (4) A larger footprint is expected to generate larger displacement when electrode area depends on the footprint directly. (5) The average force generated by electrostatic actuators is tens of micro-Newton level, which is almost 100 times smaller than electrothermal actuators. (6) The resolution of the motion from the electrostatic actuator is a few nanometers to sub-nanometer, which is similar to that of the electrothermal actuator.

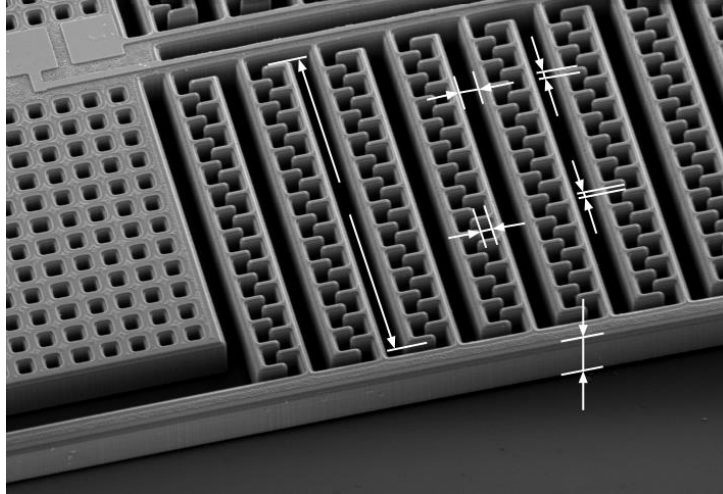
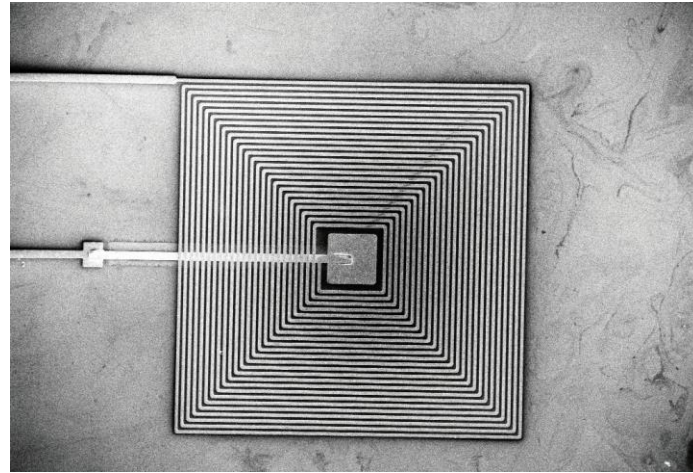


Figure 2.6: Electrostatic comb drive type [33]

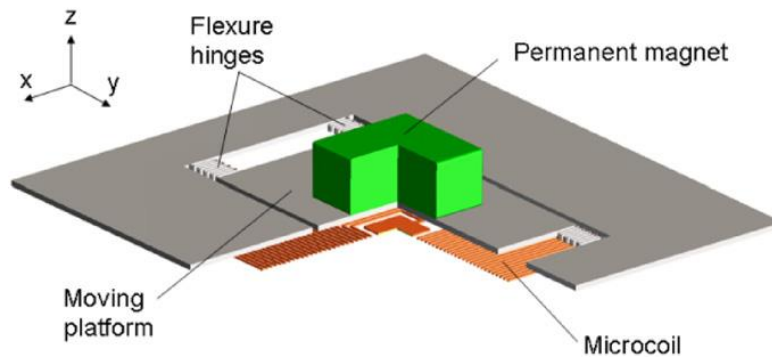
As described above, the electrostatic actuators have various advantages over electrothermal actuator in frequency response and easy electric connection. In a clean environment or well shield packaging, the high voltage for the electrostatic actuator is not an issue. However, in micro-manipulation, it is hard to maintain a clean environment for the target material and the probe. In addition to this, the electrostatic force from the high driving voltage can generate repulsive force to the target depending on the target polarity, which results in poor interaction in the micro-manipulation.

The electrostatic actuator produces tens of micro-Newton level force which is far less than that from electrothermal actuators. Additionally, high driving voltages are tremendously higher than generally used in IC-industries. This high driving voltage not only reduces the compatibility with other electronics but also attracts dust which requires additional shield or packaging during its operation. The weaknesses of the electrothermal actuator are a short bandwidth and a poor frequency response. This is because heating and cooling mechanisms of the electrothermal actuator takes relatively longer time than other actuators which results in a poor response at high frequency.

2.4 MEMS-based electromagnetic actuators



(a)



(b)

Figure 2.7: An electromagnetic actuator [97]; (a) micro coil; (b) a full view

The electromagnetic actuator controls its mechanical motion by Lorentz force [98]; when an electric current flow through the coil, the electric field formed by the current generates an electromagnetic force by interacting with the external magnetic field. This actuator has been built through conventional machining tools well and used in various applications such as Sony PlayStation to read the DVDs at accurate positions or high quality camera for fast focusing so far. However, when it comes into MEMS fabrication technologies, the coils and a magnetic field should be miniaturized. A micro-coil can be implemented by a deposition of a spiral shaped wires as shown in Fig. 2.7(a). This micro-coil interacts

with the magnetic field from a permanent magnet as shown in Fig. 2.7(b). With this set-up, the moving platform where the magnet is attached can move up and down along the Z axis by controlling the current flowing through the micro-coil. The force from the electromagnetic actuator is proportional to the strength of the magnetic field. However, the implementation of a magnetic field in MEMS is still challenging; deposition of Permalloy or permanent magnet in MEMS is limited and thus generates relatively small amount of force. In many cases, for the magnetic field an external permanent magnet [83 – 85] or electroplating [100] and a magnetization of Permalloy (Ni-Fe-Mo) [101] have been utilized. The permanent magnet is easy to manufacture and capable of generating longer range of motion, but it is difficult to manufacture a micro-meter level size and the manual assembly of this magnet into a MEMS device can have an alignment issue. The Permalloy shows a good compatibility with MEMS foundries and provides accurate alignment with existing MEMS devices, but it is difficult to generate a magnetic field similar to those from permanent magnets.

Several interesting electromagnetic actuators are summarized and listed in Table 2.4. Some noticeable features are; (1) electromagnetic actuators demonstrate their first resonant frequency near a few *kHz*, which is similar to electrostatic actuators. (2) The input voltages for the electromagnetic actuator are a few voltage levels. This is similar to electrothermal actuators and far less than electrostatic actuators. (3) Due to the volume of a permanent magnet, general footprints listed in Table 2.4 are similar to or a little larger than those from electrostatic actuators. When some properties in the actuators depend on its volume or area, it tends to have bigger footprints. (4) Due to the relative position of a

coil and a magnetic field, this actuator is more favorable at implementing out-of-plane motion rather than in-plane motion in MEMS.

Table 2.4: Electromagnetic actuators and related micro- and nano-positioning stages

Reference	DOF	Motion range (μm)	Foot print (units in mm)	Features
Wagner and Benecke 1991 [98]	1	50 - 90	9 x 9	Permanent magnet on the movable platform
Kim et al., 2005 [99]	1	30	22 x 7 x 2.3	150 mA, Chip-bonding with permanent magnet
Choi et al., 2012 [97]	1	+/- 2.7	0.5 x 0.5 x 1	Out of plane motion, Maximum force of 7.5 mN
Lee et al., 2008 [102]	1	110 by 0.6 A (2.7 W)	26 x 19 x 4.5	Maximum force of 420 μN , Electroplating
Kim et al., 2005 [35]	1	300 by 8 V	15.5 x 5.22 x 0.5 mm	For 2 fingers micro-gripper, 18 mN force by 8 V
Ji et al., 2004 [23]	1	13.4 deg. by 28500 A/m	60 x 40 x 14.5	Designed for optical switching applications
Miyajima et al., 2003 [10]	1	2.1 – 16 deg.	4.2 x 3	0.001 Nm torque
Cho et al., 2004 [103]	1	10 by 53 mA	0.5 x 0.7 x 1 μm	2.4 N/m stiffness, 1 st resonant frequency of 4.5 kHz
Culpepper and Chen, 2004 [101]	2	210	68x10 ⁻³ mm ²	1 st resonant frequency of 50 Hz
Lagorce et al., 1999 [104]	1	15 - 25 by 150 mA	-	A polymer magnet on a cantilever, 1 st resonant frequency of 42 Hz

As described above, the electromagnetic actuators have their own characteristics to make them distinguished from other MEMS actuators; especially out-of-plane motion can be built easier than other actuators. However, it is almost impossible to shield one

actuator clearly from other magnetic fields, so two or more magnetic fields cannot be engaged into the same actuator. This can be indirectly shown by Table 2.4, where it is rare to find electromagnetically actuated motion stages capable of generating 3 DOF or more. Another drawback is that this field can be an error source to other actuators working together.

2.5 Piezoelectric actuators

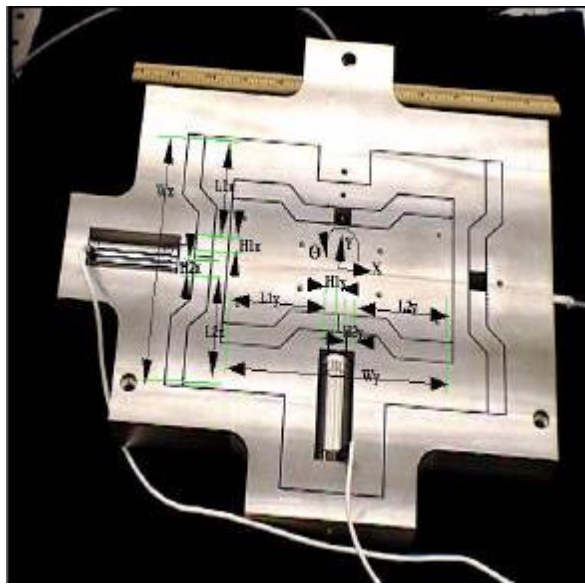


Figure 2.8: Piezoelectric poisoning stage [105]

A piezoelectric material has an electric property that an electric charge accumulates in solid materials such as zinc oxide (ZnO) or Quartz (SiO₂) when physical stress is applied to the material. This principle also works in the opposite direction; when an electric potential difference is applied to the material, this also can result in a strain change. This piezoelectric actuator has been used often in precision motion stages for its large force generate and precision motion. One example is shown in Fig. 2.8 where two piezoelectric actuators are installed into monolithic motion stage through a serial kinematic mechanism

(SKM) for 2 DOFs motion. Due to its large force and stiffness level, the small motion of the actuator can be converted into a large stroke through a mechanical lever.

Table 2.5 lists some characteristics of commercially available piezoelectric positioning stages and MEMS-based stages. From Table 2.5, several interesting features can be extracted; (1) typical piezoelectric positioning stages have 3 to 4 cm cubic volume and generates $100 \mu\text{m} \pm 15\%$ range of motion along X, Y, and Z axes. (2) Typical piezoelectric stages are well commercialized in positioning stage application for micro- and nano-positioning for its simple structure and fine motion. However, in MEMS fabrication technologies, its implementation is limited to specific materials and desirable to generate out-of-plane translational or rotational motion rather than in-plane motions.

Table 2.5: Piezoelectric actuators and related micro- and nano-positioning stages

Reference	DOF	Range of motion	Resolution	Foot print
Physik Instrumente P-611.3 NanoCube XYZ Piezo Stage[2]	3	$120 \mu\text{m} \times 120 \mu\text{m} \times 120 \mu\text{m}$	0.2 nm	$44 \text{ mm} \times 44 \text{ mm} \times 44 \text{ mm}$
P-363 PicoCube XY(Z) [106]	3	$5 \mu\text{m} \times 5 \mu\text{m} \times 5 \mu\text{m}$	0.05 nm	$30 \text{ mm (W)} \times 30 \text{ mm (D)} \times 40 \text{ mm (H)}$
nPoint nPX100 [107]	1	$100 \mu\text{m}$	0.3 nm	$40 \text{ mm (W)} \times 40 \text{ mm (D)} \times 15 \text{ mm (H)}$
nPoint nPCube [108]	3	$100 \mu\text{m} \times 100 \mu\text{m} \times 100 \mu\text{m}$	3 nm	$40 \text{ mm (W)} \times 40 \text{ mm (D)} \times 43 \text{ mm (H)}$
Queensgate NPS-XYZ-100A/15H [109]	3	$120 \mu\text{m} \times 120 \mu\text{m} \times 16 \mu\text{m}$	-	-
Mad city lab Nano-LPQ [110]	3	$75 \mu\text{m} \times 75 \mu\text{m} \times 50 \mu\text{m}$	$0.2 \text{ nm} \times 0.2 \text{ nm} \times 0.1 \text{ nm}$	$7.5 \text{ inch} \times 6 \text{ inch} \times 0.8 \text{ inch}$
Kah et al., 2012 [111]	1, 2	9 deg. by $1 V_{pp}$	-	$4.3 \text{ mm} \times 5.3 \text{ mm}$
Maeda et al., 2004 [112]	1	-	-	-

2.6 Characterization of the MEMS motion stage

Based on the advantages and drawbacks surveyed in different actuation mechanisms, some meaningful characteristics are selected for the design process of MEMS-based motion stages. These characteristics will be used as references to design the MEMS-based motion stages in this dissertation and compare them with other existing motion stages.

Basic characteristic of the motion stage are accuracy and precision of its motion. Accuracy is a degree of closeness of the motion compared with a desired result and precision is related to repeatability. One main application of motion stages is a field of metrology, including Transmission Electron Microscopy (TEM) or Atomic Force Microscopy (AFM). These microscopies consist of a sensing hardware and motion stages. In many cases, a sensing hardware measures only one fixed position. In order to scan a whole object, a motion stage moves an object to appropriate position in front of a sensing hardware. In this case, accurate and precise positioning of an object plays an important role in its scanned measurements.

In addition to these basic properties, there are a few more properties to evaluate a motion stage; the range of motion, resolution, DOFs and coupled motion error. The range of motion is the distance that the motion stage can generate repeatedly along a designated direction. This maximum range of motion can be a maximum workspace in a gripping system. At a gripping system, this property can change a whole control strategy, because a larger workspace can provide versatile operations than a smaller workspace. Contrary to a maximum range of motion, a minimum repeatable motion determines the resolution

of the motion stage. The resolution is the smallest motion the motion stage can produce repeatedly, which restricts a minimum size of a target object and a minimum motion step.

In a small form-factor nano-positioner, compliant mechanisms have been widely used as a mechanical guide for nano-meter level resolution. The compliant mechanisms transfer the force or displacement from an actuator to the motion platform through elastic body deformation. When the compliant mechanisms are monolithic or single piece, it is possible to avoid motion errors, especially backlash or friction from jointed mechanisms. The backlash is a clearance between mating components in order to avoid a jamming, however it can reduce motion accuracy.

Coupled motion error is a motion along unexpected directions when a motion stage is in its operations. When single DOF motion stages are not fully isolated from the others, coupled motion error can be shown up. No coupled motion error implies that each actuator is perfectly isolated from the others. The advantage of no coupled motion error is that a straightforward control is possible to access multi-DOF motions and actuators can work with their full range of motions without any interference. Contrary to this, when single DOF motion stage is mechanically linked to another to a certain degree, coupled motion error becomes severe. In this case, a desired motion can be obtained by solving a nonlinear relationship between inputs and required output motions.

2.6.1 Range of motion

One basic operation in a MEMS-based motion stage is to move an object, so the maximum allowable motion by a motion stage is an important feature to build an operational plan. In many cases, longer range of motion is desirable for a larger

workspace and can provide more flexible control strategy than shorter ones. This characteristic can be achieved in design processes, but it also depends on actuating mechanisms; electrostatic actuators are reported to produce their displacements ranging from 0.5 μm to more than 100 μm . The comb drive is a widely used electrostatic actuator and composed of multiple inter-digitated fingers. When these actuators are also combined with mechanical amplifiers, strokes larger than 200 μm are also reported [113,114]. However, when one electrode is too close to the other electrode, it can be stuck to the other (called a pull-in effect), which can reduce a total stroke down to 50 %.

Electromagnetic actuators have a good mechanism to generate large stroke out-of-plane motion with more powerful permanent magnets and electric field and have been commonly used in milli-meter level applications, including a laser control in Sony PlayStation 3. However, MEMS fabrication technologies are limited for strong permanent magnet or magnetic field. Permalloy is commonly used in MEMS, but cannot provide enough force for a large stroke. Alternative is to utilize conventional permanent magnets, but that causes additional problems, such as alignment issue, compatibility with MEMS processes, and volume scale differences. Considering these issues, it would be desirable to utilize electromagnetic actuator based on conventional permanent magnets for applications requiring a large stroke, but not high accuracy.

The electrothermal actuators are not favorable for a large stroke. This actuator is based on the thermal expansion of silicon, whose coefficient of thermal expansion (C.T.E.) is 2.4×10^{-6} . This value is too small to produce enough range of motions. Due to this reason, typical electrothermal actuators demonstrated displacements of 10 μm to 20 μm . However, electrothermal actuators are famous for their large force generation up to a

few mN levels. A short range motion can be compensated with additional mechanical amplifiers and their mN level of force for a large stroke. Although lever mechanisms increase a total stiffness and reduce an output displacement, a few milli-Newton level of force from electrothermal actuators can overcome this obstacle and generate desirable performances. The mechanical amplifier with an appropriate balance between a force and a stroke can be a good candidate for a large stroke.

Piezoelectric actuators have reported their products with various displacements from a few μm to 200 mm [96, 97] and many commercial products are still available. Piezoelectric actuators are relatively stiff and generate a large force. The only limitation of piezoelectric actuators is their fabrication processes to build piezoelectric materials, which is out of standard SOI-MUMPs processes.

2.6.2 Force

A maximum force from an actuator depends on mainly their actuating mechanism and design optimization, as listed in Table 2.1, Table 2.2, and Table 2.3. Piezoelectric actuators show that they can generate up to 100 N, which is 1000 times larger than other actuators and is a main reason for many commercial piezoelectric motion stages. Electrothermal actuators are also reported to produce on the order of 10 milli-Newton level of force. This value is larger than electromagnetic and electrostatic actuators, and equal to or less than piezoelectric actuators, because electrothermal actuator is based on pure thermal expansion of solid materials.

Electromagnetic actuators and electrostatic actuators are non-contact type forces, which do not have any physical connections between their main components; no

mechanical links between electrodes or between the magnetic field and the micro-coils. In these cases, it is not hard to connect actuators from its electric source and isolate one actuator from the other electrically. In MEMS, it is hard to build 3D electric connections such as jumping over other structures, so it is necessary to consider the electric path to each actuator and the electric isolation among the actuators in an early design stage. However, non-contact type actuators can reduce a stiffness of an actuator, resulting in a reduction in its force down to tens of micro-Newton level of force.

A simple way to increase a force is to make an actuator bigger or increase its footprint. However, this approach can make a whole system bulky expecting a loss of advantages of small foot print. Due to this reason, designing of a motion stage is based on design constraints like a limited footprint. In this dissertation, 10 mm x 10 mm is allowed and appropriate selection of an actuating mechanism and its optimization will be followed.

2.6.3 Mechanical amplifier

A mechanical amplifier is a mechanism to adjust a force and a displacement from an actuator. When an actuator is capable of producing desirable motion or forces, a direct connection will be enough in MEMS stages [25, 37, 39]. However, if it is difficult to meet, a mechanical amplifier can be regarded as an alternative. Displacement amplifiers are commonly used with electrothermal actuators or piezoelectric actuators, which can generate a large force. Some degree of a force will be converted into an additional displacement. Three widely used mechanical amplifiers are surveyed in this dissertation; a cascaded layout, mechanical levers, compliant mechanism or an inchworm.

Park et al. 2000 [50] reported a rotary actuator based on a cascaded layout, where two or more electrothermal actuators are used in a series for a large stroke [36, 38, 52]. With the cascaded layout, a final displacement is reported up to 33.4 μm . This cascaded layout approach is relatively simple, because existing design can be utilized without considerable modification. However, it still requires a large footprint for the cascaded layout. The bent-beam type electrothermal actuator and the interdigitated finger type comb drive are good candidates for this cascaded layout.

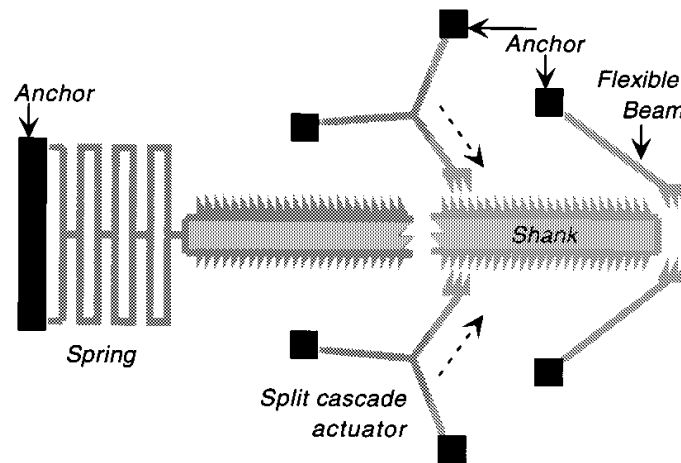


Figure 2.9: The inchworm type electrothermal actuator [58]

Another candidate for a large stroke is an inchworm [33, 36, 45], which is shown in Fig. 2.9, where multiple actuators are cooperated to move an object like conventional manufacturing factory. In Fig. 2.9, while two left actuators hold a shank in its position, two right actuators move back without touching a shaft and then hold it again. The two left actuators then release a shank and then the two right actuators move forward to actuate a shank toward a desired position. Since this system is composed of four independent actuators isolated from a target to move, this inchworm is able to generate relatively long range of motion up to hundreds μm [58]. However, a dedicated control for

four actuators is required and multiple DOF motions are hard to implement. Moreover, physic gaps among the actuators and a shank can be a source of motion errors.

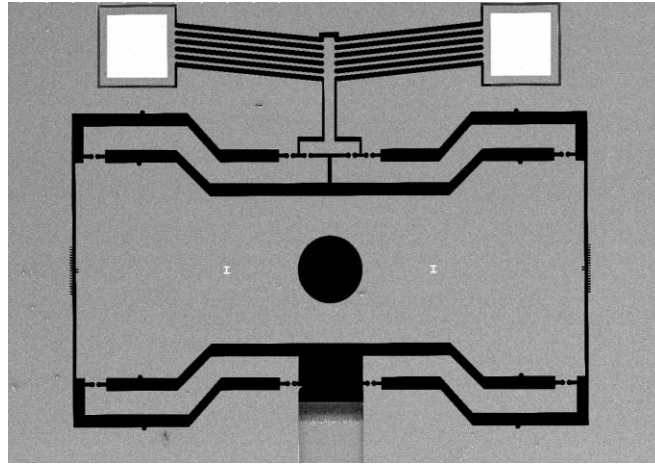


Figure 2.10: The lever between an actuator and a motion platform [44]

Most commonly used displacement amplifier is a leverage [18, 29]. A lever is composed of one long beam and one pivot. When one end of a beam is actuated by an actuator, the other end generates an amplified motion due to a pivot and a lever ratio. This lever design is simple to build on a monolithic layer, which is analyzed and described well in previous literatures [115]. One implementation of a lever in MEMS is shown in Fig. 2.9, where a pivot and two ends are on the same line for an efficient operation and each end has a flexure that is the same with the pivot. The lever is desirable to cooperate with MEMS actuator generating large force, because a lever itself increases a total stiffness of an external mechanical load and small force does not operate efficiently with a lever.

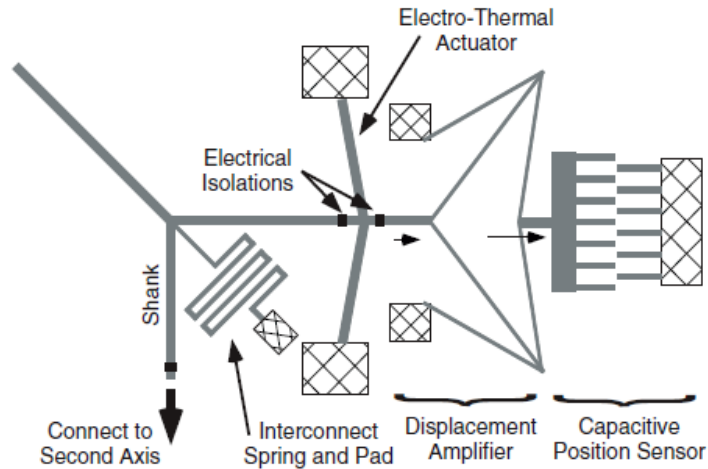


Figure 2.11: A compliant displacement amplifier [43]

The main limitation of a lever is that both ends of a lever experience rotational motions, not linear motions. In this case, a rotary actuator is supposed to work better than linear actuators. Since electrothermal actuators generate linear motions and a conversion into a rotational motion consumes additional energy and can generate motion error. In addition to these drawbacks, most strains occur near pivots and two ends, so the design of a pivot and two ends of a lever are critical for its lifetime.

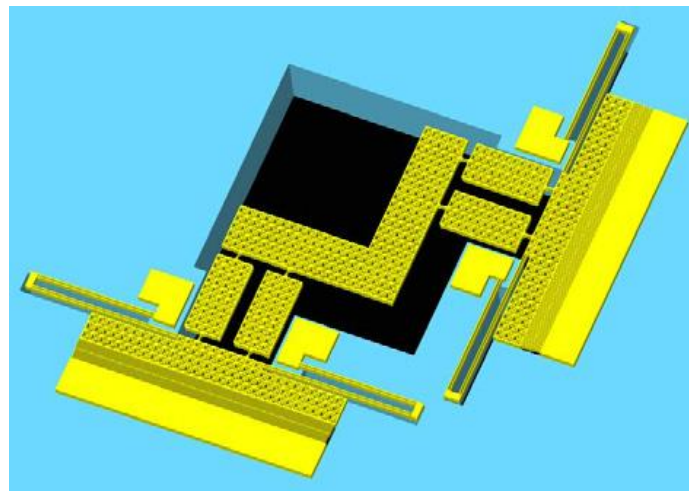
The other displacement amplifier is a compliant mechanism called a micro-transmission, which is based on an amplifying topology [43,54]. One implementation is shown in Fig. 2.11. This micro-transmission is similar with a lever, but it consists of three long slender beams. With appropriate design, a micro-transmission is able to amplify up to 3.7 times. Its advantage is reasonable reliability during fabrication and its operations. This design is stable than a lever using the pivot, because stress will distribute over beams well and thus endure larger stress than a lever, instead of concentration on a pivot of a lever during its operation. Its drawbacks are hard to analysis this micro-transmission design and needs relatively larger footprint than the lever.

2.6.4 Degrees of freedom (DOFs) and coupling errors

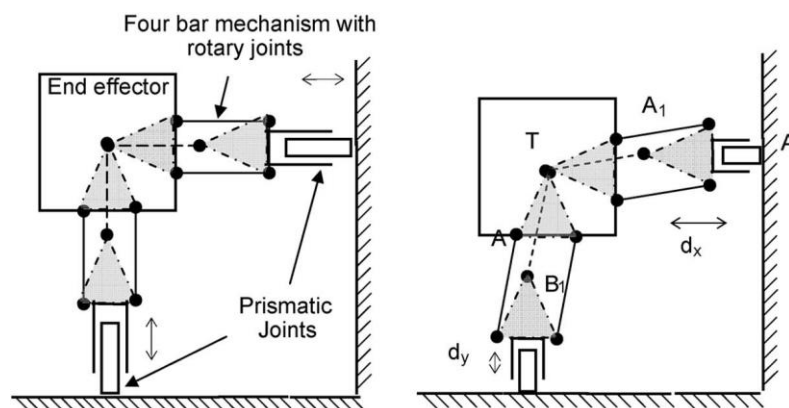
Multi-DOFs motion stages are able to generate multiple DOFs motions for applications. Contrary to conventional manufacturing, there are a few constraints to consider in design of multi-DOF motion stages in MEMS; (1) reliable electric connection to an actuator in a motion stage and electrical isolation from the other actuators; each electric path should be connected to a designated actuator without affecting other actuators to reduce coupled motion error. (2) Appropriate integration strategy to minimize mechanical coupled motion error among engaged actuators; with limited fabrication capabilities in MEMS, each engaged motion stage or actuator should be physically isolated from the others during its merging process. (3) Providing a reliable mechanical link from a motion platform to a base. When multiple actuators or motion stages are engaged, some components will be float in the MEMS stage. In this case, the mechanical links from the motion platform to a base plays an important role in merging individual actuator or stage successfully.

Most MEMS-based actuators or motion stages are designed to produce single DOF motion. When 2 or more DOFs motions are needed, it is necessary to merge multiple actuators into a single system. With limited fabrication techniques in MEMS, it would be reasonable to reuse existing single DOF motion stage or actuator, rather than developing a whole new design. In this integration process, each actuator should be organized well with the others to avoid any electric or mechanical interference. However, it is not always easy to integrate all individual actuator or motion stage successfully in MEMS. Imperfect integration indicates that there are mechanical or electrical connections or relationships among merged systems, resulting in an increment of coupled

motion error and a reduction of its maximum displacement. Coupled motion error is an unwanted motion from unexpected actuators, when the desired actuator is in its operation. When one actuator is stand-alone, there is no coupled motion error at all. But, when this actuator is mechanical linked to another for multi-DOFs motion stages, this mechanical link can cause undesirable effect on the engaged actuators. This mechanical link also can cause additional stiffness to the actuator, resulting in the reduction of its displacement.



(a)



(b)

Figure 2.12: A parallel kinematic XY stage: (a) a schematic diagram [70]; (b) the mechanical linkage in stationary mode (left) and in operation (right) [32]

For multi-DOFs motion stages, parallel kinematic mechanisms (PKM) and serial kinematic mechanisms (SKM) have been commonly used. In a PKM [14, 15, 20, 21], a motion platform is connected to a base through multiple independent parallel kinematic chains as shown in Fig. 2.12(a). The motion platform can be controlled by multiple actuators at the same time, so any motion error caused by one actuator can be compensated by other actuators. This approach can also reduce its coupled motion error.

For an implementation of a PKM, parallel kinematic chain and leaf springs [30,32] are utilized between a base and its end-effector, which are shown in Fig. 2.12(b). The parallel kinematic chain is used to reduce any rotational motion error between two actuators. The leaf spring is used in the middle of the parallel chain to allow desired motions and reduce coupled motion error from another actuator. This leaf spring avoids a fully constrained condition, but this also reduces a stiffness of an actuator and consumes additional portions of displacement, resulting in a reduction of a maximum displacement.

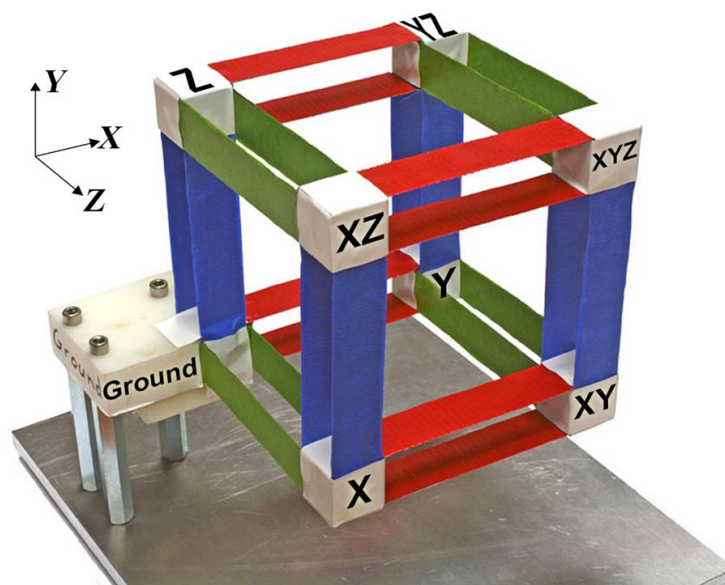


Figure 2.13: An implementation of a parallel kinematic XY stage [116]

One important advantage of PKM is its good compatibility with MEMS for in-plane motions such as in-plane 2 DOFs motion [30,86] or in-plane 3 DOFs motion [29]. Contrary to these advantages, PKM has also a few disadvantages for MEMS-based motion stages; (1) all actuators are tightly coupled with each other, which is additional stiffness to the actuators. In this case, a final workspace is the intersection of a workspace of actuators engaged. (2) PKM requires non-linear mathematical models to obtain the relationship between its outputs and inputs. The calculation of this relationship also takes considerable time to calculate its inputs for a desirable output. (3) The limitation from MEMS fabrication methods for out-of-plane structure or motions prevents PKM from 3 DOFs or higher DOFs motions [30]. The expected PKM design will be the mechanism shown in Fig. 2.13, where a same parallel chain is implemented along an out-of-plane direction. This complex out-of-plane structure is challenging to implement in MEMS and the integration of out-of-plane motions with in-plane motions in MEMS motion stages is even worse.

As an alternative of PKM, serial kinematic mechanisms (SKM) have been adapted in multi-DOF motion stages, where a motion platform is linked to a base through only one series of linkages including actuators, like a robotic arm. Each component in SKM is linked to adjacent components only. The optical lens scanner system adapts a SKM for its XY stage for decoupled 2 DOF motions [44]. Each actuator is in charge of one designated directional motion and the final displacement of the motion platform is the summation of all output from each actuator. When each actuator is well linked to the others, there is no coupled motion error or performance drop. Additionally, the control

scheme is straightforward, since each actuator is assigned to the motion along the designated direction.

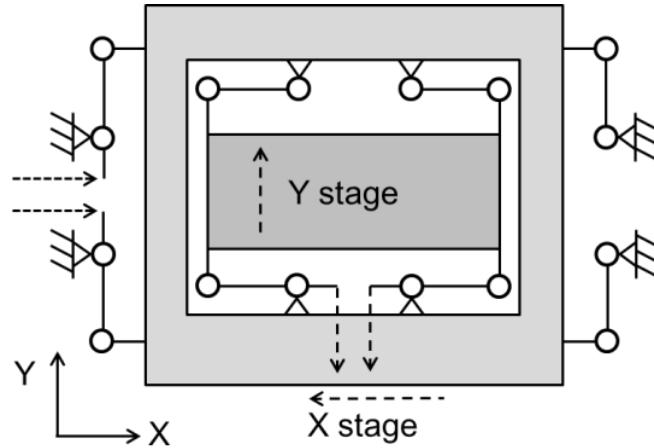


Figure 2.14: A schematic diagram of a serial kinematic XY stage [117]

However, this SKM has a few problems in MEMS. First, the components in the middle of the system are supposed to be free or float to move. In this case, reliable electric connections to floating components are necessary. Second, conventional motion stages based on SKM have been implemented by stacking one stage onto another or nesting one stage into another, as shown in Fig. 2.14. This wiring is too stiff to ignore in MEMS and its wiring process is also difficult to implement in floating components without damaging them. Third, an assembly process of a stacked structure can cause an alignment error between engaged motion stages in MEMS, which can cause a few micro-meter level errors in MEMS. These constraints require a new approach to overcome all the issues described above in MEMS.

Many commercial motion stages are based on SKM for 2 or 3 DOFs motions, especially stacked structures; NanoCube [2,106] or 2 DOF nano-positioner [105] are capable of generating 3 DOFs or 2 DOFs motions by stacking single DOF motion stage

onto another. Piezoelectric actuators are widely used in these high-precision motion stages for their precision motion and large stiffness. The nesting structure is to embed one motion stage into the other as a sub-component. In this case, a motion stage to insert tends to be smaller than another for successful integration, which can result in different frequency response and dynamic properties along different directions. However, for the motion of more than 4 DOFs, PKM is commonly used and Stewart platform [118] is famous for its 6 DOF motions. In conventional manufacturing technologies, these stacked, nested structure, and PKM are not hard to implement, but all of them are still challenging in MEMS-based micromachining technologies.

When multiple actuators are engaged in multiple DOFs motion, coupled motion error is expected, which should be reduced to an acceptable level. These coupled motion errors can be compensated through kinematic mathematical models, but it is also worthwhile to design a motion stage having less coupled motion error. In order to find an appropriate integration approach, five different 2 DOF motion stages have been surveyed and listed in Table 2.6. One simple and straightforward method is to connect two actuators directly to each other, which is based on PKM. By controlling each actuator separately, a 2 DOF motion can be expected for a gripping application [34]. However, this asymmetric connection between two actuators can cause severe coupled motion error; an actuator attached to another reduces a maximum displacement and distorts a motion direction of another. Therefore, a smaller range of motion and large coupled motion error is expected. In order to reduce its coupled motion error, an actuator has longer shaft beam to reduce its stiffness along the direction perpendicular to another actuator, which lower a whole stiffness and also cause poor frequency response.

Table 2.6: Multi-DOFs MEMS-based positioning stages

Reference	Range of motion	Actuator	Kinematic Mechanism	Coupled motion error
Duc et al. 2008 [34]	17 μm x 11 μm	Polymeric thermal	Parallel/ Direct connection	-
Kim et al. 2002 [22]	30 μm x 30 μm	Electrostatic	Parallel	Less than 1 μm for 30 μm
Dong and Ferreira 2009 [32]	24 μm x 24 μm	Electrostatic	Parallel with leaf springs and parallel chain	-
Gorman et al. 2006 [119]	5 μm x 5 μm	Electrothermal bent-beam	Parallel	1 μm for 5 μm (from FEA)
Takahashi et al. 2005 [11]	30 μm x 30 μm	Electrostatic	Parallel	-

In order to minimize coupled motion error, one MEMS-based 2 DOF motion stage [22,32] places four equivalent electrostatic actuators at their four corners symmetrically. In this case, their motion platforms are located in the middle of four actuators. All four actuators are directly connected to a motion platform through long slender beams. These long slender beams are supposed to be firm along a longitudinal direction to deliver a desired motion and be flexible along transversal directions to reduce coupled motion error. This motion stage is able to produce larger 2 DOF motion with less coupled motion than the previous case, since their mechanical links are symmetrically linked. However, long slender beams tend to reduce total stiffness of a motion stage and are vulnerable at external force. Moreover, their motion platforms are fully surrounded by four actuators, so it is difficult to utilize these motion platforms for other applications, because applications, such as grippers or manipulators, need to place an object closer to a motion platform and this is almost impossible in these 2 DOF motion stages.

2.6.5 Kinematic mechanisms

Many nano-positioners have been designed for single DOF motion. When multi-DOF motions are needed, dedicated nano-positioners or a combination of single DOF nano-positioners have been suggested. The integrated nano-positioner in a small form-factor is challenging to develop with additive manufacturing or MEMS technologies, so a combination of single DOF nano-positioner has been commonly used for its simple implementation and reusing previous single DOF nano-positioners. However, when single DOF nano-positioners are not efficiently combined together, whole performance can be reduced and coupled motion error also increases. To overcome this, two kinematic mechanisms are commonly adapted; parallel kinematic mechanism (PKM) and serial kinematic mechanism (SKM). In the PKM, the motion platform is controlled by multiple actuators at a same time. PKM has an advantage to compensate a motion error in one direction by adjusting other actuators engaged. For accurate motions, dedicate mathematical analysis between inputs and output is necessary. Moreover, multiple connections to actuators can reduce its workspace down to an intersection of all engaged actuators. Contrary to PKM, the motion platform is at end of a serial chain in SKM like a robotic arm. The advantage of SKM is simple control, because there is only one mechanical link from a base to the motion platform. Each actuator or a single DOF motion stage is fully in charge of the motion along the designated direction. If there is a motion error in SKM, it is difficult to reduce its error due to the lack of the compensation mechanism in SKM.

There is a 2 DOF motion stage based on SKM [104], where one motion stage is partially embedded onto another motion stage. It is difficult to embed one motion stage

into another on a single layer, because the embedded stage also requires various features such as a base, electric connection or anchors for the electrothermal actuator. Due to these constraints, the motion stage except its actuator is embedded onto the other. This imperfect integration results in the reduction of its maximum motion to 5 μm , which is less than 30 % of its original motion. Additionally, the coupled motion error is estimated up to 20 % from finite element analysis (FEA). Based on this observation, additional features required for SKM are key factors to guarantee its original motion range and reduce any unexpected coupled motion error.

2.6.6 Resolution

Based on the performances listed in Table 2.1 to Table 2.5, most MEMS stages based on micro-actuators and compliant mechanisms provides nano-meter level resolutions; piezoelectric stages report motions with the resolution ranging from 0.3 nm to 100 nm. Electrostatically actuated stages have resolutions from 1.5 nm to 1 μm . This is because the monolithic compliant mechanism used in MEMS stages having no mechanical joint or pivots resulting in backlash or friction to convert or deliver the force or displacement from actuators to a motion platform. A MEMS based actuator, including electrothermal, electrostatic actuators, are capable of producing micro-meter or nano-meter level resolution from its design scale in previous research.

Kinematic converters or mechanical amplifiers described in section 2.5.3 can alter a resolution of a motion stage. Sebastien et al 2005 designed a thermally actuated 1-DOF nano-positioner [44] with the resolution less than 17 nm. This device adapts the lever for a displacement amplifier with 1:10 ratio indicating that an actuator used in this presented positioner is able to produce the resolution less than 1.7 nm. This electrothermal actuator

is reported to generate a motion less than sub nanometer level as well [118]. Although a minimum resolution available in a motion stage depends on the micro-transmission or converters, the motion stage in this dissertation will be designed for nanometer level resolution based on compliant mechanisms and mechanical amplifiers.

2.6.7 Natural frequency at low frequency range

The frequency response is a useful criterion to find available operating speed of the motion stages and its future applications. Since frequency response has not been carefully discussed in previous research, first resonant frequency is compared with in this dissertation. If a motion stage has a first resonant frequency around 1 kHz, it would be desirable to operate a motion stage with less than 500 Hz to avoid any unexpected response based on its frequency response. Any operation near its resonant frequency has a possibility to give some damage to a motion stage or cause unexpected mechanical behaviors. A motion stage with first resonant frequency of 100 kHz can be utilized in high-speed applications such as optical switches for communication, Atomic Force Microscope (AFM) application or high speed motions, which runs on a few kHz range.

First resonant frequency depends on the mass and the stiffness of a motion stage, but an actuator itself is also important; many electrostatic actuators have natural frequencies on the order of a few kHz range [18,33,87,103,120]. First resonant frequencies in piezoelectric actuator or stages are several hundred Hz or higher due to their high stiffness [36,111,112]. Contrary to these, electrothermal actuators have low frequency ranges less than several hundred Hz level, due to the fact that heating and cooling of beams in an actuator takes longer time than other actuation mechanisms [50,76,117]. Due to its low frequency response and large force, electrothermal actuators

have been widely used in micro-manipulation or gripping applications. Although wider frequency response is more desirable than shorter, this frequency response property can be selected depending on the application to apply for.

2.6.8 Bulk micromachining: Silicon-on-insulator Multi-User Multi-Processes (SOI-MUMPs)

MEMS fabrication process can be categorized into two fields based on its design approaches; surface micromachining and bulk micromachining technologies. Surface micromachining technologies are based on a combination of deposition and elimination of thin layers and sacrificial layers. With the multiple depositions and sacrificial layers, floating mirrors or movable diaphragm can be built and released for their operations. Contrary to surface micromachining technologies, bulk micromachining technologies are appropriate solutions for thick structures and generally consist of a few etching deposition processes. In bulk micromachining technologies, high-aspect-ratio structures or structures a hundred micro-meter tall are available with Bosch Deep Reactive Ion Etching (DRIE) [21]. For MEMS-based motion stages for micro-meter level objects, enough stiffness and force, and micro-meter scale volumes are necessary to interact with them. Due to these reasons, the motion stage presented in this dissertation is based on bulk micromachining. Additionally, these bulk micromachining technologies are able to demonstrate similar kinematic properties to the motion stages which are commercially available and built through conventional precision micromachining. Due to these facts, many MEMS-based motion stages have been built through bulk micromachining technologies [13,27,81,121].

Silicon-on-insulator Multi-User Multi-Processes (SOIMUMPs) [39] are a widely used standard fabrication process for bulk micromachining process. This process is composed of metal deposition and deep etchings. The metal deposition is done through a lift-off process or a shadow mask with electron beam evaporation. The etching process is based on Bosch Deep Reactive Ion Etching (DRIE) [21]. This DRIE can etch silicon with etch rate of 1 $\mu\text{m}/\text{min}$ and provide good high-aspect-ratio walls. KOH or TAMH are also widely used too, but they are limited to the orientation of a crystal lattice of silicon. This DRIE is famous for its capability to form deep trenches without considering this crystal orientation of silicon. In DRIE, 10 % variation of etching rate is acceptable and the distribution of targets and the ratio of the etched area over the wafer are important factors to decide its etching rate and its uniformity over a wafer.

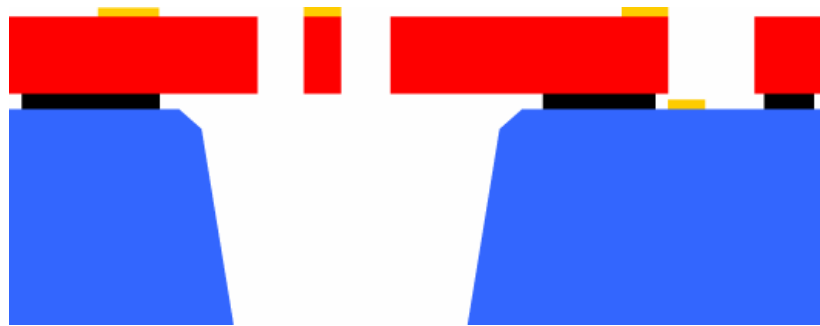


Figure 2.15: Cross sectional view of a structure with a SOI-MUMPs (not to true scale) [39]

For SOIMUMPs, SOI wafers are utilized in this dissertation. SOI wafers are purchased from commercially available ones. In this case, some dimensions can be limited by SOI wafer sellers or vendors. The SOI wafer is composed of three layers; the device layer (or a front side in red in Fig. 2.15), the buried oxide layer (in black in Fig. 2.15) and the handle layer (or a back side in blue in Fig. 2.15). For this system, the device layer is set to be 30 +/- 1 μm thick, the buried oxide is 2 +/- 0.05 μm thick and the handle

layer (substrate) is $450 \pm 10 \mu\text{m}$ thick. The resistivity of the device layer is adjustable and controlled to be less than $0.01 \Omega\text{-cm}$. The device layer can be etched down to the buried oxide layer, which is utilized for main devices such as actuators, mechanical linkages and motion platforms. The handle layer is also be patterned and etched from the bottom side to the buried oxide layer. The main purpose of this layer is to protect the device layer and improve its accessibility. But recent researches start utilizing this layer as a secondary device layer. The buried oxide layer plays an adhesive layer between the device layer and the handle layer and also operates as an electric insulation, etching stop for DRIE and thermal insulation.

In this dissertation, a silicon-on-insulator (SOI) wafer and SOI-MUMPs are utilized to build the desired motion stages for 3 DOF motions. The presented motion stages consist of two layers, which can be implemented in SOI wafers without additional fabrication processes. The device layer and the handle layer will be patterned through the DRIE. In this case the buried oxide layer of SOI wafers works as the etching stop layer for this DRIE. The presented motion stage follows the standard SOI-MUMPs and is based on SOI wafers, so no special fabrication processes is needed and the motion stage design presented in this dissertation can be built without any special equipment.

2.7 Summary

The current state of MEMS based actuation mechanism has been summarized and compared with each other in the previous sections. From this observation, we notice that various actuators and kinematic models have been developed and some of them are well analyzed and utilized in various applications. Among them, some relevant designs are surveyed and compared in Table 2.1 to Table 2.6. Designing a motion stage in MEMS is

also a sort of a trade-off among various actuators and design parameters. However, there are still challenging areas in some respects; a sufficient range of motion, lack of appropriate mechanisms between multiple DOFs, limited out-of-plane motions, and insufficient MEMS fabrication methods. These constraints indicate that a new design approach is needed to generate 3 or more DOFs motion. Hence, we believe that there are some rooms to improve in this research area and decide important features for the motion stage designs.

1. Electrothermal actuators: Many researchers on MEMS-based motion stages have utilized electrostatic actuators for their applications, because electrostatic actuators are easier to build, simple to design, high frequency response and good electric connection when multiple actuators are engaged. Since the characteristics of the motion stage are inherited from the actuator, these electrostatically actuated stages can have properties similar to electrostatic actuators. However, electrostatically actuated stages have some issues; small force and clean environment. This dissertation is to design a motion stage and to utilize it for micro-manipulation application, so interactions with external objects is necessary. In this case, this manipulation requires enough force to move external objects which might be dirt and can contaminate the motion stage. To achieve it, an electrothermal actuator can be a good alternative rather than modifying existing electrostatic actuators. High driving voltages to electrostatic actuators can cause electrostatic force, which can affect the gripping operation electrostatically. The drawbacks in the electrothermal actuator such as a short stroke are studied in this

dissertation to overcome by adapting mechanical amplifiers and optimizing the actuator.

2. Serial kinematic mechanism (SKM) for multi-DOFs motion: Many MEMS-based motion stages are based on parallel kinematic mechanism (PKM), because PKM is easy to implement in MEMS and also generate reliable motions, compensate coupled motion error, and is stiff against external disturbance. However, most implementation of PKM focuses on in-plane motions such as in-plane linear motions or in-plane rotational motions. This is because it is hard to integrate out-of-plane structures with in-plane structures in PKM. In MEMS, it is still challenging to design out-of-plane structures. This comes worse, when the out-of-plane structure needs to integrate with in-plane structure for PKM. In this dissertation, we design and build 3-axis or 3 DOF motion stage consisting of two in-plane motions and one out-of-plane motion. This 3-axis motion is more natural in manipulation applications. For this purpose, integration of three different actuation systems is introduced. Instead of PKM, serial kinematic mechanism (SKM) is chosen for integration of an out-of-plane structure in this dissertation. With SKM, the chosen out-of-plane actuator or motion stage can be integrated with another system without any significant modification. In addition to this, each motion from the motion stage based on SKM is designated to each actuator separately, so straightforward control is possible, which also can reduce its preprocessing time and make user understand its operations intuitively when multiple motion stages are engaged for manipulation such as a coordinated manipulation.

3. Design of an out-of-plane motion stage: No research has been done so far for an out-of-plane motion stage based on integration with existing in-plane motion stages. The desirable out-of-plane motion stage will have four important features; (1) it consists of an actuator and a motion platform similar to the in-plane motion stages; (2) it is also capable of generating performance similar to the in-plane motion stages such as a motion range and force; (3) its stiffness will be in the same level with the in-plane motion stages; (4) this stage should be easily integrated with the in-plane motion stages by using almost same fabrication methods. Most existing out-of-plane motion stages reported are designed to operate as a stand-alone and their fabrication methods are pretty different from them for in-plane structures. In this dissertation, a new out-of-plane motion stage is designed and proposed for the integration with in-plane motion stages. The new out-of-plane motion stage is designed to meet the four requirements described above and will be integrated with in-plane stages for 3 DOF motions.
4. The range of motion more than 50 μm along X, Y, and Z directions: In this dissertation, the expected applications of the presented motion stage are manipulation of micro- or nano-sized objects. When an object to rotate has a diameter of 10 μm , at least the motion of 50 μm is needed to rotate it up to 360 degrees with two fingers or move it onto another position. In this dissertation, we set the target range of motion as 50 μm for X, Y and Z axes.
5. A few mN level of force along X, Y, and Z axes: a few milli-Newton level of force are also required to grip and move small objects like micro-spheres. Many actuators provide hundreds micro-Newton level force and this is not enough to

move some structures near the motion stage made of the same wafer. By adapting and optimizing the electrothermal actuator, the force larger than a few mN is expected in this dissertation.

The presented motion stage in this dissertation is designed based on the considerations such as 3-axis motion, motion of 50 μm , force larger than a few mN, and coupled motion error less than 1 %. Based on the details described above, the proposed high precision motion stage in this dissertation adapts electrothermal actuators for their large force and reasonable input driving voltage. The integration of three individual motion stages is based on SKM. For the implementation of the SKM, nested structures are utilized twice; the Z-stage is embedded onto the Y-stage and the Y-stage is also embedded onto the X-stage. With this dual nested structure, the coupled motion error among the three motion stages engaged is expected to decrease. Based on these considerations, the presented motion stage in this dissertation has a capability to meet those requirements and demonstrate a manipulation of micro-meter size objects.

Chapter 3 MEMS based thermally actuated single DOF stage

In this chapter, the design and characterization of an MEMS-based single-DOF motion stage (called an X-stage) is presented. This X-stage is designed to measure the material properties of viscoelastic materials in a parallel plate type rheometer. With this rheometer device, the viscosity and elasticity of a cementitious material is tested, for its importance in a constructional industry. For appropriate measurement for this application, the presented X-stage needs to generate a shear force around 60 Pa and also have a stiffness of about 50 N/m. In order to meet these requirements, the dual bent-beam electrothermal actuator is designed and adapted. In addition to this actuator, a motion platform is also installed to provide an enough test bed for nano-liters level volume. An embedded capacitive sensor is connected at the end of the motion platform to monitor its motion with the resolution of 1.06 μm . A reference cement paste, SRM-2492 is placed onto the motion platform of the X-stage and then a stationary glass plate is installed on the top of them to measure its yield stress and plastic viscosity.

3.1 Introduction

Cement pastes are a key material in civil engineering and used in various structures and applications [122]. In many applications, the material properties of cement paste need to be adjusted to meet the requirements depending on their situations. These properties can be controlled by adjusting the combination ratio among the additive dosages. In order to find optimum ratios, many different combinations have been tested and monitored frequently. Among various properties, the viscoelastic shear properties of cement pastes have been measured importantly [123].

In order to measure these viscoelastic shear properties of cementitious materials, various rheological measurement methods have been utilized; a cone and plate type, a parallel disk type, an eccentric rotating disks type, a concentric cylinder type, sliding plate type, and a shear-sandwich type [124]. The basic principle of these rheometers is to apply shear rate to the target material and measure its corresponding response or shear stress.

Among various rheometers, a parallel disk type [125] and a sliding plate type [126] have been commonly used for their simple mechanism. These are composed of two plates; one is a stationary plate and the other is a vibrating plate in parallel. The vibrating plate is designed to generate a rotational motion or a linear motion to apply shear rate to a target material. The corresponding motion of a material to measure will be monitored to obtain its shear stress information. In the cementitious material testing, the frequency ranges from 0.2 Hz [127] to 1 Hz [128] are commonly used and the gap between two parallel plates is around 0.4 mm to 0.65 mm [127]. This gap should be large enough to reduce the effect from the grain size of a cementitious material, which is roughly 80 μm to 100 μm [124]. The measured shear or storage modulus ranges from 100 Pa to 1.3 MPa in previous researches [128]. These specific design parameters are referenced for appropriate designs in this chapter.

Conventional rheometers are bulky and expensive, so it consumes considerable amount of test materials and a cleaning process between tests is necessary. It is also impossible to run multiple tests at a same time. Considering these situations, it would be beneficial to develop a portable and disposable measurement method. With these features, it is advantageous to run multiple measurements at the same time. This is especially

important in civil engineering, since the cement paste solidifies within an hour after its cure. For these reasons, rheometers based on a micro-electro-mechanical systems (MEMS) have been developed [129]. MEMS devices have advantages in its low cost from batch process and a small form factor [20], which make multiple tests at the same time possible and also improve its portability and disposability for various industrial environment [130].

The sliding plate type rheometers composed of two plates in parallel are compatible with MEMS fabrication technologies. The motion of the plate can be implemented by electrostatic actuators or electrothermal actuators [29,87,131]. The electrostatic actuator can provide a reliable motion at high frequency. However, this actuator is able to generate micro-Newton level force, which is too small to generate enough motions. This actuator also requires a clean environment or good isolation, which results in poor reliability in rheometer, because small amount of a target material can leave a permanent damage on the device. The electrothermal actuator has a short operation frequency, which is still good in cementitious materials and reliable in dusty environment. In addition to these properties, the electrothermal actuator is able to generate mill-Newton level force for a large motion [71,132].

This paper describes a 1 DOF linear motion stage designed for rheological measurement. This stage is composed of an actuator and a motion platform. An electrothermal actuator is adapted for its large force and reliable operation in dust environment [71,132]. Instead of visual measurement in previous MEMS-based rheometer [129], a capacitive displacement sensor is embedded for its accurate measurement. This device is fabricated based on Silicon-on-insulator Multi-User Multi-

Processes (SOI-MUMPs) [39] and tested with SRM 2492 [133], which is a reference material for cement pastes. Experimental characterization process follows Bingham Paste Mixture model to calculate its viscoelastic properties.

3.2 Design of the X-stage

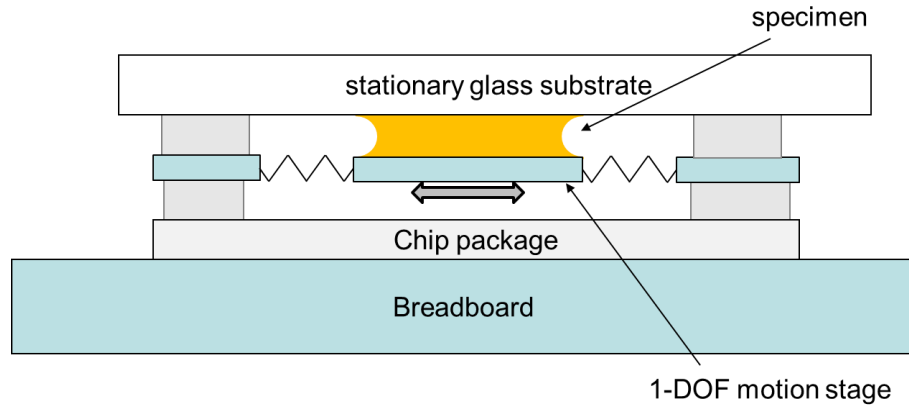


Figure 3.1: A MEMS based X-stage for rheological measurement set-up

Figure 3.1 illustrates the rheological material testing set-up with the presented X-stage stage. This implementation follows the basic mechanism of the parallel plate type rheometer. This system is composed of two plates and measures the response from a target material placed between them. One plate is stationary and the other is movable to apply the shear force to the target. In this study, the vibrating plate will be replaced by the motion platform of an MEMS-based X-stage. When the X-stage applies a shear force to the cementitious material through its motion platform, the corresponding displacement will be measured by the embedded capacitive sensor.

Figure 3.2 shows the 3D CAD model of the X-stage for the rheometer. The stage consists of a dual bent-beam electrothermal actuator, eight folded springs, one motion platform, and an embedded capacitive sensor. The dual bent-beam type electrothermal

actuator is composed of two bent-beam type actuators, which are serially connected. This actuator is designed to keep its stiffness lower to be sensitive to external load changes. The motion platform is a square plate providing an area larger than 2 mm x 2 mm, which is enough for a few nano-liter level cementitious materials. The eight folded springs are supposed to hold the motion platform in its position against any out-of-plane deformation. The embedded capacitive sensor is directly connected to the motion platform to monitor its displacement accurately. The stationary plate is made of a glass sheet and will be placed on the top of the motion platform and supported by four columns. The gap between the two plates is measured later for accuracy and is adjusted to be taller than an average grain size of the cement paste.

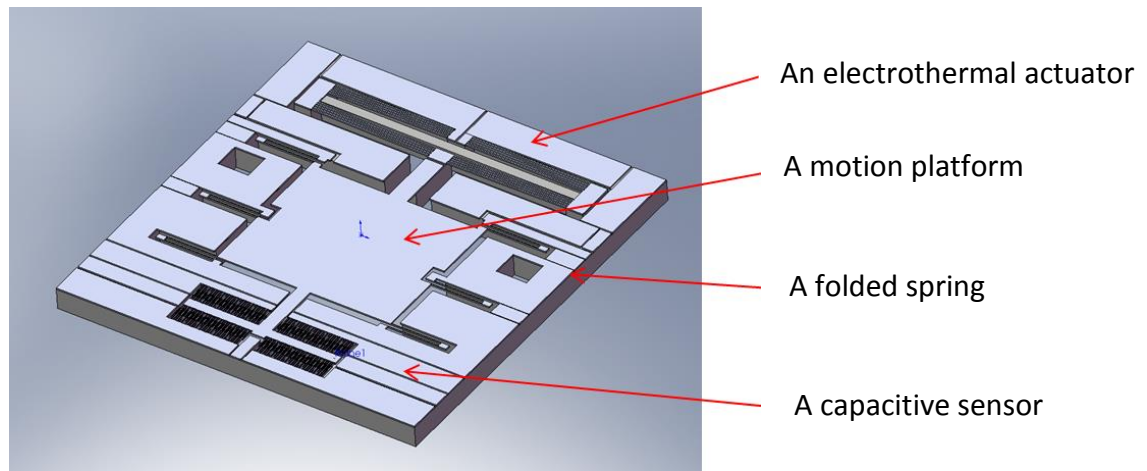


Figure 3.2: 3D CAD models of the 1-DOF motion stage

3.2.1 The analysis for the dual-bent beam electrothermal actuator

Figure 3.3(a) illustrates the schematic model of the presented X-stage to design. The dual bent-beam electrothermal actuator is implemented with a serial connection of two bent-beam type electrothermal actuator and a connecting bar. An actuator similar to this design was reported as a one-ring spring actuator [52]. With successful thermal insulation, this

bar can work as a motion constraint to increase the motion of its shaft. However, MEMS fabrication methods, SOI-MUMPs adapted in this study is difficult to implement this thermal isolation well. Thus, the dual bent-beam presented in this study is utilized a different working principle; the connecting bar will be expanded by its Joule heating or resistive heating and this expansion generates the main force to thrust the motion platform. In this case, the operation direction is opposite to that of the one-ring spring actuator [52].

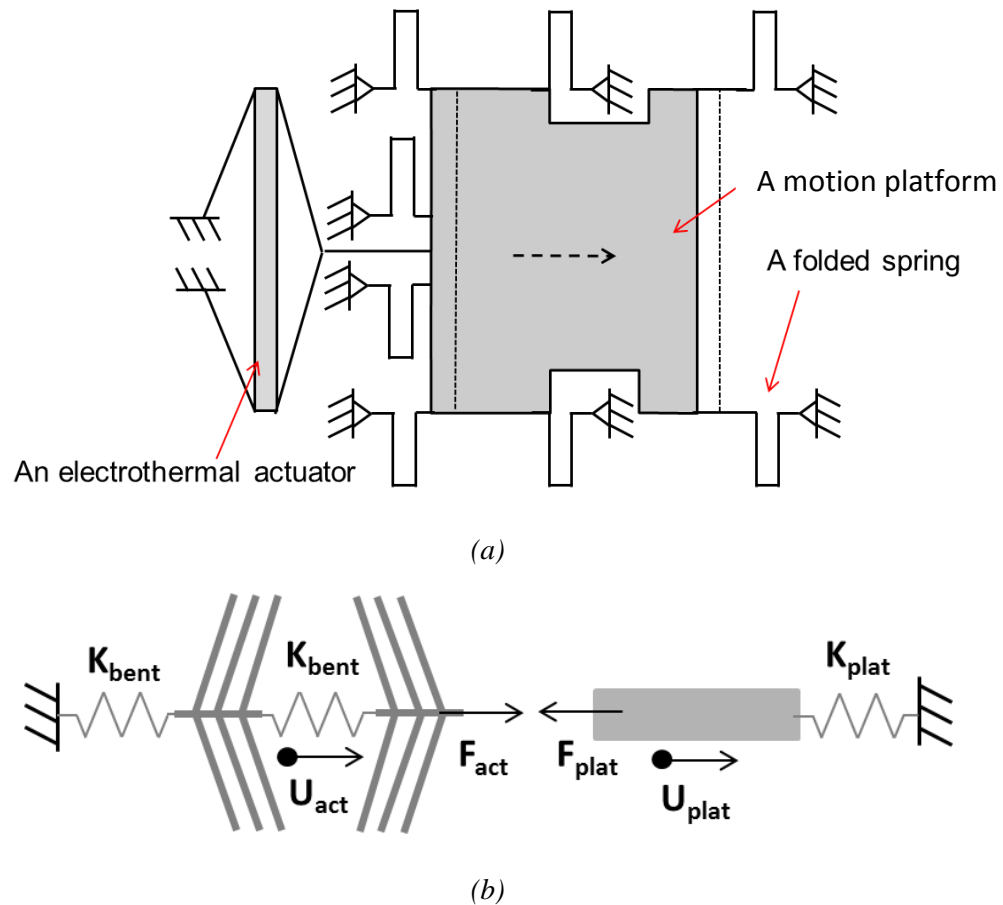


Figure 3.3: The conceptual design of the X-stage; (a) a schematic model; (b) a lumped model

The lumped model shown in Fig. 3.3(b) represents the expected forces and displacements of the X-stage, where K_{bent} is the stiffness of the bent-beam type actuator

and K_{plat} is the stiffness of the motion platform. Based on this diagram, the total stiffness of the actuator K_{act} can be expressed as:

$$\frac{1}{K_{act}} = \frac{1}{K_{bent}} + \frac{1}{K_{bent}} \quad \text{or} \quad K_{act} = \frac{K_{bent}}{2} \quad (3.1)$$

The output displacement of the motion platform can also be expressed based on a parallel connection of springs as:

$$U_{plat} = \frac{F_{act}}{K_{act} + K_{plat}} \quad (3.2)$$

where F_{act} is the force generated by the dual bent-beam type actuator. K_{bent} and K_{plat} are explained in the following.

The presented dual bent-beam electrothermal actuator is shown in Fig. 3.4(a). The lateral bar in the middle of the actuator will be thermally expanded when an electric current flows through the bent-beam actuator. In this case, the expected mechanical behavior is described in Fig. 3.4(b), where a solid line is for its original shape and a dotted line stands for the expanded shape. Based on this mechanism, the stiffness of the actuator can be expressed [53] as:

$$K_{act} = n \left(\sin^2 \theta + \cos^2 \theta \frac{W^2}{L^2} \right) \frac{EWT}{L} \quad (3.3)$$

Where n is beam number, W is beam width and L is beam length. Based on equation (3.3) and Table 3.1, the expected stiffness of the presented dual bent-beam actuator is 43.0 N/m, which is a half of the bent-beam type actuator. The calculation from Finite Element Analysis (FEA) is about 43.7 N/m, which shows an error less than 1 %.

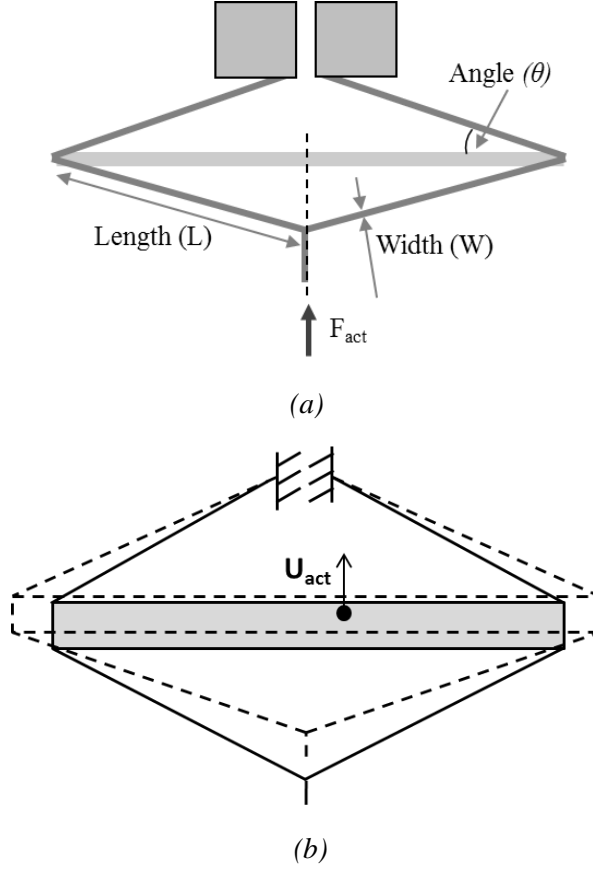


Figure 3.4: the design of the dual bent-beam electrothermal actuator; (a) a schematic diagram; (b) the expected mechanical behavior

The expected force from the actuator, F_{act} can be expressed from the thermal expansions and its related stress [27] as:

$$F_{act} = 2\alpha\Delta T_{ave}EW_{connecting}T\sin\theta \quad (3.4)$$

where α is coefficient of thermal expansion of silicon, ΔT_{ave} is an average temperature rise in the actuator, $W_{connecting}$ is the beam width of the lateral beam and T is the thickness of the actuator and θ is the beam angle in the actuator. Among the design parameters in equation (3.4), the average temperature rise ΔT_{ave} can be expressed as a function of a driving voltage [53] as:

$$\Delta T_{ave} = \frac{V^2}{3k\rho} \quad (3.5)$$

Where k is thermal conductivity of silicon, ρ is resistivity of silicon, and V is a driving voltage.

3.2.2 The motion platform with eight folded springs

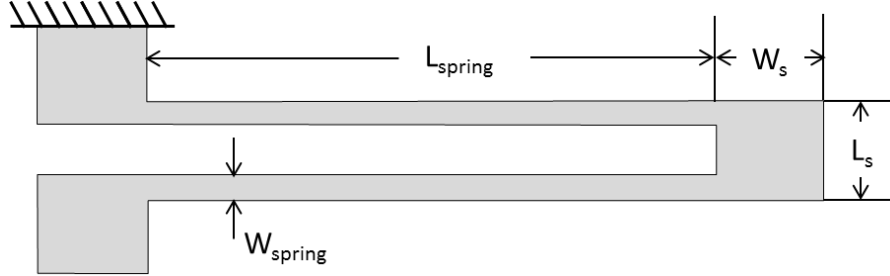


Figure 3.5: The folded spring design

The motion platform is one large square plate and supported by eight folded springs in order to reduce any out-of-plane deformation when a sticky target material is placed. The folded spring shown in Fig. 3.5 is a compliant mechanism transmitting translational motion via its elastic deformation. The stiffness of the motion platform, K_{spring} can be expressed as a combination of the stiffness of eight folded springs [52] as:

$$\frac{2}{K_{plat}} = \frac{1}{ET} \left(\frac{L_{spring}^3}{2W_{spring}^3} + \frac{6(1+\mu)L_{spring}}{5W_{spring}} + \frac{L_s}{2W_s} + \frac{3L_{spring}^3 L_s}{2W_s^3} \right) \quad (3.6)$$

Where, μ is the Poisson's ratio of silicon, and the other design parameters are described in Fig. 3.5 and Table 3.1. Based on these design parameters equation (3.3) predicts that the stiffness of the motion platform will be 53.4 N/m. The FEA calculation is 51.76 N/m, so the 3 % difference implies that it is reasonable to use equation (3.6) to obtain the stiffness of the folded springs within acceptable errors.

Based on three design parameters described above, equation (3.3) can be extended with more details as:

$$U_{plat} = \frac{2\alpha EWT\sin\theta}{3k\rho\left\{n\left(\sin^2\theta + \cos^2\theta \frac{12I}{AL^2}\right) \frac{EWT}{L} + K_{plat}\right\}} V^2 \quad (3.7)$$

Where, I is the area moment of inertia and the other parameters are described in Table 3.1. Equation (3.7) implies that the displacement of the motion platform is proportional to the square of the driving voltage, which will be verified with experimental results.

Table 3.1: The dimensional range of the design parameters

Symbol	Design parameter	Values
W	Actuator beam width	22.37 μm
θ	Actuator beam angle	0.8 degrees
L	Actuator beam length	2350 μm ,
T	Actuator beam thickness	30 μm
n	Number of beams in actuator	5
L_{spring}	Folded spring link length	1000 μm
L_s	Folded spring short link length	100 μm
W_{spring}	Folded spring link width	15 μm
W_s	Folded spring neck length	100 μm
K_{plat}	The stiffness of the motion platform	51.76 N/m
K_{act}	The stiffness of the actuator	43.7 N/m

3.2.3 Design constraints; thermal limit

The main design constraint of the presented actuator is the thermal limit of silicon. Higher temperature than the half of melting point of silicon (1414°C) has a possibility to occur permanent damage on the X-stage. This can result in a shorter life-time and a lower performance than expected. Thus, the maximum temperature rise ΔT_{max} should not

exceed this limit; various temperature limits have been reported for this; 550 °C [61], 600 °C [89] or 900 °C [134]. The lowest value among them has been selected as the maximum temperature limit in this chapter for a reliable operation. Since the room temperature is measured as 20 °C, the relationship between the maximum temperature rise and the average temperature rise can be expressed [27] as:

$$\Delta T_{\max} = \frac{3}{2} \Delta T_{\text{ave}} < 530^{\circ}\text{C} \quad (3.8)$$

The displacement of the motion platform in equation (3.7) is limited by temperature limit in equation (3.8).

3.3 Finite element analysis (FEA)

A series of Finite Element Analysis (FEA) is utilized with ANSYS [135] to predict the expected thermal and structural behavior of the proposed design. With these purposes, this FEA is also used to verify the design processes in the previous section. The material properties for this FEA are from a similar research [27]. Structural and thermal boundary conditions and thermal assumptions are applied to this FEA; (i) assumed to be fixed firmly on the ground for structural analysis, (ii) the ends of the eight folded springs and the ends of the actuator are also connected to a heat sink at room temperature of 20 °C for thermal analysis, (iii) heat conduction only is taken into consideration as a thermal energy transfer.

Figure 3.6 shows the expected displacement of the actuator and the motion platform as a function of a driving voltage. The displacement of the actuator is measured at the connecting bar between two bent-beam actuators and the motion of the motion platform is measured in its center. Figure 3.6 shows that the displacement of the motion

platform is twice of that of the connecting bar as expected. These results are also compared with the analytic results from equation (3.7) showing that equation (3.7) can predict similar values with FEA, but its trend pattern is slightly different due to limited material properties.

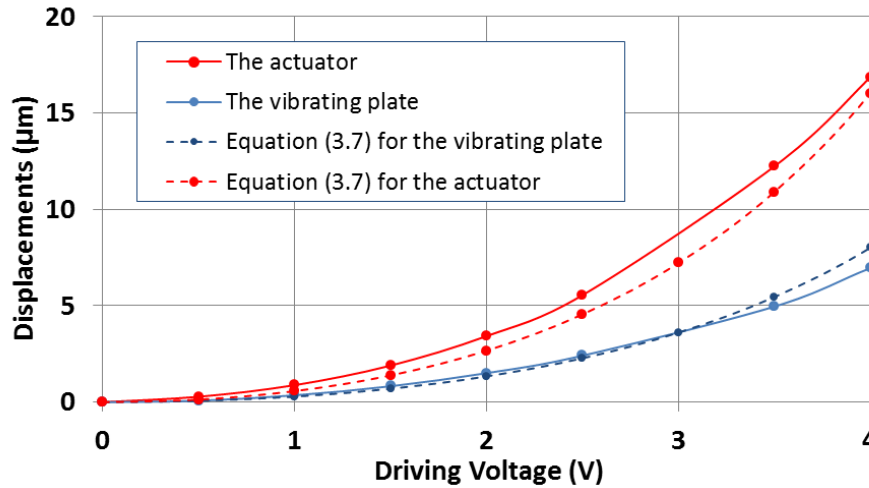
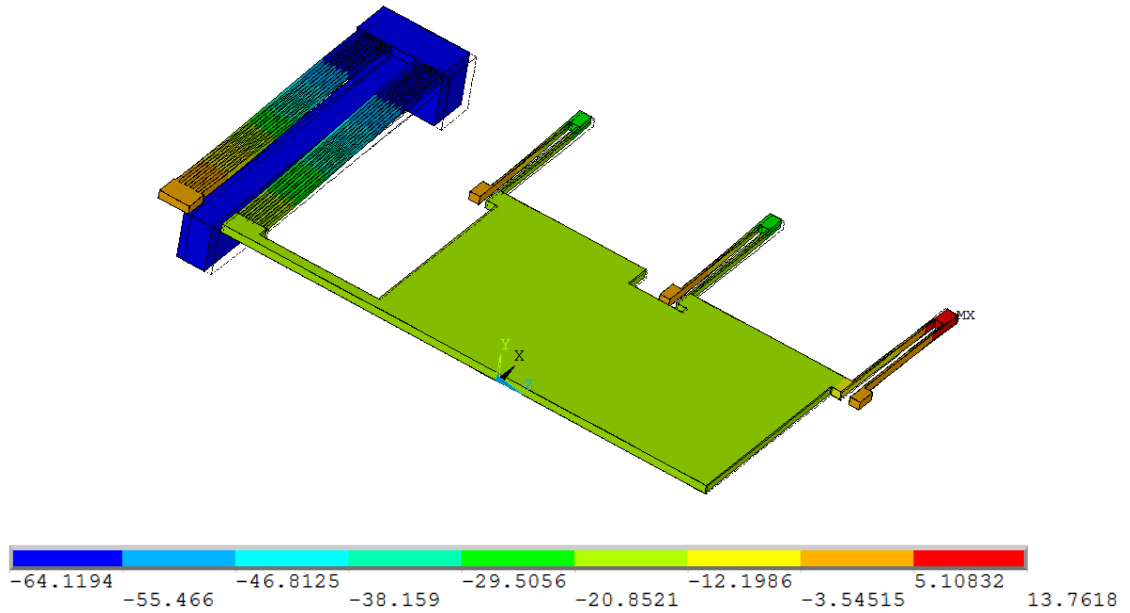


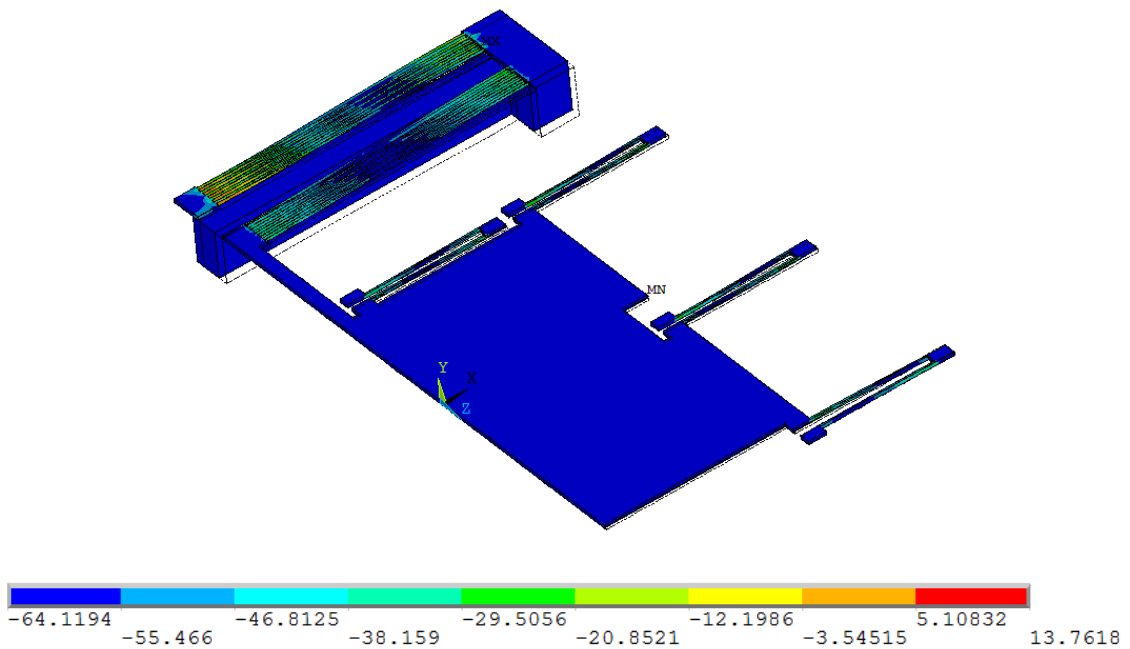
Figure 3.6: FEA result of the displacement by driving voltages

The stress distribution of the X-stage is also monitored to determine its mechanical state during its operation. Figure 3.7(a) shows the von Mises stress distribution of the half of the presented 1-DOF motion stage. Its actuation source is the temperature rise up to 542.6 °C, which is close to its maximum allowable temperature. If the stage is stable under this temperature, this can be interpreted that the stage is stable under its maximum displacement. With this temperature rise, FEA simulation reveals that von Mises stress is less than 193 MPa over the stage as shown in Fig. 6(b), where most deformation occurs around the folded springs and the other portions remain same during its operation. No mechanical deformation is expected to a target material placed on the

motion platform. In addition to this, 193 MPa is far less than 7 GPa, yield strength of silicon indicating that no structural failure is expected at its maximum displacement.



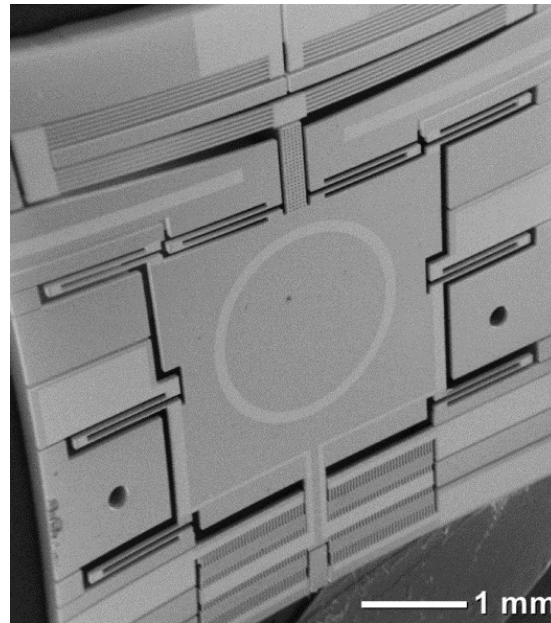
(a)



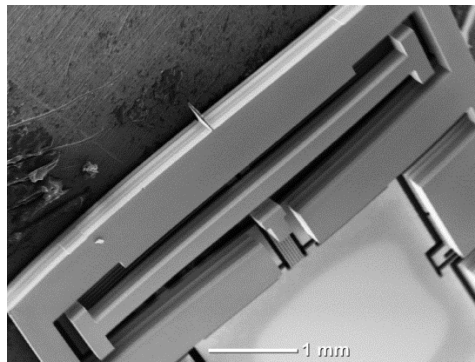
(b)

Figure 3.7: FEA simulation results by the temperature rise of 542.6 °C; (a) the displacement vector sum (in μm unit); (b) von Mises stress distribution over the stage (in MPa unit)

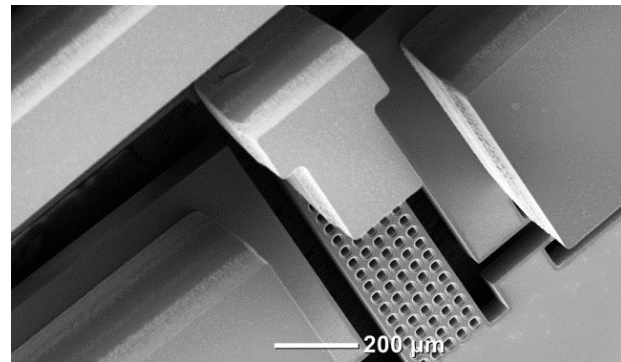
3.4 Fabrication



(a)



(b)

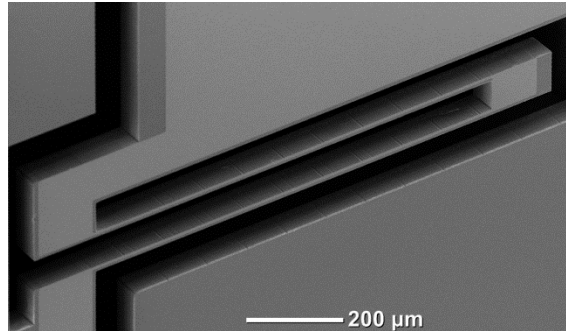


(c)

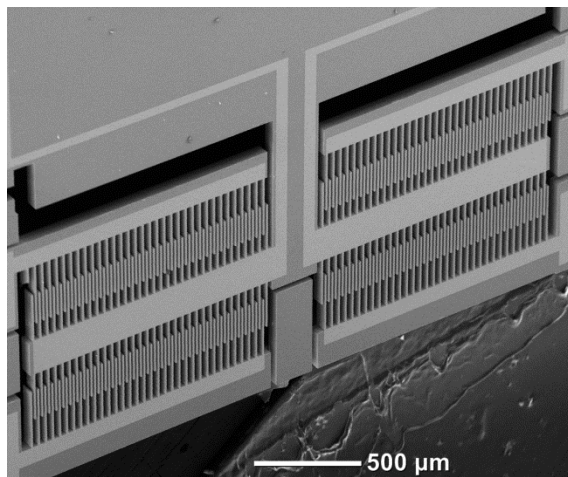
Figure 3.8: The SEM images of a fabricated X-stage; (a) a frontal full view; (b) a backside view of the connecting bar in the actuator; (c) a backside view between the actuator and the motion platform for electric isolation

The fabrication process for the proposed motion stage follows Silicon-On-Insulator Multi-User Multi-Processes (SOIMUMPs) [39]. With this standard process, a Silicon-On-Insulator (SOI) wafer is used as a starting material, which consists of a 30 μm thick device layer, a 400 μm thick handle layer and a 2 μm thick buried oxide layer. The fabrication process consists of four steps – metal layer deposition, deep reactive ion

etching (DRIE) of the device layer, DRIE of handle layer, and removal of buried oxide layer. The details about this fabrication are described in details in previous research [27].



(a)



(b)

Figure 3.9: The SEM images of a fabricated 1-DOF motion stage; (a) a closed-up view of the folded spring; (b) an embedded capacitive sensor

Based on the fabrication procedure described above, the X-stage has been fabricated and is shown in Fig. 3.8(a), where the bright areas stand for metal layers and used for electric connection of the embedded capacitive sensors and the actuator. The grey portions are silicon and constitute a most portion of the device. Figure 3.8(b) is the lateral bar and a supporting block on the backside of the actuator. The block in Fig. 3.8(c) is designed to isolate the actuator electrically and thermally from the motion platform to

reduce its effect on the platform. For this purpose, its top side has a physical gap, which will be held by this block to transfer the displacement or force from the actuator to the motion platform.

The folded spring is shown in Fig. 3.9(a), where an embedded electric path is also embedded on the folded spring for electric connection of the embedded sensor. With this feature, this folded spring works as an electric path as well as a structural supporter.

The detailed view of the embedded sensor is shown in Fig. 3.9(b). This sensor is made up of multiple inter-digitated fingers and composed of three different groups; high electrode, low electrode and a middle group. These three groups comprise a differential type capacitive sensor, which can eliminate the residual capacitance among the engaged MEMS components. The motion platform is linked to the middle group and its motion increases the capacitance with one group and decreases it with the other group.

3.5 Experimental results

The fabricated X-stage is characterized experimentally for its performance including its maximum displacement and the calibration of the embedded sensor. The displacement of the X-stage is measured with the embedded capacitive sensors. In this experiment, two metal pads in the actuator are electrically connected to a DC power supply units (Model 3322A¹ from Agilent) and three electrodes in the embedded capacitive sensor are connected to 1 channel capacitance to digital converter module, AD7747 [136]. For the calibration of the sensor, the motion platform is monitored by an optical profiler (VEECO¹ NT1100 [137]). After the displacement obtained from an optical profiler is compared with a capacitance change in AD7747, the embedded sensor can be calibrated

with a capacitance-to-displacement ratio of $106.41 \mu\text{m/pF}$. Based on the specification of AD7747 [136], this sensor has the resolution of 2.1 nm and the accuracy of $1.06 \mu\text{m}$.

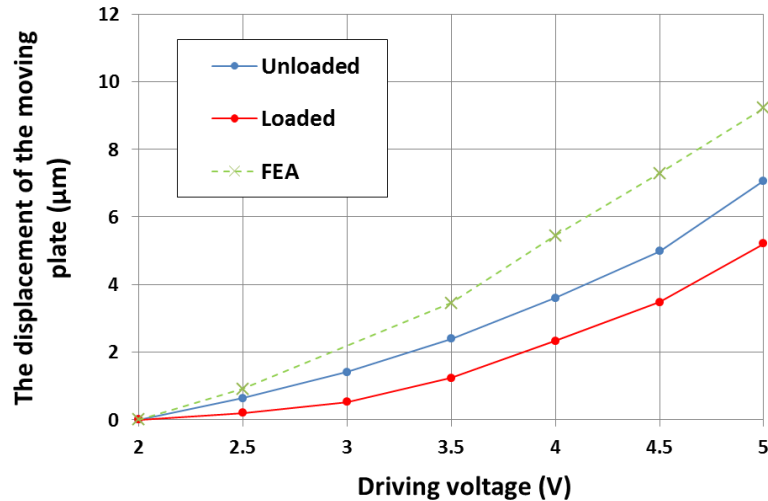


Figure 3.10: Experimental results of the displacement of the 1-DOF motion

With this calibrated embedded sensor, the displacements of the X-stage have been measured with two different cases; alone and one with a material to measure separately. Figure 3.10 shows the displacements of the X-stage experimentally measured through the embedded sensor for these two cases. This indicates that the displacement difference between a stand-alone and one with a sample shows a reduction of displacement by 25 %, which is enough noticeable different and gives enough sensitivity to the embedded sensor. FEA simulation results show similar motion pattern, but higher than the others. This comes from a limited simulation condition; thermal conduction only is taken into consideration in the FEA simulation. Based on this experimental observation, the X-stage is well adjusted to detect the motion reduction from a cementitious material to measure. The combined sensor also plays well in monitoring the motion platform.

3.6 Viscoelastic material testing for a SRM 2492

The viscosity and elasticity of the cementitious materials are commonly measured to define their viscoelastic properties [122]. When a force is applied to one plate in a parallel plate type rheometer, the shear stress (τ) can be expressed as:

$$\tau = \frac{F}{S} \quad (3.9)$$

Where, F is a shear force and S is the contact area. If $F = F_0 \cos \omega t$, then equation (3.9) will be:

$$\tau = \left(\frac{F_0}{S}\right) \cos \omega t = \tau_0 \cos \omega t \quad (3.10)$$

Where ω is angular velocity. In this case, the displacement of the other plate or shear strain γ will be expressed as:

$$\gamma = \gamma_0 \cos(\omega t - \phi) \quad (3.11)$$

Where, ϕ is a phase shift between the actuating plate and the other. The phase angle ϕ will be 0 for a perfect solid and $\pi/2$ for pure viscous liquid. For viscoelastic material like cement paste, the phase angle ϕ will be between them and is one important material property that depends on frequency.

The linear constitutive equation about the shear stress and shear strain is

$$\tau^* = G^* \gamma^* \quad (3.12)$$

Where G^* is the complex shear modulus. By definition, G^* is composed of a real component and an imaginary component as follow:

$$G^* = G' + iG'' \quad (3.13)$$

The real part G' is the elastic shear modulus or storage modulus and the imaginary part G'' is the viscous shear modulus or loss modulus. In this case, each them can be expressed based on the given geometries [126] as:

$$G' = \frac{\tau_0 d \cos \delta}{Ax_0} \quad (3.14)$$

$$G'' = \frac{\tau_0 d \sin \delta}{Ax_0} \quad (3.15)$$

Where x_0 is the displacement amplitude and τ_0 is the stress amplitude. The term G' and G'' are commonly used in rheological measurements and Bingham model has been widely used [125,133] to predict the viscoelastic behavior of the cement pastes, which is shown in Fig 3.11. The yield stress (YS) in Fig. 3.11 is the stress needed to initiate deformation and the plastic viscosity (VS) is the deformation rate when the shear stress is applied to.

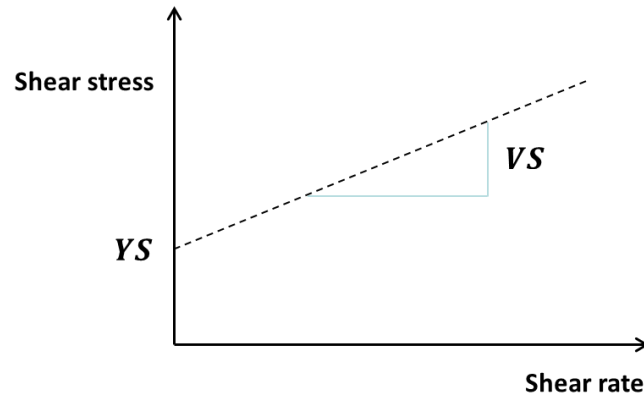


Figure 3.11: A Bingham model plot [19]

Based on Bingham model, the shear stress can be described as:

$$\tau = YS + VS\dot{\gamma} \quad (3.16)$$

Where σ is shear stress and $\dot{\gamma}$ is shear rate. In order to obtain the plastic viscosity (VS) and a yield stress (YS), the shear stress and the shear rate in Fig. 3.11 need to be measured. The shear stress (τ) can be defined from the basic definition of shear force and the affected area [138] and expressed as:

$$\tau = \frac{F_{act}}{A} \quad (3.17)$$

Where A is the contact area between the cementitious material and the vibrating plate, which needs to be measured after placing a material onto the plate. The force from the actuator, F_{act} can be also obtained from equation (3.3). With these two equations, the shear stress in equation (3.10) can be calculated.

The shear rate is defined [122] as:

$$\dot{\gamma} = \frac{\Delta x}{\delta \Delta t} \quad (3.18)$$

Where Δx is the displacement of the top plate measured by the embedded capacitive sensor, δ is the gap between two parallel plates, and Δt is the time applied to produce the displacement of Δx . The operating frequency used for the whole tests is 0.5 Hz, so Δt will be a 1 sec for triangular motion.

For accurate measurement, the X-stage is measured without a material to test first, because this parallel plate type rheometer have an embedded sensor on the vibrating plate side, not a stationary plate. With this test, the original shear force from the X-stage can be calculated and can be used later as a reference. After placing the target cementitious

material between two plates and applying the shear force, the displacement is also monitored by the embedded capacitive sensor. This procedure will be repeated with different driving voltage or different shear rate in order to have enough data to plot the Bingham model shown in Fig. 3.11.

Based on the analytic relationship based on equation (3.17) and (3.18), Bingham model is plotted based on experimental data and shown in Fig. 3.12. In this test, SRM-2492 mixture, a reference material for the cement paste is selected. This mixture is placed on the stationary plate, a transparent slide and then is installed on the top of the X-stage as described in Fig. 3.1. For different shear rate, the displacement of the X-stage is controlled by different input voltages ranging from 2 V to 5 V. With these repeated tests, the trend line can be plotted in Fig. 3.12 indicating that YS is 7.09 Pa and VS is 1.42 KPa/s. The experimental data from conventional traditional rheometer [133] shows the yield stress (YS) is around 20 to 35 Pa and the plastic viscosity (VS) is 5 to 15 Pa/s with the shear rate up to 40 /s. The rheological results using the MEMS-based X-stage have lower YS and higher VS then those from the conventional rheometers [133].

When the experimental results in Fig. 3.12 is combined with the data obtained from a conventional rheometer [133], a new graph can be plotted as shown in Fig. 3.13. This combined plot shows that the rheological measurement from the presented X-stage can be utilized to improve the resolution of current conventional rheometers at its low shear rate. This is because MEMS-based rheometer can detect more detailed results in small range of shear rate.

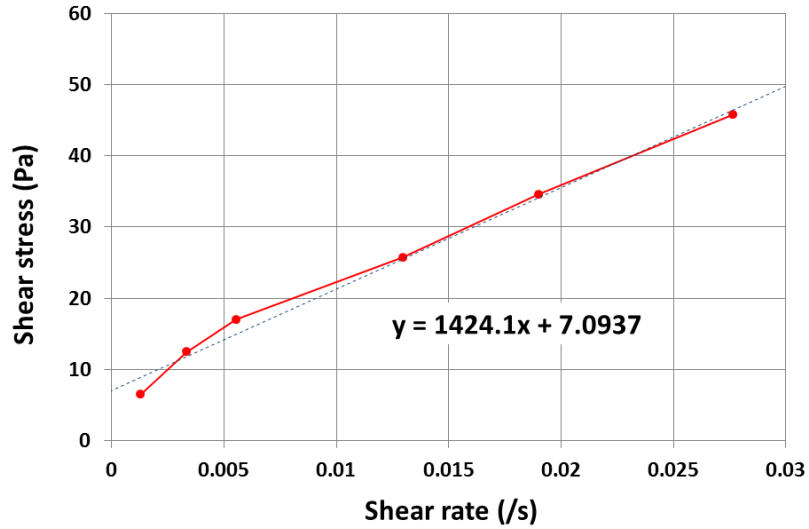


Figure 3.12: Measured experimental data of SRM 2492 from the presented method in this study

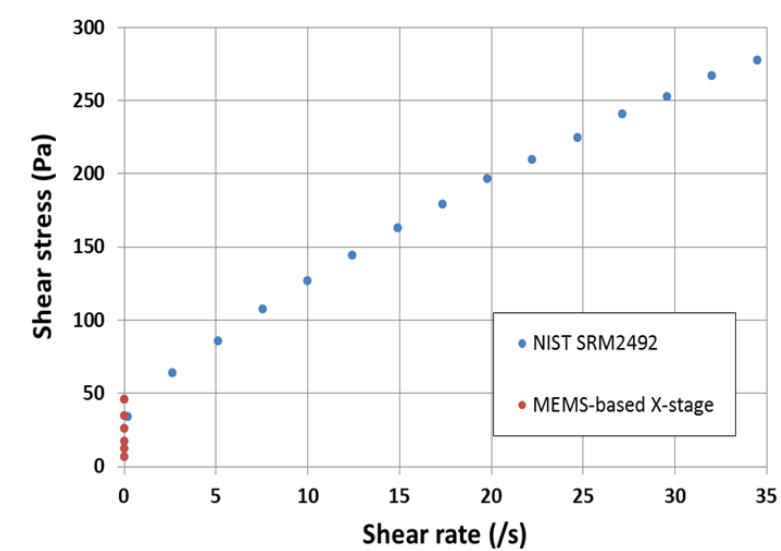


Figure 3.13: The combination of experimental data with the results previously reported [133]

3.7 Summary

The design, fabrication, and testing of a MEMS based X-stage has been presented for rheological measurement of cementitious materials. This presented stage is designed to replace the vibrating plate in a parallel plate type rheometer. For this purpose, the X-stage adopts (1) the dual bent-beam type electrothermal actuator for a low stiffness, (2) a large

motion platform to place enough volume of cementitious materials, (3) an embedded capacitive sensor to monitor the displacement of the motion platform, and (4) adapting Bingham model to analyze the cementitious material. Through these procedures, a presented rheometer is able to generate up to the shear rate of 0.0275 /s and the shear stress of 45 Pa. Compared with conventional rheometer, this MEMS-based rheometer shows more detailed information in relatively short shear rate range, which can be utilized in various micro-structure made by viscoelastic materials where a small shear rate is meaningful.

Chapter 4 Optimization of MEMS electrothermal actuator for a single DOF stage

Figure 4 illustrates the 3D CAD model of chosen MEMS in-plane single DOF motion stage. This stage is composed of one actuator, four links and one motion platform. The actuator is a bent-beam type electrothermal actuator and its shaft is connected to the motion platform through the two links. Four links supports four corners of the motion platform in position firmly. Among them, two links adjacent to the actuator also operate as a lever to amplify the displacement in the motion platform appropriately. Due to the lever mechanism, the motion direction of the motion platform is the opposite of that of the actuation direction. In Fig. 4.1, the small circles stand for the flexure hinge allowing a rotational motion and the lines represent rigid bars of the links. The combination of the flexure hinges and the rigid bars is able to deliver the force or displacement from the actuator to the motion platform. The design of the flexure hinge and the lever ratio are decided depending on the maximum force from the actuator and the stiffness of the motion platform.

The compliant flexure design determines the total stiffness of the motion platform which results in the maximum displacement. Due to this reason, the compliant flexure design was discussed in Section 4.1, which reveals the maximum allowable rotation or the maximum displacement of the motion platform. Based on the stiffness information of the motion platform, the appropriate lever ratio is studied in order to maximize its displacement in Section 4.2. Through these analyses, the electrothermal actuator is designed in Section 4.3. Through these analyses, final design parameters have been decided to increase its maximum displacement in section 4.6.

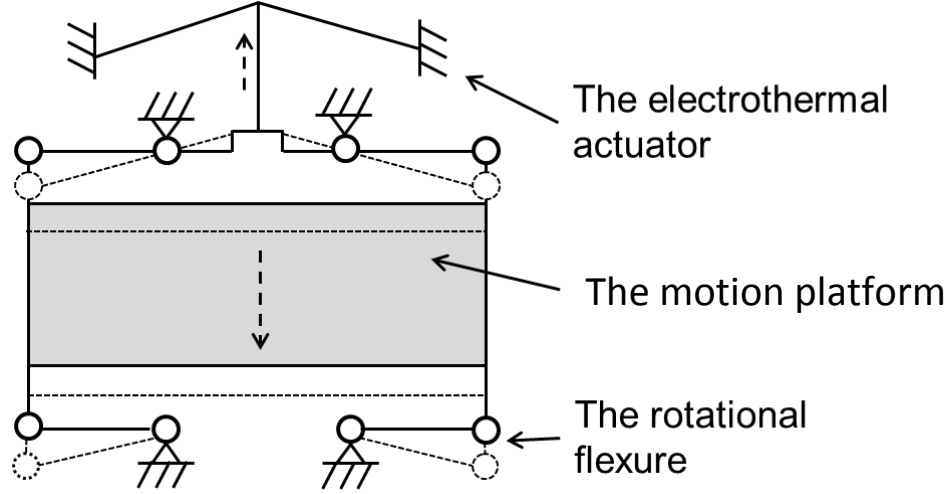


Figure 4.1: The schematic diagram of the X-stage

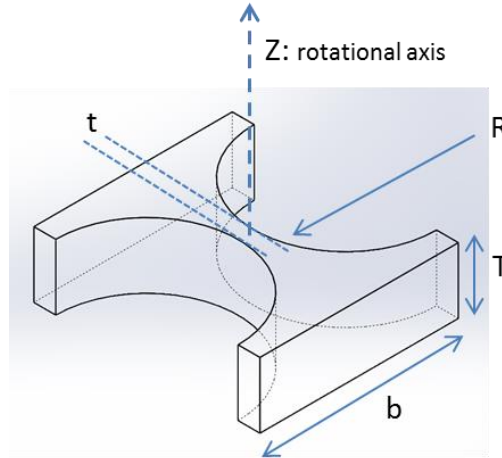
4.1 The flexure hinge design

The flexure hinge used in this study is a compliant mechanism transmitting translational or rotational motion via its elastic deformation. Figure 4.2(a) shows the basic shape of a flexure hinge employed in the proposed X-stage. This flexure hinge is composed of a cantilever beam with circular curvatures around its corners and will be aligned along the Z axis to be bent easily along the Z axis and be stiff against other directions such as torsional motion or out-of-plane bending or deformation.

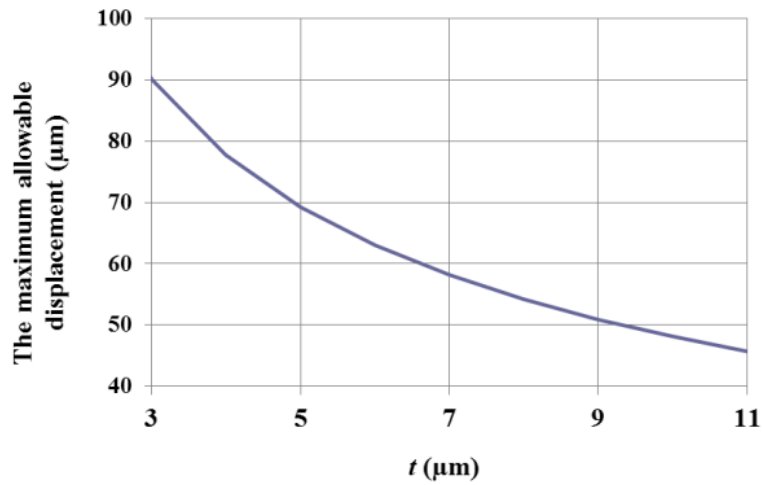
The angular compliance C_z of this flexure hinge can be represented using the Paros and Weisbro formula [139]:

$$C_z = \frac{3}{2EbR^2} \left[\frac{1}{2\beta + \beta^2} \right] \left\{ \left[\frac{1+\beta}{\gamma^2} + \frac{3+2\beta+\beta^2}{\gamma \cdot (2\beta + \beta^2)} \right] \left[\sqrt{1 - (1+\beta-\gamma)^2} \right] + \left[\frac{6(1+\beta)}{(2\beta + \beta^2)^{\frac{3}{2}}} \right] \left[\tan^{-1} \left(\frac{\sqrt{2+\beta}}{\beta} \frac{\gamma-\beta}{\sqrt{1-(1+\beta-\gamma)^2}} \right) \right] \right\} \quad (4.1)$$

Where $\beta = t/2R$, $\gamma = h/2R$. E is Young's modulus of silicon and α_z is the angular deformation of the flexure about the Z-axis in radians.



(a)



(b)

Figure 4.2: The flexure hinge compliant mechanism; (a) the flexure hinge design (t : thinnest width in the flexure, R : radius of curvature, $h=2R+t$, b : width); (b) the maximum allowable translational motion of the flexure hinge before its failure

Equation (4.1) predicts well about the stiffness after experimental comparison; Seungho et al [19] used this flexure hinge with the design parameters of $t = 4 \mu\text{m}$, $R = 10.6 \mu\text{m}$, $b = 2R + t$, $b = 30 \mu\text{m}$, and a lever length = $800 \mu\text{m}$. This design had been

fabricated with MEMS fabrication technologies and its stiffness was measured by an atomic force microscopy (AFM). This experimentally measured result show the flexure has the stiffness of 45.34 N/m [19]. This result is compared with equation (4.1) showing that the analytic stiffness is expected to be 47.82 N/m. This result is less than 5 percent difference from the experimental value. Thus equation (4.1) is reasonable to utilize for the current design process.

With the angular compliance of the flexure hinge, this property can be converted into a linear stiffness. When M_z is the external bending moment applied to the flexure hinge, its maximum value can be expressed as:

$$M_z = \frac{2\sigma I_{\min}}{t} \quad (4.2)$$

Where σ is the rotational stress and I is for the inertial of moment. Based on the equation (4.2), the maximum allowable bending moment can be expressed as a function of maximum allowable stress and as:

$$M_{\max} = \frac{2\sigma_{\max} I_{\min}}{t} \quad (4.3)$$

Since the maximum allowable rotation angle occurs under the maximum bending moment M_{\max} , the maximum angle α_{\max} can be expressed as a function of a maximum bending moment as:

$$\alpha_{\max} = M_{\max} \cdot C_z \quad (4.4)$$

Equation (4.4) reveals the maximum allowable rotational angle. Based on this equation, the maximum displacement of the motion platform can be described based on

the link geometries, especially the lever length, L_{lever} . In this case, the maximum displacement can be described in terms of the maximum allowable rotation angle α_{max} of the flexure as:

$$\Delta U_{\text{max}} = \alpha_{\text{max}} \cdot L_{\text{lever}} = M_{\text{max}} \cdot C_z \cdot L_{\text{lever}} = \frac{2\sigma_{\text{max}} I_{\text{min}}}{t} C_z L_{\text{lever}} \quad (4.5)$$

Where the area moment of inertia $I_{\text{min}} = \frac{bt^3}{12}$ and σ_{max} is the yield strength of silicon (5 - 9 GPa [140]). Based on equation (4.5), the design parameters in the flexure hinge are selected to maximize the displacement of the motion platform with acceptable reliability. The flexure hinges experience the significant stress during the operation, so most mechanical failures such as cracking or breaking down occur near the flexure hinges. There are a few design constraints; the Silicon-on-insulator (SOI) wafers purchased for this design has 30 μm thicknesses for its device layer, the thickness of the flexure (T) is set to be 30 μm .

Based on the equations (4.1) to (4.5) and the other parameters used in reference [19], the output displacement has a strong relationship with the flexure thinnest width (W) as plotted in Figure 4.2(b). Figure 4.2(b) also shows that the narrower thinnest width (t) can endure larger deformation indicating a longer displacement. However, the narrow thinnest width (t) is more vulnerable at noise and vibration during operations resulting in a poor yield rate. Due to this property, the thinnest width (t) should be determined in advance in order to guarantee reliable operations. In order to compare its yield rate depending on the thinnest width (t), three different models are prepared and fabricated. The fabrication results are listed in Table 4.1. Table 4.1 shows that the survival rate is more than 80 % with the thinnest width of 7 μm after fabrication. These also show the

maximum displacement of more than 60 μm displacement, which is acceptable in this study. The full devices with the thinnest width of 9 μm survived, but its performance is less than 20 μm . The thinnest width of 5 μm shows less than 40 % survival rate and its maximum displacement is observed larger than 80 μm . In order to generalize this relationship, more experiments are needed to exclude any unexpected environmental effects. However, it is still valid that the smaller thinnest width (t) is desirable for its maximum displacement and the larger thinnest width (t) is good for reliable fabrication and operation. In this study, the thinnest width (t) is decided to be 7 μm to meet both the acceptable reliability and the maximum displacement.

Another design parameter is the radius of curvature (R). The larger radius of curvature (R) reduces the rotational stiffness and increases the maximum displacement. Given the allowable geometry, the radius of curvature (R) is set to be its maximum; 40 μm . In this case, the width (b) is automatically set to be $2R+t$ from its geometric relationship.

Table 4.1: Three different flexure hinge models

Symbol	The thinnest width(t)	Yield rate	Maximum displacement
A	5 μm	38 %	\sim 80 μm
B	7 μm	82 %	\sim 60 μm
C	9 μm	98 %	\sim 20 μm

With the determined design parameters, the stiffness of the flexure hinge will be 7.52 $\text{Nm}/\mu\text{rad}$ from equation (4.1) and the maximum rotational angle will reach up to 0.163 rad from equation (4.4). The maximum displacement of the presented X-stage is

expected to be 58.2 μm from equation (A.5) with the appropriate levers and an actuator. These two components are studied in the following sections.

4.2 The lever ratio

The lever mechanism used in the proposed X-stage also plays an important role between the actuator and the motion platform. The previous 1 DOF MEMS nano-positioner adapting a lever mechanism prefers a higher lever ratio for larger stroke [29] within permitted space. Contrary to the conventional micro-stages, the affordable lever ratio in MEMS has relatively narrow choice due to its small form factor and limited fabrication technologies. In the presented X-stage, the lever ratio should be than 1:11 due to the limited space for the flexure hinge. With this design constraint, the appropriate position of the pivot in the lever is studied for the maximum displacement of the X-stage.

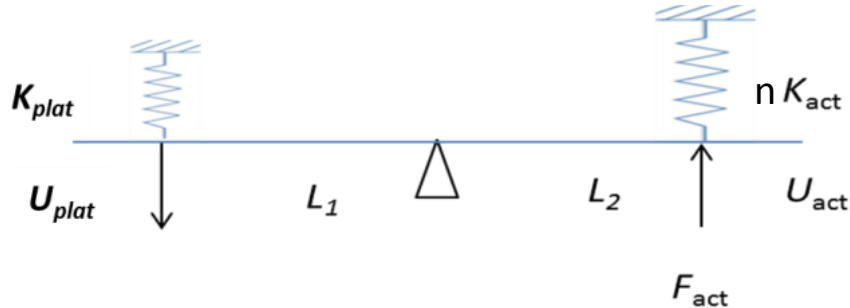


Figure 4.3: The schematic diagram of the lever mechanism adapted in the XY-stage

The X-stage can be regarded as the combination of two springs and a lever. One spring represents the actuator and the other spring stands for the motion platform. The lever is located between them to convert and transfer the force and the displacement. This relationship is described in Fig. 4.3. The force generated from the actuator can be regarded as an external force applied to the actuator, which is indicated by F_{act} in Fig. 4.4. The term n is introduced for the beam number of the actuator to analyze the beam number

separately and the term K_{act} is the stiffness of the actuator with a single beam. Based on this schematic diagram in Fig. 4.3, the conservation of the moment can be expressed as:

$$F_{act}V_{act} = F_{plat}V_{plat} \quad (4.6)$$

where V_{act} and V_{plat} are the velocities of the actuator and the motion platform, respectively. Equation (4.6) can be written as:

$$F_{act} \frac{dU_{act}}{dt} = F_{plat} \frac{dU_{plat}}{dt} \quad (4.7)$$

Where U_{act} is the displacement of the actuator, U_{plat} is the displacement of the motion platform. The existing lever ratio can be expressed as;

$$\left(\frac{L_1}{L_2}\right) dU_{act} = dU_{plat} \quad (4.8)$$

Substituting equation (4.7) into equation (4.8) gives the relationship between the two forces as:

$$F_{act} = \left(\frac{L_1}{L_2}\right) F_{plat} \quad (4.9)$$

In this case, the stiffness of the actuator can be rewritten as:

$$K_{act} = \frac{F_{act}}{dU_{act}} = \frac{\left(\frac{L_1}{L_2}\right)F_{plat}}{dU_{act}} = \frac{\left(\frac{L_1}{L_2}\right)F_{plat}}{\frac{dx_{plat}}{\left(\frac{L_1}{L_2}\right)}} = \left(\frac{L_1}{L_2}\right)^2 \frac{F_{plat}}{dU_{plat}} = \left(\frac{L_1}{L_2}\right)^2 K_{plat} \quad (4.10)$$

Therefore, the stiffness relationship between the actuator and the motion platform can be summarized as:

$$K_{act} = \left(\frac{L_1}{L_2}\right)^2 K_{plat} \quad (4.11)$$

Based on the stiffness relationship in equation (4.11), the kinematic relation can be expressed as:

$$\left(\frac{L_1}{L_2}\right)^2 K_{\text{plate}} U_{\text{plate}} = nF_{\text{act}} - K_{\text{act}} U_{\text{act}} \quad (4.12)$$

Where, L_1 and L_2 are the length of lever, F_{act} is the force from the actuator and, K_{act} and K_{plat} are the stiffness of the actuator and the motion platform, respectively. In this case, equation (4.12) can be rearranged for the displacement of the actuator or the motion platform as:

$$U_{\text{act}} = \frac{nF_{\text{act}}}{K_{\text{act}} + \left(\frac{L_1}{L_2}\right)^2 K_{\text{plat}}} \quad (4.13)$$

$$U_{\text{plat}} = \left(\frac{L_1}{L_2}\right) U_{\text{act}} = \left(\frac{L_1}{L_2}\right) \frac{nF_{\text{act}}}{K_{\text{act}} + \left(\frac{L_1}{L_2}\right)^2 K_{\text{plat}}} \quad (4.14)$$

Equation (4.14) indicates that the stiffness concerned to the lever is proportional to the square of the lever ratio. This relationship can be verified through FEA, which agreed with equation (4.14). This relationship implies that more force or stiffness is needed from the actuator for an efficient operation.

4.3 The number of beam in the actuator

The lever mechanism used in the proposed X-stage was analyzed in the previous section. Equation (4.14) indicates that the number of beam (n) is also important parameter for a large displacement. For better understanding, the maximum displacements are calculated based on different lever ratios (L_1/L_2) and beam numbers (n). These relationships are plotted in Fig. 4.5, where the displacement is linearly proportional to the lever ratio with the lever ratio less than 1:3. With higher lever ratio, its increment rate starts decreasing.

When the lever ratio is over its optimum value, the displacement tends to decrease gradually. The detail values for each parameter used to plot Fig. 4.4 are listed in Table 4.2. From this observation, it is desirable to find the optimum number of beams (n) and the lever ratio. It is difficult to increase the number of beams and the lever ratio due to the limited space in the X-stage. In this chapter, the beam number of 15 and 1:11 lever ratio are selected for the X-stage design. As a result the ideal displacement is expected to reach up to $115 \mu\text{m}$ at the motion platform based on equation (4.14). But this can be limited by other components including the actuator and the rotational flexure hinge.

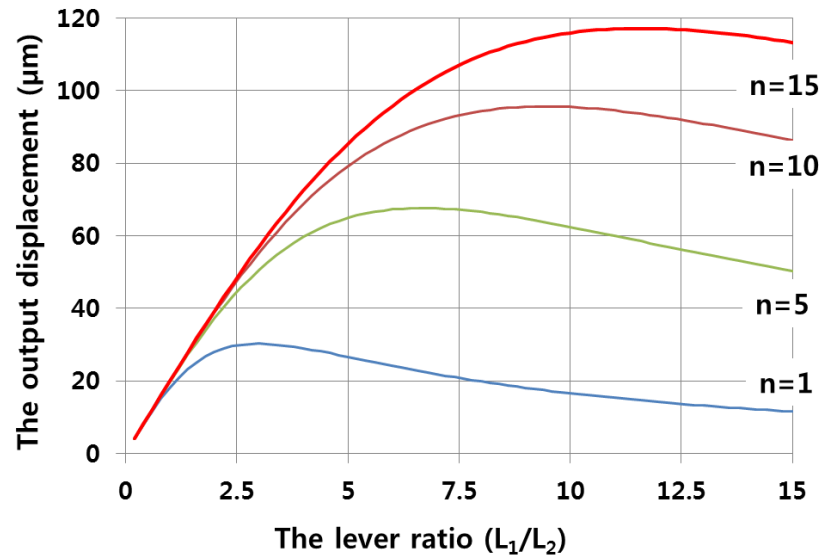


Figure 4.4: The expected maximum displacement with various lever ratios and beam numbers(n)

4.4 The analytic analysis for the electrothermal actuator

In the previous sections, the stiffness of the motion platform and the lever are analyzed. These components can be regarded as an external mechanical load for the actuator to move. In this section, the actuator is discussed for maximizing its displacement. The

actuator selected for this study is a traditional bent-beam type electrothermal actuator for its large force and linear motion.

The main design parameters for the bent-beam type electrothermal actuator are a beam length (L), a beam width (W), a beam angle (θ), a number of beams (n), and a beam thickness (T). These parameters are illustrated in Fig. 4.5. The thermal expansion of each beam produces a displacement along its shaft as indicated by the arrow in Fig. 4.5 with the symmetric layout of the beams.

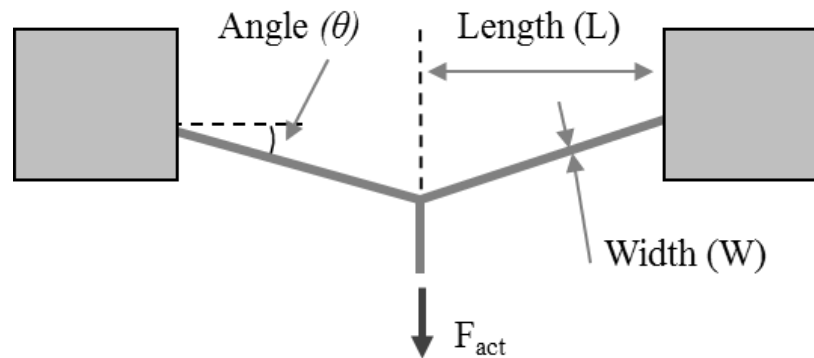


Figure 4.5: the design parameters engaged in the adapted electrothermal actuator

The design constraints for this actuator are described below;

- (1) The beam thickness (T) is limited by the commercially available wafer, because it is difficult to control the thickness over the wafer within acceptable ranges.
- (2) The total footprint of the X-stage should be smaller than 10 mm x 10 mm.
- (3) The beam length (L) is limited by the length of the link or the lever (L_1) in Fig. 4.1. Longer beam length is favorable at generating a longer motion, but it is limited by the allowable footprint described in (2). Additionally, if the beam length L is longer than the lever length L_1 , then the actuator becomes bigger than

the motion platform. In this case, unnecessary area around the motion platform is expected. Thus, the beam length L is set to be less than or equal to the link or the lever length L_1 for utilizing the whole area given to the X-stage.

- (4) The beam width (W) should be smaller than the beam thickness (T) to avoid any out-of-plane bending or buckling prior to in-plane motion. If not, the out-of-plane motion is expected to occur rather than the in-plane motion.
- (5) All parameters should be larger than 110 % of the beam thickness (T .) Bosch deep reactive ion etching (DRIE) process [21] recommends the 1:10 high-aspect ratio for a reliable operation. Although it is possible to build higher than 1:10 high-aspect ratio, this can result in a poor vertical profile or an unstable etching rate.
- (6) The beam length (L) should be much longer than the beam width (W) to avoid any meaningless design.

Based on the design constraints above, the analytic relationships have been derived based on several previous studies. The stiffness of the electrothermal actuator can be build based on its chevron type shape and be expressed as [53]:

$$K_{\text{act}} = 2 \left(\sin^2 \theta + \cos^2 \theta \frac{12I}{AL^2} \right) \frac{EWT}{L} \quad (4.15)$$

where E is the Young's modulus of silicon and, I is the area moment of inertia and A is the cross-sectional area of the beam. Equation (4.15) demonstrates more accurate results when the beam angle (θ) is larger than 10 degrees. With this stiffness, the force generated by the electrothermal actuator can be described from classic thermal strain [44] and expressed as:

$$F_{\text{act}} = 2\alpha\Delta T_{\text{ave}}EWT\sin\theta \quad (4.16)$$

The stiffness of the motion platform can also be represented as a combination of the compliance of the flexures in equation (4.1) as:

$$K_{\text{plat}} = \frac{m}{L_1^2 C_z} \quad (4.17)$$

where L_l is the long side length of the link or the lever and m is the total number of flexure hinges connected to the motion platform.

The equations (4.15), (4.16), and (4.17) explain the three parameters described in the lumped parameter model in Fig. 3.1(c). The displacement of the motion platform can be expressed as a function of the three parameters in Fig. 3.1(c) as:

$$U_{\text{plat}} = \left(\frac{L_1}{L_2}\right) \frac{2\alpha n E W T \sin\theta}{3k\rho \left\{ 2\left(\sin^2\theta + \cos^2\theta \frac{12I}{AL^2}\right) \frac{EA}{L} + \left(\frac{L_1}{L_2}\right)^2 \frac{m}{L_1^2 C_z} \right\}} V^2 \quad (4.18)$$

From equation (4.18), the expected displacement of the motion platform is described as a function of the engaged design parameter. Here, equation (4.18) is based on the assumption that some parameters are constant independent of temperature and structural or thermal constraints such as buckling or thermal melting down are excluded. With these properties, the maximum displacement of the motion platform can be numerically obtained in the following section.

4.5 Design constraint: buckling

The buckling of the beams in the actuator should be taken into consideration for the actuator design. When the buckling occurs, some portion of the force generated by the actuator spends on deforming the actuator beams itself and results in poor performance in

its range of motion. The boundary condition of the bent-beam type electrothermal actuator is that one end of the beam is connected to a fixed end and the other is connected to sliding guide or a central shaft [53]. With this boundary condition, the critical buckling load can be derived [141] as:

$$P_{\text{buckling}} = \frac{\pi^2 EI}{L^2} \sin\theta \quad (4.19)$$

where P_{buckling} is the maximum buckling load that a single beam can withstand. The maximum force of the electrothermal actuator cannot over the summation of the critical buckling load of each beam. Based on the bent-beam geometries in the actuator, the maximum force from the actuator can be expressed as:

$$F_{\text{thrust}} = 2nP_{\text{buckling}}\sin\theta \quad (4.20)$$

In this study, equation (4.20) is used as a criterion to determine the beam condition and the maximum force. From equations (4.16) and (4.20), the beam width (W) can be expressed as a function of the other design parameters:

$$W \geq \sqrt{\frac{12\alpha\Delta T_{\text{ave}}}{n\pi^2}} L \quad (4.21)$$

When the beam length (L) is 1 mm, equation (4.21) recommends that the beam width (W) should be wider than 9.9 μm . With this dimension, buckling can be prevented before the actuator generates its maximum force.

In addition to this buckling property, the beam width (W) should be narrower than the beam thickness (T) to prevent any out-of-plane buckling from occurring prior to the in-plane buckling.

4.6 Design constraint: thermal melting down

The maximum allowable temperature of the electrothermal actuator is also another important factor to consider in a design level, since the electrothermal actuator is based on Joule heating of the beams. Higher temperature over its limit can cause serious structural damage or permanent deformation. For this reason, the heat transfer of the actuator is briefly analyzed in this section to figure out its effect on the actuator. For simplicity, the conduction is only considered. In this case, the temperature distribution along the beam can be expressed by the classic heat transfer equation [52] as:

$$k \frac{d^2T}{dx^2} + \left(\frac{V}{\rho L}\right)^2 \rho = 0 \quad \text{for } -L \leq x \leq L \quad (4.22)$$

The general solution for equation (4.22) will be:

$$\Delta T = -\frac{V^2 \rho}{2k} (x - L)(x + L) \quad \text{for } -L \leq x \leq L \quad (4.23)$$

where V is an applied voltage, k is the thermal conductivity, and ρ is the resistivity of silicon. The resistivity of silicon (ρ) is an important property and can be expressed as a function of the temperature. The resistivity of the silicon is manually measured with three different temperature points and interpolated to be used in equation (4.23) as:

$$\rho = -5 \times 10^{-5} (\Omega - m/V)V + 0.0004(\Omega - m) \quad (4.24)$$

The measured resistivity tends to increase with a rising temperature. This pattern indicates that the displacement increment rate reduces as the temperature rises. Equation (4.24) is utilized in Finite Element Analysis (FEA). The average of the measured

resistivity is 0.000275 Ωm , which is used in equation (4.23). The solution of equation (4.24) shows the temperature rise in the beam as:

$$\Delta T_{\text{ave}} = \int_{-L}^L \frac{\Delta T(x)}{2L} dx = \frac{V^2}{3k\rho} \quad (4.25)$$

Where ΔT_{ave} is the average temperature rise in the beam, which is proportional to square of the driving voltage. The maximum temperature rise ΔT_{max} in the beam can be expressed as a function of ΔT_{ave} as:

$$\Delta T_{\text{max}} = \frac{V^2}{2k\rho} = \frac{3}{2} \Delta T_{\text{ave}} < 530^\circ\text{C} \quad (4.26)$$

This ΔT_{max} from a room temperature of 20 $^\circ\text{C}$ should not exceed 530 $^\circ\text{C}$ to prevent any thermal issues [??].

4.7 The optimization process for the displacement of the X-stage

Based on the analyses in the previous sections, the X-stage is optimized to increase its range of motion with the given footprint. For this purpose, an objective function J_{obj} , is defined as:

$$J_{\text{obj}} = \frac{1}{\Delta U_{\text{plat}}} \quad (4.27)$$

where ΔU_{plat} represents the displacement of the moving platform and can be expressed as a function of the engaged design parameters in the previous sections. The objective function J_{obj} will be minimized during the optimization process, which physically means maximizing the displacement of the motion platform. The optimization process evaluates Hessian gradient of the objective function and sets up a new conjugate

direction for the updated parameters [142]. During this process, all the design parameters will be updated iteratively. The details in the optimization procedure are described below:

- (1) Set up the range of each design parameter. The mean value in this range is automatically set as an initial value.
- (2) ΔT_{ave} is obtained from equation (4.25) with current design parameters.
- (3) ΔU_{plat} is calculated from equation (4.18), with the temperature obtained in step (2).
- (4) The maximum force is also calculated from equation (4.16) and check if this is less than the critical buckling load from equation (4.20).
- (5) When the objective function reaches its minimum within the user-defined tolerance, the optimization process is terminated. If not, proceed to step (6).
- (6) A numerical sensitivity analysis is performed to get the gradient function, then a new set of the undetermined design parameters will be obtained and then go back to step (2).

For this optimization process, the design constraints used in this process are also defined and described below:

- (1) The maximum temperature rise that the electrothermal actuator can endure is less than 530 °C, which will be monitored with equation (4.26).
- (2) The X-stage is designed to generate an in-plane motion, so out-of-plane buckling should be avoided. This constraint is described in equation (4.23).
- (3) The maximum force generated by the electrothermal actuator should be less than its maximum buckling load. This constraint can be monitored by equation (4.21).

- (4) The beam length (L) is larger than the beam width (W) or thickness (T). This constraint avoids any unexpected results for the bent-beam type electrothermal actuator.
- (5) The beam length (L) range is limited not to be longer than the motion platform width of $2000\ \mu\text{m}$, so each beam length (L) in the actuator is less than $1000\ \mu\text{m}$.
- (6) The beam angle (θ) range is set between 3° and 7° , which are values reported in previous literatures.
- (7) The beam thickness (T) is determined by the commercially available SOI wafers with $30\ \mu\text{m}$ thickness.

The design parameters and their range are listed in Table 4.1. The optimization processing is implemented in MATLAB [142] and the optimized values are listed in the Table 4.2. With the optimized values listed in Table 4.2, at least $60\ \mu\text{m}$ range of motion will be expected under the constraints including thermal and structural limits.

Table 4.2: The dimensional range of the design parameters

Symbol	Design parameter	Initial Range
W	Width of beam	$10 \sim 30\ \mu\text{m}$
θ	Angle of the bent-beam	$0.05 \sim 0.12\ \text{rad}$
L	Length of beam	$600 \sim 1000\ \mu\text{m}$
T	Thickness of beam	$30\ \mu\text{m}$

The material properties used in this optimization process are assumed constant and independent of temperature. This can make the analytic equations simple, but be a

source causing experimental errors. In order to overcome this limit, the candidate model in the optimization process is verified through the FEA in the following section.

Table 4.3: The dimensional range of the design parameters

Symbol	Design parameter	Values
W	Actuator beam width	22.3 μm
θ	Actuator beam angle	0.068 rad
L	Actuator beam length	1000 μm
T	Actuator beam thickness	30 μm
n	Number of beams in actuator	15
L_1	Link length	1000 μm
L_2	Short link length	100 μm
m	Links connected to the platform	8
t	Flexure hinge neck width	7 μm
b	Flexure hinge width	87 μm
R	Flexure hinge radius of curvature	40 μm
ΔT_{ave}	Actuator average temperature	< 530 $^{\circ}\text{C}$
ΔT_{max}	Actuator maximum temperature	< 530 $^{\circ}\text{C}$
U_{plat}	Platform displacement	> 50 μm
K_{act}	Actuator stiffness with a single beam	889.16 N/m
K_{plat}	Platform stiffness without the levers	46.28 N/m
$F_{\text{act,max}}$	Maximum generated force by the actuator with 15 beams	125.3 mN

4.8 Finite element analysis (FEA)

A series of Finite Element Analysis (FEA) in ANSYS [135] is utilized to verify the X-stage based on the optimized design parameters obtained from the previous sections. The material properties used in the FEA are listed in Table 3.3.

This simulation includes electrical, thermal, and structural analyses; an electrical potential difference is applied to both ends of an electrothermal actuator. Due to the resistance of the beam, Joule heating occurs, which results in temperature rise in the actuator. This leads to the thermal expansion of the beam, which is the main source to thrust the motion platform.

The boundary conditions applied to this simulation are; (a) there is no electrical connection except the actuator. (b) All the ends of the flexure hinges and both ends of the actuator are firmly fixed during the simulation and assumed to be connected to a heat sink with a room temperature of 20 °C. (c) Among heat transfer methods, conduction and natural convection are considered. (d) No adjacent objects are included in the simulation such as a packaging chip or electric wires.

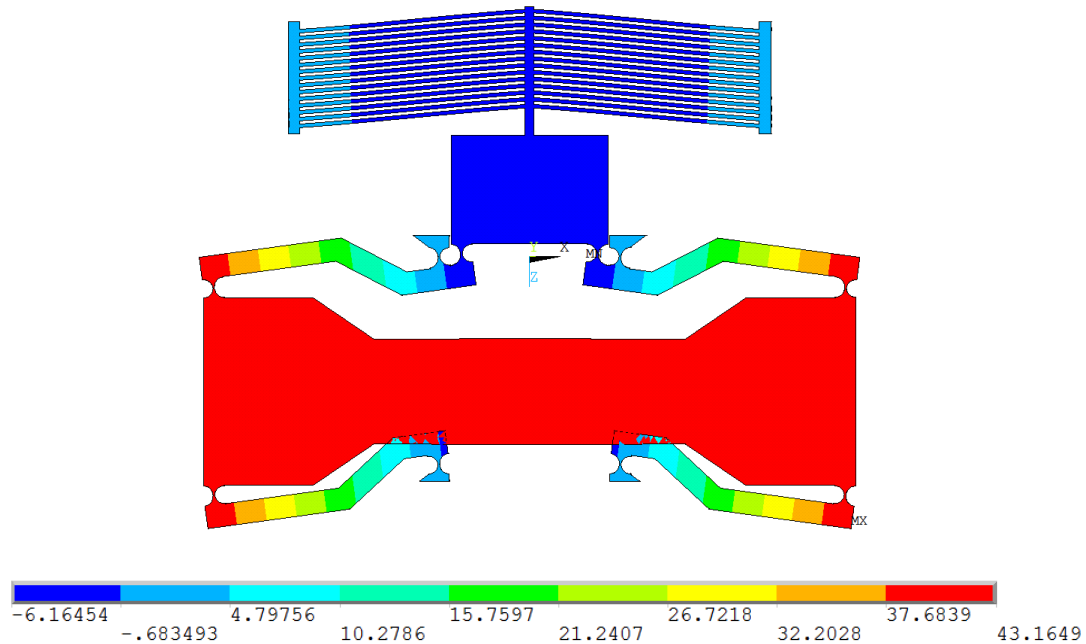
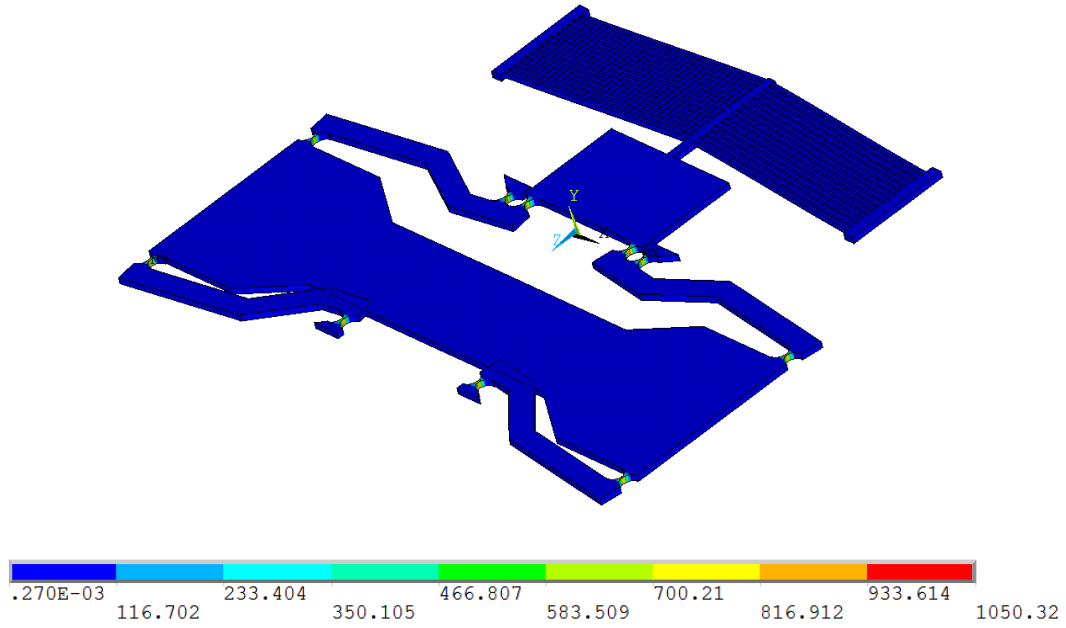
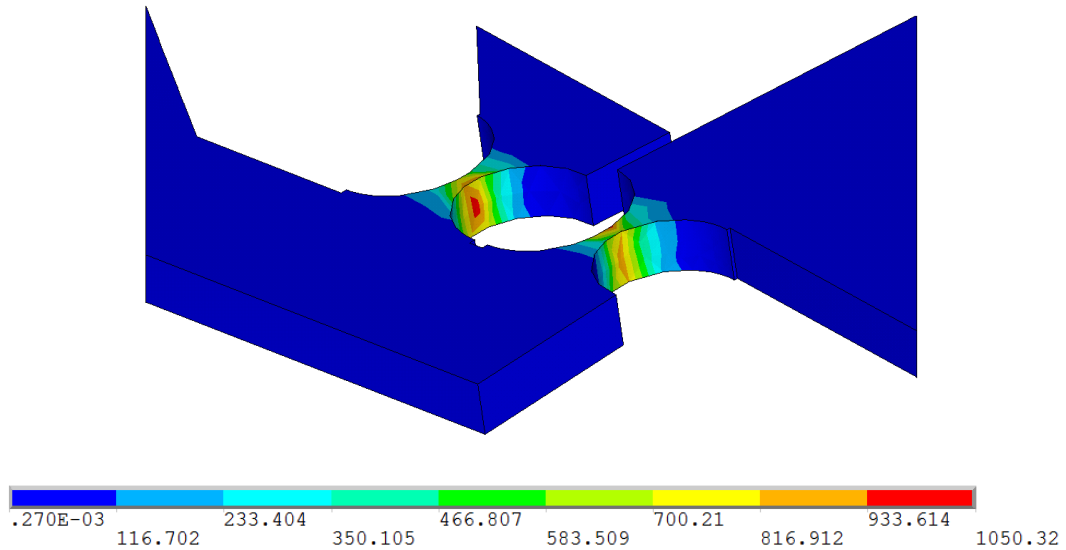


Figure 4.6: The calculated displacement of the motion platform with the excitation of the temperature rise of 530 °C (in μm unit)



(a)



(b)

Figure 4.7: The calculated stress distribution over the X-stage; (a) von Mises stress distribution over the stage; (b) von Mises stress distribution near the flexure hinge (in MPa unit)

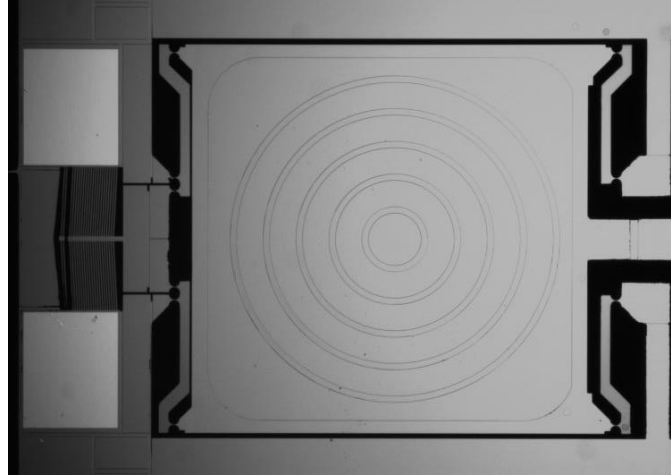
Figure 4.6 shows the simulation result of the displacements of the X-stage corresponding to the temperature rise of 530 °C. The result shows that the X-stage is expected to move the motion platform up to 43.2 μm . During this movement, the

simulation calculates the maximum von Mises stress on the X-stage, which is less than 1.05 GPa and shown in Fig. 4.7(a). This stress distribution shows that most deformation occurs near the flexure hinges as expected and there is no deformation in the motion platform. The zoom-in view of the flexure hinge is in Fig. 4.7(b) showing the thinnest width area is under the maximum stress. These values are still less than the yield strength of silicon of 7 GPa indicating that no structural failure is expected with this flexure hinge design during the operation.

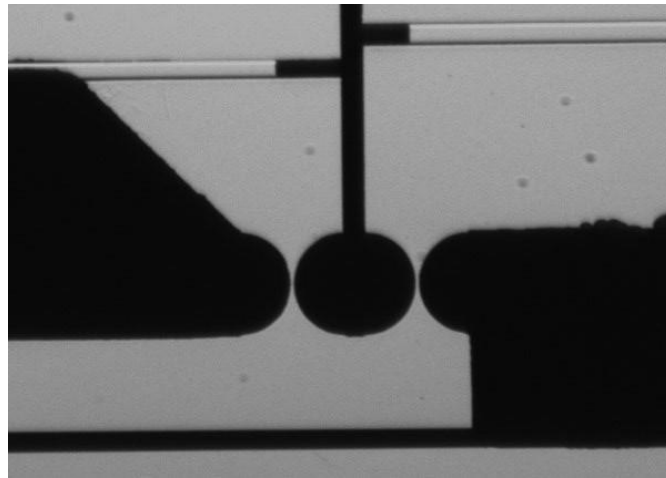
4.9 Experimental results

The fabrication process for the X-stage follows the same used in the XY-stage in chapter 4. A 30 μm thick device layer is used for the main device structures and a 400 μm thick handle layer is utilized as a backside frame. A 2 μm thick buried oxide layer is placed between the two silicon layers. The whole process follows Silicon-On-Insulator Multi-User Multi-Processes (SOIMUMPs) [39]. After SOIMUMPs, buffered hydrofluoric acid (B.H.F.) is applied to release the movable structures.

After the fabrication, an X-stage is fabricated and shown in Fig. 4.8. Figure 4.8(a) is the frontal full view of the X-stage composed of an actuator, four links and a motion platform. The motion platform has five circular shapes for future applications. The detailed image of the flexure hinge is in Fig. 4.8(b).



(a)



(b)

Figure 4.8: The optical microscopic images of the MEMS based X-stage: (a) a full view of the fabricated X-stage; (b) a closed view of the flexure hinge

4.9.1 The range of motion of the MEMS X-stage

The fabricated X-stage is experimentally tested for its maximum motion range and frequency response. For these experiments, two metal pads near the actuator are electrically connected to a DC power supply units (Model 3322A from Agilent) which controls the driving voltages. The motion corresponding to the input voltage is measured by an optical profiler (VEECO NT1100 [137]). The measured data through this profile is plotted in Fig. 4.9. The displacement of the X-stage is larger than $50\ \mu\text{m}$ with the voltage

less than 5.0 V indicating that the electric power around 200 mW is required to generate at least 50 μm displacements. Since any mechanical failure has not been observed during this operation, the expected maximum displacement of the X-stage is larger than 50 μm .

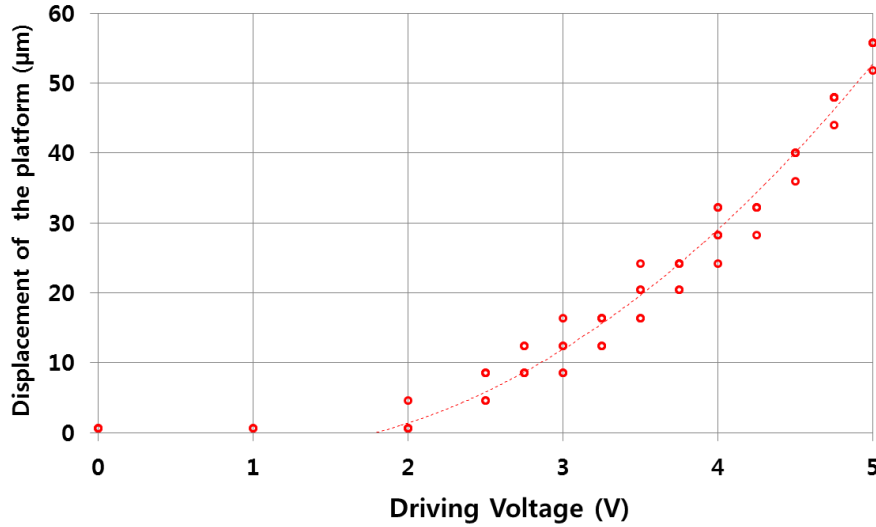
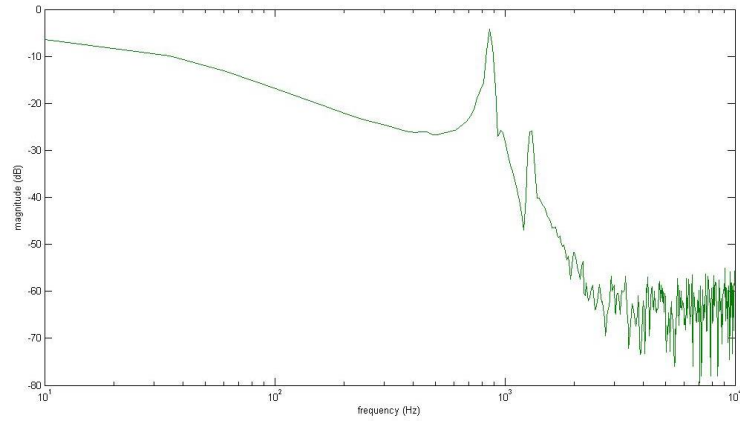


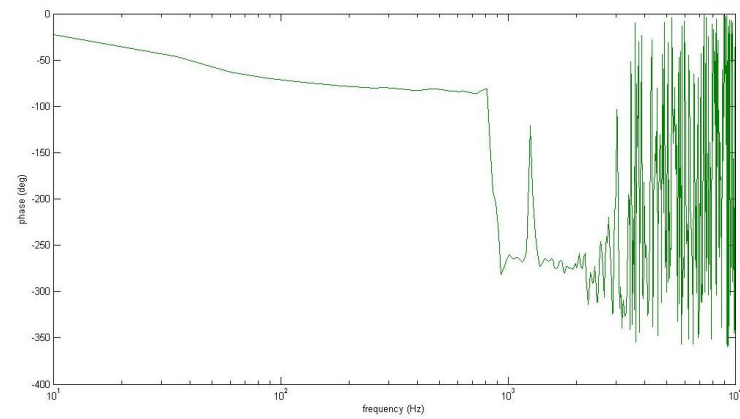
Figure 4.9: The experimentally measured displacement of fabricated X-stages

4.9.2 The frequency response

The frequency response of the X-stage is also measured experimentally while the actuator is in operation. This frequency response is detected through an Agilent Fast-Fourier-Transform (FFT) analyzer [143]. More details on the experimental set-ups for this measurement are explained in Gorman. et Al. [119]. The 1st resonance frequency of the X stage occurred at 705 Hz as shown in Fig. 4.10(a). At the low frequency less than 100 Hz, the frequency response shows a slow decrement. This property indicates that the electrothermal actuator is stable at a low-speed operation less than 10 Hz. Near 1 kHz frequency range, a rocking mode is observed from Fig. 4.10(b).



(a)



(b)

Figure 4.10: Frequency response of the X-stage; (a) magnitude (in dB); (b) phase (in degree)

4.10 Summary

The design, fabrication, and testing of a MEMS based X-stage is presented for the displacement larger than $50\ \mu\text{m}$. The presented X-stage is designed to be used as a base material for the XY-stage in Chapter 5 and the XYZ-stage in Chapter 7 for their in-plane motions. For this purpose, the presented X-stage adopts (1) the optimized bent-beam type electrothermal actuator under external mechanical loads including levers and a motion platform, (2) a motion platform is introduced for the nested structure in Chapter 5, which is also big enough to embed one X-stage, (3) the optimum lever ratio is studied under a

given environment, and (4) electrical isolation is also tested for the XY-stage between the actuator and the motion platform. Through these procedures, the presented X-stage is able to generate up to 50 μm without any permanent damage. Compared with previous motion stage, the presented stage has advantages in its large motion platform and well optimized actuator and levers for more than 50 μm . During this design process, the structural and electrical requirements of the X-stage are studied for the nested structure in the following chapters.

Chapter 5 MEMS-based in-plane 2-DOF motion stage

In this chapter², we present a MEMS-based in-plane 2-DOFs motion stages based on the 1-DOF motion stage described in Chapter 4. In micro-electro-mechanical systems (MEMS) it is difficult to obtain large range of motion with a small coupled error. This limitation can be overcome by implementing a nested structure which is a kind of a serial kinematic mechanism (SKM). This XY stage is built by embedding a single degree-of-freedom (DOF) stage into another identical stage with a different orientation. This XY-stage has a capability to generate more than 50 μm displacements along each X and Y axes with the coupled motion error less than 0.6 %. This nested structure approach is also helpful at suppressing the coupled motion error. With the presented XY stage, multi-finger manipulation is demonstrated in this chapter. For the micro-particle manipulation, a 14.8 μm sized polypropylene particle is manipulated and rotated by two individual fingers extruded from two XY-stages.

5.1 Introduction

A precision-positioning stage is capable of moving an end-effector in its work space to a desired position precisely within allowable degrees-of-freedom (DOF). The end-effector is a last end of the positioning stage and interacts with external applications or environment. The stage can be evaluated by basic features such as range of motion, coupled motion error and resolution. Various stage designs have been investigated to achieve longer range of motion with acceptable coupled motion error based on a reasonable stage size [131]. Micro-electro-mechanical system (MEMS) approaches have a great advantage in small footprint, which then increases an integration capability to external applications [25]. Hence, MEMS positioning stages have been widely used in

³ The work in this chapter is derived from the published work in [33, 125]

many applications such as optical systems [8,9], atomic force microscopes (AFM) [17], nano-manufacturing assembly [13,14].

The basic issue of a MEMS-based XY-stage is to increase the range of motion for one DOF without disturbing the other DOF (called a coupled motion error). Various approaches have been tried to improve in-plane 2 DOF in the stage design using existing MEMS fabrication techniques. One simple approach is to align two actuators along X and Y axes and then connecting their ends directly [34], which is the simplest implementation of a parallel kinematic mechanism (PKM). But this results in a reduction of motions down to $17\ \mu\text{m} \times 11\ \mu\text{m}$ and an increase in the coupled error between the actuators. To overcome the coupled motion error, accurate mathematical kinematic model or additional kinematic features are necessary to compensate this error. However, generally the kinematics model of PKM is nonlinear and difficult to analyze, so additional features are required for this based on applications and environments. One reliable compensating structure in PKM is a combination of a parallel four-bar chain and a leaf spring. This combination can reduce the unwanted motions such as rotations at the end-effector or coupled motion errors [29,32]. However, the parallel chain increases the total stiffness and the leaf springs loosen the connection between an actuator and an end-effector. These features result in a shorter range of motion at last.

A serial kinematic mechanism (SKM) is an alternative approach for PKM [144], where each link is connected to two neighboring links only like robotic arms. In this approach, the final displacement of the end-effector can be expressed by the accumulation of the motion by each moving component. Since there are no mechanical coupled structures between specified DOFs, each actuator in a SKM is expected to

generate its original range of motion with acceptable coupled motion error, once the SKM is well implemented. Compared with PKMs, SKMs have; (a) easy-to-solve forward kinematics, (b) high dexterity, and (c) no reduction in range of motion when multiple actuators are combined [131]. However, the implementation of SKMs in MEMS is a challenge, because stacking up of single DOF stages requires structures in height, which is difficult to implement with planar design approach. Moreover, electrical access to each moving component without disturbing the others should be taken into consideration.

Other important features in MEMS stages are flexure hinges and actuators. Flexure hinges have been used in various MEMS applications [14,32,131,145], because they are free of backlash and also compatible with a monolithic design. About the MEMS-based actuators, electrostatic [29,32], electromagnetic [100] and electrothermal actuators [44] have been commonly used for positioning the end-effector. Among them, electrothermal actuators can generate mN level force, which is stronger than the other actuators. A large force or large displacement are key parameters to characterize motion stages, so the design process to optimize them is common and the appropriate selection of an actuator plays an important role in this design process.

This chapter focuses on the design, fabrication and test of an MEMS-based XY-stage, whose implementation is based on a nested structure or a SKM. The SKM is realized by embedding a single DOF stage into the other. With this approach, the end-effect can generate 2 DOF in-plane motions. In this study, the single DOF stage is chosen from conventional motion stage designs and then modified for large motion more than 50 μm . For a successful implementation of SKM, additional features are investigated and also implemented in the following section. The kinematic design of the stage, the finite

element analysis results, fabrication process and the experimental results are also discussed in an order.

5.2 Design of the XY-stage

The proposed XY-stage is composed of two single DOF stages. In the XY stage, one single DOF stage is aligned to the X axis (called an X-stage) and the other is aligned along the Y axis (called a Y-stage) as shown in Fig. 5.1(a), where the arrows indicate the direction of the actuators motion. The X stage is designed to correspond to the X axis motion of the end-effector and the Y stage is to the Y axis motion. The Y stage is fully embedded into the X-stage for the XY-stage, where the Y-stage is fully isolated from the X-stage to guarantee its own motions and minimize a coupled motion error. The end-effector will be the motion platform of the Y-stage in the XY-stage and is linked to a fixed ground through the neighboring Y-stage and the X-stage in an order.

The chosen single DOF stages is made up of an actuator, a motion platform and four mechanical links as shown in Fig. 5.1(b) [44]. The white circles in Fig. 5.1(a) and 5.1(b) represent flexure hinges, which are compliant mechanism and operate as joints and solid lines stand for the mechanical links connecting the actuator to the motion platform. Among four mechanical links, two links are designed to operate as a lever to convert some portion of the force from the actuator into the displacement of the motion platform to increase its displacement. The lever ratio can be controlled by adjusting L_1 and L_2 and the optimum lever ratio between the actuator and the motion platform. Due to the lever, the motion direction of the motion platform is opposite to the motion of the actuator as shown in Fig. 5.1(b).

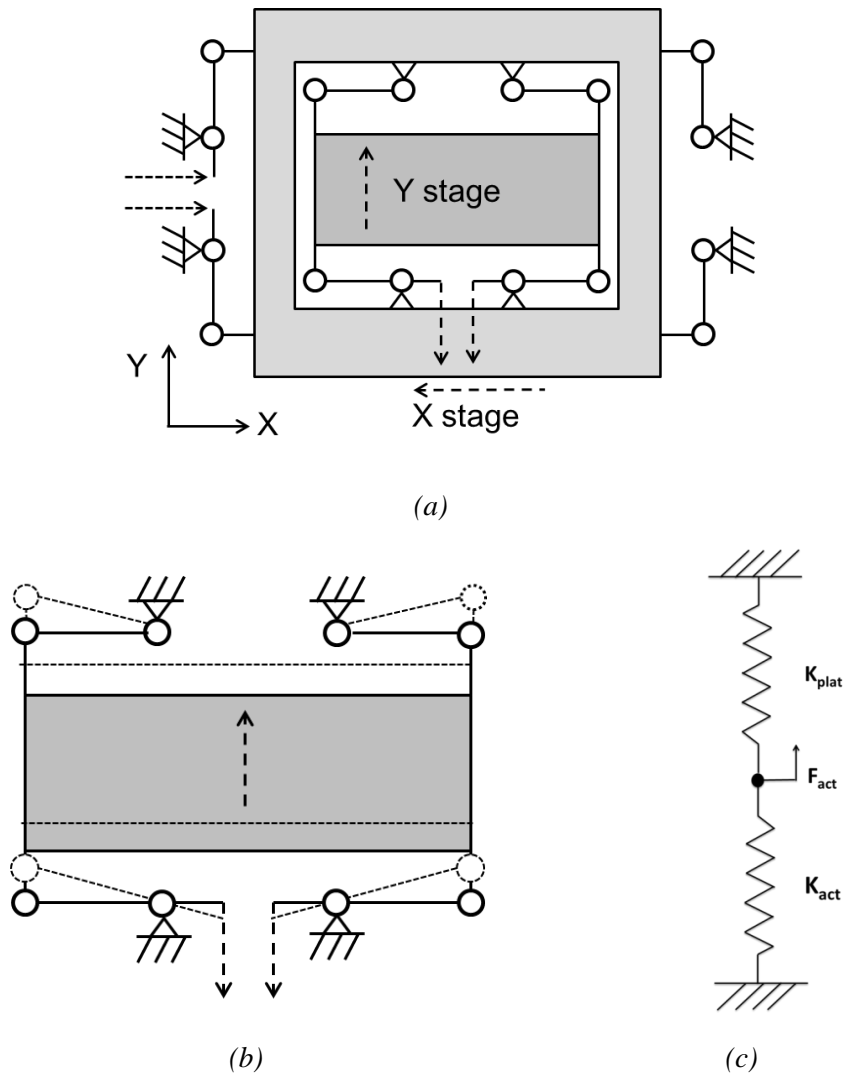


Figure 5.1: The schematic diagrams of the XY stage; (a) the nested structure; (b) the expected behavior of the chosen single DOF stage; (c) the free body diagram of the single DOF stage in (b)

The single DOF stage is composed of an actuator, levers and a motion platform and their relationship is represented in Fig. 5.1(c), where K_{act} and K_{plat} stand for the stiffness of the actuator and the platform, respectively, and F_{act} is the force generated by the actuator. Based on this diagram, the expected displacement of the platform can be expressed as:

$$U_{plat} = \left(\frac{L_1}{L_2}\right) U_{act} = \left(\frac{L_1}{L_2}\right) \frac{F_{act}}{K_{act}+K_{plat}} \quad (5.1)$$

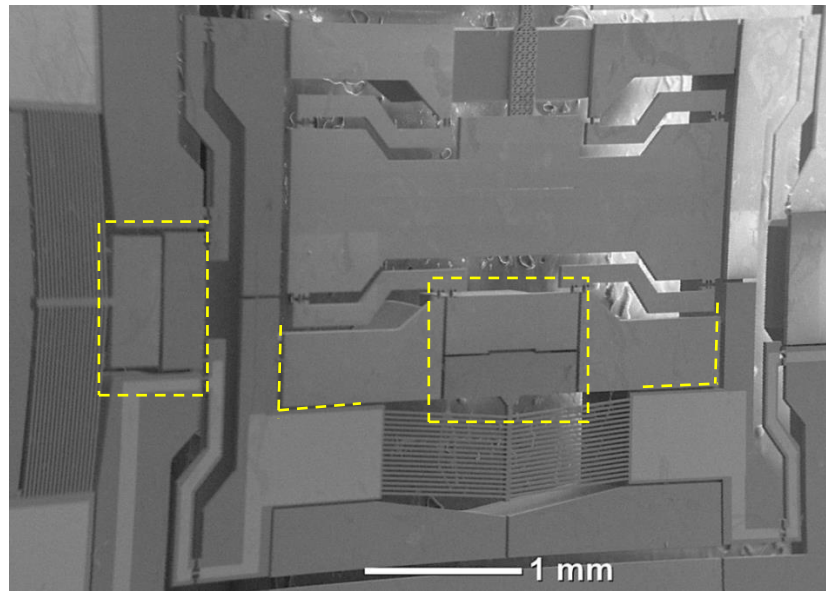
where, U_{act} and U_{plat} stand for the displacement of the actuator and the platform, respectively. Each term in equation (5.1) is analyzed in following sections.

5.2.1 The MEMS design of the SKM

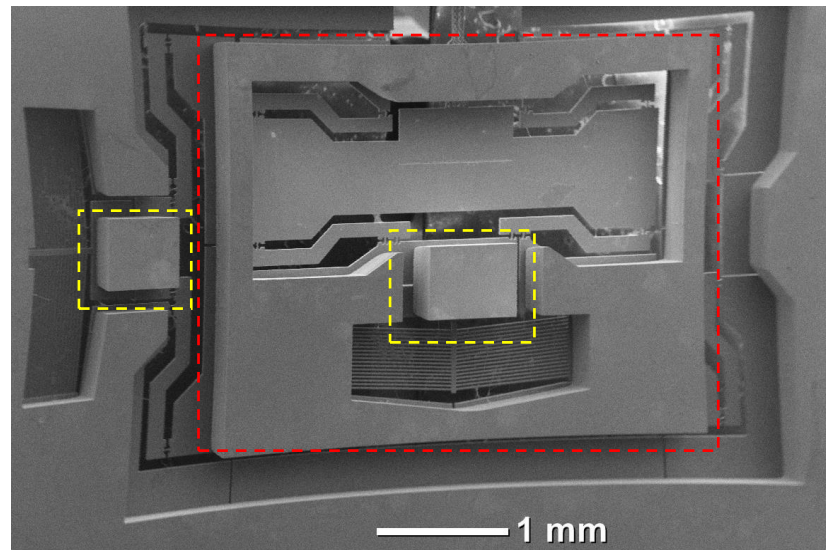
The implementation of the XY stage requires a few additional features to minimize side-effects such as a coupled motion error; (i) the two single DOF stages should be electrically isolated. Otherwise, the electric leaking from one actuator can exacerbate the coupled motion error between them. (ii) The Y-stage needs an appropriate electrical connection from outside. It is necessary to have an electric connection to control the Y-stage. However, an inappropriate connection such as conventional wire-bonding can damage floating components in the Y-stage. Moreover, wrong wiring or faulty connection can distort the desired motion due to the stiffness of the wire itself. (iii) Both ends of electrothermal actuator in the Y stage and four links should be firmly fixed on the Y-stage during its operation. Otherwise the force generated by the actuator cannot be transferred to the motion platform efficiently and the levers are also difficult to perform their operation properly.

In order to implement the features described above, a dual layer structure was adopted, which was implemented by utilizing both sides of silicon-on-insulator (SOI) wafers. The SOI wafers consist of three layers; a top silicon layer (called device layer), a substrate silicon layer (called handle layer) and a buried oxide layer between them. With SOI wafers, the separated structures in the device layer can hold their positions by connecting them in the device layer. Due to the buried oxide layer between them, the

gaps operate as electrical and thermal insulation. In addition, this additional feature in the device layer increases the stiffness, which can be used to hold both ends of the actuator. Based on this approach, electrical isolation and additional stiffness can be applied by adding structures in the handle layer.



(a)



(b)

Figure 5.2: SEM images of the SKM XY-stage: (a) a full view of the fabricated XY stage; (b) a backside frame to hold the Y stage and two connecting blocks for electric isolation

The proposed XY stage is fabricated with SOI-MUMPs and the scanning electron microscope (SEM) images are shown in Fig. 5. Fig. 5.2(a) is for the top side of the XY-stage and bright grey area is for the metal layer and grey area is for silicon itself. The physical gaps for electrical isolation are in yellow boxes in Fig. 5.2(a), which are supported by the connecting blocks in yellow boxes in Fig. 5.2(b). These physical gaps work as both electric isolation and thermal insulation of the Y-stage from the X-stage. There physical gaps surround the whole electric path to the Y-stage as shown in the yellow dotted lines in Fig. 5.2(a). Some of the gaps are held by the connecting blocks and some are by the supporting frame which is shown in red box in Fig. 5.2(b). This supporting frame also plays an important role in holding both ends of the actuator in the Y-stage and the ends of four links.

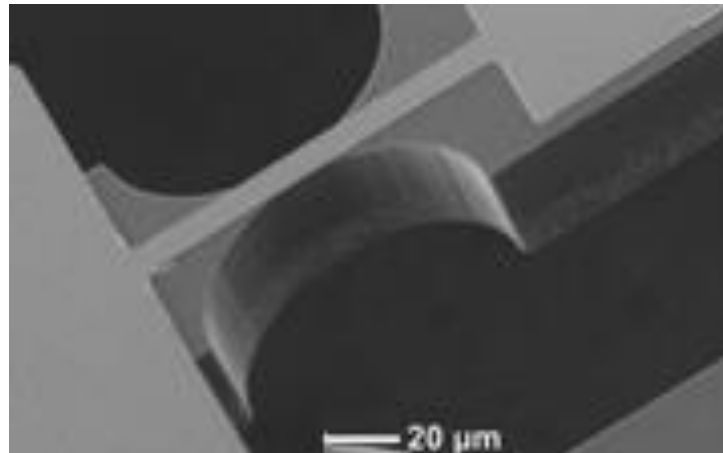


Figure 5.3: SEM images of the electric path over the flexure hinge

For the electrical connection to the Y-stage, a thick metal layer is deposited from the actuator of the Y-stage to an outside metal pad available for conventional wire bonding. This embedded electric path goes over the levers and flexures and one SEM image is shown in Fig. 5.3. This metal layer consists of 20 nm thickness Chrome, 1.8 μm

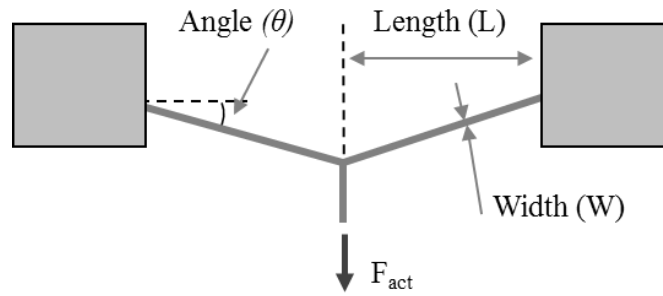
thickness Copper, 100 nm Titanium and 0.2 μm thickness Gold. The total thickness will be 2 μm thick. This is because the embedded electric path is relatively long so its total electric resistance can be minimized with this thickness. With this electric connection, the metal lines of the Y-stage can be extruded to a firm ground where conventional wire bonding is available.

5.2.2 The mathematical analysis for the chosen single DOF stage

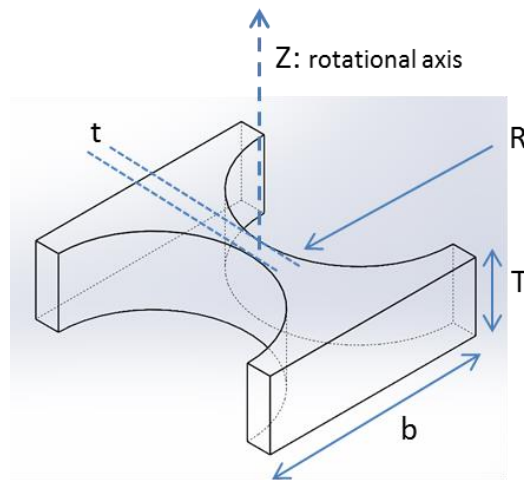
The old version of the single DOF stage has a maximum displacement of 12 μm and a resolution of 12 nm [44], which is not enough at manipulation of micro particles. For longer range of motion, design of the single DOF stage needs to be modified. One of advantages of a SKM is that all components except interfaces to adjacent components can be modified without redesigning whole SKM. As the coupled motion error can be decreased by adapting a SKM as described in the previous section, enough range of motion can be achieved by modifying the single DOF stage separately. Analytic relationships were developed in this section and design parameters were modified.

5.2.2.1 The electrothermal actuator

Figure 5.4(a) shows the schematic diagram of the electrothermal actuator adapted in the X-stage. This actuator is also known for a bent-beam electrothermal actuator or a chevron type actuator for its shape. When the beams of the actuator are thermally expanded, the bent angle guides the thermally expanded beams to generate one directional force, F_{act} along its central shaft.



(a)



(b)

Figure 5.4: The schematic diagrams of the actuator and the rotational flexure; (a) the electrothermal actuator; (b) the flexure hinge compliant mechanism (t : flexure neck width, R : radius of curvature, b : flexure width)

The main design parameters in the actuator are; beam length (L), beam width (W), bent beam angle (θ), number of beams (n), and beam thickness (T). These five design parameters are described in Fig. 5.4(a). For large force or displacement, these design parameters are analyzed and optimized in this chapter. With analytic relationships among the design parameters engaged, there are also several design constrains; (a) beam thickness (T) is predefined by the thickness of wafers purchased for this fabrication. This is because it is difficult to have good uniformity over the whole wafer during its fabrication. (b) Beam length (L) is limited by the size of the motion platform. A longer

beam length (L) is favorable for a longer range of motion, but the actuator will be longer than the motion platform when beam length (L) is longer. This can result in unnecessary area around the motion platform. Therefore, beam length (L) is set to be equal to or less than the half of the width of the motion platform. (c) Number of beam (n) is a discontinuous variable. This parameter is associated with the stiffness of the actuator and lever ratio and will be analyzed separately from the others four parameters. (d) Beam width (W) should be smaller than beam thickness (T) to avoid any out-of-plane bending or buckling prior to in-plane motion. (e) All parameters should be greater than 10 % of beam thickness (T) due to the 1:10 high-aspect ratio from the Bosch¹ deep reactive ion etching (DRIE) process [39]. Now 1:20 or higher ratio becomes available with Bosch process, but the whole design will be analyzed in a conservative approach in this chapter.

With the design parameters mentioned above, several analytic relationships are derived. The stiffness of the electrothermal actuator, K_{act} in equation (5.1) can be expressed with engaged design parameters [53] as:

$$K_{\text{act}} = 2n \left(\sin^2\theta + \cos^2\theta \frac{12I}{WT L^2} \right) \frac{EWT}{L} \quad (5.2)$$

where E is the Young's modulus of silicon, and I is the area moment of inertia. The force generated by the actuator is calculated from thermal stress as:

$$F_{\text{act}} = 2\alpha n \Delta T_{\text{ave}} EWT \sin\theta \quad (5.3)$$

where, α is the coefficient of thermal expansion of silicon and ΔT_{ave} is the average temperature rise in the whole beams of the actuator.

5.2.2.2 The flexure hinge design

The motion platform is supported by four links where the rotational flexure hinges shown in Fig. 5.4(b) play an important role in characterizing the motion platform. The flexure hinges are compliant mechanisms transmitting rotational motions via their elastic deformation. In this case, the stiffness of the platform K_{plat} can be expressed with the combination of the compliance of the flexure hinges and the lever ratio as:

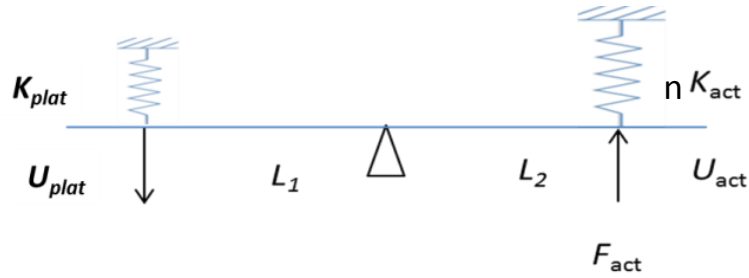
$$K_{\text{plat}} = \frac{m}{L_1^2 C_z} \quad (5.4)$$

where, m is a number of flexure hinges, L_1 is the link lengths shown in Figure 5.1(b), and C_z is its angular compliance about the Z axis of the flexure hinge [139]. A narrower flexure neck width (t) leads to higher C_z which is a design favorable for longer displacements, but this also makes the flexure hinges vulnerable to external vibration or noise during its fabrication. On considering the fabrication yields and stiffness of the flexure hinges, the flexure neck width (t) of $7 \mu\text{m}$ is chosen for its reliability at fabrication and reasonable performance. The flexure hinge thickness (T) was set to be $30 \mu\text{m}$, which is consistent with the thickness of SOI wafer used. The radius of curvature (R) is set to be $40 \mu\text{m}$ under available area for flexures. With this design, the flexure width (b) is automatically obtained from the equation; $b = 2R + t$. With these determined parameters, equation (5.4) predicts that the rotational stiffness of the selected flexure hinge design and the linear stiffness of the platform, K_{plat} are $7.52 \text{ Nm}/\mu\text{rad}$ and 46.28 N/m , respectively.

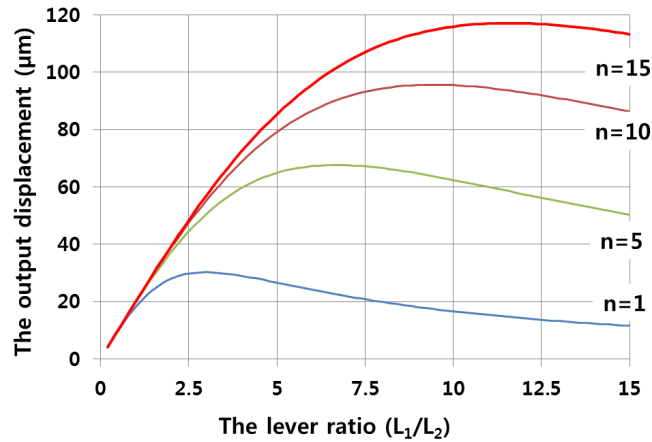
5.2.2.3 The lever ratio and the number of beams

The schematic diagram of the lever, the actuator and the platform is shown in Fig. 5.5(a). The force equilibrium equation can be expressed in Chapter 4 from the given lever mechanism as:

$$\left(\frac{L_1}{L_2}\right)^2 K_{\text{plat}} U_{\text{act}} = nF_{\text{act}} - K_{\text{act}} U_{\text{act}} \quad (5.5)$$



(a)



(b)

Figure 5.5: the lever mechanism adapted in the XY-stage: (a) schematic diagram; (b) maximum elastic displacement via lever ratio

Where, L_1 is the link outside in the lever and L_2 is the link inside in the lever, U_{act} is the displacement of the actuator, F_{act} is the force from the actuator with a single beam. In this case, L_1/L_2 will be a lever ratio and nF_{act} will be the total force the actuator can

produce. Equation (5.5) can be rearranged and expressed for the displacement of the actuator as:

$$U_{\text{act}} = \frac{nF_{\text{act}}}{\left(\frac{L_1}{L_2}\right)^2 K_{\text{plat}} + K_{\text{act}}} \quad (5.6)$$

With equation (5.6), U_{plat} can also be expressed as:

$$U_{\text{plat}} = \left(\frac{L_1}{L_2}\right) U_{\text{act}} = \left(\frac{L_1}{L_2}\right) \frac{nF_{\text{act}}}{\left(\frac{L_1}{L_2}\right)^2 K_{\text{plat}} + K_{\text{act}}} \quad (5.7)$$

Based on equation (5.7), the effect of different beam numbers (n) and various lever ratios (L_1/L_2) can be obtained. With five different beam numbers, the expected displacements are calculated and plotted in Fig. 5.5(b). In Fig. 5.5(b), K_{act} can be obtained from equation (5.2) based on a maximum allowable temperature, F_{act} comes from equation (5.3), and K_{plat} from equation (5.4) with the design parameters listed in Table 5.1. Fig. 5.5(b) indicates that the increase in the number of beams results in an increase in the range of motion. Further, different numbers of beams have their own optimum lever ratio for its maximum output displacement. However, with a limited space for the XY-stage, it is difficult to increase the number of beams to more than 15. Thus 15 beams are selected for the XY-stage design and 1:10 lever ratio is also selected for its optimum ratio. As a result, a displacement of 115 μm is possible at the motion platform based on equation (5.7). But this can be limited by other design constraints such as material and structural issues, which will be investigated in the following section.

5.2.3 Design constraints; thermal melting and buckling

The XY-stage is made of silicon, so its structural limits depend on silicon as well. Based on various literature review, the maximum temperature of the electrothermal actuator should be below 550 °C for reliable operations [61]. Based on pure thermal conduction, the temperature distribution along the beam can be expressed [52] as:

$$k \frac{d^2T}{dx^2} + \left(\frac{V}{\rho L}\right)^2 \rho = 0 \quad \text{for } -L \leq x \leq L \quad (5.8)$$

The solution for equation (5.8) will be:

$$\Delta T(x) = \frac{V^2}{2k\rho L^2} (L^2 - x^2) \quad \text{for } -L \leq x \leq L \quad (5.9)$$

where V is an voltage applied to an actuator, k is the thermal conductivity, and ρ is the resistivity of silicon. The resistivity (ρ) varies with the applied voltage since the applied voltage raises the temperature of the electrothermal actuator with its Joule heating. The measured resistivity as function of the applied voltage was: $\rho = 5 \times 10^{-5} (\Omega\text{m/V})V + 0.0004 (\Omega\text{-m})$. The temperature ranges from 20 °C to 550 °C and the average value of the measured resistivity is 0.000275 $\Omega\text{-m}$. The maximum temperature change ΔT_{max} , and the average temperature change ΔT_{ave} of the electrothermal actuator can be derived from equation (5.9) as:

$$\Delta T_{\text{ave}} = \int_{-L}^L \frac{\Delta T(x)}{2L} dx = \frac{V^2}{3k\rho} \quad (5.10)$$

$$\Delta T_{\text{max}} = \frac{V^2}{2k\rho} = \frac{3}{2} \Delta T_{\text{ave}} < 530^\circ\text{C} \quad (5.11)$$

As described in equation (5.11), the maximum allowable temperature change, ΔT_{\max} will be less than 530 °C to prevent any thermal issues. This is because a room temperature is assumed as 20 °C. Based on equation (5.11) and appropriate doping for the resistivity of silicon, the applied voltage (V) can be adjusted to be less than 10 V.

Table 5.1: The dimensional range of the design parameters

Symbol	Design parameter	Values
W	Actuator beam width	22.3 μm
θ	Actuator beam angle	0.068 rad
L	Actuator beam length	1000 μm
T	Actuator beam thickness	30 μm
n	Number of beams in actuator	15
L_1	Link length	1000 μm
L_2	Short link length	100 μm
m	Links connected to the platform	8
t	Flexure hinge neck width	7 μm
b	Flexure hinge width	87 μm
R	Flexure hinge radius of curvature	40 μm
ΔT_{ave}	Actuator average temperature	< 550 °C
ΔT_{max}	Actuator maximum temperature	< 550 °C
U_{plat}	Platform displacement	> 50 μm
K_{act}	Actuator stiffness with a single beam	889.16 N/m
K_{plat}	Platform stiffness without the levers	46.28 N/m
$F_{\text{act,max}}$	Maximum generated force by the actuator with 15 beams	125.3 mN

Another design constraint to investigate is buckling of the beam in the actuator, because these long slender beams are vulnerable at buckling when its load is over its

critical buckling load. When the buckling occurs, the force generated by the actuator starts decreasing because some portion of force will be consumed as a form of deformation of the actuator beams. The boundary condition of the bent-beam type electrothermal actuator is fixed-sliding ends [53]. The maximum buckling load based on this boundary condition will be [141]:

$$F_{act} \leq F_{buckling} = 2n \frac{\pi^2 EI}{L^2} \sin\theta \quad (5.12)$$

where, $F_{buckling}$ is the critical buckling load of a beam. From equations (5.3) and (5.12), the design constraint to avoid buckling can be expressed as a function of the beam width (W) as:

$$W \geq \sqrt{\frac{12\alpha\Delta T_{ave}}{n\pi^2}} L \quad (5.13)$$

In addition, the beam width (W) should be narrower than the beam thickness (T) to avoid any out-of-plane buckling in operation.

Based on equations (5.2), (5.3), (5.7), and (5.10), U_{plat} in equation (5.1) can be rewritten as:

$$U_{plat} = \left(\frac{L_1}{L_2}\right) \frac{2\alpha n E W T \sin\theta}{3k\rho \left\{ 2\left(\sin^2\theta + \cos^2\theta \frac{12I}{AL^2}\right) \frac{EA}{L} + \left(\frac{L_1}{L_2}\right)^2 \frac{m}{L_1^2 C_2} \right\}} V^2 \quad (5.14)$$

Equation (5.14) shows the output displacement of the platform has a proportional relationship with the square of the driving voltage. Based on equation (5.14) and the two design considerations, design parameters of the actuator and the flexure hinge are selected and listed in Table 5.1. The details of the design process are described in Chapter

4. With these values, the XY-stage is able to generate at least 50 μm in X and Y axes, respectively with the given chip size of 7000 μm x 3500 μm . This result from equation (5.14) is compared with experiment data in section 5.5.

5.3 Finite elements analysis (FEA)

A series of Finite Element Analysis (FEA) simulations are utilized to predict the thermal and structural behavior of the proposed XY-stage. The material properties used in this FEA are listed in Table 5.2. Doped SOI wafers are used to maintain low resistivity, which is also measured experimentally later.

Table 5.2: Material properties of silicon

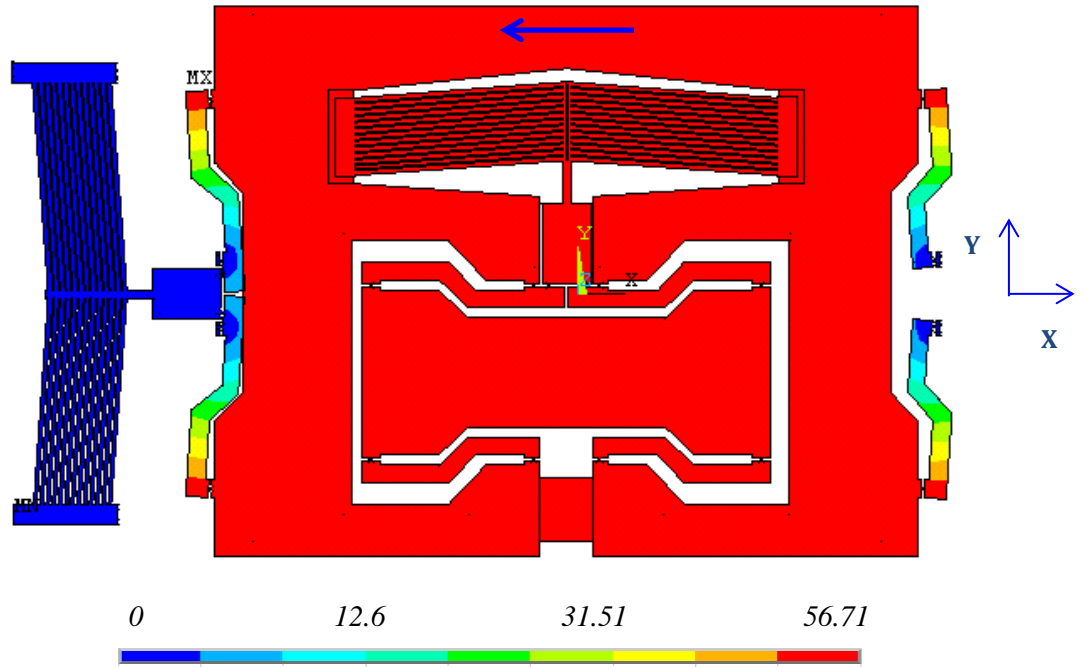
Material properties	Value
Young's modulus	130 GPa
Poisson's ratio	0.28
Resistivity	$-4.72 \times 10^{-7}T + 4 \times 10^{-4} \Omega\text{-m}$
Coefficient of thermal expansion	$3 \times 10^{-9}T + 3 \times 10^{-6} (/^{\circ}\text{C})$
Thermal conductivity (T is in $^{\circ}\text{C}$)	$5 \times 10^{-4}T^2 - 0.4706T + 164.15 \text{ W}/(\text{m } ^{\circ}\text{C})$
Yield strength	7 GPa

Boundary conditions and simulation assumptions are applied to the FEA to simplify the model; (a) electrical analysis: An electrical potential difference is applied between two ends of an electrothermal actuator. When one is in motion, the other electrothermal actuator is configured to be isolated electrically. (b) Structural analysis: The ends of the outermost four flexures and both ends of the actuator in the X stage are assumed to be fixed. (c) Thermal analysis: The four ends of flexure hinges and both ends of the actuator in the X stage are assumed to be at room temperature of 20 $^{\circ}\text{C}$. In the simulation for a

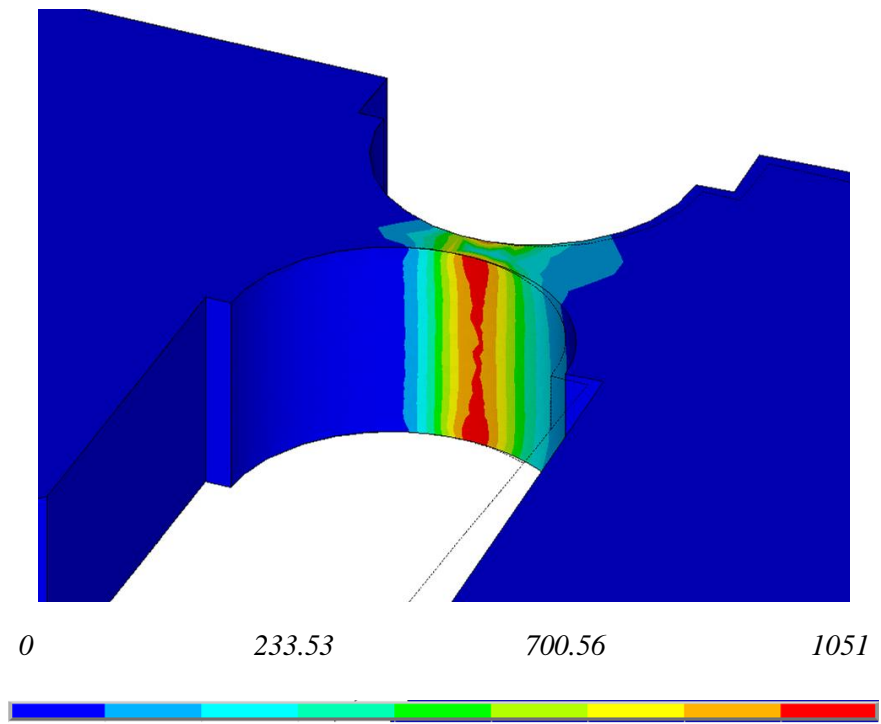
range of motion, only heat conduction thermal energy transfer is taken into consideration. For thermal distribution simulation, both conduction and natural convection heat transfer are included.

Figures 5.6(a) and 5.7(a) show the FEA results of the moving displacements under the temperature which is below 550 °C. Results showed that the X stage generates displacement of 51.41 μm at the temperature of 546°C , and the Y stage generates 54 μm under the peak temperature of 478 °C. With the displacements greater than 50 μm , FEA revealed that von Mises stress and the 1st principal stress on the flexure hinge are less than 1.1 GPa and are shown in Figure 5.5(b) and 5.6(b). These values indicate that no structural failure is expected at the flexure hinges with 50 μm displacement since the known yield strength of silicon is 7 GPa. .

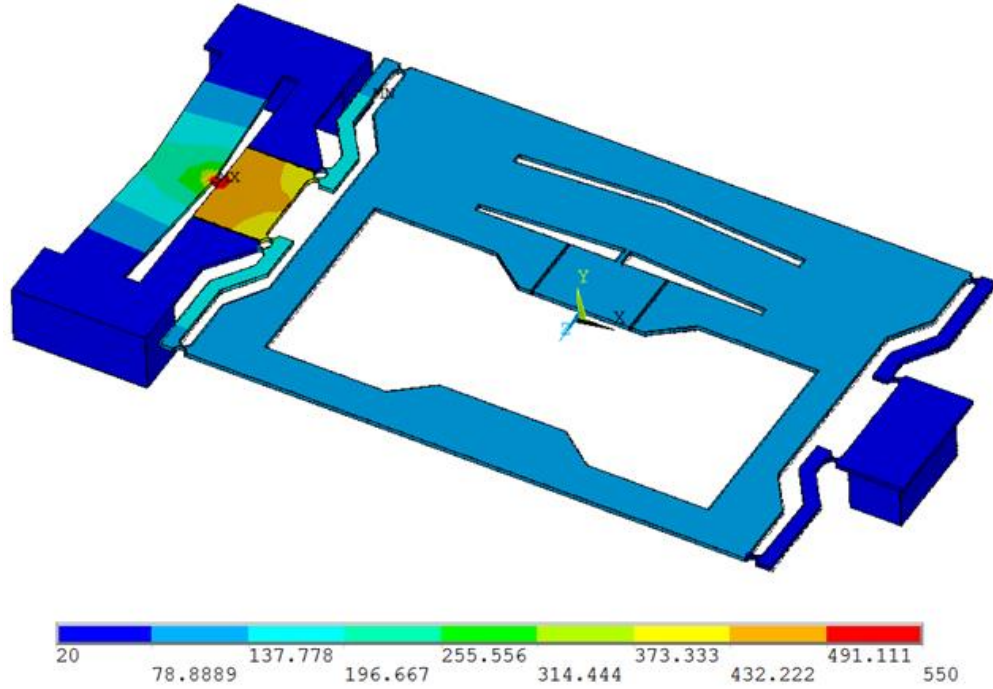
The temperature distribution over the XY-stage is numerically obtained with the actuators in operation. Figures 5.6(c) and 5.7(c) depicted the temperature distributions of the stage, when the maximum temperature of the actuator in the X stage or the Y stage reaches around 550 °C. These simulations indicate that the temperature distribution is well controlled and remains around the actuator area only. However, due to the difference in thermal boundary conditions, the Y-stage tends to produce higher temperatures than the X-stage. This difference can result in different displacement with the same voltages applied to the X-stage and the Y-stage. In addition, the temperature is well isolated in Fig. 5.6(c), but the temperature of the motion platform in the Y-stage causes temperature rise up to 130 °C around the Y-stage. From this observation, it is possible to have a coupled motion error by the Y-stage, rather than the X-stage.



(a)

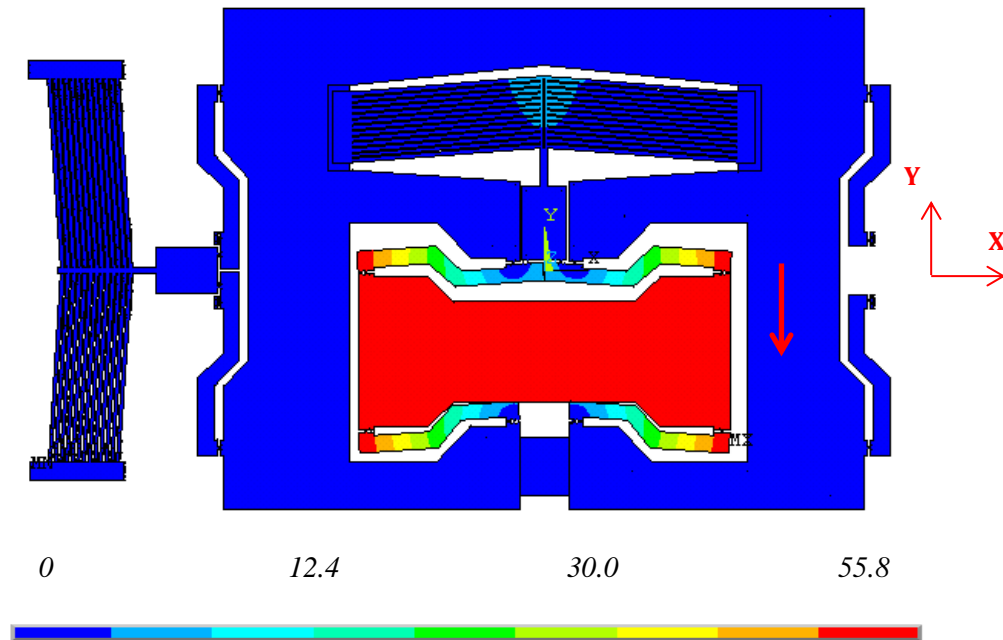


(b)

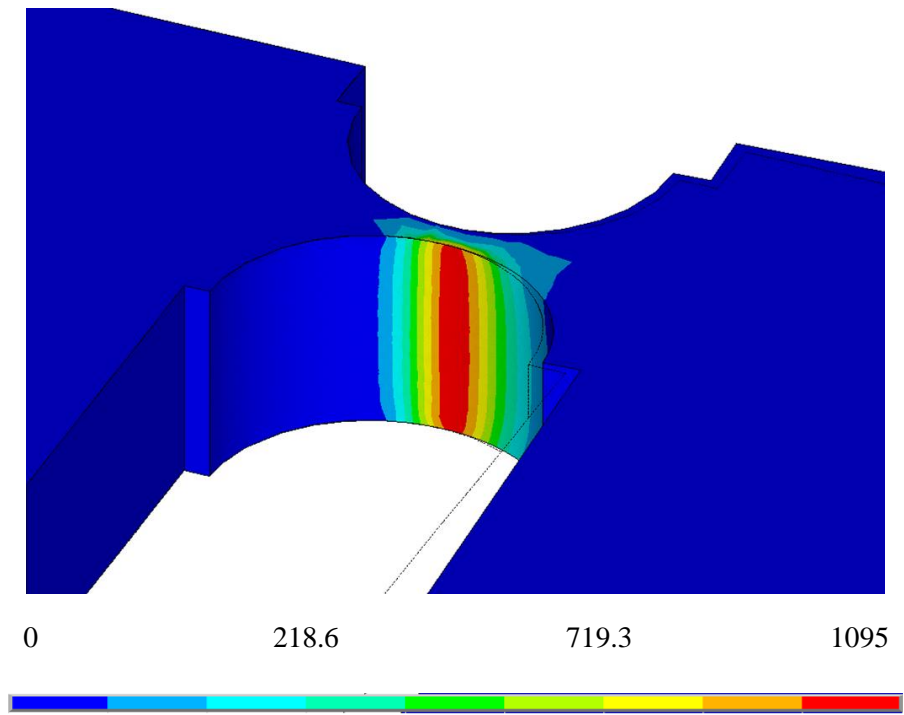


(c)

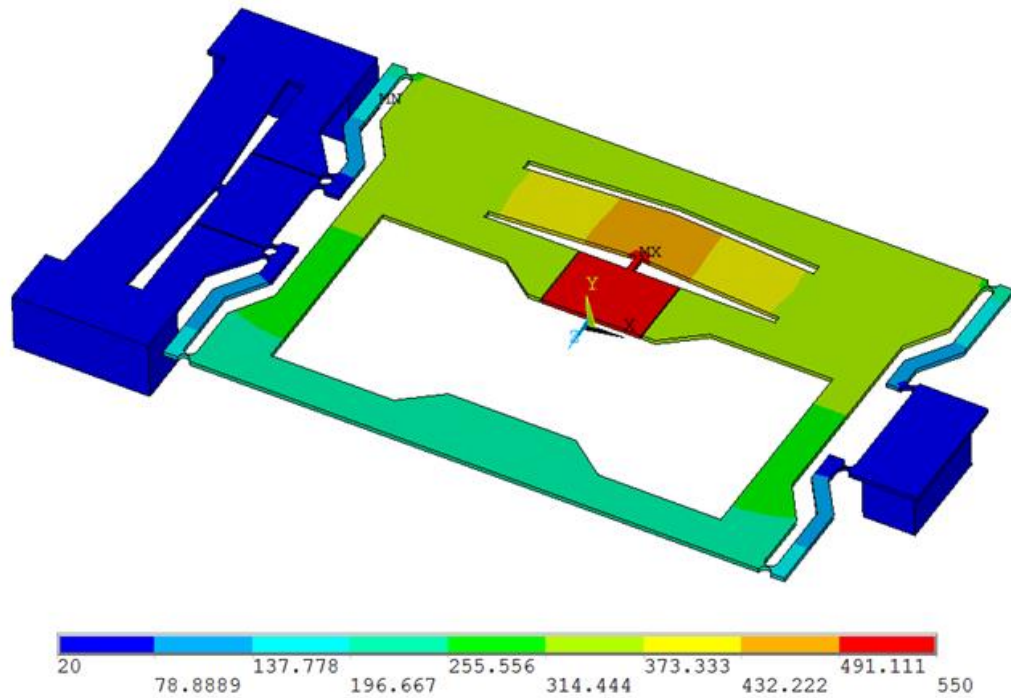
Figure 5.6: FEA of the proposed XY stage: (a) the displacement in X axis; (b) von Mises stress of a flexure hinge; (c) temperature distribution when the maximum temperature of the X stage is 550 °C



(a)



(b)



(c)

Figure 5.7: FEA of the proposed XY stage: (a) the displacement in Y axis; (b) first principal stress on a flexure hinge; (c) temperature distribution when the maximum temperature of the Y stage is 550 °C

5.4 Fabrication

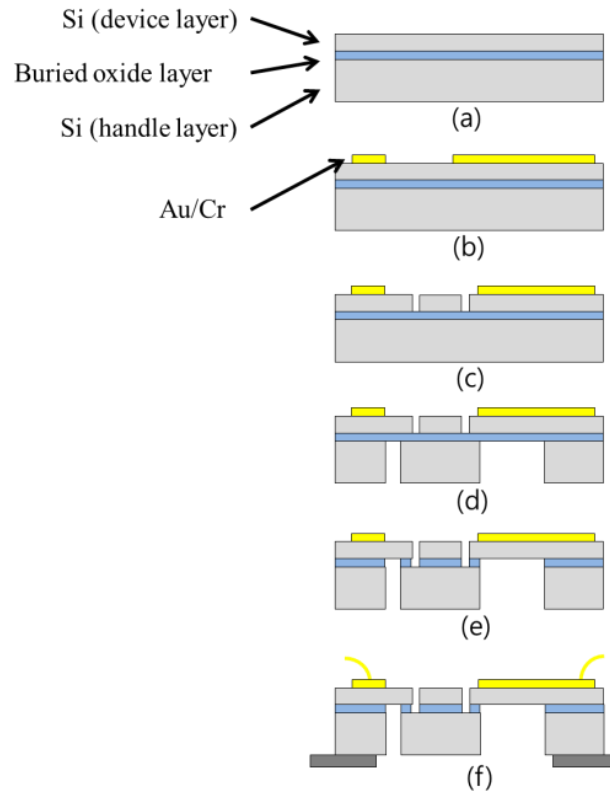


Figure 5.8: Fabrication sequence of SOI wafer for the XY stage: (a) a SOI wafer as a starting material; (b) metal deposition for electrical connections; (c) device layer etching by DRIE; (d) handle layer etching with DRIE; (e) removal of the buried oxide layer using B.H.E; (f) installation with bottom spacer and wire-bonding

The fabrication process for the proposed MEMS XY stage is schematically described in Fig. 5.8. A 30 μm thick device layer (upper thin grey area in Fig. 5.8(a)) is used for the main device structures and a 400 μm thick handle layer (lower thick grey area in Fig. 5.8(a)) is utilized as a backside supporting structure. A 2 μm thick buried oxide layer (blue thin strip in Fig. 5.8(a)) is located between the two silicon layers. The whole process follows Silicon-On-Insulator Multi-User Multi-Processes (SOIMUMPs) [39]. For reliable electrical connection, a layer of 10 nm of chrome and 700 nm of gold are deposited. The fabrication process consists of four steps – metal layer deposition, DRIE

of the device layer, DRIE of handle layer and removal of buried oxide layer. The two DRIE processes are carried out up to the buried oxide layer from both sides of SOI wafers. Using Buffered hydrofluoric acid (B.H.F.) movable structures are released.

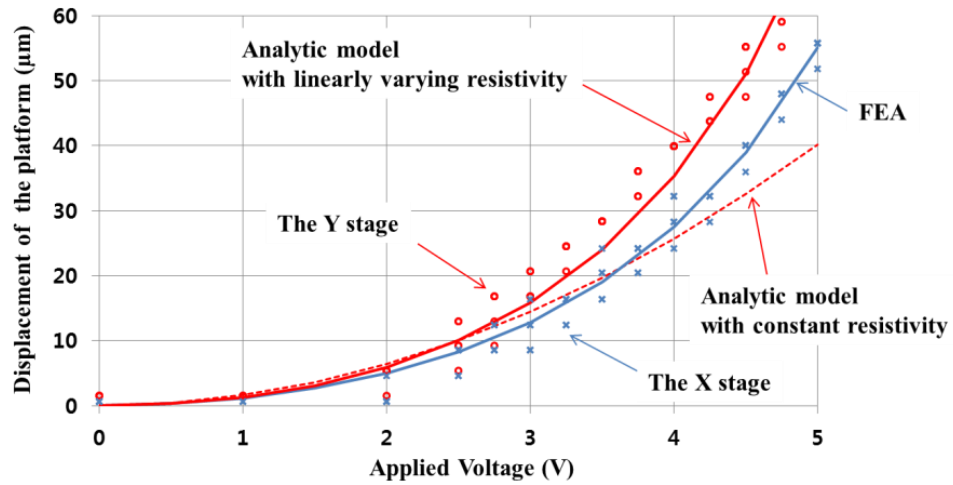
5.5 Experimental characterization of the MEMS XY-stage

5.5.1 The range of motion of the MEMS XY-stage and its coupled motion error

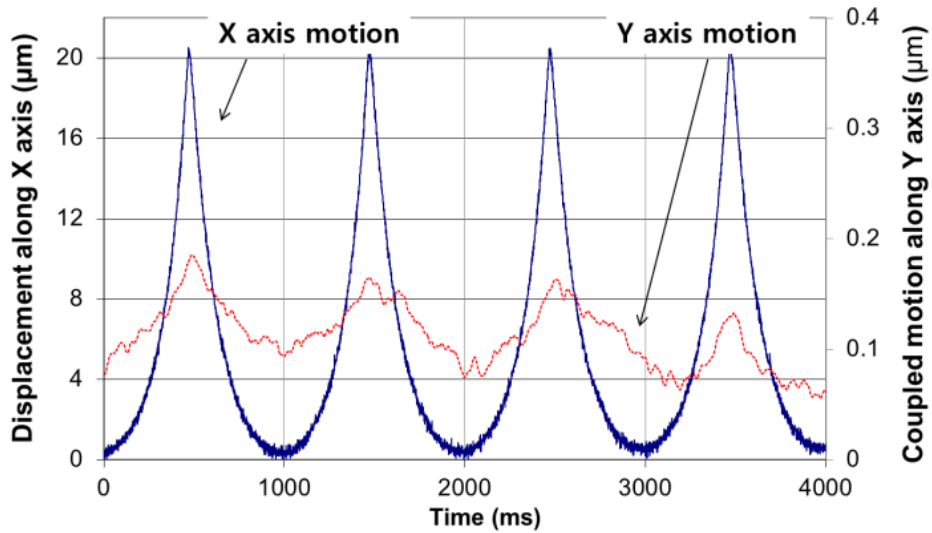
The range of motion of the presented XY-stage and its corresponding coupled motion error are measured experimentally. In this experiment, four metal pads are electrically connected to two DC power supply units (Model 3322A from Agilent). The corresponding X and Y positions are measured by an optical profiler (VEECO NT1100 [137]). It is evident from Fig. 5.9(a) that both X- and Y-stages displacements are greater than 50 μm within the driving voltages around 4.75 V to 5.0 V. Repeated tests with displacement larger than 50 μm indicates that there is no permanent damage with 50 μm or large motions. From the FEA it is noted that the Y stage reached higher temperature than the X stage, which results in longer displacement for the same driving voltage.

The experimental results, FEA and the analytical results from equation (5.14) are compared with each other and shown in Fig. 5.9(a). The FEA shows the similar trend line with the experimental results of the X-stage than the Y-stage, because the thermal boundary condition applied to FEA is the same with the X-stage. The analytical result shows a lower slope curve than the experimental result. This is because the resistivity of silicon used for this equation is an average value ranging from room temperature to 550 $^{\circ}\text{C}$. This value is not accurate to predict the motion of the X-stage at high temperature. For this issue, additional analytical results are numerically obtained with linearly varying

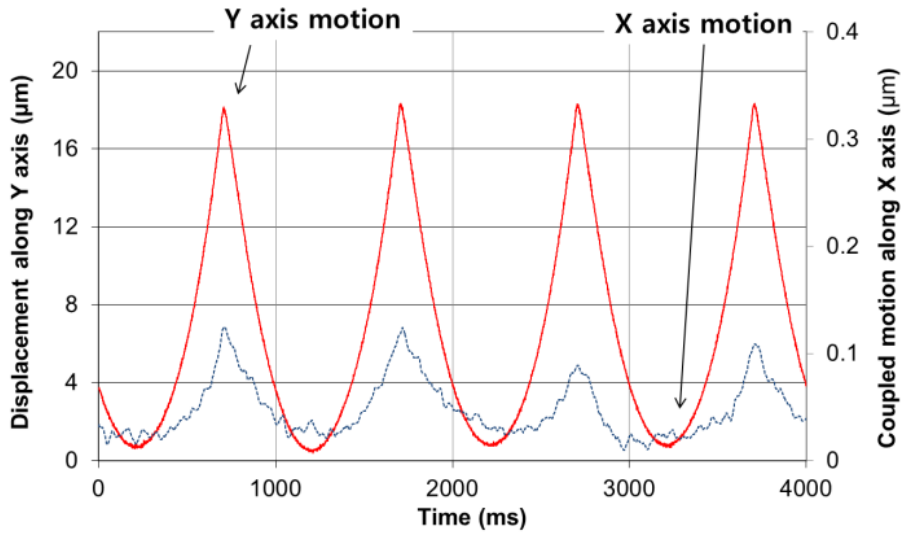
resistivity as shown in the red solid line in Fig. 5.9(a). This has a similar trend pattern with the Y-stage indicating that the linearly varying resistivity can predict the motion of the electrothermal actuator more accurately. Since the equation (5.14) takes into account only conduction heat transfer, this analytic results are closer to the Y-stage than the X-stage.



(a)



(b)



(c)

Figure 5.9: Experiments with fabricated XY-stages: (a) range of motions; (b) the coupled motion error in Y axis by the displacement along X axis; (c) the coupled motion error in X axis by the displacement along Y axis (the displacement along X axis is in blue and along Y axis is in red)

The coupled motions between the X- and the Y-stages are measured with an intensity-based laser reflectometer; the intensity of the reflected light from the edge of the motion platform is measured and its displacement is calculated based on the calibrated intensity and displacement relationship. To get the relationship between this intensity and the actual displacement, a calibration test is performed by measuring the reflected intensity with the motion of a commercially available nano-positioning stage (P-733.3 XYZ Piezo-Nanopositioning Stage [146]). This positioning stage is equipped with embedded X-Y displacement sensors. With the calibration completed, the coupled motions by the X- and the Y-stages are measured. The results are plotted in Fig. 5.9(b) and 5.9(c), respectively. From the Fig. 5.9(b) 20.48 μm motion by the X-stage (a blue curve) makes a coupled motion less than 0.5% (the red curve), which is negligible for its motion. With a similar set-up, the coupled motion error less than 0.6 % is observed while the Y-stage produces 17.67 μm motions. All these results are summarized in the Table

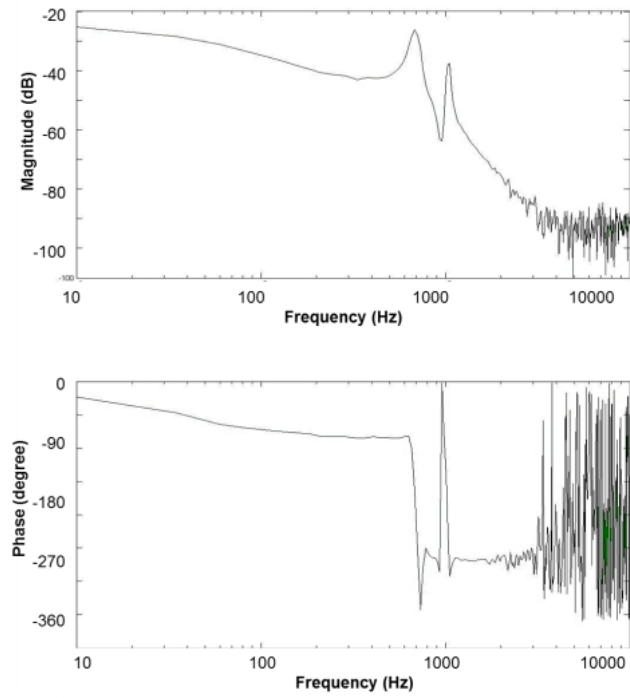
5.3. In summary, the coupled motion error of the proposed XY-stage will be expected to be less 0.6 % for around 20 μm motions.

Table 5.3: The coupled motion between the X- and Y-stages

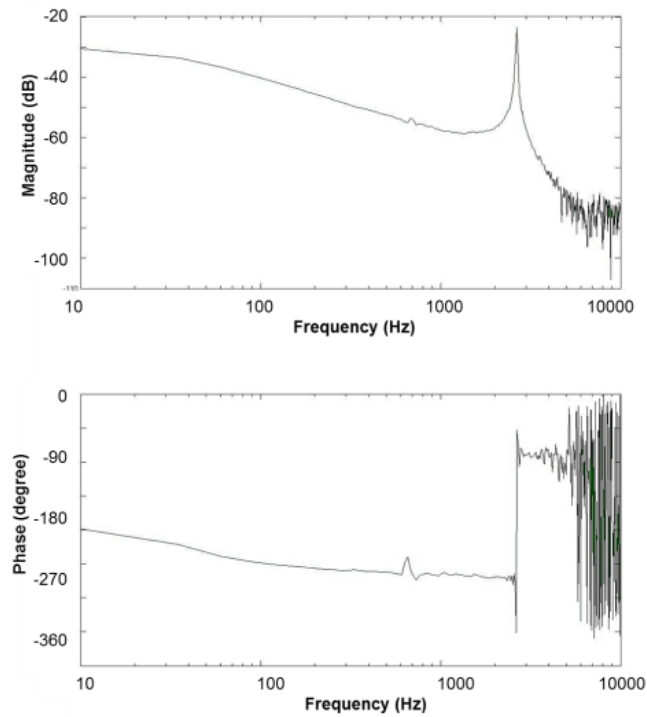
The target stage	Intended motion (μm)	Coupled motion (μm)
The X stage	-	0.1006 (0.569 %)
The Y stage	17.67	-
The X stage	20.48	-
The Y stage	-	0.0902 (0.44 %)

5.5.2 The frequency response

The frequency response of the proposed XY-stage is experimentally measured by the excitation of its two actuators in the X- and the Y-stages. The frequency responses are recorded by an Agilent Fast-Fourier-Transform (FFT) analyzer, whose details are explained in metrological research [119]. The 1st resonance frequency of the X-stage occurred at 0.71 kHz and of the Y stage at 2.63 kHz as plotted in Fig. 5.10. The 1st resonance frequency of the X stage is relatively lower than that of the Y stage. The frequency difference between the two stages can be explained by the different motion platform size and additional mass from the backside supporting frame beneath the X-stage. From these bode plot, it would be beneficial to utilize the presented motion stages at low frequencies less than 100 Hz and micro-manipulation or assembly can be promising applications.



(a)



(b)

Figure 5.10: Frequency response bode diagram: (a) the X-stage; (b) the Y stage

5.6 The multi-probe finger manipulation system

In order to verify the usability of the proposed XY-stage, a micro-manipulation [147] is designed by exploiting two XY-stages. The micro-manipulation is to control or access micro-scale objects. Due to the scale difference, a conventional bulk manipulator has shown limited access in micro-meter level objects. One common approach is to utilize optical tweezers which utilize a laser to trap and move micro-scale particles [148–153]. However, the optical tweezers are non-contact methods and not able to produce enough force for micro-scale objects, so the main manipulations have been implemented in aqueous environment. This micro-manipulation system is composed of two XY stages as shown in Fig. 5.11. One finger probe is extruded from the motion platform of each stage toward the workspace. Two probes can meet each other between two XY-stages and their collaboration can handle complex manipulating operations. Since each stage is able to generate more than 50 μm by 50 μm workspace, the well overlapped two probes can form a workspace similar to that size. With this layout, it is possible to pick up a micro-scale object, rotate it along the z-axis and position it within the workspace.

The demonstration of the micro-manipulation is done and several images are captured inside a scanning electron microscope (SEM) as shown in Fig. 5.12; Figure 5.12(a) shows a SEM picture of the two fingers gripping a 15 μm sized polypropylene particle. After being gripped, this object is rotated and translated by two probes along the Y axis as shown in Fig. 5.11(b), (c), and (d). In addition, the gripped objects can be moved along the X and Y axes by moving the two fingers in a coordinated fashion.

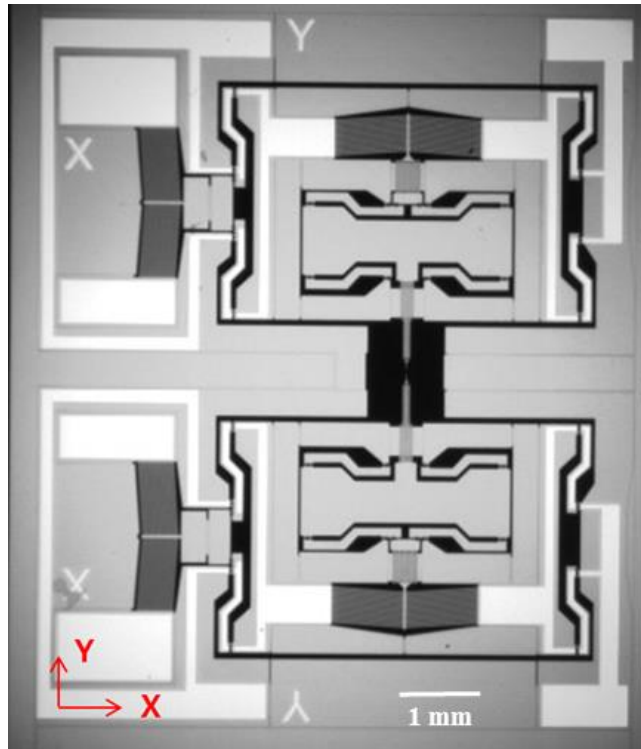


Figure 5.11: A multi-finger manipulation system with a 2x1 layout

The demonstration of the micro-manipulation is done and several images are captured inside a scanning electron microscope (SEM) as shown in Fig. 5.12; Figure 5.12(a) shows a SEM picture of the two fingers gripping a 15 μm sized polypropylene particle. After being gripped, this object is rotated and translated by two probes along the Y axis as shown in Fig. 5.11(b), (c), and (d). In addition, the gripped objects can be moved along the X and Y axes by moving the two fingers in a coordinated fashion.

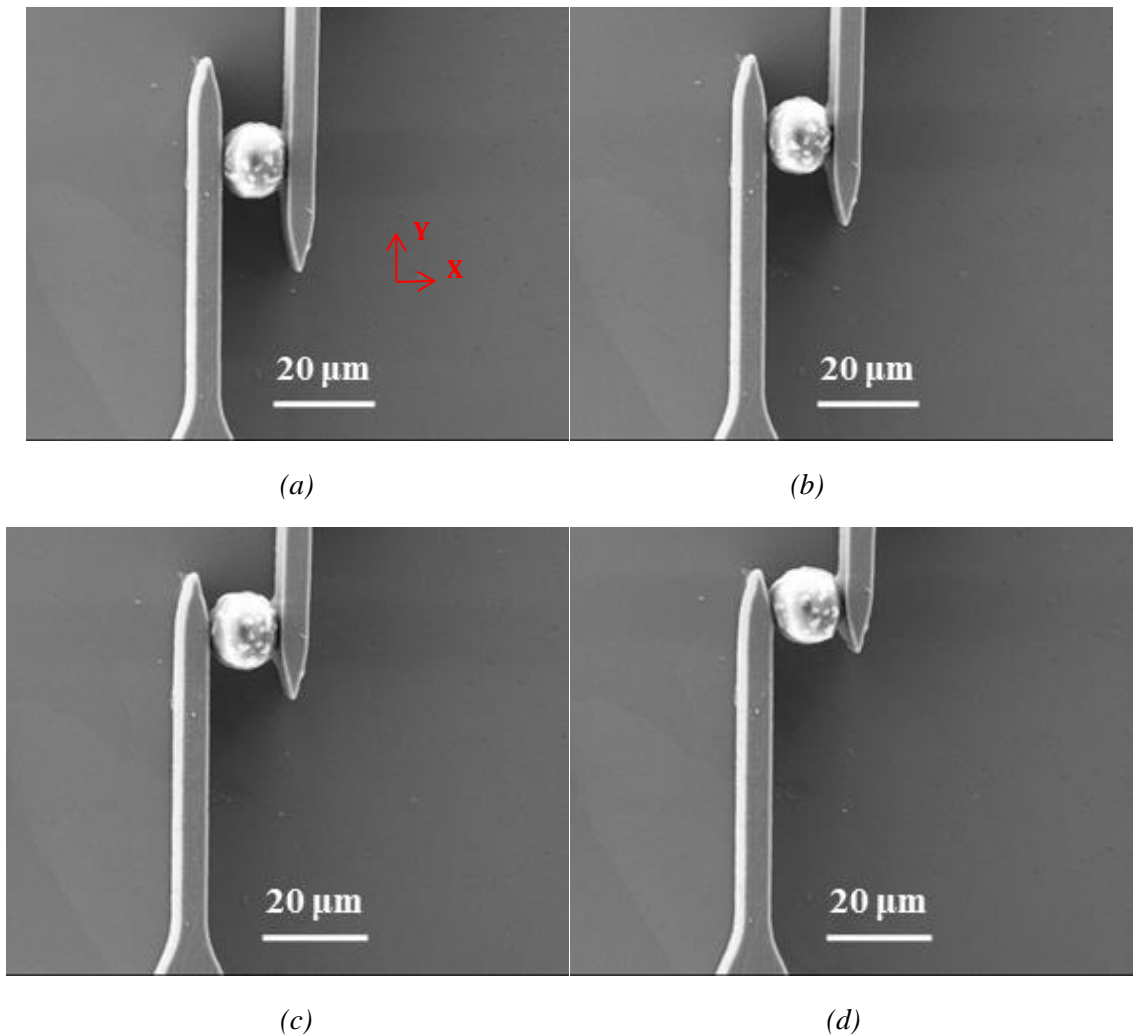


Figure 5.12: A multi-finger manipulation system: (a) 2x1 layout with two stages; (b) gripping a 14.8 μm sized micro particle; (c - e) rotating and moving the particle by controlling the motion of the two fingers

5.7 Summary

The design, fabrication and testing of MEMS based XY-stage for large stroke and negligible coupled motion is successfully accomplished. This presented stage is designed for applications such as micro/nano dynamic metrology, coordinate measurement machine metrology machining, manipulation and assembly.

For successful implementation, the following features have been adopted: (1) design of the single DOF stage to have more than 50 μm in motion displacement, (2) utilization of the nested structure to merge the two single DOF stages to build an in-plane 2 DOF stage with negligible coupled motion, (3) the electric isolation between the two stages to avoid any electrical leakage, and (4) embedded electrical connection for the Y stage. With these features, the fabricated XY-stage demonstrates at least 50 μm in displacements in X and Y axes, respectively. The FEA and the analytic solutions shows that when applying less than 5V, the electrothermal actuator is below its thermal or buckling limits and operates without any damage or side-effect. With a nested structure, its coupled motion is successfully depressed down to 0.6 % of the other axis motions. The first resonance frequencies for the X-stage and the Y-stage are at 705 Hz and 2.63 kHz, respectively. Successful demonstration on the micro-sized particle with the two fingers actuated by the two neighboring XY stages is presented as well.

This system can be extended for further operations by embedding or stacking different devices into it. Instead of the Y stage, two X stages can be employed for extending the motions greater than 100 μm . Additionally one more stage can be embedded into the Y-stage for 3 DOF motions or rotational motions. Instead of a Z-stage, a gripper or embedded sensor can be placed in the platform of the Y-stage for manipulation.

Chapter 6 MEMS-based out-of-plane motion stage

This chapter³ presents the design of an out-of-plane motion stage containing similar properties to the X-stage described in Chapter 4. Spatial motions are so common in manipulation or assembly applications that appropriate out-of-plane motion stage is necessary in designing 3-DOFs motion stage. In this chapter, the design and experimental results of a MEMS-based out-of-plane motion stage is presented based on similar fabrication methods and characterization used in the X-stage described in Chapter 4. This stage is also thermally actuated for out-of-plane motion by incorporating beams with step features. The fabricated motion stage has demonstrated the displacement of 85 μm with 0.4 $\mu\text{m}/\text{mA}$ rates and generated up to 11.8 mN forces with stiffness of 138.8 N/m. These properties obtained from the presented stage are in a similar level to in-plane motion stages which improve its usefulness when used in collaboration with in-plane motion stages.

6.1 Introduction

In micro-electro-mechanical systems (MEMS), precise positioning of micro-objects finds important applications in biomedical research [6], micro-assembly [15], micro-grippers [36], and scanning probe microscopy [97]. Since the target objects are getting smaller, MEMS technologies have been applied to develop a wide variety of miniaturized motion stages [6,27,36,97]. In many applications, the MEMS-based motion stages capable of generating both in-plane and out-of-plane (or vertical) motions can provide additional positioning options and improved controllability. But the realization of such a stage based on conventional MEMS processes is still challenging. This is due to the considerable difference in designs and fabrication methods between the in-plane and the out-of-plane

³ The work in this chapter is derived from the published work in [62, 130].

actuation mechanisms. Additionally, the out-of-plane stages reported so far demonstrate relatively lower performance than in-plane stages. Therefore, it is necessary to develop a new out-of-plane motion stage that is equivalent to in-plane motion stages. This equivalence implies similar performances between in-plane and out-of-plane stages, such as motion range, force generation, stiffness, and frequency response. For example, one of the commercial nano-positioners PI NanoCube [2] has demonstrated its usefulness from its cubic-shaped workspace. This workspace comes from the similar motion range in both in-plane and out-of-plane directions, which is more practical than a skewed workspace in real applications. Many reported in-plane motion stages have motion ranges from 25 μm [31] to 60 μm [27] or more, while most out-of-plane motion stages are limited to less than 15 μm (e.g., 1.5 μm reported in [87], 3.5 μm reported in [31]). Additionally, similar force and stiffness scales are also desirable in micromanipulation applications where the same stiffness level along different orientations can reduce unwanted bending motions or distortions at the interaction with a stiff target object. In addition, similar fabrication methods to in-plane stages are also another requirement. Requiring special tools like wafer bonding [31] or focused ion beam (FIB) [87] for out-of-plane stages has been a major obstacle to expand their applications. Thus, this paper focuses on the development of an out-of-plane MEMS motion stage that can provide equivalent performance to one of the existing in-plane stages and follows the same fabrication methods with the chosen in-plane stage.

There have been various approaches for out-of-plane motion stages. Among them, one of the most efficient methods is to utilize existing in-plane actuators. This method requires no additional effort on the actuator design and has an advantage to provide

similar stiffness and motion range. However, in order to utilize an existing actuator, converting structures such as inclined planes [87] or polarity hinges [16, 24] are necessary. The gap and the friction from the motion direction converting mechanisms restrict the precision that can be achieved. One of the other simple methods for generating out-of-plane motion is rotating an in-plane actuator by 90° and then inserting it into a fixed base frame during the post-processing step [66]. Since the erected actuator is exactly the same as the in-plane one, these actuators can provide similar motion range and force. However, the manual rotation and assembly process make it difficult to ensure good quality over multiple devices and cannot be used in mass production situations.

Instead of utilizing existing in-plane actuators, dedicated out-of-plane actuators have also been developed based on widely used actuation methods such as electrostatic, electromagnetic, and electrothermal. The electrostatic actuators are well known for their low power dissipation, fast frequency response, and simple geometries[120]. Based on this actuation method, parallel plate [31, 117] and asymmetrical vertical combs [154] have been commonly used for out-of-plane motions. One of the parallel plate types demonstrated $3.5 \mu\text{m}$ out-of-plane motions [120], but requires two big parallel plates, which can require different fabrication methods such as a wafer bonding [31]. Asymmetrical combs for out-of-plane motions have a similar design to in-plane comb drives, but its motion range is relatively smaller than in-plane motion due to the limited area between electrodes [154]. Another candidate is the electromagnetic actuators which are based on the Lorentz force principle and have been implemented as a combination of micro-coils and magnetic fields [98, 145–147]. These electromagnetic actuators have high bandwidth and also perform bidirectional displacement up to a few micro-meters.

The magnetic field for the actuator can be obtained through electroplating [145, 146], polymer deposition [157], and permanent magnets [78, 97]. Among them, the permanent magnets are stronger than the others, but are not compatible with MEMS fabrication processes. In addition, the magnetic field for one actuator can interfere with the other actuators, because it is difficult to isolate one magnetic field completely from the others. This can reduce the integration capability with other in-plane electromagnetic actuators.

As an alternative, electrothermal actuators have been utilized [27,68,75,157] for their large forces (on the order of a few mN) and stiffness (on the order of tens of N/m), which are attractive in micro-manipulation applications. One of commonly used out-of-plane electrothermal actuators is a cold and a hot arm that can generate out-of-plane motions up to 9 μm from the electrical resistance difference between the two arms [68]. This actuator is simple to fabricate and available for both in-plane and out-of-plane motions. But with this kind of actuator, it is difficult to generate linear motions. In order to generate a linear motion, symmetric beam designs with additional shapes like bridges or steps have been adapted to demonstrate 7 μm [75] to 14 μm [71] out-of-plane motions. The additional shapes have been fabricated mainly through surface micromachining technologies for multiple depositions and partial etchings. Contrary to surface micromachining technologies, bulk micromachining technologies have been rarely used for out-of-plane structure due to its limited fabrication processes. However, there are many needs for the out-of-plane actuator based on bulk micromachining technologies, because this approach can provide stiffness and forces greater than those from surface micromachining technologies.

In this chapter, an existing in-plane stage based on bulk micromachining has been selected as a target and a new electro-thermally actuated out-of-plane motion stage has been designed to provide characteristics similar to the selected one including motion range, stiffness, and force. The chosen motion stage can provide an in-plane displacement of 60 μm and a stiffness of 39.5 N/m [27,44]. The basic design concept and its details are described in section 6.2. In order to achieve similar properties to the chosen in-plane stage, theoretical analyses and finite element analysis (FEA) were utilized and are explained in section 6.3 and section 6.4, respectively. The fabrication procedures for the out-of-plane motion stage are depicted in section 6.5. Experimental results including its range of motion, stiffness, frequency response, and resistivity check are presented in section 6.6.

6.2 Design of the motion stage

In many MEMS electrothermal actuators, one commonly used electrothermal actuator is a bent-beam type or chevron type in-plane actuator [27,44,50] due to its simple structure and linear motion. This type of actuator is composed of aligned V-shaped beams pointing towards its actuation direction that convert thermal expansion of the beams into a linear motion. In this case, the bent beam angle plays an important role in determining its actuation direction. If this angle can be aligned toward a vertical direction, this actuator can generate out-of-plane motion. There have been several designs to fabricate this out-of-plane bent beam through a step-bridge shape [71] or trench [72,73]. But, many of them still have their own limitations such as smaller motion range and more complex fabrication processes than in-plane actuators due to lack of appropriate MEMS fabrication technologies.

The proposed actuator consists of four flat beams that have two steps at their ends and are connected at their center, as described in Fig. 6.1(a). When a current flows through the beam, it would generate a temperature rise by Joule heating and thermally expand. The height difference from the step features in the beam generates a bending moment from this thermal expansion, which results in an upward or downward out-of-plane motion. By placing two steps at the ends of the beam, the bending moment is utilized for creating an upward out-of-plane displacement.

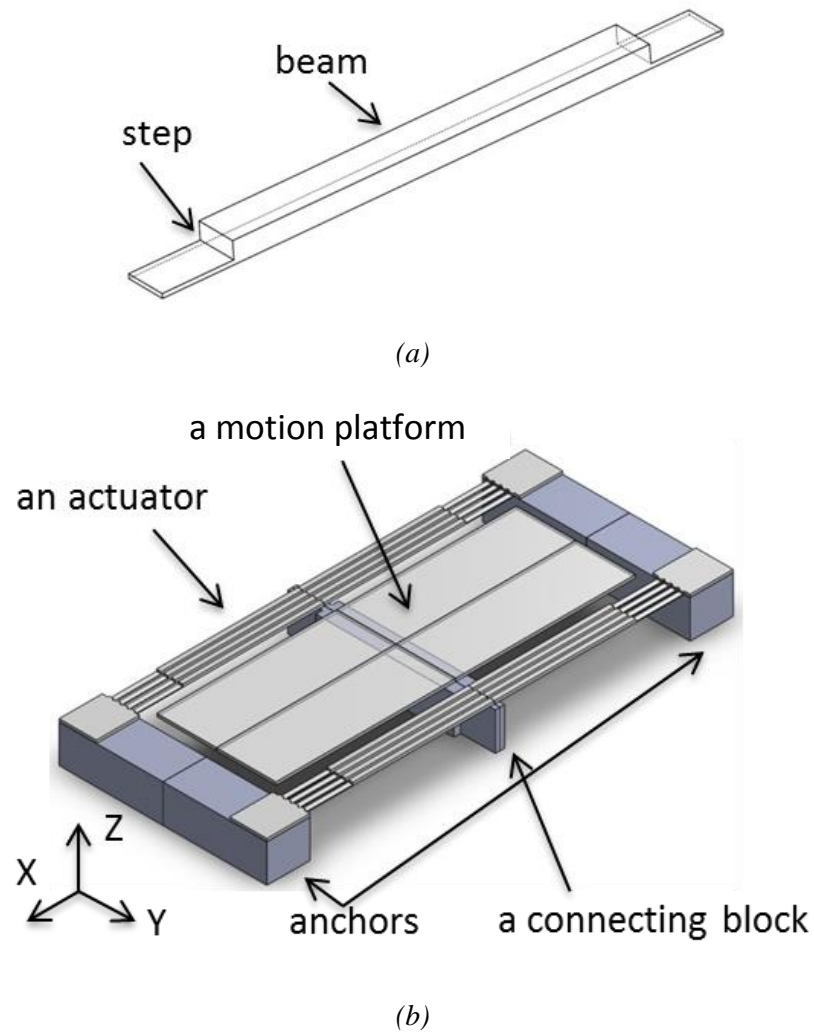


Figure 6.1: 3D models of the Z-stage; (a) A schematic illustration of a single beam with step features; (b) a 3D design of the motion stage actuated by the proposed two out-of-plane actuators that utilize four beams with step features (the device layer in grey and the handle layer in blue)

Based on this electrothermal actuator, a MEMS motion stage is designed and illustrated in Fig. 6.1(b), where the stage is composed of two out-of-plane electrothermal actuators and a moving platform. The actuators are located symmetrically at both sides of the platform and connected through a connecting block to compensate for any rotational motion. The motion platform is supposed to provide an interface or a base frame for external applications such as grippers or mirrors. The device is implemented based on a silicon-on-insulator (SOI) wafer which is the same materials used for the X-stage in Chapter 4 and the XY-stage in Chapter 5. The insulation layer between them isolates the actuators from the moving platform, which makes the platform electrically and thermally isolated from the actuator. Main components such as actuators and the moving platform are located in the first layer of silicon, called a device layer, and the other components like anchors and the connecting block are in the second layer of silicon, called a handle layer. These layers and components are described in Fig. 6.1(b). Since the fabrication process for this stage is composed of pure etching steps, it can be fabricated based on bulk micromachining technologies, especially silicon-on-insulator multiuser multi-processes (SOI-MUMPs) [102].

6.3 Design analysis

Figure 6.2(a) shows a schematic diagram of the beam in Fig. 6.1(a) for analysis. Two step features connect a lower portion of the beam to a fixed base. The force generated from the thermal expansion of the beam is denoted as P and P' . The free-body diagram of the beam is described in Fig. 6.2(b), where the step height from the action line of load P to the center line of the beam is denoted as e . The eccentric force P can be replaced with force P acting on the beam cross section center and a moment M_a ; $M_a = M_b = Pe$, as

illustrated in Fig. 6.2(c). Since the lower portion of the beam is connected to a fixed base, the steps produces eccentric load which results in an upward out-of-plane motion.

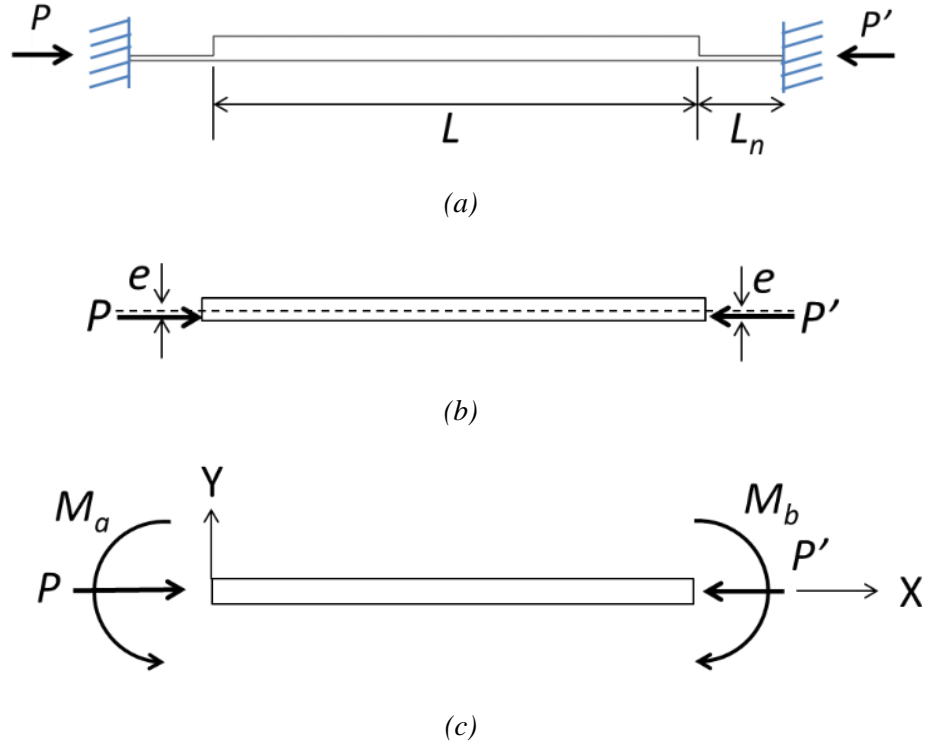


Figure 6.2: Diagrams for the analysis; (a) the schematic diagram of one beam of the actuator; (b) A diagram with an eccentric load P from a thermal expansion of the beam; (c) a converted free-body diagram of the beam

With a pinned-pinned boundary condition, $y(0) = 0$ and $y(L) = 0$, the analytic relationship for the beam deformation profile can be expressed [124] as:

$$y = e \left\{ \tan \left(\sqrt{\frac{P}{EI}} \frac{L}{2} \right) \sin \left(\sqrt{\frac{P}{EI}} x \right) + \cos \left(\sqrt{\frac{P}{EI}} x \right) - 1 \right\} \quad (6.1)$$

where, E is the Young's modulus of silicon and I is the area moment of inertia of the beam. Based on equation (6.1) and the dimensions listed in Table 6.1, the deformation profile of the actuator is calculated and plotted in Fig. 6.3, where this profile was verified by comparing with the profile from finite element analysis (FEA).

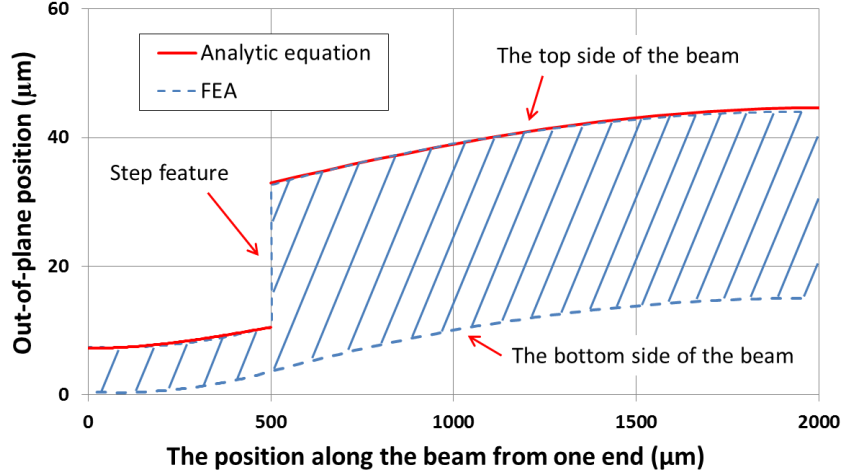


Figure 6.3: A comparison of out-of-plane deformation from equation (6.1) and FEA as a function of the position along the beam from one end

The value of the maximum deflection y_{max} can be obtained at the middle of the beam ($x = L/2$) and can be expressed as:

$$y_{max} = e \left\{ \sec \left(\sqrt{\frac{P L}{EI}} \frac{L}{2} \right) - 1 \right\} \quad (6.2)$$

Equation (6.2) implies that the step depth (e), a beam length (L), and the force (P) are the main parameters in determining the beam displacement performance. The longer L can produce a longer displacement, but this is vulnerable at buckling and also limited by the allowable chip area. The load P can be expressed from a classic beam theory as:

$$P = 2\alpha\Delta T_{ave}EWH \quad (6.3)$$

where, α is the coefficient of thermal expansion of silicon, W is the beam width, H is the beam height, and an average temperature rise over the beam ΔT_{ave} is studied in [52] and can be expressed as:

$$\Delta T_{ave} = \frac{V^2}{3k\rho} = \frac{2}{3}\Delta T_{max} \quad (6.4)$$

where, k is the thermal conductivity of silicon, ρ is the resistivity of silicon, and V is the driving electrical voltage applied to the actuator.

The load P can be expressed as a function of temperature and this relationship is described in equations (6.3) and (6.4). In this case, the maximum P is also determined through the maximum allowable temperature ΔT_{max} , which causes silicon to deform permanently. These values are reported as 550 °C [61] or 800 °C [134,158]. In this chapter, the temperature of 550 °C is selected as a constraint, since this is the lowest value among the candidates. Since longer beam length (L) and larger load (P) are desirable, the two parameters L and P are eventually limited by the available chip area and the thermal properties of silicon.

Table 6.1: The design parameters in the Z-actuator

Components	Symbol	Design parameters	Dimensions (μm)
Beam	W	Width	33
	H	Height	30
	L	Length	3000
Step	L_n	Length	500
	e	distance from the central line of the beam to the central line of the step	11

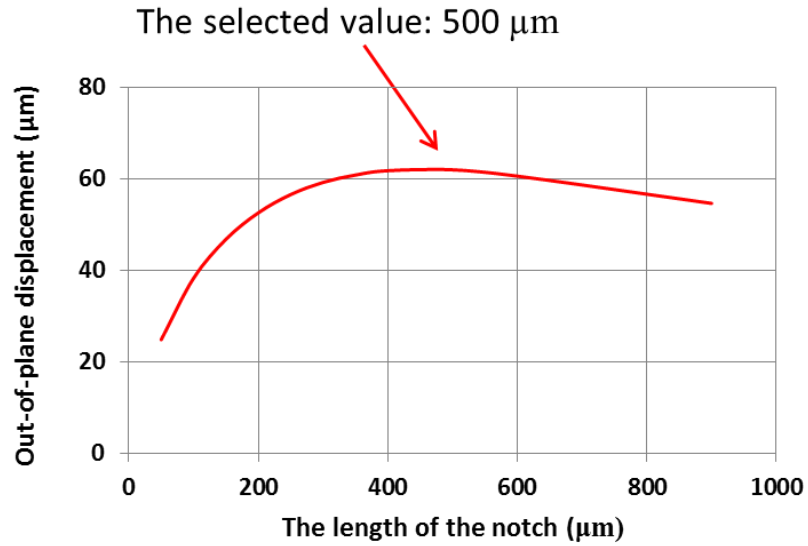
The other remaining design parameters are step depth (e) and step length (L_n), which are investigated in the following FEA section to increase the performance of the actuator. Except for these design parameters, the remaining parameters of the beam have

been selected based on the theoretical analysis and available area or material properties. The same SOI wafers used for the XY-stage are also selected as a starting material and its 30 μm thick device layer determines the beam height (H). The beam width (W) should be larger than the beam height (H) by at least 10 percent in order to prevent any in-plane deformation from starting prior to out-of-plane deformation. Since the longer beam is favorable at its maximum displacement, the beam length (L) is determined from the allowable area size for the device. For the device reported in this paper, the total chip size is set to be less than 4 mm x 4 mm, so L is set as $L = 4\text{mm} - 2L_n$. All parameters are listed in Table 6.1 with their corresponding values.

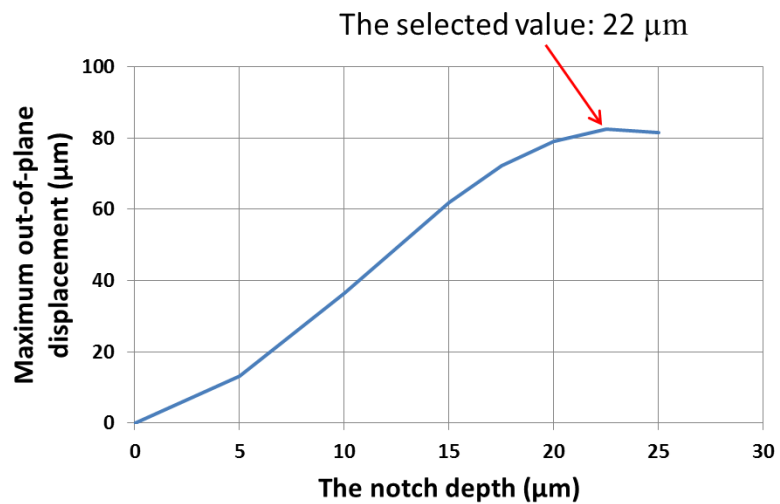
6.4 Finite element analysis (FEA)

Commercial finite element analysis (FEA) software, ANSYS [135] is utilized to simulate the behaviors of the presented actuator and find the optimum values for the design parameters step depth (e) and step length (L_n). The actuator is made of silicon and its material properties are the same with that for the XY-stage listed in Table 5.2. The same boundary conditions and conditions applied to the XY-stage are used for the Z-stage as well; an electric potential difference as electric excitation is applied between both ends of the actuator and this analysis include electric, thermal, and structural beam response. For thermal analysis, both ends of the actuator beam are assumed to be linked directly to a heat sink which is at room temperature (20 °C) and heat conduction heat transfer was taken into consideration. In each FEA, the maximum temperature and the stress are monitored in order to be kept under the maximum allowable temperature of 550 °C and yield strength of 7 GPa to avoid any plastic deformation or mechanical failure.

6.4.1 The optimization of the step feature



(a)



(b)

Figure 6.4: The out-of-plane displacement based on the step length and step; (a) An out-of-plane displacement as a function of the step length (L_n); (b) an out-of-plane displacement as a function of the step depth (e)

The optimization of the step feature can increase the performance. For this optimization, step length (L_n) and step depth (e) are separately evaluated through multiple FEAs. The expected displacements are calculated based on temperature rise of 530 $^{\circ}\text{C}$ as an external excitation. During this FEA, various L_n have been tested, ranging from 50 μm to 900 μm .

Their corresponding responses are plotted in Fig. 6.4(a) where a local maximum displacement of 62 μm is observed at 500 μm step length. With the step length (L_n) of 500 μm , the step depth (e) was also examined through FEA with the same thermal excitation of 530 $^\circ\text{C}$ increment. Their corresponding responses are in Fig. 6.4(b) where a local maximum of 82 μm is possible with the step depth of 22.5 μm . These values are applied to the step design parameters, enabling a displacement larger than 80 μm

6.4.2 Stress distribution

In order to monitor any mechanical failure during operation, its von Mises stress distribution can be numerically calculated with the displacement of 85.1 μm . The response from the stage is shown in Fig. 6.5(a) where the whole actuator except the step features experiences stress less than 140 MPa. Around the step feature, the maximum stress increases and found to be 318.9 MPa as depicted in Fig. 6.5(b). These values imply that most deformation occurs near the step feature, which can be an active design limit. However, the calculated number is still far less than the yield strength of silicon 7 GPa, so there is no mechanical failure expected during its normal operations up to 85 μm . Since 94 μm motion produces a stress still less than 500 MPa, the presented stage for 85 μm displacements can operate without any mechanical failure or fatigue.

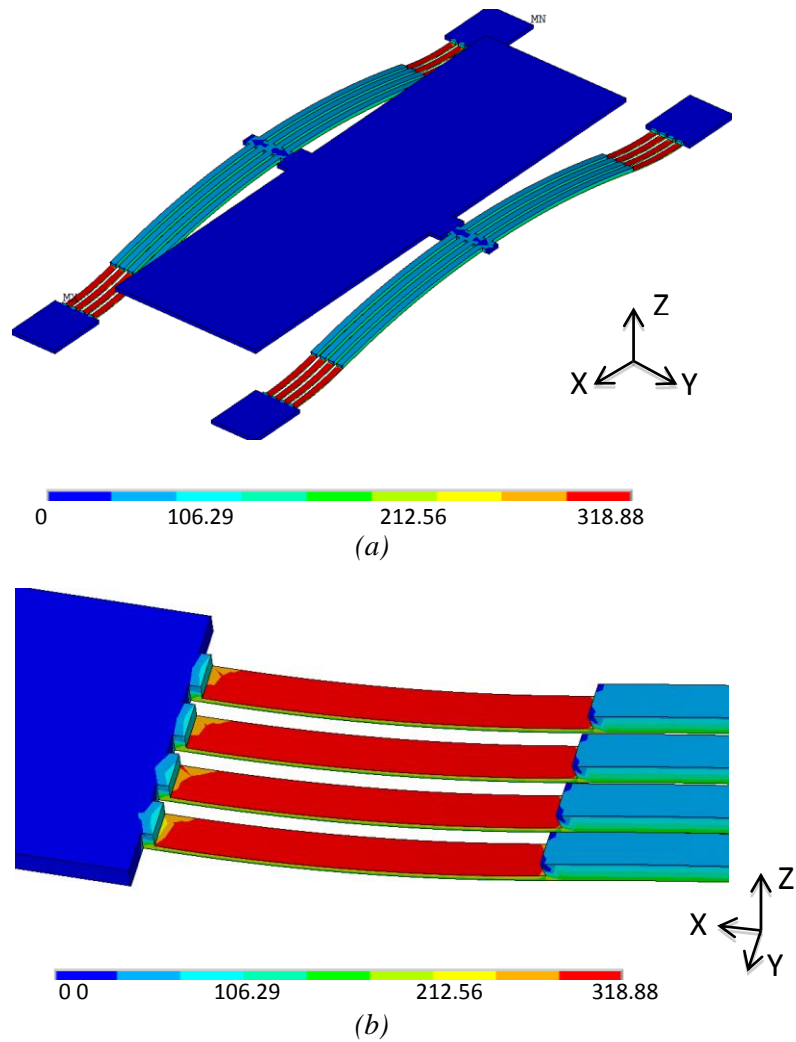


Figure 6.5: Stress distribution calculated by finite element analysis; (a) von Mises stress distribution on the full model; (b) a close-up view near the step

6.4.3 The frequency response, stiffness, and maximum force of the motion stage

The dynamic behavior of the moving stage is also analyzed; three natural frequencies and the corresponding mode shapes. The first mode has a natural frequency of 4.567 kHz and a mode shape of pure translational motion normal to the moving platform as shown in Fig.6.6. The second and third modes are rocking modes at 8.532 kHz along the X axis and at 9.850 kHz along the Y axis, respectively. These two modes are at least 80 percent

larger than the first mode, so the presented design provides enough separation between the desired motion and potential parasitic motions.

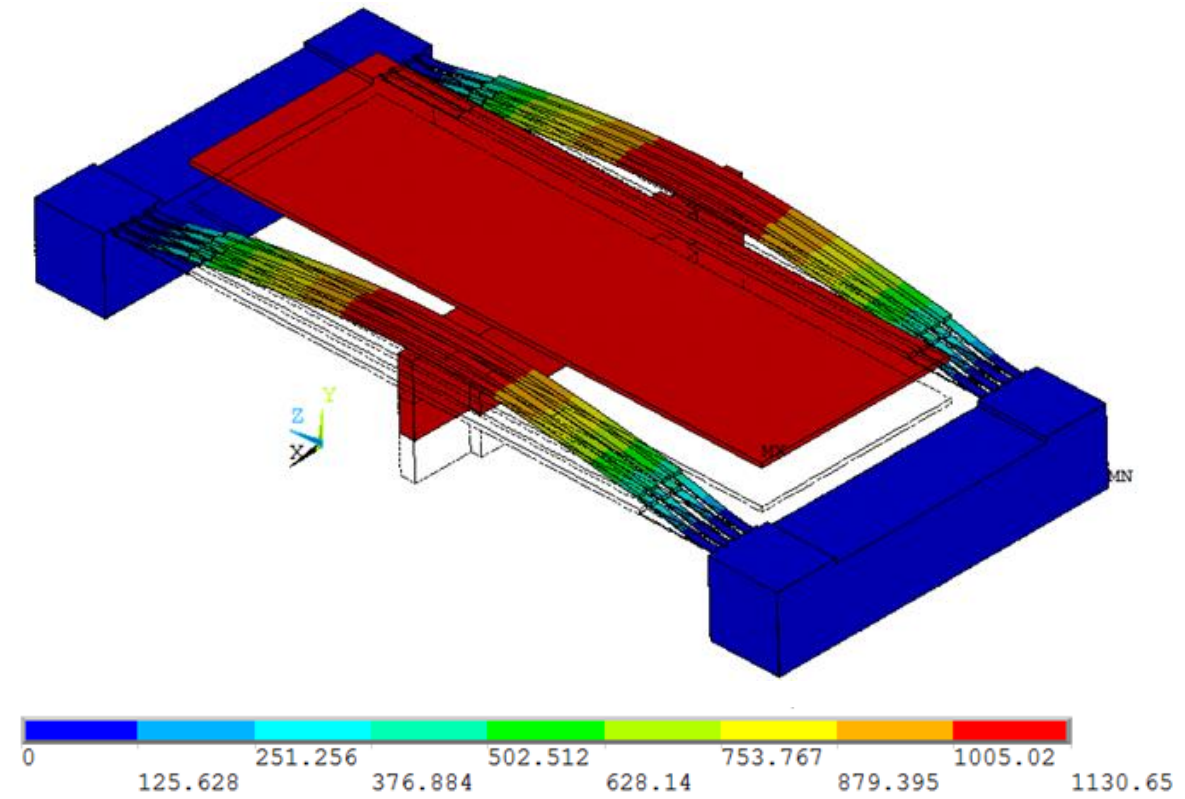


Figure 6.6: The mode shape of the Z-stage at its first resonant mode

The stiffness of the motion stage is also calculated under the situation that a $1 \mu\text{N}$ force is applied to the middle of the moving platform as mechanical excitation. From this, the moving stage is expected to have a stiffness of 128.2 N/m along the out-of-plane direction. The maximum force from the actuator is calculated under the case that the temperature increment of $530 \text{ }^\circ\text{C}$ is used as a thermal excitation and the moving platform firmly held at zero displacement as a mechanical constraint. The corresponding result was found to be 13.81 mN . Based on these two values, the ideal maximum displacement is approximately $107.7 \mu\text{m}$ without considering any thermal or structural limits. These properties obtained from FEA are compared with measured data in section 5.

6.5 Fabrication

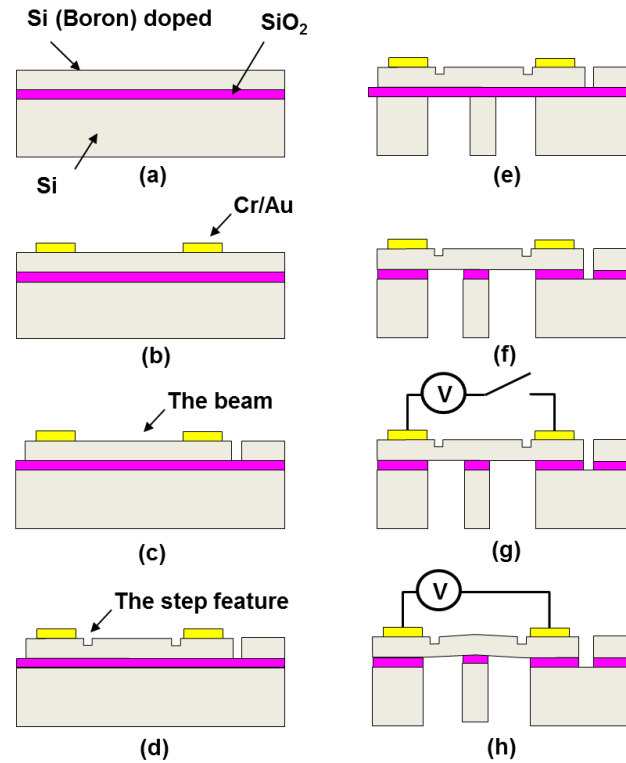


Figure 6.7: The fabrication flow: (a) SOI wafer as a starting material; (b) Au/Cr layer deposition for an electrical connection; (c) first etching for the beam and the motion stage except for the steps using DRIE; (d) second etching for the steps using DRIE; (e) etching of the handle layer using DRIE; (f) etching the buried oxide layer to release the motion platform; (g) electrical connection by wire-bonding; (h) an expected deformation during its operation

The fabrication process flow is based on the SOI-Multi User Manufacturing Processes (MUMPs) [39] and each process step is described in Fig. 6.7. The device is fabricated on the same SOI wafer used in Chapter 4 and Chapter 5 as shown in Fig. 6.7(a). The fabrication process consists of a metal deposition step for generating the electrical connection pads and wires [Fig. 6.7(b)], the first deep reactive ion etching (DRIE) of the device layer to build the main devices [Fig. 6.7(c)], the second DRIE to fabricate the step features [Fig. 6.7(d)], and the third DRIE to form the anchors and the connecting block and to release the main devices for operation [Fig. 6.7(e)]. After these three DRIE steps, a

buried oxide layer between the device layer and the handle layer is partially eliminated to make the moving stage free [Fig. 6.7(f)]. All the etching steps are implemented by the Bosch process (Deep RIE-Unaxis SHUTTLELINE DSEII) [21] and the metal deposition step by an electron-beam evaporator (Denton Infinity 22) [159]. The fabricated device is connected to external electrical DC actuation voltage for its operation [Fig. 6.7(g)] and its expected operation is depicted in Fig. 6.7(h).

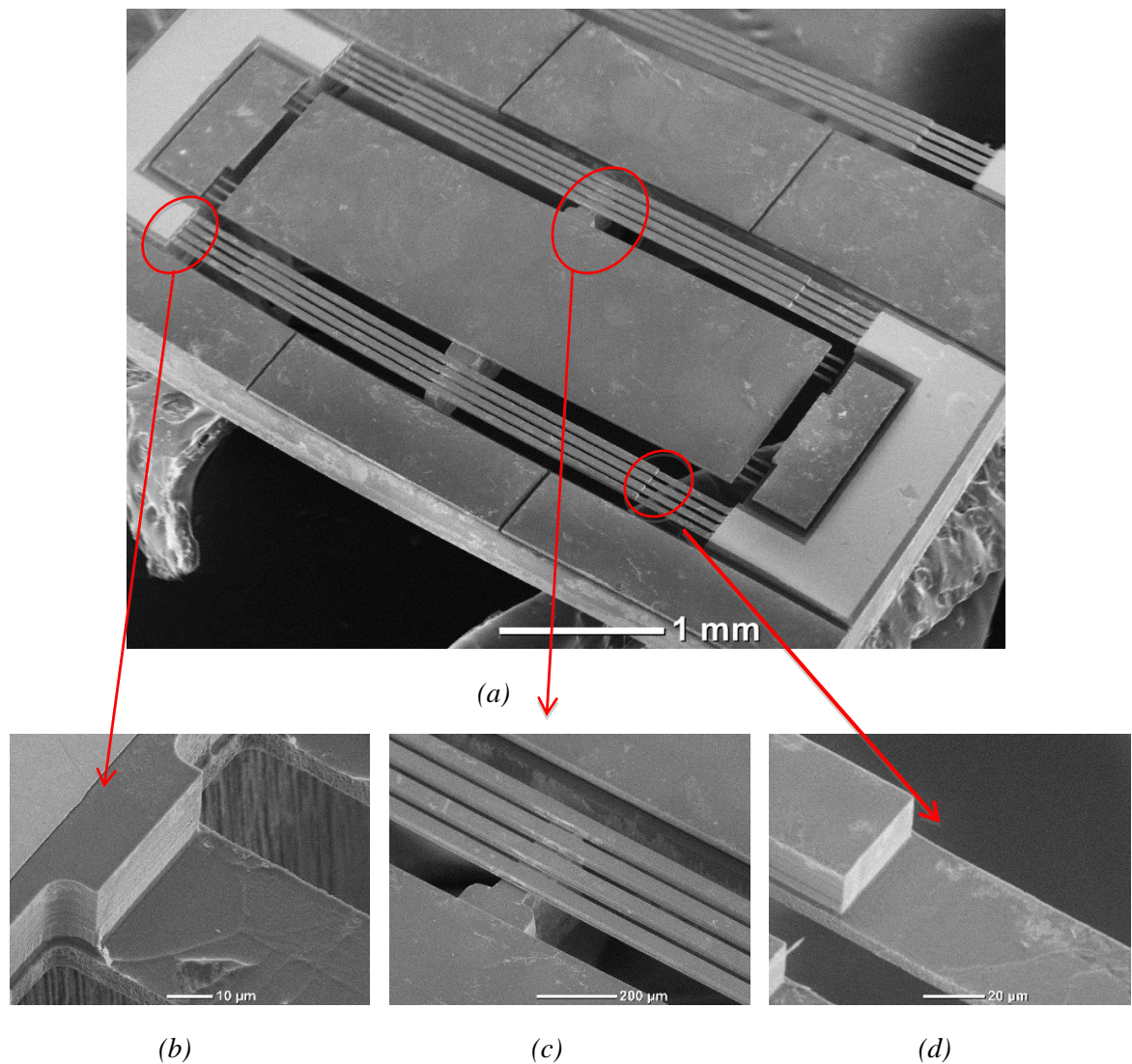


Figure 6.8: The scanning electron microscope (SEM) images of the Z-stage; (a) a full view; (b) the sidewall of the step near the metal pad; (c) a close-up view of the block connecting the actuator to the platform; (d) the sidewall of the step near the beam

Based on the fabrication flow described in Fig. 6.7, the presented stage has been successfully fabricated and its captured images from a scanning electron microscope (SEM) are shown in Figs. 6.8. Figure 6.8(a) is the full view of the proposed motion stage where two 'C'-shaped bright areas stand for metal pads for electrical connection and the grey areas represent the motion stage made of silicon. For reliable fabrication, the moving platform has three holding fingers at each corner that connect the moving platform to the fixed boundary frame during the fabrication and will be released after the fabrication process described in Fig. 6.7(f). Close-up views for the step feature near the metal pad and the beam are shown in Fig. 6.8(b) and 6.8(d), respectively. First and second independent DRIE etching described in Fig. 6.7(c) and 6.7(d) creates the step features without damaging other features. The connecting block underneath the actuator and the motion platform is shown in Fig. 6.8(c). This blocking delivers the out-of-plane motion from the actuators to the motion platform and electrically isolates the moving platform from the actuators.

6.6 Experimental results

In order to assess the static performance of the motion stage, a fringe-counting type optical profiler (VEECO WYKO NT1100 [137]) has been used as an out-of-plane displacement sensor. The optical profiler scans a target area and a reference area to generate its depth information and measures the relative position between them to obtain displacement data. This measurement has less than 1 μm error but its measurable range is up to 1 mm which is necessary in this case. The stage is electrically connected to a DC power supply unit (Agilent model 3322A) for its static performance test. Figure 6.9 shows the measured out-of-plane displacement of the moving platform as a function of

the input DC current ranging from 0 mA to 250 mA. This curve is also compared with the secant curve from equation (1) showing a similar trend. For a current from 40 mA to 220 mA, output displacement increases with the constant rate of $0.4 \mu\text{m} / \text{mA}$. At 220 mA, the stage generates $85 \mu\text{m}$ of out-of-plane displacement and a current of 245 mA produces a motion up to $95 \mu\text{m}$, but the rate of movement gets smaller after 220 mA. Thus, operation up to $85 \mu\text{m}$ can be considered stable without any mechanical or thermal failure. During this experiment, the driving voltage goes up to 7 V, which indicates the electric power has been used up to 1.2 W for $85 \mu\text{m}$ displacement.

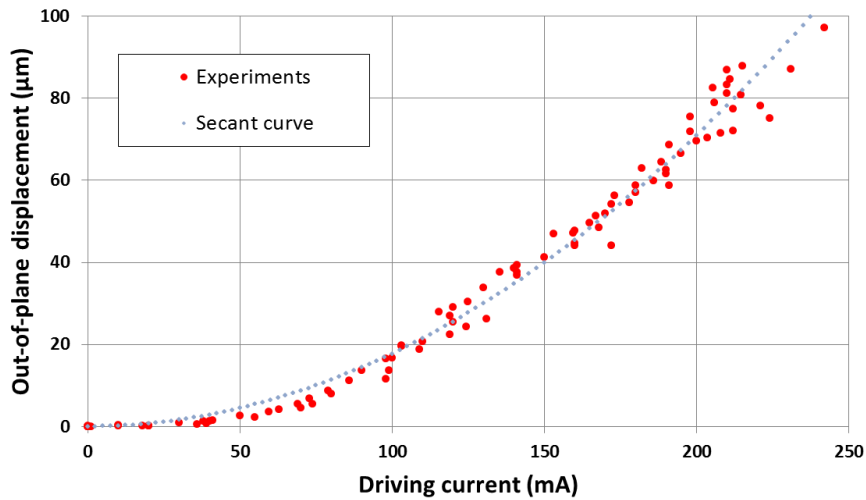
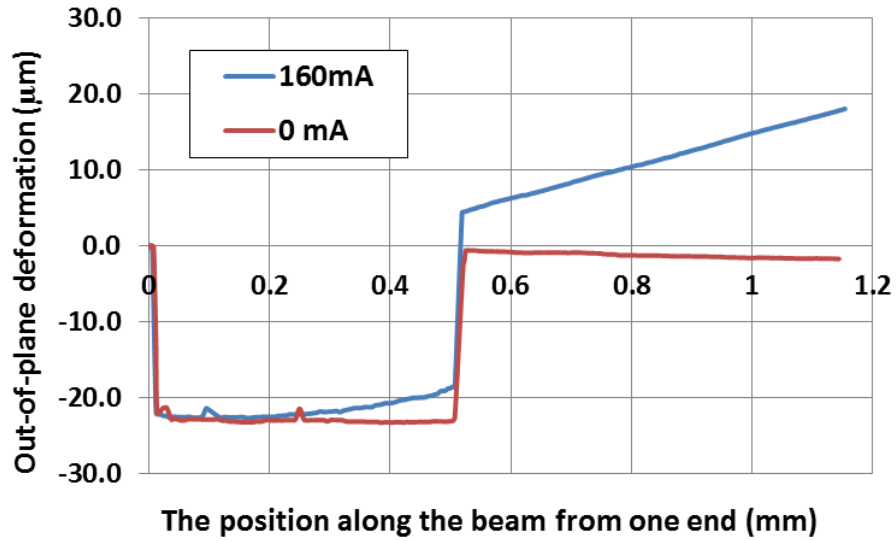
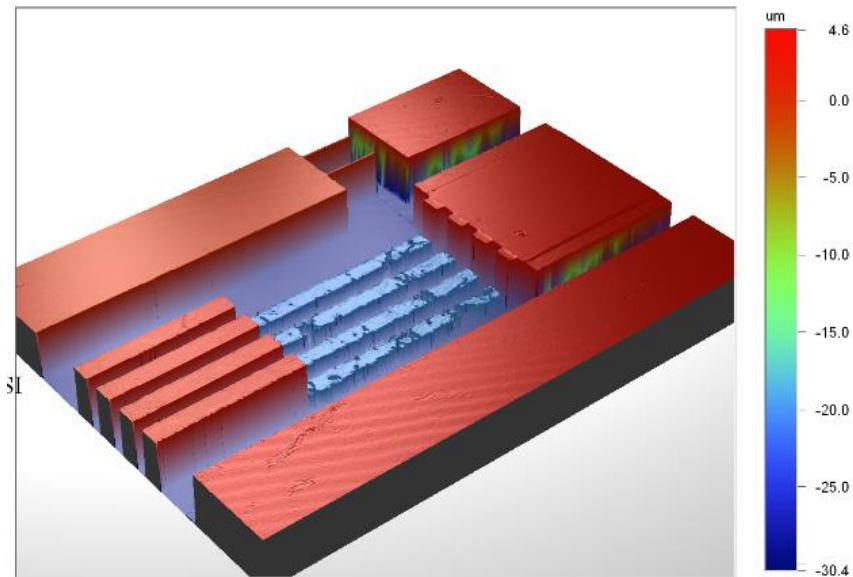


Figure 6.9: Experimentally measured displacement results with analytic ones

The stiffness of the motion stage was measured using a contact profilometer (Veeco Dektak 6M [160]) varying the pushing force from 1 mg to 10 mg that yields the value of 138.8 N/m , which is slightly larger than the value estimated from FEA. From the stiffness and the motion range, the actual force generated from the electrothermal actuator is calculated to be 11.80 mN .



(a)

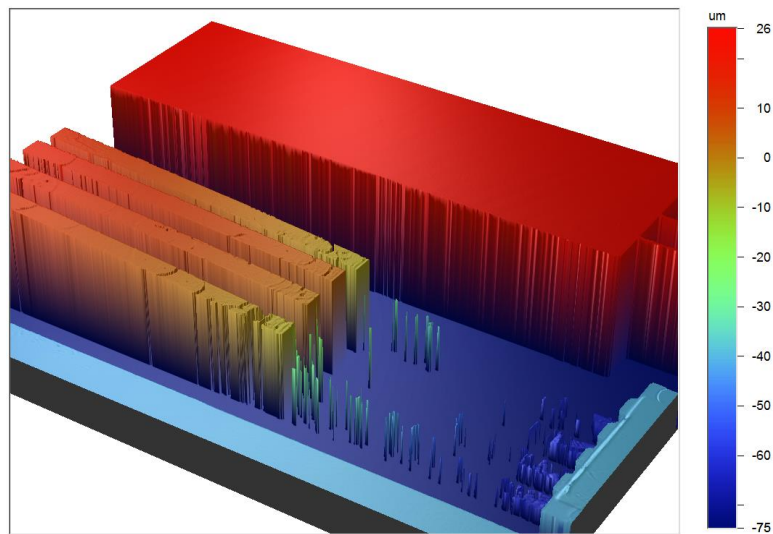


(b)

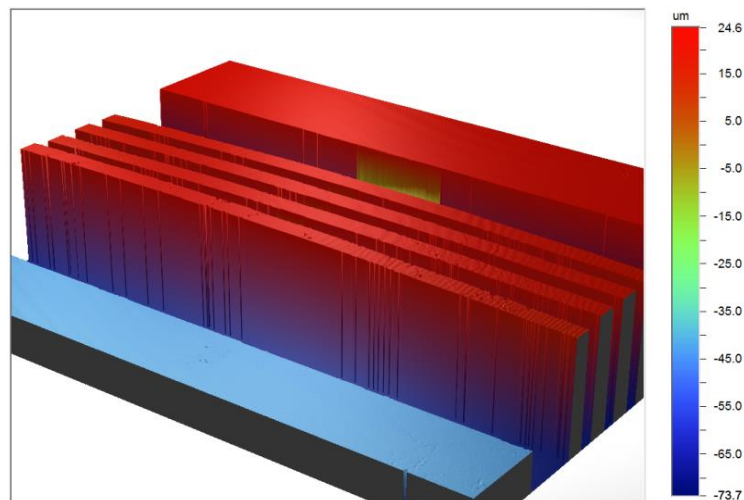
Figure 6.10: Measured deformation profiles in the actuation; (a) Two measured deformation profiles of the step with 0 mA and 160 mA current; (b) a 3D scanned image of the step with 0 mA current

In order to look at the deformation behavior of the beam near its step feature during its operation, its deformation was experimentally scanned during displacement and compared with its original shape. In Fig. 6.10(a), the deformation profiles are plotted showing that the out-of-plane deformation is well distributed over the step feature. The

shape in 3D images is shown in Fig. 6.10(b) and 6.11(a). The deformation profile of the middle of the beam was also scanned in Fig. 6.11(b), showing a smooth concave curve. This concave shape matches up with the estimated shape from equation (6.1) and FEA. In addition, this shape is completely different from the profile under buckling [141] and indicates that the current beam is not under buckling but pure elastic bending.



(a)



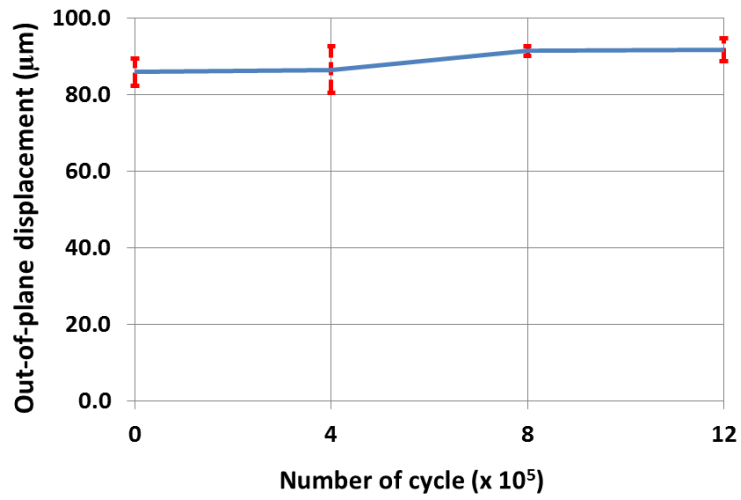
(b)

Figure 6.11: Measured deformation profiles in the actuation; (a) a 3D scanned image of the step with 200 mA current; (b) a 3D scanned images of the beam at its center with 200 mA current

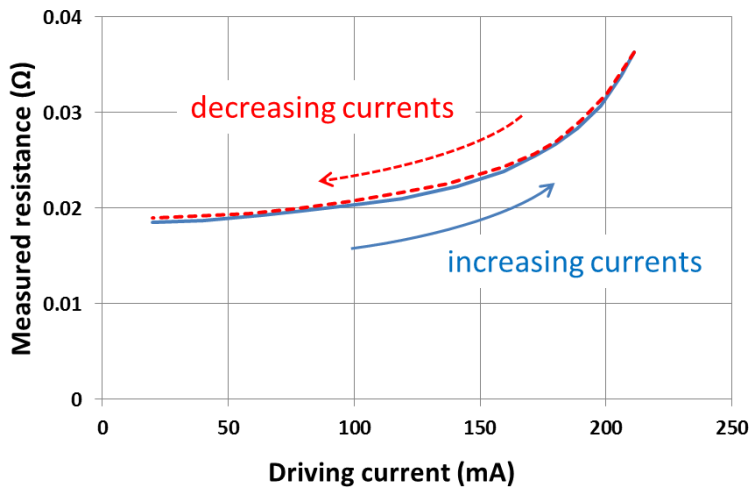
The dynamic frequency response of the presented motion stage has been measured with a Polytec Micro System Analyzer (MSA-500) [161], which has been mainly used for atomic force microscope (AFM) applications. From the measurement, the resonant frequencies of the first three modes are measured and found to be 4.41 kHz, 8.00 kHz and 9.72 kHz, respectively. Each peak has a magnitude high enough to identify the difference and the first three modes have 1 % to 6 % differences from the estimated FEA values which are very close to its FEA considering variations and deformations during MEMS fabrication.

The repeatability of the presented system is also quantitatively measured; the stage has been operated more than 1 billion cycles at its natural frequency. The displacements after every 400k cycles have been measured with three fabricated devices and their results are shown in Fig. 6.12(a). The stages generate 85 μm to 90 μm displacements by 220 mA currents and have demonstrated similar displacement after 4×10^5 , 8×10^5 , and 1.2×10^6 cycles.

The resistance of the actuator was monitored during all experiments and can be used as an indicator of the internal condition of the actuators. Figure 6.12(b) shows the resistance of the actuator as a function of a driving current where the blue solid line is for the stage by an increasing current and the red dotted line is by a decreasing current. This plot shows a slow increase of resistance with an increasing current and a return to its original value after testing. This trend is similar with the measured data [48] and no discontinuous increment has been observed implying no plastic deformation or internal changes occur during its operation.



(a)



(b)

Figure 6.12: Reliability test; (a) A repeatability test over 12x10⁵ cycles with (220 to 225) mA driving currents; (b) a resistance change as a function of driving currents

6.7 Discussion

The goal of this work is to develop a MEMS motion stage that generates out-of-plane motion and provides similar range to existing in-plane motion stages. For this purpose, stiffness larger than tens of N/m, a few milli-Newton level force, and a motion range of

close to 100 micrometers have been achieved. The similarity of their performance plays an important role in some applications such as collaboration between in-plane and out-of-plane stages or integration of out-of-plane actuation with in-plane actuation. Due to lack of versatility in MEMS fabrication, it is hard to find MEMS motion stages or manipulators having similar performance with conventional stages fabricated from precision machining are rare. In this situation, the collaboration among several individual MEMS devices can overcome it. As a first step for this purpose, an out-of-plane stage with equivalent performance to in-plane stages is required, because in-plane structures are considerably different from out-of-plane structures in MEMS fabrication approaches.

When comparing with other in-plane stages, the presented stage with the stiffness of 133 N/m has a similar level to the selected in-plane stage of 39.5 N/m [19,44]. The maximum range of motion is 85 μm , which is larger than 60 μm of the in-plane stage [27]. The expected maximum force of 13 mN is of a comparable level to that of the in-plane stage, which achieves 2 mN to 3 mN force. These properties depend mainly on the thick device fabricated through bulk micromachining technologies. This comparison is not meant to claim that the presented stage is better than the target in-plane stage. Rather, it focuses on the fact that the presented stage is designed to provide similar performance or characteristics to the existing in-plane stage, which is an advantage at integration with previous in-plane stages for future collaboration work. Due to this reason, its fabrication method is also limited to the same method as the in-plane stage for easy implementation.

Although the presented motion stage meets the required specifications, there are a few design modifications to increase its usability. As mentioned in the analytic analysis section, the relative position of the step determines the direction of out-of-plane motion.

Current design has two step features near the beam ends and generates upward motion. Alternatively, the step feature could be placed in the middle of the beam and therefore generate downward out-of-plane motion. Additionally, the combination of the downward out-of-plane actuator and the upward motion actuator presented in this paper can generate rotational motion of the platform.

6.8 Summary

In this chapter, a thermally actuated upward out-of-plane motion stage has been presented with similar mechanical characteristics with in-plane motion stages, especially in terms of motion range, stiffness, and maximum force capability. In addition to these features, the fabrication methods for the presented Z-stage are based on electrothermal actuation type and bulk micromachining technologies. This feature is also compatible with that for in-plane motion stages described in Chapter 4 and Chapter 5. For this purpose, the newly designed Z-stage utilizes a step feature of the beam for its eccentric load for out-of-plane motions, which can minimize additional fabrication process for the compatibility with the XY-stage in Chapter 5. The fabricated motion stage has demonstrated an 85 μm range of motion and a maximum force capability of 11.8 mN. The measured properties were found to be in similar ranges to existing in-plane motion stages [27,44]. These results demonstrate that the presented out-of-plane electrothermal motion stage based on the step feature has potential in extending its role in various applications through collaboration or integration with in-plane stages for a coordinated manipulation or higher degrees-of-freedom (DOF) motion stages.

Chapter 7 MEMS-based 3-DOFs motion stage

This chapter⁴ presents a newly designed three degrees-of-freedom (DOF) translational motion stage composed of two DOF in-plane motion and one DOF out-of-plane motion (called an XYZ-stage). This XYZ-stage is also based on micro-electro-mechanical systems (MEMS) and implemented by integrating three existing 1-DOF motion stages into one. By utilizing the motion stages previously developed, this approach can save some efforts and time rather developing a whole new system. Moreover, an appropriate selection on the candidates can ensure minimum reliability from previous experiences. For successful implementation, electrical connection to the engaged stages, electrical isolation among them, and structural floating frames are applied to the chosen 1-DOF motion stages during their integration. With these features, the presented XYZ-stage is successfully fabricated and demonstrates the range of motion of 53.98 μm , 49.15 μm , and 22.91 μm along X, Y, and Z axes, respectively. The coupled motion errors among the engaged stages is observed less than 1 μm with the presented compensation algorithm.

Keywords: MEMS, 3-axis, motion stage, nested structure, serial kinematic mechanism

7.1 Introduction

Micro-scale devices based on micro-electro-mechanical systems (MEMS) have various advantages, such as their small form factors, low cost from batch process, and nano-meter level resolution [6,15,97,162–164]. These strengths have made MEMS-based systems attractive in various applications, such as micro-assembly [15], manipulation [6], and metrology [97]. However, many MEMS fabrication methods can only realize planar designs and hence have limited operations. Multiple degrees-of-freedom (DOF) motion or a combination of in-plane motions and an out-of-plane motion are still difficult to

⁴ The work in this chapter is derived from the published work in [141, 142]

implement or require considerable efforts in their design process and fabrication process [6,162]. In contrast to MEMS motion stages, the commonly used approach for conventional meso-scale motion stages is stacking up multiple stages one by one [163,164]. In this case, existing designs or stages can be reused, which can not only save the total design process time, but also provide predictable reliability. However, this method is difficult to utilize with MEMS; manual stacking-up can damage MEMS devices during the assembly process or provide relatively poor alignment among the engaged stages. Moreover, the devices stacked on the others should be free to move and this is also challenging at their electric connections. Due to these reasons, it is rare to find motion stages utilizing a stacking-up approach in MEMS.

Many MEMS motion stages have been developed for 2 or 3 DOF motion, especially for the combination of in-plane translational and in-plane rotational motions [13,29,131], but MEMS stages for 3-axis motion or XYZ motion are not common [31,87,165]. The main reason for this is that the difference in design and fabrication between the out-of-plane motion (called a Z-motion) and the in-plane motions (called an X-motion or a Y-motion) is too large to combine them together. In order to overcome this issue, additional efforts and fabrication methods have been tried; the focused ion beam (FIB) milling for the out-of-plane slope [87], wafer bonding for parallel plate type electrostatic actuation [31], or silicon-on-insulator wafer (SOI) for a dual layer [165] were used for the Z-motions. With these approaches, researchers have achieved various ranges of motion as listed in Table 7.1. These results indicate that the resulting Z-motions are considerably smaller than X- or Y-motions and relatively high driving voltages are needed to realize them. This smaller Z-motion comes from the structural difference between in-plane

structures and out-of-plane structure in MEMS fabrication methods. The high driving voltages are not compatible with general electric circuits and attracting dust easily results in electrical shorting of circuits. Based on the limitations in MEMS 3-axis motion stages, it is beneficial to develop a 3-axis motion stage having larger displacements than existing designs with less effort and time in development.

Table 7.1: 3 DOF MEMS-based positioning stages

Reference	Range of motion						Features
	X-axis		Y-axis		Z-axis		
	Motion (μm)	Voltage (V)	Motion (μm)	Voltage (V)	Motion (μm)	Voltage (V)	
[87]	1.1	100	1.1	100	1.1	100	FIB milling
[31]	25	30	25	30	3.5	14.8	Wafer bonding
[165]	19	100	19	55	2.12	200	SOI wafer

7.2 Design of the 3-DOF motion stage

The presented XYZ-stage is designed to generate translational motions along the X, Y, and Z axes. For the 3-DOF translational motions, at least three independent single DOF actuators or actuating mechanisms are required. Since this study focuses on utilizing existing designs, appropriate in-plane and out-of-plane 1-DOF motion stages are selected from previous designs. The conceptual designs of the chosen systems are shown in Fig. 7.1; Fig. 7.1(a) for the X-stage, Fig. 7.1(b) for the Y-stage, and Fig. 7.1(c) for the Z-stage. The X- and Y- stages are composed of one bent-beam type electrothermal actuator, four links, and one motion platform [27,44,117]. Two of four flexure links for each of the X and Y axes stages are used as a lever for large stroke. The actuator actuates the levers which amplify the displacement of the motion platform. The fabrication of the X-stage

and the Y-stage is based on the Silicon-On-Insulator Multi-User Multi-Processes (SOI-MUMPs) for SOI wafers [39] and generates the force of more than 45 mN and the displacement of 50 μm [27]. The Z-stage is also chosen from existing designs [27,117] and generates 25 μm [166] to 80 μm [76] displacements depending on the designs reported in the papers.

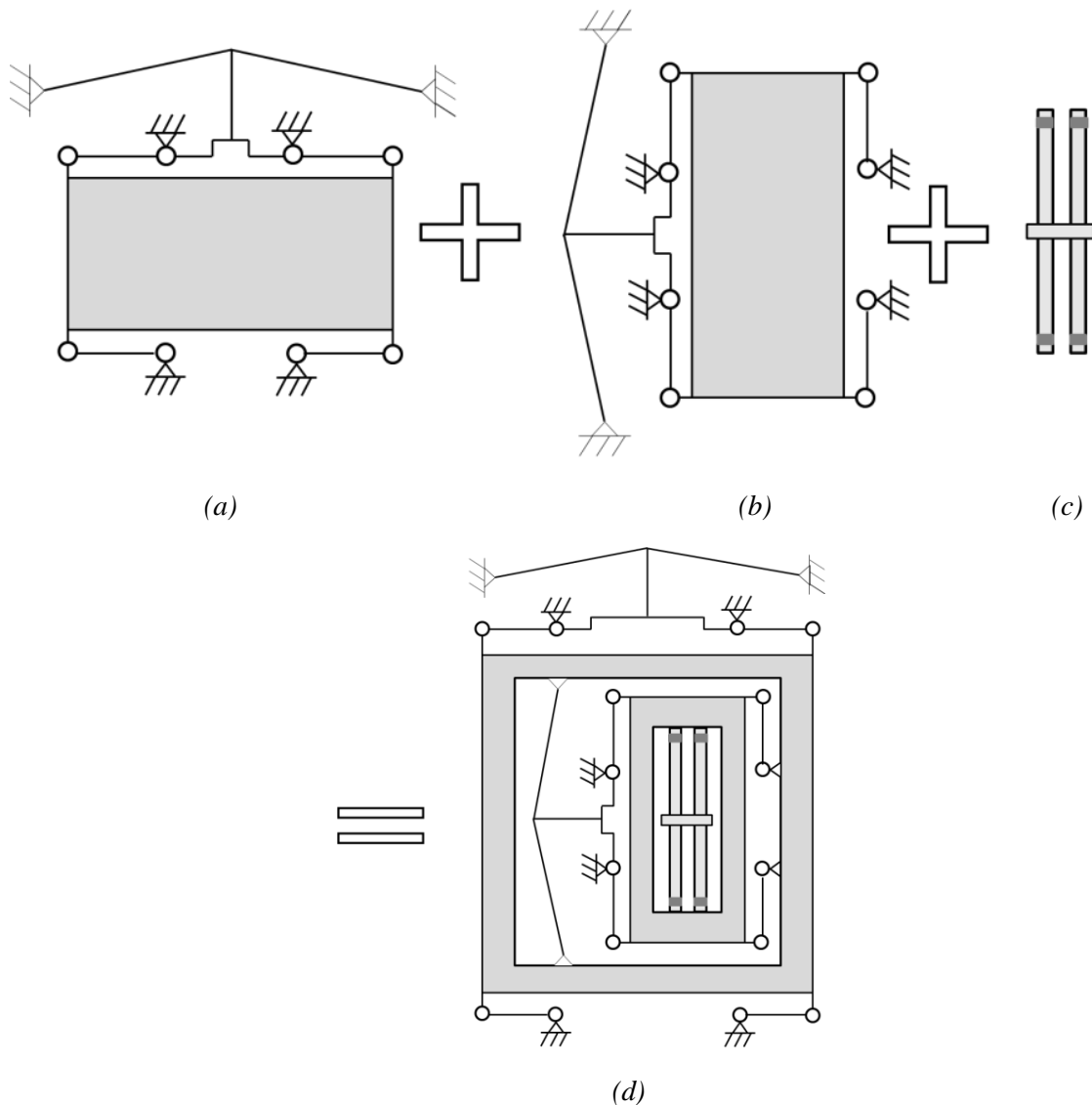


Figure 7.1: Integration strategy of three individual stages for the XYZ-stage; (a) the X-stage; (b) the Y-stage; (c) the Z-stage; (d) the integration of (a), (b) and (c) for the XYZ-stage

The integration strategy for the three independent stages described above is schematically shown in Fig 7.1 [167]. The motion platform of the X-stage is utilized to embed the Y-stage, which is also designed to contain the Z-stage as shown in Fig. 7.1(a), 7.1(b), and 7.1(c). The expected merged shape is shown in Fig. 7.1(d). This approach is called the nested structure, through which the XYZ-stage can be built. Both ends of the bent-beam type electrothermal actuators in the XYZ-stage should keep a same gap during their operations for efficient performance. To meet this requirement, a floating frame is introduced. This floating frame is attached to the bottom of the actuator and stiff enough to hold both ends of the actuator in their position firmly. This frame also should be free to move in order not to prevent any motion generated by the XYZ-stage. For this purpose, a dual layer approach is utilized through SOI wafers in this study; SOI wafers are bi- or triple-layer structures. If the XYZ-stage is built on the top layer of the SOI wafers and the floating frame is made of the bottom layer of the SOI wafers, then additional bonding process can be avoided, since the two layers are already attached to each other. The integration strategy for the three independent stages or actuator described above is schematically shown in Fig 7.1 [167]. The motion platform of the X-stage is utilized to embed the Y-stage, which is also designed to contain the Z-stage as shown in Fig. 7.1(a), 7.1(b) and 7.1(c). The expected merged shape is shown in Fig. 7.1(d). This approach is called the nested structure, through which the XYZ-stage can be built. Both ends of the bent-beam type electrothermal actuators in the XYZ-stage should keep a same gap during their operations for efficient performance. To meet this requirement, a floating frame is introduced. This floating frame is attached to the bottom of the actuator and stiff enough to hold both ends of the actuator in their position firmly. This frame also should be free to

move in order not to prevent any motion generated by the XYZ-stage. For this purpose, dual layer approach is utilized through SOI wafers in this study; SOI wafers are bi- or triple-layer structures. If the XYZ-stage is built on the top layer of the SOI wafers and the floating frame is made of the bottom layer of the SOI wafers, then additional bonding process can be avoided, since the two layers are already attached to each other.

The X-stage, the Z-stage, and additional features like the floating frames are explained in the following section separately. Since the Y-stage is identical to the X-stage, the X-stage only is discussed. These explanations include working principles, basic analysis, and Finite Elements Analysis (FEA) results. There is no modification or significant change made in the chosen X-stage [27] except the motion platform size and the floating frame; the motion platform is adjusted to embed the other device without any lack of space. The Z-stage is composed of one shaft and the actuator used for the Z-motion stage [166].

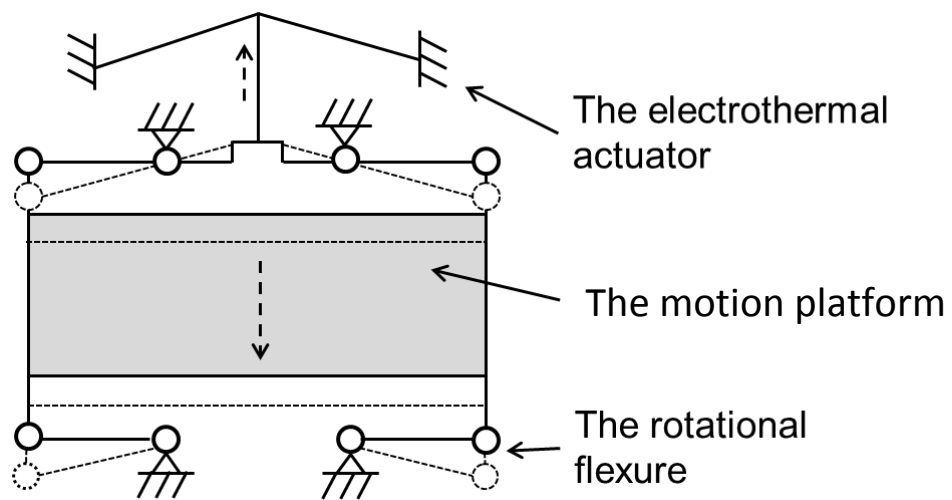


Figure 7.2: The schematic diagram of the X-stage

7.2.1 The X-stage and the Y-stage

The X-stage is composed of a bent-beam type electrothermal actuator, one motion platform, and four links [44]. The schematic diagram of the X-stage is shown in Fig. 7.2, where the arrows stand for the expected direction of motion, the circles represent rotational flexure hinges as compliant mechanisms, and the solid lines for rigid links. The four links support the four corners of the motion platform, so the motion platform can be fully constrained. The two of the four links work as a lever which transfers the displacement to the motion platform with the amplifying ratio of 1:10. Due to this lever, the motion direction of the motion platform is opposite to that of the actuator. The details about the X-stage are described in the previous study [117].

In the X-stage, the combination of the motion platform and the actuator can be interpreted as a combination of springs in a parallel connection. In this case, the expected displacement of the motion platform can be expressed [27] as:

$$U_{\text{plate}} = \frac{F_{\text{actuator}}}{K_{\text{actuator}} + K_{\text{plat}}} \quad (7.1)$$

where the subscript ‘plat’ indicates the motion platform and the subscript ‘actuator’ means the electrothermal actuator. The term ‘U’ stands for displacement, ‘F’ for force, and ‘K’ for stiffness. Each term in equation (7.1) can be expanded as:

$$F_{\text{actuator}} = 2\alpha b\Delta T_{\text{ave}}EWT\sin\theta \quad [27] \quad (7.2)$$

$$K_{\text{actuator}} = 2\left(\sin^2\theta + \cos^2\theta \frac{12I}{WTL^2}\right)\frac{EWT}{L} \quad [53] \quad (7.3)$$

$$K_{\text{plat}} = \frac{n^2m}{L_1^2C_z} \quad [139] \quad (7.4)$$

where, C_z is the compliance of the rotational flexure hinge, n is a lever ratio, and m is the number of the links. The details and dimensions for other terms are explained in Table 7.2.

Table 7.2: Design parameters in the X-stage, the Y-stage and the Z-stage

Symbol	Design parameter	Values
W	beam width	23 μm
θ	beam angle	3 degrees
L	beam length	1000 μm
L_l	link length	1000 μm
T	beam thickness	30 μm
b	Number of beams	15
α	Coefficient of thermal expansion	2×10^{-6}
C_z	The compliance of the rotational flexure hinges	$7.52 \text{ Nm } \mu\text{rad}^{-1}$
E	Young's modulus of silicon	169 GPa
k	Thermal conductivity	50 μm
m	Lever ratio	10
I	Area moment of inertia	-
ρ	Resistivity of silicon	$2 \times 10^{-3} \Omega \text{ cm}$
ΔT_{ave}	Actuator average temperature	-
ΔT_{max}	Actuator maximum temperature	< 530 $^{\circ}\text{C}$
U_{plate}	Platform displacement	45 - 60 μm
V	Driving voltage	1 – 8.5 V
e	The notch depth for the Z-stage	7.5 μm
L_z	Beam length for the Z-stage	1000 μm
P, P'	Eccentric load in the Z-stage	-
L_w	Beam width for the Z-stage	33 μm

The temperature rise ΔT_{ave} is the average temperature rise from the room temperature of 20 °C and ΔT_{max} is the maximum temperature rise in the actuator. In this case, temperature rise can be expressed based on the material properties of silicon [52] as:

$$\Delta T_{\text{ave}} = \frac{V^2}{3k\rho} = \frac{2}{3}\Delta T_{\text{max}} \quad (7.5)$$

Where, V is a voltage applied to the actuator, k is the thermal conductivity of silicon, and ρ is the resistivity of silicon. Their material properties are cited from the previous research [27]. Based on equations (7.2) - (7.5), equation (7.1) can be written as:

$$U_{\text{plate}} = \frac{2\alpha bEWT\sin\theta}{\left(\sin^2\theta + \cos^2\theta \frac{12I}{WTL^2}\right) \frac{EWT}{L} + \frac{n^2m}{L_1^2 C_z}} \Delta T_{\text{ave}} \quad (7.6)$$

where each design parameter is described with its dimension in Table 7.2. From equation (7.6), the output displacement of the motion platform is expected to be a linear function of the average temperature rise in the actuator. With equation (7.5), equation (7.6) can be expressed as:

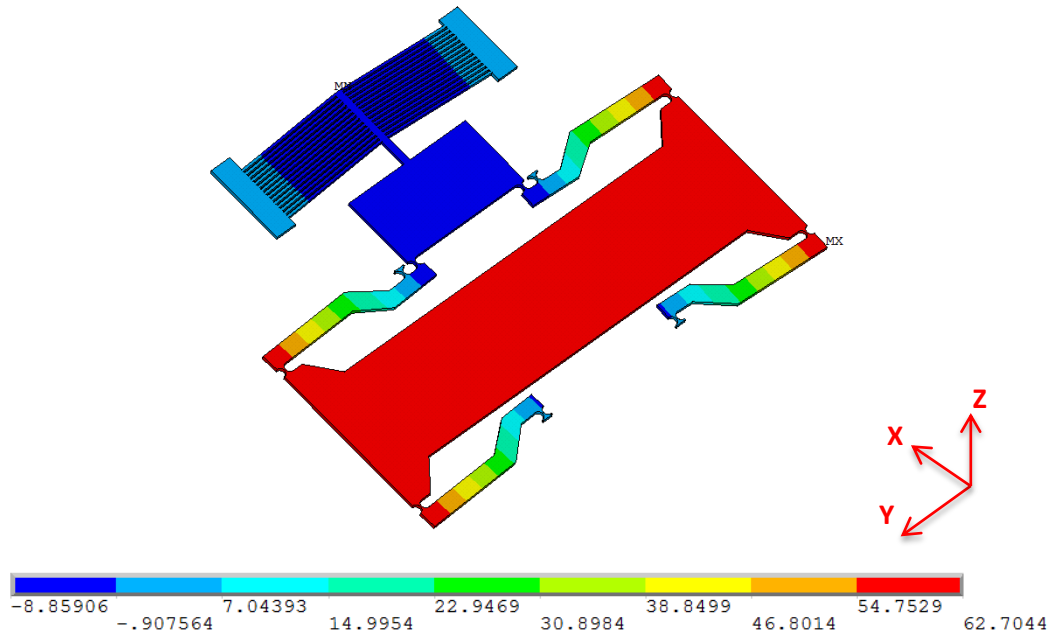
$$U_{\text{plate}} = \frac{2\alpha bEWT\sin\theta}{3k\rho \left(\sin^2\theta + \cos^2\theta \frac{12I}{WTL^2}\right) \frac{EWT}{L} + \frac{n^2m}{L_1^2 C_z}} V^2 \quad (7.7)$$

Equation (7.7) shows that the displacement of the motion platform is also proportional to the square of the driving voltages, which is similar to the findings of previous electrothermal actuator studies [50,53]. This property can be utilized to reduce the coupled motion errors in the experimental section to control the motion platform precisely.

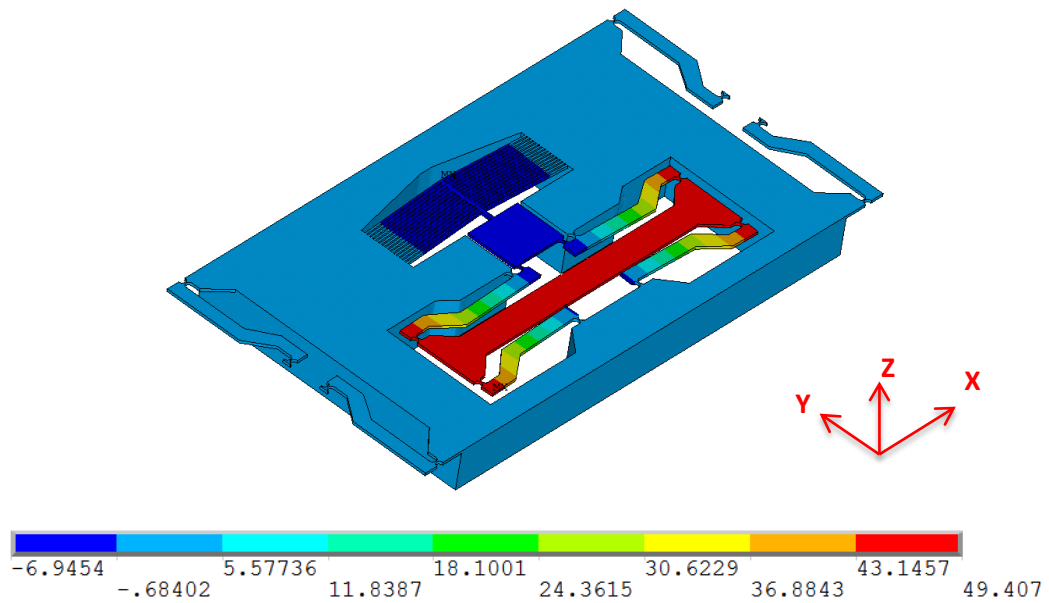
The maximum displacement of the motion platform is determined by a structural failure or a maximum reliable temperature of silicon. Since the structural limit is well described in the previous research [27], the temperature limit only is discussed in this paper. Above the temperature limit, plastic deformation initiates in silicon. Various temperatures have been reported for this limit; 550 °C [61], 600 °C [89], or 900 °C [134]. The lowest value among them is selected as the maximum temperature limit in this study for a reliable operation. The room temperature is measured as approximately 20 °C and the maximum temperature change, ΔT_{\max} is set to be 530 °C.

Based on the above temperature limit, the design parameters listed in Table 6.2 and the material properties of silicon [27], the mechanical behavior of the X-stage is calculated in FEA. For this FEA, the ends of the rotational flexure hinges and the bottom side of the motion platform are assumed to connect to a heat sink at room temperature for its thermal boundary condition. The maximum allowable temperature of 550 °C is applied to the actuator as an external thermal excitation to calculate its displacement. The corresponding mechanical behavior of the X-stage is shown in Fig. 6.3(a) generating the displacement of 62.7 μm larger than the maximum displacement of the X-stage. When the X-stage is stable under this large displacement, the stage will be reliable within its maximum displacement. The calculated stress, in particular von Mises stress, is close to zero in most of the area of the stage except for the rotational flexure hinges, which have a stress of 1.47 GPa. This stress distribution pattern indicates that most deformation occurs in the rotational flexure hinges and plastic deformation is hardly expected with the yield strength of 6 to 7 GPa. This result fits well with the response of the X-stage, though not

the Y-stage, because the Y-stage is located inside the motion platform of the X-stage and has different thermal and structural boundary conditions.



(a)



(b)

Figure 7.3: Mechanical response by the temperature rise of 530 °C in finite element analysis: (a) the X-stage with a displacement of 62.7 μm (unit in μm); (b) the Y-stage with a displacement of 49.4 μm (unit in μm)

The expected mechanical behavior of the Y-stage is shown in Fig. 7.3(b). This FEA is also based on the same test condition applied to the X-stage. The calculated maximum displacement of the Y-stage is 49.1 μm , which is smaller than the X-stage. This FEA shows that this difference comes from the structural boundary conditions; the bent-beam type electrothermal actuator and the pivots in the lever require firmly fixed anchors at its ends for efficient operation. However, the Y-stage is supported by the floating frames to avoid any interference with the motion of the X-stage. This floating frame is the thick block underneath the Y-stage, which is not a perfect rigid body and not capable of holding the pivots in their position without any minor deformation. In this case, some amount of force generated by the electrothermal actuator will be used to deform the floating frame. Thus this difference results in a shorter stroke than the X-stage as simulated using FEA.

7.2.2 The Z-stage

The Z-stage is selected from out-of-plane electrothermal actuators [76,166], which is made up of four flat beams and one shaft rod. Each beam consists of one flat beam and two notches as shown in Fig. 7.4(a). The two notches are located near both ends of the beam and lead to a pop-up motion in the Z-stage. When the electric current flows through the beam, Joule heating causes thermal expansion of the beams. This thermal expansion can be regarded as a repulsive force P from both its ends as indicated in Fig. 7.4(b). Due to the notches, this repulsive force P generates an eccentric load. This eccentric load P can be expressed as a combination of a beam center line load P and a bending moment M whose converted free-body diagram is shown in Fig. 7.4(c). This diagram indicates that

the eccentric load bending moment can be utilized to generate the out-of-plane motion of the beam.

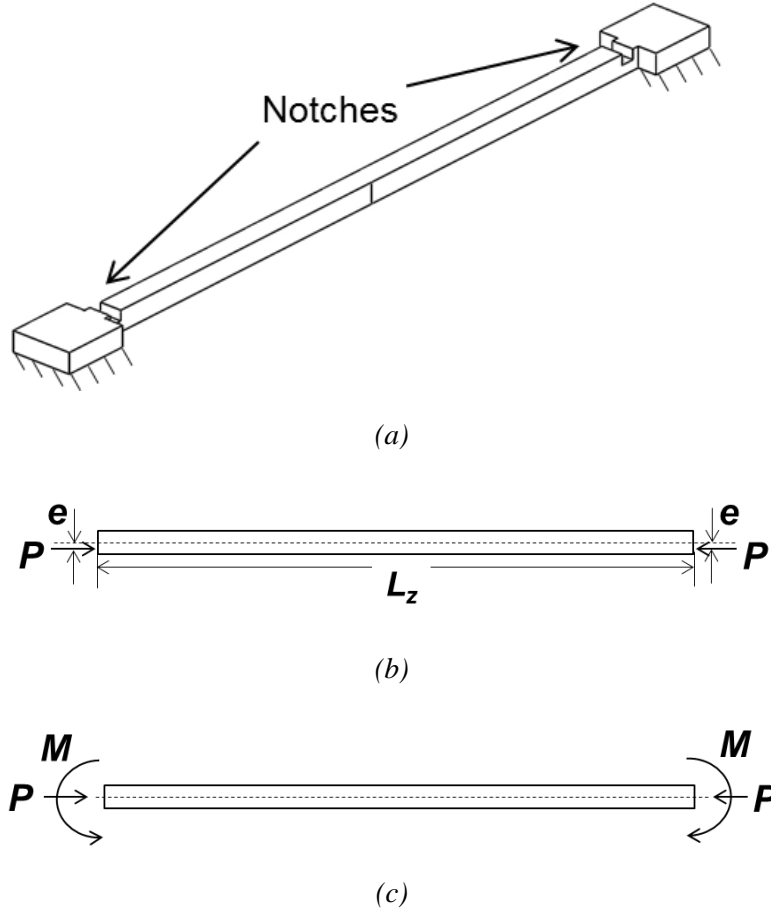


Figure 7.4: The design of the Z-actuator from the Z-stage; (a) the side view; (b) a free-body diagram of (a); (c) the converted free-body diagram of (b) (L_z : beam length, P : repulsive force, M : a bending moment, e : eccentric distance from the central line)

In this case, the deformation profile at pre-buckling mode or pure thermal expansion mode can be expressed [168] based on a fixed-fixed boundary condition as:

$$y = e \left[\tan \left(L_z \sqrt{\frac{P}{EI}} \right) \sin \left(\sqrt{\frac{P}{EI}} x \right) + \cos \left(\sqrt{\frac{P}{EI}} x \right) - 1 \right] \quad (7.8)$$

where, I is the area moment of inertia of the beam and the other terms are listed in Table 7.1. This thermal expansion by the bending moment M generates smaller stroke than the X-stage and this result makes the expected workspace look like a thin pizza box. Many commercially available XYZ-stages have tried to provide a workspace close to a cubic-shape for more convenience [2]. In order to generate more practical workspace in MEMS, the range of motion of the Z-stage needs to be close to that of the X-stage. For this purpose, the chosen Z-stage utilizes a buckling effect [76]. The buckling is also called a wrinkling and commonly occurs in thin plate or long slender beams [168,169]. Since the two notches already determine the deformation direction, this buckling accelerates this deformation without changing its direction.

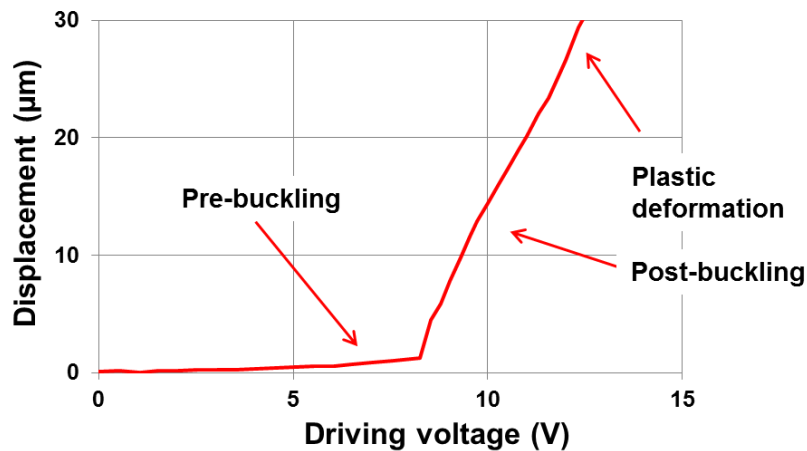
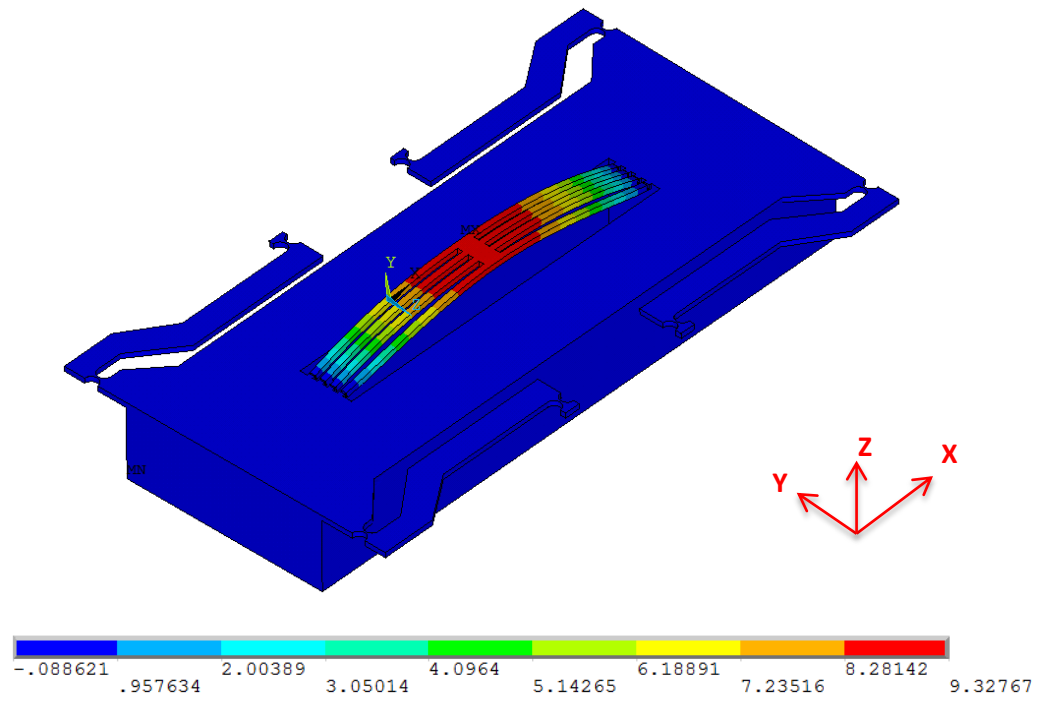


Figure 7.5: Experimentally measured out-of-plane displacement of the Z-actuator

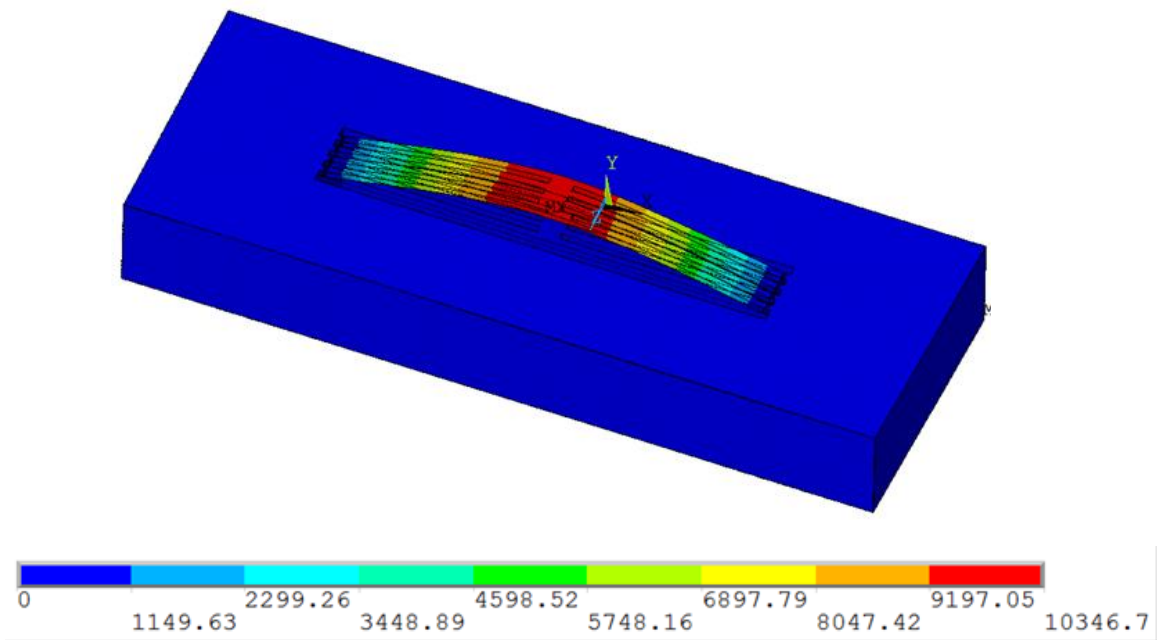
The mechanical behavior of the Z-stage is composed of three different modes; the pre-buckling, the post-buckling and the plastic deformation mode. The pre-buckling mode is the bending moment by pure thermal expansion of the beams at early stage. The thermal expansion of the beam is the main thrust to generate a few micro meter motions with low voltages. Above the critical voltage, the beam starts buckling and the post-

buckling mode begins. In this mode, the out-of-plane displacement accelerates rapidly. This mode will be used in the XYZ-stage to generate large displacement. Above the post-buckling mode, the plastic deformation mode starts which damages the beams. The deformed beams are not able to come back to their original positions and shows different mechanical behaviors, so these beams cannot be utilized again. In order to prevent this plastic damage, the available driving voltage range should be carefully chosen within its elastic range.

The FEA is utilized to better understand the mechanical behavior of the Z-stage. Figure 7.6(a) shows the expected structural response to the external excitation for the temperature of 550 °C in the actuator for pre-buckling mode. This result shows that the notches guide the Z-stage well to generate a popping up motion. The motion platform of the Y-stage does not show any structural deformation indicating that the floating frame in the motion platform performs its duty well. For stress distribution analysis an external excitation is applied to the actuator to generate an out-of-plane motion of 30 μm . For this displacement the von Mises stress distribution over the Z-stage is calculated. This value is less than 1.5 GPa and its maximum occurs inside the notches. The expected maximum displacement of the Z-stage is less than 25.1 μm , so this stress distribution implies that no structural failure is expected in the Z-stage with the displacement of 22.91 μm . Figure 7.6(b) also shows the mode shape of the Z-actuator at its first resonant frequency. Its expected resonant frequency will be 75.8 kHz and an out-of-plane deformation is expected. This mode shape shows that there is no structural issue in the Z-actuator related to the motion near its first resonant frequency.



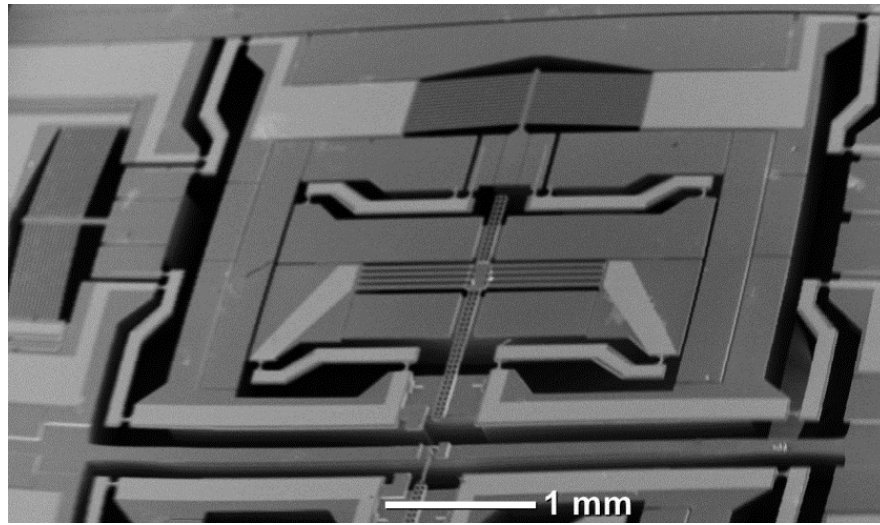
(a)



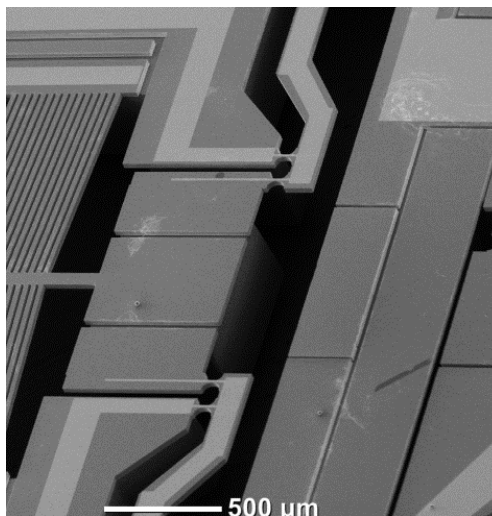
(b)

Figure 7.6: The mechanical response of the Z-actuator: (a) the mechanical response by the temperature rise of 530 °C as an external excitation, (b) the expected mode shape at its first resonant frequency

7.3 Fabrication



(a)



(b)

Figure 7.7: SEM images of the fabricated full XYZ-stage; (a) the frontal view of the XYZ-stage; (b) the close-up view of the lever and the actuator in the X-stage

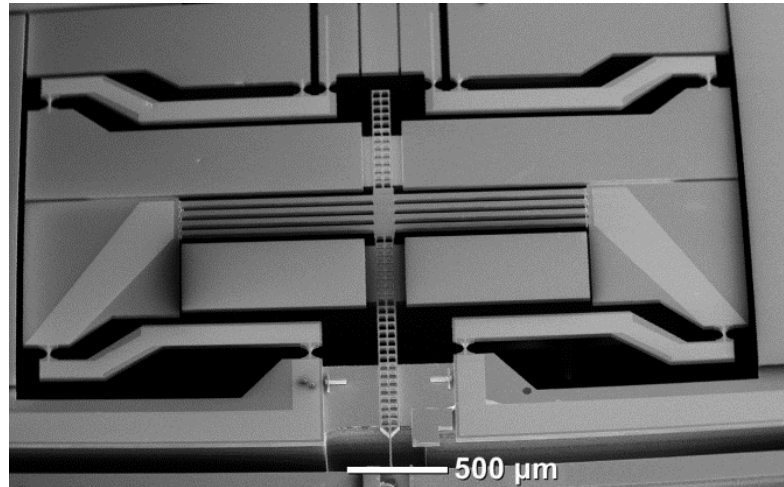
The main fabrication process of the presented XYZ-stage follows the Silicon-On-Insulator Multi-User Multi-Processes (SOIMUMPs) [39] and uses SOI wafers as a starting material. One more partial etching step was added to the SOIMUMPs for the fabrication of the notches in the Z-stage. The SOI wafer selected for the XYZ-stage is

composed of a 30 μm thick device layer, a 400 μm thick handle layer and a 2 μm thick buried oxide layer. The main processes consist of one metal deposition step and three etching steps. The first step is the metal deposition of four layers for electrical connections; 100 nm of chrome, 2 μm of Copper, 100 nm of Titanium and 0.2 μm of gold. This metal deposition is relatively thicker than conventional metallization for reliable electric connection, since the Z-stage and the Y-stage have longer electrical paths in the nested structure. The second step is to build the main device shown in Fig. 6.7(a) onto the device layer through Deep Reactive Ion Etching (DRIE). The third step is to etch the notches in the Z-stage by partial DRIE. The fourth step is to etch the additional structures in the handle layer indicated by A, B, C and D in Fig. 6.7(d). After a series of three etchings, the buried oxide layer is removed to release the Y-stage and the Z-stage. Details for each step are explained in SOIMUMPs [39] and the cited studies [27,44,76,117,166,167].

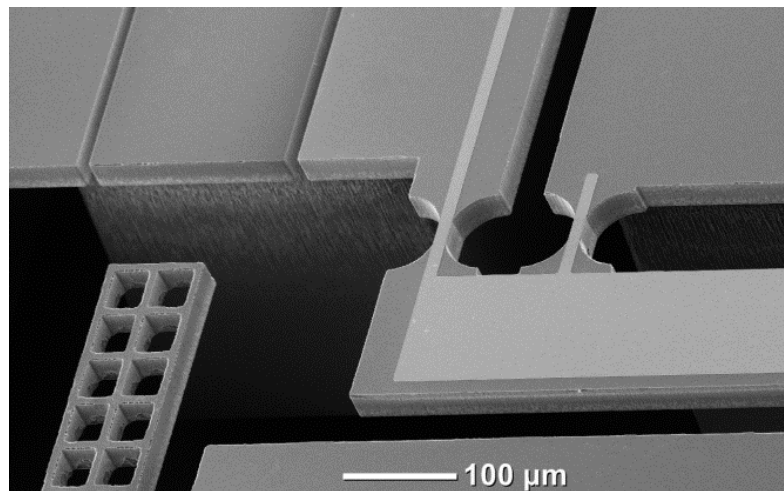
Based on the fabrication processes described above, the XYZ-stage can be successfully implemented. The frontal views of the fabricated main devices are shown in Fig. 7.7(a). This image was taken inside a scanning electron microscope (SEM). In Fig. 7.7(a), the bright white color indicates the metal layer and the gray area silicon. In the middle of Fig. 7.7(a) is the Z-stage. The actuator in the X-stage is Fig. 7.7(b) where its connection to the lever. The trenches between the actuator and the motion platform are designed to isolate the motion platform from the actuator electrically.

A closed-up view of the Z-stage is shown in Fig. 7.8(a) where a probe is embedded on the middle of the Z-stage for future applications such as micro-manipulation. Detail view of the electric connection over the rotational flexure hinge is also shown in Fig.

7.8(b). As shown in Fig. 7.8(a), the Z-stage is surrounded by the Y-stage, which is also surrounded by the X-stage. These images show the cascaded pattern in the nested structure clearly.



(a)



(b)

Figure 7.8: SEM images of the fabricated XYZ-stage; (a) a close-up view of the Z-stage and the motion platform of the Y-stage; (b) a deposited electrical connectivity wire paths over the flexure link (left) and the rotational flexure hinge (right)

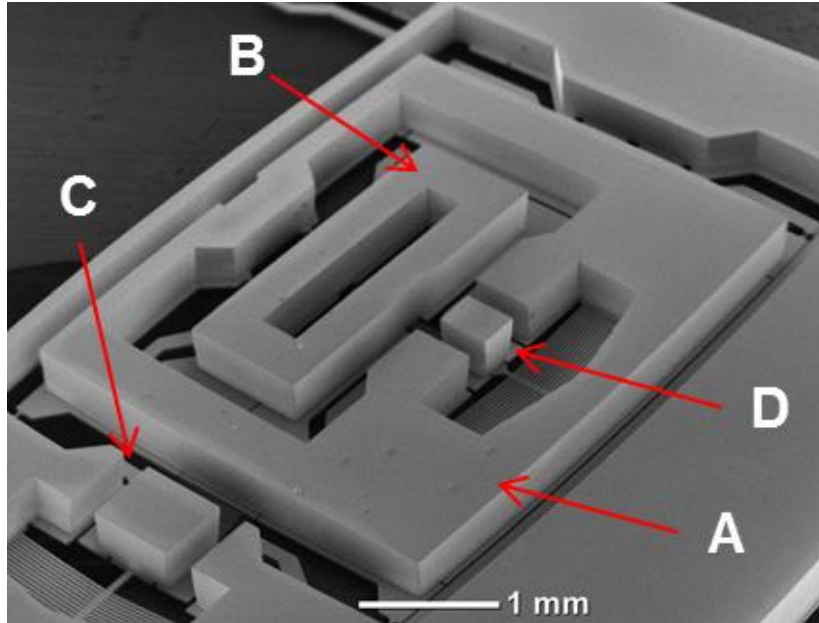
For successful implementation of the nested structure, three features are added; the floating frames, the remote electric access and electrical isolation among the X, Y, Z

stages in the system. The electrothermal actuators used in the Y-stage and the Z-stage need anchors for their proper operation, which is implemented through the floating frames. These floating frames are built on the device layer or the bottom layer of a SOI wafer as indicated by A and B in Fig. 6.9(a). The floating frame A holds the Y-stage in its position and supports both ends of the actuator in the Y-stage and the floating frame B supports the Z-stage for proper operation. Both frames are free to move along the X- or Y-axes to avoid any interference with the X- or Y-stages. These floating supporting blocks are made of the handle layer in the SOI wafer, which skips additional process like wafer bonding or multi-layer deposition and saves the total process time.

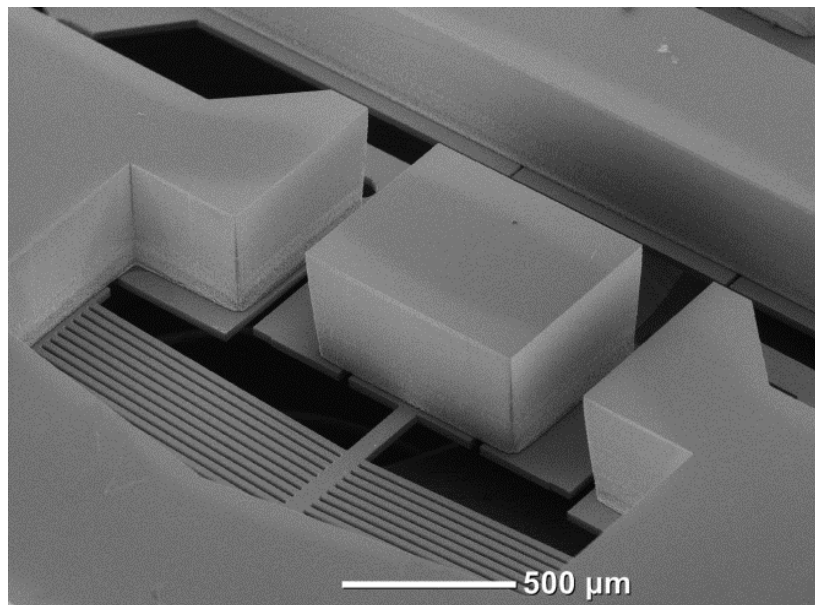
Remote electrical access to the Y-stage and the Z-stage are also important; direct connection by a conventional wire-bonding machine utilizes a few mg level forces to bond the wires on the metal pads. This amount of force can damage the Y-stage or the Z-stage which are free to move. In addition to this problem, the stiffness or the shape of the wire itself can distort the motion of the target stages [170]. In order to overcome these constraints, the embedded electric connection needs to connect the Y-stage and the Z-stage to the external electrical power source. These electric paths are deposited on the device layer during the fabrication and shown in Fig. 7.7(a), Fig. 7.7(b), Fig. 7.9(a) and Fig. 7.9(b). This electric path is also connected over the flexure hinge as shown in Fig. 7.8(b).

The electrical isolation among the stages is also necessary to reduce the coupled motion error from any electrical current leaks among the stages. For this electric isolation, the trenches surround the electrothermal actuator shown in Fig. 7.8(a) or Fig. 7.8(b). These trenches are physical gaps on the device layer and cause the electric current to flow

into the designated actuator only. The floating blocks C and D hold the trenches in the X-stage and the Y-stage, respectively.



(a)



(b)

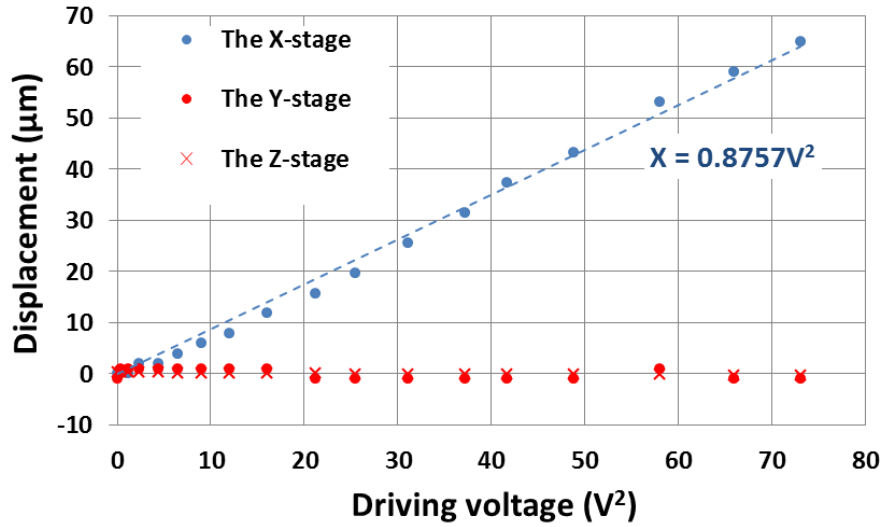
Figure 7.9: SEM images of the backside of the fabricated XYZ-stage; (a) the floating frames and floating blocks in the backside of the XYZ-stage; (b) the closed-up view of the floating block C

7.4 Experimental characterization of the MEMS 3 axis-stage

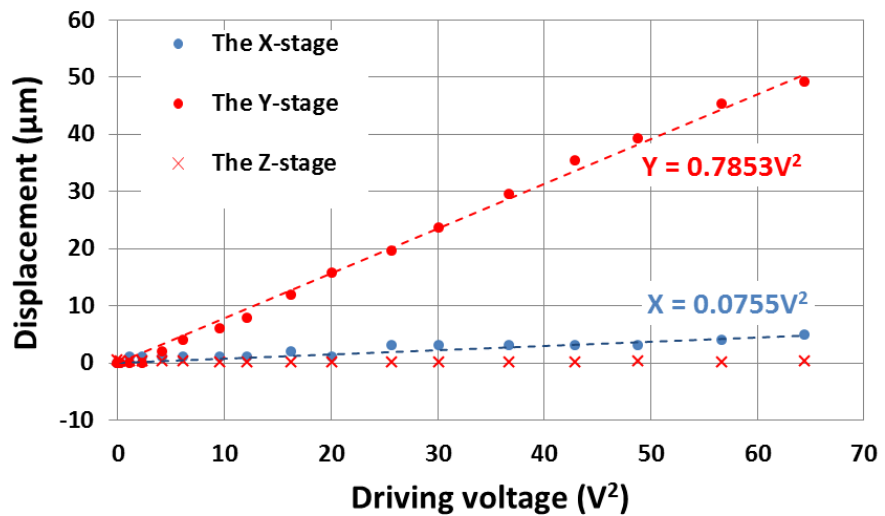
7.4.1 The range of motion

The maximum range of motion of the fabricated XYZ-stage is experimentally measured. When the operator controls the power supplies, the corresponding behaviors from the XYZ-stage are measured with an optical profiler (VEECO NT1100 [137]). The optical profiler is adjusted to have the in-plane resolution of 1 μm and the vertical resolution of 0.1 μm , which are minimum available resolution in this paper. The XYZ-stage is designed for large displacement and decoupled motions. When the control to the X-stage generates certain predictable pattern in the Y-stage after enough repetition, this can be regarded as a coupled motion error. Various factors such as fabrication defects, asymmetric design or thermal energy leaks can impact on this coupled motion error.

Three experiments were performed to measure the displacement of the designated motion and the corresponding coupled motion errors for the X-stage, the Y-stage and the Z-stage separately. The experimental results are plotted in Fig. 7.10(a) for the X-stage, Fig. 7.10(b) for the Y-stage and Fig. 7.11(a) for the Z-stage. In order to verify equation (7.9), these plots have the trend lines and use V^2 for their x-axes. The trend lines in Fig. 7.10(a) and 7.10(b) shows that the mechanical behaviors of the X-stage and the Y-stage are proportional to the square of the driving voltage (V^2) as described in equation (7.9). This indicates that the mathematical analysis in the previous section is valid to predict and control the stages motions. There is still small difference between the trend line and the real experimental data. One main reason for this is material properties used in equation (7.9); most material properties of silicon is nonlinear and temperature dependent, but equation (7.9) is based on constant material properties.



(a)



(b)

Figure 7.10: Experimental results of the X-stage and the Y-stage motion: (a) when the X-stage is actuated; (b) when the Y-stage is actuated

Figure 7.10(a) and 7.10(b) also indicate that both the X-stage and the Y-stage are able to generate about 50 μm for driving voltages of 7.62 V and 8.0 V, respectively. Between them, the X-stage demonstrates more than 60 μm displacement. These results fit well with the expected behavior from FEA in the previous section. Concerning the

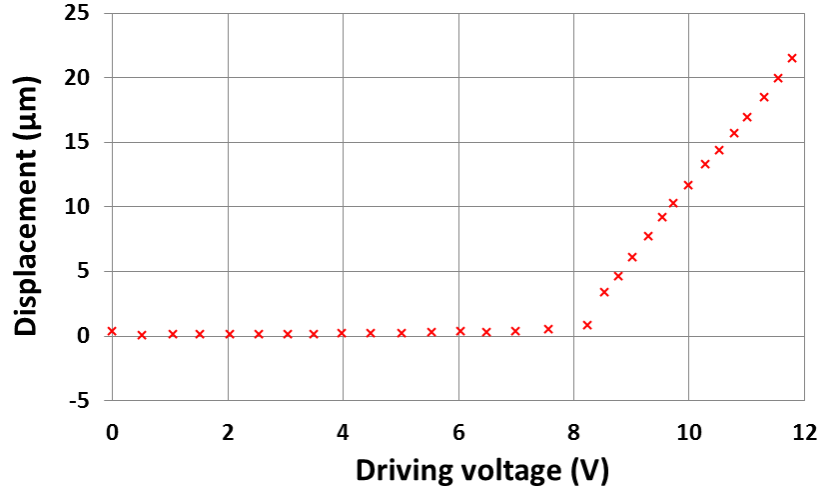
coupled motion error, when the X-stage or the Y-stage is in operation, the Z-stage shows random motions with less than 1 μm amplitude. These motions do not show any pattern and a motion with the amplitude of less than 1 μm is small enough to be negligible in the XYZ-stage, so it is difficult to regard them as coupled motion errors. Based on this observation, the coupled motion errors related to the Z-stage can be considered insignificant. However, the X-stage shows a repeatable motion pattern when the Y-stage is in its operation as shown in Fig. 7.10(b). This pattern can be regarded as coupled motion error. The main reason for this coupled motion error is that the temperature rise in the Y-stage affects the temperature of the actuator in the X-stage and comes from thermal energy leak, not structural coupling. However, the heat generated in the X-stage is well dissipated to the heat sink near the actuator of the X-stage, not affecting its coupled motion error substantially. The Z-stage is also close to the Y-stage, but its coupled motion error is insignificant. This is because the form factor of the Z-stage is relatively smaller than the others and the Z-stage utilizes a different working principle: buckling. Detailed performance data are presented in Table 7.3.

Table 7.3: The maximum displacements and the coupled motions of the XYZ-stage without compensation

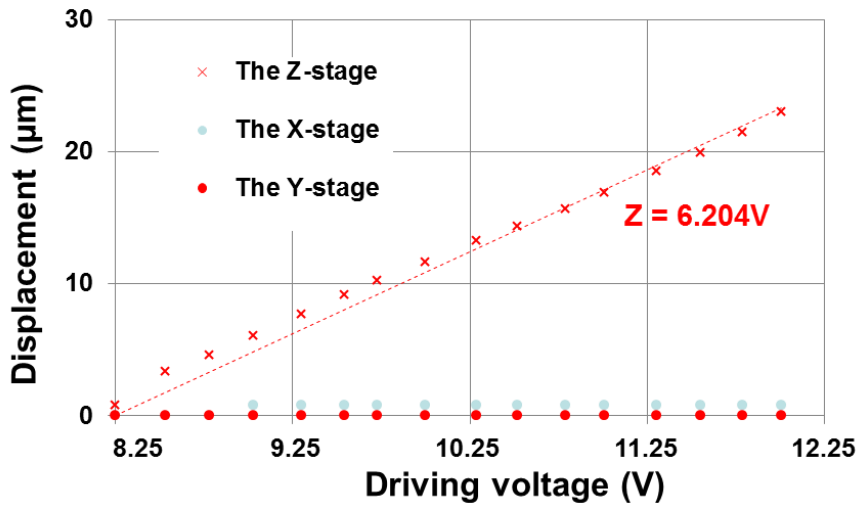
Actuation		Coupled motion error without compensation		
		X-stage	Y-stage	Z-stage
Target	Displacement	Displacement	Displacement	Displacement
The X-stage	58.90 μm	-	Less than 0.98 μm	0.32 μm
The Y-stage	49.15 μm	4.92 μm	-	0.17 μm
The Z-stage	22.91 μm	Less than 0.98 μm	Less than 0.98 μm	-

The displacement of the Z-stage is plotted in Fig. 7.11(a), which shows different mechanical behaviors from the actuation of the X-stage or the actuation of the Y-stage. This is because the actuation of the Z-stage operates based on the buckling of the beam, not thermal expansion of the bent beams. The pre-buckling mode or bending moment by pure thermal expansion produces the displacement of $1.25 \mu\text{m}$ with the driving voltage of 8.25 V and the post-buckling mode shows an increment up to $22.91 \mu\text{m}$ with the voltage of 12.01 V . Since this post-buckling mode will be used in the XYZ-stage, this post-buckling mode is plotted separately in Fig. 6.11(b) with its trend line and the corresponding coupled motion errors. The slope of a pre-buckling mode is $0.15 \mu\text{m} / \text{V}$ and that of a post-buckling mode is $6.76 \mu\text{m} / \text{V}$. This big difference indicates not only how the buckling is useful in its stroke, but also when the buckling starts. Over the post-buckling mode, the plastic deformation starts with approximate 12 V after several tests, so the Z-stage needs to be operated within the driving voltage range between 8.25 V and 11.78 V to utilize the buckling effect efficiently and assure reliable operations to avoid any plastic deformation.

Detailed values for the maximum displacements and the corresponding coupled motion errors are listed in Table 7.3. The coupled motion error in the X-stage by the Y-stage is relatively bigger than other factors and needs to be reduced. The compensation algorithm is adapted in the following section in order to reduce these coupled motion error.



(a)



(b)

Figure 7.11: Experimental results of the Z-axis displacement in the XYZ-stage: (a) when the Z-stage is actuated; (b) the post-buckling mode of (a); (the results from actuating the X-stage are in blue dots, the results from actuating the Y-stage in red dots and the results from actuating the Z-stage in red crosses)

7.4.2 Compensation for reducing coupled motion errors

The coupled motion error of the X-stage by the Y-stage must be reduced to an acceptable level. As described in equation (7.7), the displacement of the motion platform is linearly proportional to the square of the driving voltages. This property indicates that the superposition of the actuators rising temperature can be expressed as a summation.

The whole response of the XYZ-stage can be expressed by the combination of the driving voltages as:

$$\begin{bmatrix} X (\mu m) \\ Y (\mu m) \\ Z - 1.25 \mu m \end{bmatrix} = \begin{bmatrix} 0.8757 & 0.0755 & 0 \\ 0 & 0.7853 & 0 \\ 0 & 0 & 6.204 \end{bmatrix} \begin{bmatrix} V_x^2 (V) \\ V_y^2 (V) \\ V - 8.25V \end{bmatrix} \quad (7.9)$$

Based on equation (7.9), the expected displacement from the XYZ-stage can be calculated according to the input voltages. Each term in the matrix in equation (7.9) is extracted from the slopes of the trend lines in Fig. 7.10 and Fig. 7.11. The offset applied to the Z-stage is for excluding the pre-buckling mode and utilizing the post-buckling mode only for a straightforward control. One thing to notice is that the matrix in equation (7.9) is not a diagonal matrix. This means that the coupled motion error is observable at the X-stage while the Y-stage is in its operation. This coupled motion error can be compensated by controlling the input voltage to the X-stage which corresponds to the input voltage to the Y-stage. This compensation is described in equation (7.10),

The components in the matrix in equation (7.9) are extracted from the slopes of the trend lines in Fig. 7.10 and Fig. 7.11. The offset in the Z-stage is to exclude the pre-buckling mode and utilize the post-buckling mode only for simple analysis. When the driving voltages to each stage are set, the expected displacement from the XYZ-stage can be calculated based on equation (7.9). The matrix in equation (7.9) can have its inverse form and that is shown in equation (7.10). The desired position information can be used to calculate the appropriate input voltages by equation (7.10). Since the matrix is not a diagonal matrix, the coupled motion error can also be identified.

$$\begin{bmatrix} X - X_{off} (\mu m) \\ Y (\mu m) \\ Z - 1.25 (\mu m) \end{bmatrix} = \begin{bmatrix} 0.8757 & 0.0755 & 0 \\ 0 & 0.7853 & 0 \\ 0 & 0 & 6.204 \end{bmatrix} \begin{bmatrix} V_x^2 (V) - V_{off}^2 (V) \\ V_y^2 (V) \\ V - 8.25(V) \end{bmatrix} \quad (7.10)$$

where X_{off} is an x-directional offset and V_{off} is the corresponding input voltage to reduce coupled motion error. The relationship for V_{off} is $V_{off} = 0.294V_y$ and its maximum value is 2.75 V for the maximum X_{off} of 4.92 μm . Based on these terms, the coupled motion error can be reduced. However, the electrothermal actuators in the XYZ-stage are not bi-directional actuators, so it is impossible to actuate the stage in a reverse direction for this compensation. In order to overcome this issue, the offset will be utilized when a backward motion is needed for the compensation operation. Due to the offsets, the maximum displacement of the X-stage will be reduced to 53.98 μm from 58.90 μm .

The matrix in equation (7.9) can be expressed as its inverse form as equation (7.10). The appropriate input voltages can be calculated for the desired position information based on equation (7.10).

$$\begin{bmatrix} V_x^2 - V_{xoff}^2 (V) \\ V_y^2 (V) \\ V - 8.25V \end{bmatrix} = \begin{bmatrix} 1.1419 & -0.1098 & 0 \\ 0 & 1.2734 & 0 \\ 0 & 0 & 0.1612 \end{bmatrix} \begin{bmatrix} X - X_{off} \mu m \\ Y \mu m \\ Z - 1.25 \mu m \end{bmatrix} \quad (7.11)$$

Figure 7.12 compares the original experimental data with this compensation based on equation (7.11). With this compensation, the X-stage remains at its designated position with less than 1 μm variation while the Y-stage generates motions up to 49.15 μm .

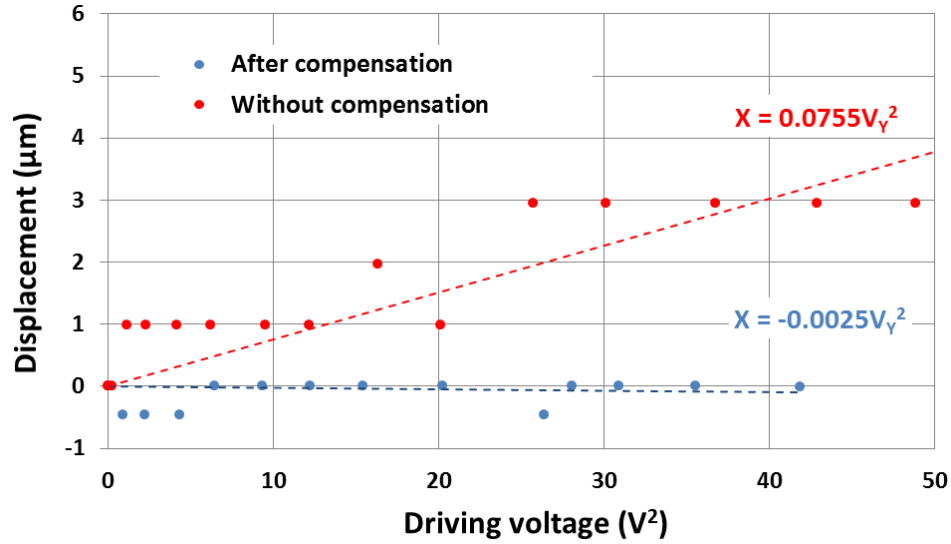


Figure 7.12: The compensation of the coupled motion error in the X-stage by the motion of the Y-stage; the red dots for original behavior and blue dots for compensated behavior

7.4.3 The frequency response of the proposed XYZ-stage

The frequency responses of the XYZ-stage are measured separately for in-plane motions and out-of-plane motions. For the X-stage and the Y-stage, an Agilent1 Fast-Fourier-Transform (FFT) analyzer with the frequency response measurement method [119] is used. With this experimental set-up, the 1st resonance frequency of the X-stage is observed near 0.51 kHz and the Y-stage is 1.06 kHz. These values are similar to those in their original XY-stage [27] as expected. Based on the observation on the frequency responses, the presented XYZ-stage is appropriate for the operations with less than 100 Hz frequency. Considering a force larger than a few mN level, these specifications indicate that the presented stages are desirable at micro-manipulation for micro-assembly or cell-manipulation.

In addition to this property, the first frequency of the X-stage is half of that of the Y-stage. This comes from the design difference between the X-stage and the Y-stage; the

X-stage supports both the Y-stage and the Z-stage, but the Y-stage holds the Z-stage only. This difference from the nested structure results in different mass which is common in a serial kinematic mechanism (SKM). In order to overcome this property, the stiffness of the X-stage and the Y-stage need to be re-designed, because the frequency response has a relationship with its stiffness and mass. The stiffness can be analytically evaluated from equation (7.3) and equation (7.4). In this case, a modification of the flexure design or adjustment of the lever ratio can be one method. Another approach to overcome this limit is to utilize the parallel kinematic mechanism (PKM), where two identical X-stages which are perpendicular to each other are connected for the in-plane motions [131,164]. However, PKM makes its output tightly coupled, which needs a non-linear mathematical model to obtain its relationships between the input voltages and the output displacements. This requires considerable design effort to build the mathematical model and preprocessing time before each operation.

For the Z-stage, a Polytec MSA-500 Micro System Analyzer [161] is utilized for out-of-plane responses. First resonant frequency of the Z-stage is observed at 78.3 kHz. This value is very close to the value calculated in FEA in section 7.2.2. However this value is relatively higher than the Z-stage [76], because the Z-actuator used in the XYZ-stage is smaller than a quarter of the Z-stage described in Chapter 5. The reduction in the volume not only reduces its mass but also increases its stiffness, which results in almost 20 times difference.

7.4.4 The characteristics of the proposed XYZ-stage

The range of motion and the frequency response of the presented stage are analyzed in the previous section. The presented stage demonstrates relatively larger strokes,

especially for the Z-motion than the stages in Table 7.1. This indicates the usability of the nested structure design to merge the three independent stages into one without significant interference. In addition to this, no special fabrication methods are needed. This is because an appropriate Z-stage can be chosen without design constraints or fabrication limitations from the other engaged stages in the nested structure design.

Table 7.4: MEMS-based positioning stages in specific cases

Reference	Range of motion (μm)		1 st mode resonant frequency (Hz)		Stiffness (N/m)	Force (mN)	Actuation mechanism and applications
	X	Y	X	Y			
Lantz et al. 2007 [37]	± 60	± 60	185	210	90.5	~ 10	Electromagnetic actuator Probe-storage
Fowler et al. 2012 [38]	16	15	816	820	-	-	Electrostatic actuator AFM scanning
Duc et al. 2008 [39]	17	11	-	-	74	0.814	Polymer actuator Micro-gripper
This study	53.98	49.15	510	1060	900	~ 4.5	Electrothermal actuator

Based on these features, the presented stage in this study can be regarded as a good candidate for the environment requiring a displacement larger than 50 μm , a force larger than 1 mN, a stiffness of more than 100 N/m, a driving voltage of less than 20 V, and a reliable operation at low frequency less than 500 Hz. As listed in Table 4, the nano-positioner designed for probe-storage applications should generate large strokes and be stable against any external disturbance [171]. The nano-positioner designed for Atomic Force Microscope (AFM) applications has to operate at high frequency [18]. The micro-

gripper needs to be stiff and able to generate enough displacement at low frequency [34]. Based on these features, micro-manipulation or micro-assembly can be reasonable applications for the presented stage, which does not require high speed operation, but large force and displacement. Two 2 DOF motion stages with probes are reported to grip and rotate a particle of 14.8 μm diameter successfully [27]. These operations can be extended with the presented XYZ-stage for more delicate operations. The cooperation of three 2 DOF stages are reported for 6 DOF motions in MEMS [118], which also can be implemented by two XYZ-stage presented in this study.

7.5 Summary

In this chapter, we have demonstrated design, fabrication, and testing of the MEMS based XYZ-stage. The presented XYZ-stage is designed and built by merging three individual stages through the nested structure. With this approach, 3-DOF motions are obtained with tens of microns of strokes. This implementation shows that utilizing existing MEMS actuators, instead of developing totally new designs, can be one way to develop a device with various advantages, such as reduction in the design process time and expected risks.

For successful implementation of the XYZ-stage, several additional features were required and incorporated; (i) the embedded electric connection to control the Y-stage and the Z-stage inside the X-stage reliably, (ii) the electric isolation among three stages to prevent any motion error by leaking electrical currents, (iii) the floating frames to hold the embedded Y- and Z-stages in their positions for accurate motions, and (iv) the floating blocks to hold the electrothermal actuators in their positions for efficient operations. With these features, the presented XYZ-stage demonstrates successfully the range of motion of 53.98 μm x 49.15 μm x 22.91 μm along X, Y, and Z axes respectively.

During this demonstration, the coupled motion error is observed but can be reduced to less than 1 % with the presented compensating algorithm.

The nested structures for the XYZ-stage prove its usefulness to achieve design goals with low cost and high reliability by merging already existing MEMS systems. When their fabrication methods are compatible with others, more various MEMS devices are possible; instead of the Z-stage, a micro-gripper can be embedded onto the motion platform of the Y-stage. This approach can provide a pick-move-and-release operation through the combination of the XY-stage and the micro-gripper without significant design process and effort.

Chapter 8: Conclusions

This Chapter presents the intellectual contributions and anticipated benefits from the work proposed in this dissertation.

8.1 Intellectual contributions

The research issues listed in Chapter 1 broadly aim toward building an XYZ motion stage through the development of a different integration approach based on existing in-plane motion stages and out-of-plane motion stages. In this dissertation, various issues in developing multi-DOF motion stages are described and their corresponding solutions are also given. Some important contributions are described as follows:

1. Nested structure framework for SKM: The presented XYZ motion stage is implemented based on a nested structure, which is a type of SKM (serial kinematic mechanism). A nested structure necessitates embedding one foreign system into another completely as a sub-component. This approach has significant advantages in the implementation of a modular design concept or a “divide and conquer” concept. For a successful nested structure, the X-stage is designed to include a large motion platform. With the same pattern, the motion platform in the Y-stage is utilized for the Z-stage. Because these fabrication procedures for the engaged systems are compatible with each other, they can be integrated into one system for further applications. Additional features, like electrical connections and structural frames, are described in Chapter 4 and Chapter 5 for successful implementation.
2. The other advantage of the presented motion stage is its reliability. In general, it takes a longer time to develop a whole new motion stage with reasonable

reliability than recycling existing systems. It is also hard to claim that newly developed systems have better performance and reliability than existing ones. Therefore, appropriately selected sub-modules or sub-systems can provide reliability in the final system and also reduce design time and efforts by avoiding the problems already shown in the literature review. These procedures are experimentally described in Chapter 6 and Chapter 7.

3. The optimization process of the electrothermal actuator and a mechanical transmission: Many electrothermal actuator designs study the actuation mechanism itself. The presented XYZ-stage in this dissertation requires a relationship between a motion platform and an actuator, so the electrothermal actuator should be investigated under external mechanical load. In addition to this motion platform, a mechanical transmission needs to convert some degree of force from an electrothermal actuator into a large stroke. The relationship between the external mechanical load and the lever is analyzed in Chapters 4 and 5. Based on these constraints, such as an external mechanical load and a lever, the electrothermal actuator is optimized for a larger stroke, which is described in Chapter 4, and Matlab optimization algorithms [108].
4. A new design for out-of-plane motion stage: There are not enough MEMS based out-of-plane motion stages to compare with each other, due to the lack of appropriate fabrication technologies in MEMS. In Chapter 6, a thermally actuated out-of-plane motion stage is designed and demonstrated by introducing step features to generate an out-of-plane motion with fabrication methods compatible with XY-stages. Considering the fact that out-of-plane actuators or motion stages

are rare based on bulk micromachining technologies or SOIMUMPs process [102], this system can be utilized for other MEMS devices to extend their capabilities.

5. The supporting frame for the inner stages: As discussed in Chapter 2, it is unusual to find thermally actuated multi-DOFs MEMS stages, given their limitations; both ends of the actuator should be fixed firmly because its operation and thermal response does not perform well at a high-frequency. In order to overcome this issue, floating anchors are introduced by utilizing the handle layer of the SOI wafer. The electrothermal actuator in the inner stage should be free to move; otherwise this can interfere with the motions in other stages. In addition to this feature, a supporting frame also needs to hold the links and the levers in position. In addition to these, physical gaps on the front side need to be held by a supporting frame underneath them. These gaps are useful for thermal isolation among different electrothermal actuators.

8.2 Anticipated Benefits

This dissertation addresses the key issue of MEMS precision positioning stages for 3 DOF motions and the possibility of an implementation approach; a nested structure with floating frames. As discussed in Chapter 2, the main limitation of MEMS-based motion stages is a relatively small travel distance and force or a lack of 3 DOF or more motions, including both in-plane and out-of-plane motions. It is valid for a motion stage with a larger workspace, it is easier to build a manipulation plan and its process would be simpler and faster. The XYZ-stage discussed in Chapter 7 will help manipulation applications for micro-meter scale objects.

Complex operations or multi-purpose operations are hard to implement in a single device in MEMS due to its limited fabrication approaches. The integration strategy discussed in Chapter 5 and Chapter 7 can help merge various operations into one device and also support the design concept; a divide and conquer algorithm [172]. The divide and conquer algorithm starts by breaking down the target design into sub-designs until these are easy to fabricate in MEMS or already exist in MEMS. These sub-designs are then combined together for its original purpose. For example, a MEMS-based scanning-type sensor can be divided into two sub-designs; one is a sensor and the other is the in-plane positioner.

The analysis of the electrothermal actuator discussed in Chapter 4 is a useful resource in designing actuators under a mechanical load. Most analyses of the thermal actuator focus on the actuator itself, but the analysis in Chapter 4 discusses the optimization of the actuator under an external load and a mechanical amplifier, such as leverage. The analysis and simulation discussed in Chapter 4 and Chapter 5 can help design utilizing electrothermal actuators and a mechanical amplifier under the expected mechanical load.

The coordinated manipulation demonstrated in Chapter 6 can contribute to dexterous operations in MEMS for micro-manipulation; the manipulation of a micron-sized object is demonstrated by two XY-stages in Chapter 6. Gripping, rotating and moving operations of a micro-meter scale object are implemented by controlling the two probes extruded from two coordinating XY-stages. A manipulator capable of accessing and even rotating a micro particle is not common in MEMS. In addition to these, the presented XY-stage has its own motion platform for further applications. For example,

the probe extended from the motion stages is also beneficial to manipulation or assembly works and doesn't require additional processes to implement contrary movement to a complex shape shown in previous research [101].

8.3 Future Directions

This dissertation provides a solid foundation for multi-DOF motion stages based on a SKM, especially a nested structure. The approaches discussed here can be extended to various applications by simply merging different systems through the nested structure. For example, a longer range of motion can be made through an XX-stage, which is a modification of the XY-stage where two X-stages are used to increase its range of motion instead of a Y-stage. In addition to this, an X(-X)-stage is also made by the X-stage and the (-X)-stage for bi-directional 1 DOF motion. The XYZ stage is also utilized by replacing the Z-stage with a sensor. In this case, this can be a 2 dimensional scanner for metrological applications.

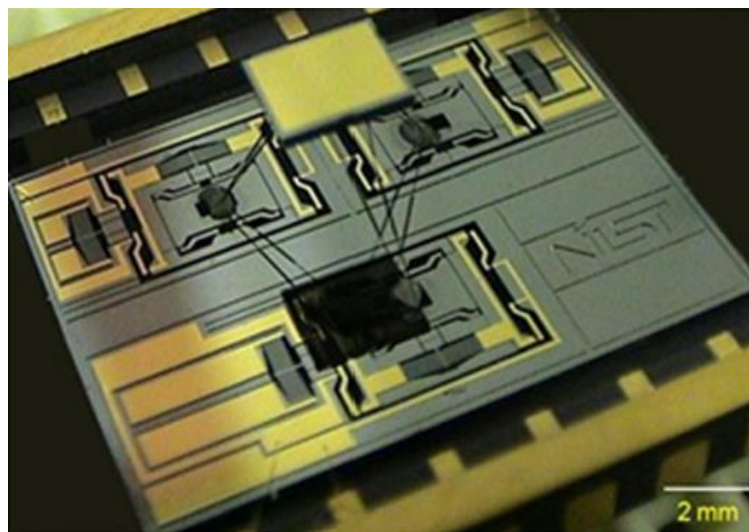


Figure 8.1: A hexapod for 6 DOF motion based on three XY-stages [118]

1. Micro-gripper: In Chapter 7 the XY-stage is extended into the XYZ-stage by embedding the Z-stage in the middle of the XY-stage. Instead of the Z-stage, a micro-gripper can be utilized. In this case, the final system will be a micro-gripper system with 2 DOF in-plane motions. In this case, the pick-move-and-release operation is possible without any external help. There are various micro-grippers and 2 DOF motion stages in MEMS, but it is rare to find one having simultaneous gripping and moving capabilities due to the lack of appropriate MEMS fabrication methods.
2. Long range motion: In Chapter 3 and 4, we have introduced the X-stage and its optimization for a large stroke or a sensitive motion. Among them, the longer range of motion can be implemented through the different combinations for the XY-stage. Instead of having the Y-stage perpendicular to the X-stage, the same X-stage can be utilized (called an XX-stage). In this case, the range of motion will increase proportionally to the number of engaged X-stages. The more X-stages that are integrated, the larger the stroke this stage is able to generate without optimizing the X-stage itself.
3. The XY-stage with embedded sensors: In Chapter 5 we have introduced the XY-stage and in Chapter 6, it was shown how this XY-stage can be extended into the XYZ-stage. This indicates that the XY-stage has room for the Z-stage or other instruments. Instead of the Z-stage, a sensor compatible with SOI-MUMPs can be adapted for further applications. This sensor can be an AFM tip or TIM. The same electric connection or isolation can be utilized. If the sensor is not sensitive to any thermal change, this can be utilized to scan the surface of an object.

4. A three-finger manipulation system based on three XY-stages: The XY-stage generates in-plane motion on the XY plane. When three XY-stages are engaged together with probes, this system can provide a three-finger manipulation system on the XY plane as shown in Fig. 8.1. The three-finger manipulation system is expected to manipulate an object with more of a variety of motions.
5. A hexapod: A hexapod is a sort of Stewart platform generating 6 DOF motions [118]. By incorporating three XY-stages and one motion platform, 6 DOF motion can be established which is similar to the three-finger manipulation system.

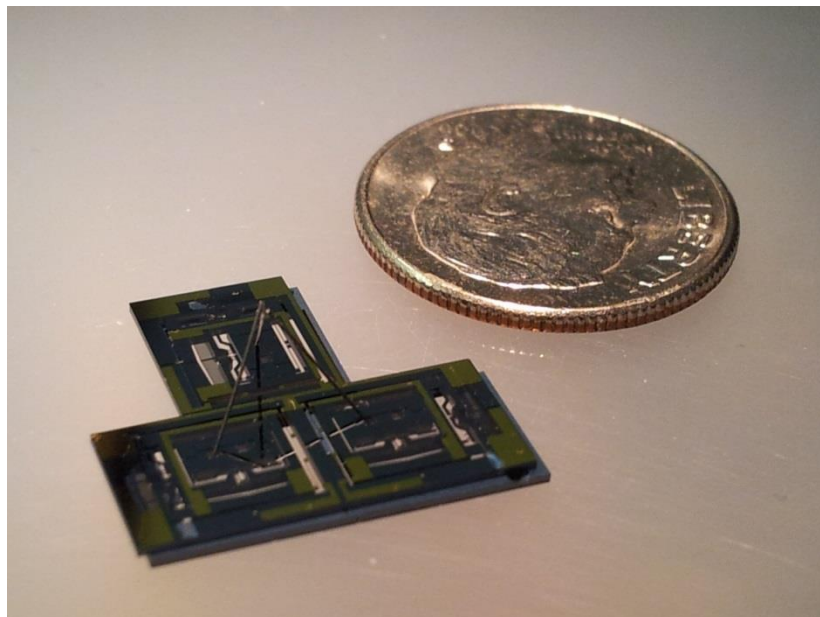


Figure 8.2: Three finger manipulation system

6. Motion stages with heterodyne actuators: Almost identical actuators have been used in various MEMS motion stages. It is hard to find motion stages composed of electrothermal actuators and electrostatic actuators. When they are fully isolated, various actuation mechanisms can be merged together into a single system. For example, an XYZ-motion stage can be based on thermally actuated X

and Y stages and an electrostatically actuated Z-stage. In this case, the Z motion corresponds at high speeds and the X and Y motion does at low speeds. Different actuation mechanisms have their own advantages and disadvantages, so a combination of them without significant problems can widen their applications to various fields.

Glossary

AFM	Atomic Force Microscopy
CTE	Coefficient of Thermal Expansion
DOF	Degree Of Freedom
DRIE	Deep Reactive Ion Etching
FEA	Finite Element Analysis
MEMS	Micro-Electro-Mechanical System
MRI	Magnetic Resonance Imaging
OpenCV	Open source Computer Vision library
PKM	Parallel Kinematic Mechanism
SEM	Scanning Electron Microscopy
SKM	Serial Kinematic Mechanism
SOI-MUMPs	a Silicon-On-Insulator Multi-User Multi-Processes
SOI	Silicon-On-Insulator
TEM	Transmission Electron Microscopy
VS	Plastic Viscosity
YS	Yield Stress

Bibliography

- [1] Anon ANSxyz50 compact xyz-scanner
- [2] Anon P-611.3 NanoCube® XYZ Piezo Stage Compact Multi-Axis Piezo System for Nanopositioning and Fiber Alignment
- [3] Anon Nuclear Cover Up: World's Largest Movable Structure to Seal the Wrecked Chernobyl Reactor
- [4] Zhang W, Gnerlich M, Paly J J, Sun Y, Jing G, Voloshin A and Tatic-Lucic S 2008 A polymer V-shaped electrothermal actuator array for biological applications *J. Micromechanics Microengineering* **18** 075020
- [5] Al Aioubi M Y, Djakov V, Huq S E and Prewett P D 2004 Deflection and load characterisation of bimorph actuators for bioMEMS and other applications *Microelectron. Eng.* **73** 898–903
- [6] Beyeler F, Neild A, Oberti S, Bell D J, Sun Y, Dual J and Nelson B J 2007 Monolithically fabricated microgripper with integrated force sensor for manipulating microobjects and biological cells aligned in an ultrasonic field *Microelectromechanical Syst. J. Of* **16** 7–15
- [7] Kim K, Liu X, Zhang Y and Sun Y 2008 Nanonewton force-controlled manipulation of biological cells using a monolithic MEMS microgripper with two-axis force feedback *J. Micromechanics Microengineering* **18** 055013
- [8] Kim C-H and Kim Y-K 1999 Integration of a microlens on a micro XY-stage *Asia Pacific Symposium on Microelectronics and MEMS* (International Society for Optics and Photonics) pp 109–17
- [9] Laszczyk K, Bargiel S, Gorecki C, Krężel J, Dziuban P, Kujawińska M, Callet D and Frank S 2010 A two directional electrostatic comb-drive X–Y micro-stage for MOEMS applications *Sens. Actuators Phys.* **163** 255–65
- [10] Miyajima H, Asaoka N, Isokawa T, Ogata M, Aoki Y, Imai M, Fujimori O, Katashiro M and Matsumoto K 2003 A MEMS electromagnetic optical scanner for a commercial confocal laser scanning microscope *Microelectromechanical Syst. J. Of* **12** 243–51
- [11] Takahashi K, Kwon H N, Saruta K, Mita M, Fujita H and Toshiyoshi H 2005 A two-dimensional f-. THETA. micro optical lens scanner with electrostatic comb-drive XY-stage *IEICE Electron. Express* **2** 542–7
- [12] Miyajima H, Murakami K and Katashiro M 2004 MEMS optical scanners for microscopes *Sel. Top. Quantum Electron. IEEE J. Of* **10** 514–27

- [13] Sun L, Wang J, Rong W, Li X and Bao H 2008 A silicon integrated micro nano-positioning XY-stage for nano-manipulation *J. Micromechanics Microengineering* **18** 125004
- [14] Gorman J J, Kim Y-S, Vladar A E and Dagalakis N G 2007 Design of an on-chip microscale nanoassembly system *Int. J. Nanomanufacturing* **1** 710–21
- [15] Donald B R, Levey C G and Paprotny I 2008 Planar microassembly by parallel actuation of MEMS microrobots *Microelectromechanical Syst. J. Of* **17** 789–808
- [16] Johnstone R W and Parameswaran M 2001 Self-assembly of surface-micromachined structures using electrostatic attraction *Proc. SPIE* vol 4561 pp 66–76
- [17] Indermühle P-F, Jaecklin V P, Brugger J, Linder C, De Rooij N F and Binggeli M 1995 AFM imaging with an xy micropositioner with integrated tip *Sens. Actuators Phys.* **47** 562–5
- [18] Fowler A G, Laskovski A N, Hammond A C and Moheimani S O R 2012 A 2-DOF electrostatically actuated MEMS nanopositioner for on-chip AFM *Microelectromechanical Syst. J. Of* **21** 771–3
- [19] Yang S H, Kim Y, Purushotham K P, Yoo J-M, Choi Y-M and Dagalakis N 2010 AFM characterization of nanopositioner in-plane stiffnesses *Sens. Actuators Phys.* **163** 383–7
- [20] Madou M J Fundamentals of microfabrication. 2002 *Boca Raton Fla. CRC Press* **200** 298–205
- [21] Anon Bosch DRIE process
- [22] Kim C-H and Kim Y-K 2002 Micro XY-stage using silicon on a glass substrate *J. Micromechanics Microengineering* **12** 103
- [23] Miller R A, Tai Y-C, Xu G, Bartha J and Lin F 1997 An electromagnetic MEMS 2 x 2 fiber optic bypass switch *Solid State Sensors and Actuators, 1997. TRANSDUCERS'97 Chicago., 1997 International Conference on* vol 1 (IEEE) pp 89–92
- [24] Fan L, Wu M C, Choquette K D and Crawford M H 1997 Self-assembled microactuated XYZ stages for optical scanning and alignment *Solid State Sensors and Actuators, 1997. TRANSDUCERS'97 Chicago., 1997 International Conference on* vol 1 (IEEE) pp 319–22
- [25] Sahu B, Leang K K and Taylor C R 2010 Emerging challenges of microactuators for nanoscale positioning, assembly, and manipulation *J. Manuf. Sci. Eng.* **132** 030917

- [26] Eleftheriou E, Antonakopoulos T, Binnig G K, Cherubini G, Despont M, Dholakia A, Durig U, Lantz M., Pozidis H, Rothuizen H E and Vettiger P 2003 Millipede - a MEMS-based scanning-probe data-storage system *IEEE Trans. Magn.* **39** 938–45
- [27] Kim Y-S, Yoo J-M, Yang S H, Choi Y M, Dagalaks N G and Gupta S K 2012 Design, fabrication and testing of a serial kinematic MEMS XY stage for multifinger manipulation *J. Micromechanics Microengineering* **22**
- [28] Nordström Andersen K, Petersen D H, Carlson K, Mølhave K, Sardan Sukas Ö, Horsewell A, Eichhorn V, Fatikow S and Bøggild P 2009 Multimodal electrothermal silicon microgrippers for nanotube manipulation *IEEE Trans. Nanotechnol.* **8** 76–85
- [29] Mukhopadhyay D, Dong J, Pengwang E and Ferreira P 2008 A SOI-MEMS-based 3-DOF planar parallel-kinematics nanopositioning stage *Sens. Actuators Phys.* **147** 340–51
- [30] Koo B, Zhang X, Dong J, Salapaka S M and Ferreira P M 2012 A 2 degree-of-freedom SOI-MEMS translation stage with closed-loop positioning *Microelectromechanical Syst. J. Of* **21** 13–22
- [31] Liu X, Kim K and Sun Y 2007 A MEMS stage for 3-axis nanopositioning *J. Micromechanics Microengineering* **17** 1796
- [32] Dong J and Ferreira P M 2009 Electrostatically Actuated Cantilever With SOI-MEMS Parallel Kinematic Stage *Microelectromechanical Syst. J. Of* **18** 641–51
- [33] Kim B-H and Chun K 2001 Fabrication of an electrostatic track-following micro actuator for hard disk drives using SOI wafer *J. Micromechanics Microengineering* **11** 1
- [34] Duc T C, Lau G-K and Sarro P M 2008 Polymeric thermal microactuator with embedded silicon skeleton: Part II—Fabrication, characterization, and application for 2-DOF microgripper *Microelectromechanical Syst. J. Of* **17** 823–31
- [35] Kim D-H, Lee M G, Kim B and Sun Y 2005 A superelastic alloy microgripper with embedded electromagnetic actuators and piezoelectric force sensors: a numerical and experimental study *Smart Mater. Struct.* **14** 1265
- [36] Jeon C-S, Park J-S, Lee S-Y and Moon C-W 2007 Fabrication and characteristics of out-of-plane piezoelectric micro grippers using MEMS processes *Thin Solid Films* **515** 4901–4
- [37] Anon H-840 6-Axis Hexapod
- [38] Anon Parallel and Serial Kinematics / Metrology

- [39] Miller K, Cowen A, Hames G and Hardy B 2004 SOIMUMPs design handbook *MEMScAP Inc Durh.*
- [40] Syms R R A 2002 Long-travel electrothermally driven resonant cantilever microactuators *J. Micromechanics Microengineering* **12** 211
- [41] Oliver A D, Vigil S R and Gianchandani Y B 2003 Photothermal surface-micromachined actuators *Electron Devices IEEE Trans. On* **50** 1156–7
- [42] Anon Coefficient of Thermal expansion (C.T.E.) of silicon
- [43] Chu L L and Gianchandani Y B 2003 A micromachined 2D positioner with electrothermal actuation and sub-nanometer capacitive sensing *J. Micromechanics Microengineering* **13** 279
- [44] Bergna S, Gorman J J and Dagalakis N G 2005 Design and modeling of thermally actuated MEMS nanopositioners *ASME 2005 International Mechanical Engineering Congress and Exposition* (American Society of Mechanical Engineers) pp 561–8
- [45] Guan C and Zhu Y 2010 An electrothermal microactuator with Z-shaped beams *J. Micromechanics Microengineering* **20** 085014
- [46] Sehr H, Tomlin I S, Huang B, Beeby S P, Evans A G R, Brunnschweiler A, Ensell G J, Schabmueller C G J and Niblock T E G 2002 Time constant and lateral resonances of thermal vertical bimorph actuators *J. Micromechanics Microengineering* **12** 410
- [47] Park J-S, Chu L L, Oliver A D and Gianchandani Y B 2001 Bent-beam electrothermal actuators-Part II: Linear and rotary microengines *Microelectromechanical Syst. J. Of* **10** 255–62
- [48] Lott C D, McLain T W, Harb J N and Howell L L 2002 Modeling the thermal behavior of a surface-micromachined linear-displacement thermomechanical microactuator *Sens. Actuators Phys.* **101** 239–50
- [49] Abbas K, Alaie S and Leseman Z C 2012 Design and characterization of a low temperature gradient and large displacement thermal actuators for in situ mechanical testing of nanoscale materials *J. Micromechanics Microengineering* **22** 125027
- [50] Que L, Park J-S and Gianchandani Y B 2001 Bent-beam electrothermal actuators-Part I: Single beam and cascaded devices *Microelectromechanical Syst. J. Of* **10** 247–54
- [51] Cao A, Kim J and Lin L 2007 Bi-directional electrothermal electromagnetic actuators *J. Micromechanics Microengineering* **17** 975

- [52] Luo J K, Flewitt A J, Spearing S M, Fleck N A and Milne W I 2005 Three types of planar structure microspring electro-thermal actuators with insulating beam constraints *J. Micromechanics Microengineering* **15** 1527
- [53] Zhu Y, Corigliano A and Espinosa H D 2006 A thermal actuator for nanoscale in situ microscopy testing: design and characterization *J. Micromechanics Microengineering* **16** 242
- [54] Chu L L, Hetrick J A and Gianchandani Y B 2002 High amplification compliant microtransmissions for rectilinear electrothermal actuators *Sens. Actuators Phys.* **97** 776–83
- [55] Murthy R and Popa D O 2009 A four degree of freedom microrobot with large work volume *Robotics and Automation, 2009. ICRA'09. IEEE International Conference on* (IEEE) pp 1028–33
- [56] Comtois J H, Michalicek M A and Barron C C 1997 Characterization of electrothermal actuators and arrays fabricated in a four-level, planarized surface-micromachined polycrystalline silicon process *Solid State Sensors and Actuators, 1997. TRANSDUCERS'97 Chicago., 1997 International Conference on* vol 2 (IEEE) pp 769–72
- [57] Cragun R and Howell L L 1999 Linear thermomechanical microactuators *Proc. ASME IMECE* pp 181–8
- [58] Maloney J M, Schreiber D S and DeVoe D L 2004 Large-force electrothermal linear micromotors *J. Micromechanics Microengineering* **14** 226
- [59] Lin C-Y and Chiou J-C 2012 MEMS-based thermally-actuated image stabilizer for cellular phone camera *J. Micromechanics Microengineering* **22** 115029
- [60] Kapels H, Aigner R and Binder J 2000 Fracture strength and fatigue of polysilicon determined by a novel thermal actuator [MEMS] *Electron Devices IEEE Trans. On* **47** 1522–8
- [61] Baker M S, Walraven J A, Headley T J and Plass R A 2004 *Final Report: Compliant Thermo-mechanical MEMS Actuators, LDRD# 52553* (United States. Department of Energy)
- [62] Chen R-S, Kung C and Lee G-B 2002 Analysis of the optimal dimension on the electrothermal microactuator *J. Micromechanics Microengineering* **12** 291
- [63] Hubbard N B and Howell L L 2005 Design and characterization of a dual-stage, thermally actuated nanopositioner *J. Micromechanics Microengineering* **15** 1482
- [64] Shay B, Hubbard T and Kujath M 2008 Planar frictional micro-conveyors with two degrees of freedom *J. Micromechanics Microengineering* **18** 065009

- [65] Moulton T and Ananthasuresh G K 2001 Micromechanical devices with embedded electro-thermal-compliant actuation *Sens. Actuators Phys.* **90** 38–48
- [66] Tsang S-H, Sameoto D and Parameswaran M 2006 Out-of-plane electrothermal actuators in silicon-on-insulator technology *Electr. Comput. Eng. Can. J. Of* **31** 97–103
- [67] Yan D, Khajepour A and Mansour R 2004 Design and modeling of a MEMS bidirectional vertical thermal actuator *J. Micromechanics Microengineering* **14** 841
- [68] Atre A 2006 Analysis of out-of-plane thermal microactuators *J. Micromechanics Microengineering* **16** 205
- [69] Girbau D, Llamas M A, Casals-Terré J, Simó-Selvas X, Pradell L and Lázaro A 2007 A low-power-consumption out-of-plane electrothermal actuator *Microelectromechanical Syst. J. Of* **16** 719–27
- [70] Li L and Uttamchandani D 2009 Dynamic response modelling and characterization of a vertical electrothermal actuator *J. Micromechanics Microengineering* **19** 075014
- [71] Chen W-C, Yeh P-I, Hu C-F and Fang W 2008 Design and characterization of single-layer step-bridge structure for out-of-plane thermal actuator *Microelectromechanical Syst. J. Of* **17** 70–7
- [72] Ogando K, La Forgia N, Zárate J J and Pastoriza H 2012 Design and characterization of a fully compliant out-of-plane thermal actuator *Sens. Actuators Phys.* **183** 95–100
- [73] Varona J, Tecpoyotl-Torres M and Hamoui A A 2009 Design of MEMS vertical–horizontal chevron thermal actuators *Sens. Actuators Phys.* **153** 127–30
- [74] McCarthy M, Tiliakos N, Modi V and Fréchet L G 2007 Thermal buckling of eccentric microfabricated nickel beams as temperature regulated nonlinear actuators for flow control *Sens. Actuators Phys.* **134** 37–46
- [75] Chen W-C, Chu C-C, Hsieh J and Fang W 2003 A reliable single-layer out-of-plane micromachined thermal actuator *Sens. Actuators Phys.* **103** 48–58
- [76] Kim Y, Dagalakis N and Gupta S 2013 Creating large out-of-plane displacement electrothermal motion stage by incorporating beams with step features *J. Micromechanics Microengineering* **23** 055008–10pp
- [77] Hoen S, Bai Q, Harley J A, Horsley D A, Matta F, Verhoeven T, Williams J and Williams K R 2003 A high-performance dipole surface drive for large travel and force *TRANSDUCERS, Solid-State Sensors, Actuators and Microsystems, 12th International Conference on, 2003* vol 1 (IEEE) pp 344–7

- [78] Horsley D A, Wongkomet N, Horowitz R and Pisano A P 1999 Precision positioning using a microfabricated electrostatic actuator *Magn. IEEE Trans. On* **35** 993–9
- [79] Jaecklin V P, Linder C, De Rooij N F and Moret J M 1992 Micromechanical comb actuators with low driving voltage *J. Micromechanics Microengineering* **2** 250
- [80] Cheung P, Horowitz R and Rowe R T 1996 Design, fabrication, position sensing, and control of an electrostatically-driven polysilicon microactuator *Magn. IEEE Trans. On* **32** 122–8
- [81] Jaecklin V P, Linder C, De Rooij N F and Moret J-M 1993 Comb actuators for xy-microstages *Sens. Actuators Phys.* **39** 83–9
- [82] Sun Y, Piyabongkarn D, Sezen A, Nelson B J and Rajamani R 2002 A high-aspect-ratio two-axis electrostatic microactuator with extended travel range *Sens. Actuators Phys.* **102** 49–60
- [83] Milanovic V, Matus G A and McCormick D T 2004 Gimbal-less monolithic silicon actuators for tip-tilt-piston micromirror applications *Sel. Top. Quantum Electron. IEEE J. Of* **10** 462–71
- [84] De Jong B R, Brouwer D M, de Boer M J, Jansen H V, Soemers H M J R and Krijnen G J M 2010 Design and Fabrication of a Planar Three-DOFs MEMS-Based Manipulator *J. Microelectromechanical Syst.* **19** 1116–30
- [85] Brouwer D M, De Jong B R and Soemers H 2010 Design and modeling of a six DOFs MEMS-based precision manipulator *Precis. Eng.* **34** 307–19
- [86] Dong J, Mukhopadhyay D and Ferreira P M 2007 Design, fabrication and testing of a silicon-on-insulator (SOI) MEMS parallel kinematics XY stage *J. Micromechanics Microengineering* **17** 1154
- [87] Ando Y 2004 Development of three-dimensional electrostatic stages for scanning probe microscope *Sens. Actuators Phys.* **114** 285–91
- [88] Pang C K, Lu Y, Li C, Chen J, Zhu H, Yang J, Mou J, Guo G, Chen B M and Lee T H 2009 Design, fabrication, sensor fusion, and control of a micro-XY stage media platform for probe-based storage systems *Mechatronics* **19** 1158–68
- [89] Kim J, Choo H, Lin L and Muller R S 2006 Microfabricated torsional actuators using self-aligned plastic deformation of silicon *Microelectromechanical Syst. J. Of* **15** 553–62
- [90] Han C-H, Choi D-H and Yoon J-B 2011 Parallel-plate MEMS variable capacitor with superior linearity and large tuning ratio using a levering structure *Microelectromechanical Syst. J. Of* **20** 1345–54

- [91] Takahashi K, Mita M, Fujita H and Toshiyoshi H 2009 Switched-Layer Design for SOI Bulk Micromachined XYZ Stage Using Stiction Bar for Interlayer Electrical Connection *Microelectromechanical Syst. J. Of* **18** 818–27
- [92] Kwon H N, Lee J-H, Takahashi K and Toshiyoshi H 2006 Micro< i> XY</i> stages with spider-leg actuators for two-dimensional optical scanning *Sens. Actuators Phys.* **130** 468–77
- [93] Liu X, Tong J and Sun Y 2007 A millimeter-sized nanomanipulator with sub-nanometer positioning resolution and large force output *Smart Mater. Struct.* **16** 1742
- [94] Chiou J-C, Lin Y-J and Kuo C-F 2008 Extending the traveling range with a cascade electrostatic comb-drive actuator *J. Micromechanics Microengineering* **18** 015018
- [95] Su S X, Yang H S and Agogino A M 2005 A resonant accelerometer with two-stage microleverage mechanisms fabricated by SOI-MEMS technology *Sens. J. IEEE* **5** 1214–23
- [96] Ren H, Tao F, Wang W and Yao J 2011 An out-of-plane electrostatic actuator based on the lever principle *J. Micromechanics Microengineering* **21** 045019
- [97] Choi Y-M, Gorman J J, Dagalakis N G, Yang S H, Kim Y S and Yoo J M 2012 A high-bandwidth electromagnetic MEMS motion stage for scanning applications *J. Micromechanics Microengineering* **22** 105012
- [98] Wagner B and Benecke W 1991 Microfabricated actuator with moving permanent magnet *Micro Electro Mechanical Systems, 1991, MEMS'91, Proceedings. An Investigation of Micro Structures, Sensors, Actuators, Machines and Robots. IEEE (IEEE)* pp 27–32
- [99] Kim K H, Yoon H J, Jeong O C and Yang S S 2005 Fabrication and test of a micro electromagnetic actuator *Sens. Actuators Phys.* **117** 8–16
- [100] Wright J A, Tai Y-C and Chang S-C 1997 A large-force, fully-integrated MEMS magnetic actuator *Solid State Sensors and Actuators, 1997. TRANSDUCERS'97 Chicago., 1997 International Conference on* vol 2 (IEEE) pp 793–6
- [101] Culpepper M L and Chen S-C 2004 Modeling and design of a digitally actuated compliant mechanism for Cartesian micro/nano-manipulators *J. Precis. Eng.* **12** 240–64
- [102] Lee C-Y, Chang H-T and Wen C-Y 2008 A MEMS-based valveless impedance pump utilizing electromagnetic actuation *J. Micromechanics Microengineering* **18** 035044

- [103] Cho I-J, Song T, Baek S-H and Yoon E 2005 A low-voltage and low-power RF MEMS series and shunt switches actuated by combination of electromagnetic and electrostatic forces *Microw. Theory Tech. IEEE Trans. On* **53** 2450–7
- [104] Anon [PDF] from upenn.edu
- [105] Dagalakis N G, Kramar J A, Amatucci E and Bunch R 2001 Kinematic modeling and analysis of a planar micropositioner *Proc. of the American Society of Precision Engineering, 16th Annual Meeting* (Citeseer)
- [106] Anon P-363 PicoCube XY(Z) Piezo Scanner High-Dynamics Nanoscanner for Scanning Probe Microscopy
- [107] Anon npoint nPX100 compage stage with 100 μm range and sub-nm resolution
- [108] Anon npoint nPCube Compact XYZ stage with 100 μm range
- [109] Anon Queensgate NPS-XYZ-100A/15H
- [110] Anon Mad city lab Nano-LPQ
- [111] Koh K H, Kobayashi T and Lee C 2012 Investigation of piezoelectric driven MEMS mirrors based on single and double S-shaped PZT actuator for 2-D scanning applications *Sens. Actuators Phys.* **184** 149–59
- [112] Maeda R, Tsaur J J, Lee S H and Ichiki M 2004 Piezoelectric microactuator devices *J. Electroceramics* **12** 89–100
- [113] Olfatnia M, Sood S, Gorman J J and Awtar S 2013 Large Stroke Electrostatic Comb-Drive Actuators Enabled by a Novel Flexure Mechanism *J. Microelectromechanical Syst.* **22** 483–94
- [114] Olfatnia M, Cui L, Chopra P and Awtar S 2013 Large range dual-axis micro-stage driven by electrostatic comb-drive actuators *J. Micromechanics Microengineering* **23** 105008
- [115] Amatucci E G, Dagalakis N G, Marcinkoski J, Scire F E and Kramar J A 2002 *Positioning stage* (Google Patents)
- [116] Awtar S, Ustick J and Sen S 2012 An XYZ Parallel-Kinematic Flexure Mechanism With Geometrically Decoupled Degrees of Freedom *J. Mech. Robot.* **5** 015001–015001
- [117] Kim Y-S, Dagalakis N G and Gupta S K 2011 A TWO DEGREE OF FREEDOM NANOPOSITIONER WITH ELECTROTHERMAL ACTUATOR FOR DECOUPLED MOTION *Proceedings of IDETC/DTM 2011, ASME 2011 International Design Engineering Technical Conferences & Computers and Information in Engineering Conference, August 29-31, 2011, Washington, DC.*

- [118] Yang S H, Kim Y-S, Yoo J-M and Dagalakis N G 2012 Microelectromechanical systems based Stewart platform with sub-nano resolution *Appl. Phys. Lett.* **101** 061909
- [119] Gorman J J, Kim Y-S and Dagalakis N G 2006 Control of MEMS nanopositioners with nano-scale resolution *Proceedings of the ASME International Mechanical Engineering Conference and Exhibition*
- [120] He S and Ben Mrad R 2005 Large-stroke microelectrostatic actuators for vertical translation of micromirrors used in adaptive optics *Ind. Electron. IEEE Trans. On* **52** 974–83
- [121] Kim Y-S, Dagalakis N G and Gupta S K 2014 Design of MEMS based three-axis motion stage by incorporating a nested structure *J. Micromechanics Microengineering* **24** 075009
- [122] Jarny S, Roussel N, Rodts S, Bertrand F, Le Roy R and Coussot P 2005 Rheological behavior of cement pastes from MRI velocimetry *Cem. Concr. Res.* **35** 1873–81
- [123] Lynne Brower and Ferraris, Chiara F. 2003 Comparison of Concrete Rheometers: International Tests *Concr. Int.* 41–7
- [124] Marin G, Collyer A A and Clegg D W 1988 *Rheological Measurements* (Collyer, AA, Clegg, D. W., Eds)
- [125] Ferraris, C.F., Li, Z., Zhang, M-H. 2012 Development of a Reference Material for the Calibration of Cement Paste Rheometers *Accept. Publ. ASTM-Adv. Civ. Eng. Mater.*
- [126] Chan R W and Rodriguez M L 2008 A simple-shear rheometer for linear viscoelastic characterization of vocal fold tissues at phonatory frequencies *J. Acoust. Soc. Am.* **124** 1207–19
- [127] Struble L J and Schultz M A 1993 Using creep and recovery to study flow behavior of fresh cement paste *Cem. Concr. Res.* **23** 1369–79
- [128] Sun Z, Voigt T and Shah S P 2006 Rheometric and ultrasonic investigations of viscoelastic properties of fresh Portland cement pastes *Cem. Concr. Res.* **36** 278–87
- [129] Christopher G F, Yoo J M, Dagalakis N, Hudson S D and Migler K B 2010 Development of a MEMS based dynamic rheometer *Lab. Chip* **10** 2749–57
- [130] Ronaldson K A, Fitt A D, Goodwin A R H and Wakeham W A 2006 Transversely Oscillating MEMS Viscometer: The “Spider” *Int. J. Thermophys.* **27** 1677–95

- [131] Yao Q, Dong J and Ferreira P M 2007 Design, analysis, fabrication and testing of a parallel-kinematic micropositioning XY stage *Int. J. Mach. Tools Manuf.* **47** 946–61
- [132] Park J-S, Chu L L, Siwapornsathain E, Oliver A D and Gianchandani Y B 2000 Long throw and rotary output electro-thermal actuators based on bent-beam suspensions *Micro Electro Mechanical Systems, 2000. MEMS 2000. The Thirteenth Annual International Conference on (IEEE)* pp 680–5
- [133] Ferraris C F, Stutzman P, Winpigler J and Guthrie W 2011 *Certification of SRM 2492: Bingham Paste Mixture for Rheological Measurements* (US Department of Commerce, National Institute of Standards and Technology)
- [134] Gallagher C J 1952 Plastic deformation of germanium and silicon *Phys. Rev.* **88** 721–2
- [135] Fluent A 2009 12.0 User's Guide *User Inputs Porous Media* 6
- [136] Analog Device AD7747, 24-bit, 1 channel capacitance to digital converter
- [137] Anon DMEMS Dynamic MEMS Measurement Option for Wyko NT1100 Optical Profilers
- [138] Hackley V A and Ferraris C F 2001 *The use of nomenclature in dispersion science and technology* vol 960 (US Department of Commerce, Technology Administration, National Institute of Standards and Technology)
- [139] Paros J M 1965 How to design flexure hinges *Mach Des* **37** 151–6
- [140] Petersen K E 1982 Silicon as a mechanical material *Proc. IEEE* **70** 420–57
- [141] Jones R M 2006 *Buckling of bars, plates, and shells* (Bull Ridge Corporation)
- [142] Guide M U 1998 *The mathworks Inc Natick MA* **5**
- [143] Anon Agilent FFT analyzer 35670A 2 channel
- [144] Gao P, Swei S-M and Yuan Z 1999 A new piezodriven precision micropositioning stage utilizing flexure hinges *Nanotechnology* **10** 394
- [145] P. Gao, S-M Swei and Z. Yuan 1999 A new peizo-driven precision micropositioning stage utilizing flexure hinges *Nanotechnology* **10** 394–8
- [146] Anon PI Piezo Nano Positioning 2009 2-62–2-63
- [147] Banerjee A G and Gupta S K 2013 Research in Automated Planning and Control for Micromanipulation *IEEE Trans. Autom. Sci. Eng.* **10** 485–95

- [148] Chowdhury S, Thakur A, Svec P, Wang C, Losert W and Gupta S K 2014 Automated Manipulation of Biological Cells Using Gripper Formations Controlled By Optical Tweezers *IEEE Trans. Autom. Sci. Eng.* **11** 338–47
- [149] Wang C, Chowdhury S, Gupta S K and Losert W 2013 Optical micromanipulation of active cells with minimal perturbations: direct and indirect pushing *J. Biomed. Opt.* **18** 045001–045001
- [150] Thakur A, Chowdhury S, Švec P, Wang C, Losert W and Gupta S K 2014 Indirect pushing based automated micromanipulation of biological cells using optical tweezers *Int. J. Robot. Res.* 0278364914523690
- [151] Chowdhury S, Svec P, Wang C, Seale K T, Wikswo J P, Losert W and Gupta S K 2013 Automated Cell Transport in Optical Tweezers-Assisted Microfluidic Chambers *IEEE Trans. Autom. Sci. Eng.* **10** 980–9
- [152] Banerjee A G, Chowdhury S, Losert W and Gupta S K 2011 Survey on indirect optical manipulation of cells, nucleic acids, and motor proteins *J. Biomed. Opt.* **16** 051302–051302 – 11
- [153] Bista S, Chowdhury S, Gupta S K and Varshney A 2013 Using GPUs for Realtime Prediction of Optical Forces on Microsphere Ensembles *J. Comput. Inf. Sci. Eng.* **13** 031002–031002
- [154] Wang J, Yang Z and Yan G 2012 Silicon-on-insulator out-of-plane electrostatic actuator with in situ capacitive position sensing *J. MicroNanolithography MEMS MOEMS* **11** 033006–1
- [155] Cho H J and Ahn C H 2002 A bidirectional magnetic microactuator using electroplated permanent magnet arrays *Microelectromechanical Syst. J. Of* **11** 78–84
- [156] Liu C, Tsao T, Lee G-B, Leu J T, Yi Y W, Tai Y-C and Ho C-M 1999 Out-of-plane magnetic actuators with electroplated permalloy for fluid dynamics control *Sens. Actuators Phys.* **78** 190–7
- [157] Lagorce L K, Brand O and Allen M G 1999 Magnetic microactuators based on polymer magnets *Microelectromechanical Syst. J. Of* **8** 2–9
- [158] Patel J R and Chaudhuri A R 2004 Macroscopic Plastic Properties of Dislocation-Free Germanium and Other Semiconductor Crystals. I. Yield Behavior *J. Appl. Phys.* **34** 2788–99
- [159] Anon Denton infinity 22 e-beam evaporator
- [160] Anon Stylus Profilometer - Veeco Dektak-8, Characterization Equipment | NUFAB Administrator, Northwestern University Micro/Nano Fabrication Facility
- [161] Anon Polytec MSA-500 Micro System Analyzer

- [162] Greminger M A, Sezen A S and Nelson B J 2005 A four degree of freedom MEMS microgripper with novel bi-directional thermal actuators *Intelligent Robots and Systems, 2005.(IROS 2005). 2005 IEEE/RSJ International Conference on (IEEE)* pp 2814–9
- [163] Physik Instrumente Low Inertia 6DOF Parallel Kinematic Mechanisms (PKM)
- [164] Pizeo-University in Physik Intrumente Parallel and Serial Kinematics / Metrology
- [165] Kazuhiro Takahashi, Makoto Mita, Hiroyuki Fujita and Hiroshi Toshiyoshi 2007 Topological layer switch technique for monolithically integrated electrostatic XYZ-stage (IEEE) pp 651–4
- [166] Kim Y-S, Dagalakis N G and Gupta S K 2012 Design, fabrication, and characterization of a single-layer out-of-plane electrothermal actuator for SOI-MEMS applications *Proceedings of 2012 Performance Metrics for Intelligent Systems Workshop, College Park, MD, USA, March 20-22, 2012*
- [167] Kim Y S, Dagalakis N G and Gupta S K 2012 Design and Fabrication of a Three-DoF MEMS Stage Based on Nested Structures *Proceedings of the ASME 2012 International Design Engineering Technical Conference & Computers and Information in Engineering Conference IDETC/CIE 2012, Chicago, IL, USA*
- [168] Beer F P and Johnston Jr E R *Mechanics of materials, 1992* (McGraw-Hill, New York)
- [169] Cerda E and Mahadevan L 2003 Geometry and physics of wrinkling *Phys. Rev. Lett.* **90** 074302
- [170] Ebefors T, Mattsson J U, Kälvesten E and Stemme G 1999 A walking silicon micro-robot *Proc. Transducers '99* (Citeseer) pp 1202–5
- [171] Lantz M A, Rothuizen H E, Drechsler U, Haberle W and Despont M 2007 A vibration resistant nanopositioner for mobile parallel-probe storage applications *Microelectromechanical Syst. J. Of* **16** 130–9
- [172] Cormen T H, Leiserson C E, Rivest R L and Stein C 2009 *Introduction to Algorithms, 3rd Edition* (Cambridge, Mass: The MIT Press)